NATIONAL TECHNICAL UNIVERSITY OF ATHENS

DOCTORAL THESIS

Modeling and Reliability Assessment of Rocking Structures under Seismic Loading

Author:
Spyridon DIAMANTOPOULOS

Supervisor:
Dr. Michalis FRAGIADAKIS

A Thesis submitted in fulfillment of the requirements
for the degree of Doctor of Philosophy
in the
Laboratory for Earthquake Engineering
School of Civil Engineering

May 2022

NATIONAL TECHNICAL UNIVERSITY OF ATHENS

DOCTORAL THESIS

Modeling and Reliability Assessment of Rocking Structures under Seismic Loading

Author:
Spyridon DIAMANTOPOULOS

Supervisor:
Dr. Michalis FRAGIADAKIS

A Thesis submitted in fulfillment of the requirements
for the degree of Doctor of Philosophy
in the
Laboratory for Earthquake Engineering
School of Civil Engineering

May 2022

ΕΘΝΙΚΟ ΜΕΤΣΟΒΙΟ ΠΟΛΥΤΕΧΝΕΙΟ

ΔΙΔΑΚΤΟΡΙΚΗ ΔΙΑΤΡΙΒΗ

Προσομοίωση και Ανάλυση Αξιοπιστίας Λικνιζόμενων Κατασκευών υπό Σεισμική Φόρτιση

Συγγραφέας:
Σπυρίδων ΔΙΑΜΑΝΤΟΠΟΥΛΟΣ

Επιβλέπων:
Δρ. Μιχάλης ΦΡΑΓΚΙΑΔΑΚΗΣ

Η εργασία υποβλήθηκε σύμφωνα με τις απαιτήσεις για τον επιστημονικό τίτλο του Διδάκτορα Μηχανικού
στο

Εργαστήριο Αντισεισμικής Τεχνολογίας
Σχολή Πολιτικών Μηχανικών

Μάιος 2022

Advisory committee:

Michalis Fragiadakis
Associate Professor, NTUA (Supervisor)

Ioannis Psycharis
Emeritus Professor, NTUA

Anastasios Sextos
Professor, University of Bristol, UK

Examination committee:

Michalis Fragiadakis
Associate Professor, NTUA (Supervisor)

Ioannis Psycharis
Emeritus Professor, NTUA

Anastasios Sextos
Professor, University of Bristol, UK

Ioannis Stefanou
Professor, Ecole Centrale de Nantes

Elias Dimitrakopoulos
Associate Professor, Hong Kong University of Science and Technology

Haris Mouzakis
Associate Professor, NTUA

Dimitrios Vamvatsikos
Associate Professor, NTUA

"Scientists dream about doing great things. Engineers do them."

James A. Michener

Abstract

Despite the apparent lack of a mechanism to resist lateral forces, rocking structures have a remarkable capacity against earthquake loading. The Thesis presents a novel modeling approach for the seismic response assessment of free-standing, rigid or flexible, pure rocking systems. The simplified models adopted use beam elements which are connected to a nonlinear rotational spring with negative stiffness that describes the self-centering capacity of the rocking members. The loss of energy at impact is treated with an "event-based" approach consistent with Housner's theory. The efficiency and the accuracy of the proposed modeling is demonstrated with the aid of carefully chosen case studies either using simple wavelets or historical ground motion records. This modeling approach is extended to rocking frames providing a holistic approach suitable for modeling a variety of rocking systems.

In addition, the Thesis presents for the first time a fully performance-based seismic reliability and risk assessment framework for freestanding structural components and contents that can be modeled as rocking rigid blocks. The seismic response of building contents depends on several parameters such as the geometry of the object, the dynamic characteristics of the building and the storey that the object is located. The main interest is focused on the capped structure-content reliability assessment. The procedure of risk and fragility assessment considering the symmetric rocking blocks is extended to asymmetric blocks while the cases of arrays of freestanding columns capped with an architrave and rocking frames with unequal in height columns are investigated. In the latter case one more Intensity Measure (IM) is examined.

The protection of cultural heritage structures and museum treasures against earthquakes is a subject of top priority. Large scale shake table tests, that took place at CEA, Saclay, are presented on cultural heritage assets emphasizing on the use computing models in tandem with experimental testing. More specifically, an extensive experimental campaign on the seismic response of artefacts, with emphasis on statues and busts is presented. The aim is to understand the seismic response of statues and busts and then develop novel and cost-effective risk mitigation schemes for improving the seismic resilience of museum valuable contents. Both non-isolated and seismically isolated artefacts here considered.

Εκτεταμένη Περίληψη

Εισαγωγή

Το πρόβλημα της λικνιστικής συμπεριφοράς των κατασκευών, είναι ευρύ και σύνθετο και αφορά συνήθως σε απλά εδραζόμενα, άκαμπτα ή εύκαμπτα σώματα. Συγχρόνως, περιλαμβάνει τη σεισμική διερεύνηση της συμπεριφοράς περιεχομένων κατασκευών. Στα πρώτα στάδια της Διδακτορικής Διατριβής μελετήθηκε η συμπεριφορά ελεύθερα εδραζόμενων άκαμπτων σωμάτων. Ως άκαμπτα απλά εδραζόμενα σώματα μπορούν να θεωρηθούν τα περιεχόμενα μίας κατασκευής καθώς και μουσειακά εκθέματα. Η πιο απλή μορφή τέτοιων σωμάτων είναι τα ορθογωνικά στα οποία πραγματοποιήθηκε ανάλυση θεωρώντας λικνιστική κίνηση γύρω από δυο σημεία. Το πρόβλημα της λικνιστικής κίνησης εξαρτάται από τη γεωμετρία των σωμάτων και συγκεκριμένα από την παράμετρο μεγέθους και τη ραδινότητα. Αρχικά, επιλύθηκε η εξίσωση κίνησης απλά εδραζόμενων σωμάτων. Στην επίλυση αυτή υπεισέρχεται η απώλεια ενέργειας που λαμβάνει χώρα, σύμφωνα με πολλές προηγούμενες μελέτες, μόνο κατά τη στιγμή της κρούσης.

Για την επίλυση του προβλήματος του λικνισμού προτάθηκαν απλοποιητικά προσομοιώματα βασιζόμενα στη μέθοδο των Πεπερασμένων Στοιχείων κατάλληλα να προσομοιώσουν τη λικνιστική απόκριση άκαμπτων σωμάτων που εδράζονται σε μια άκαμπτη βάση. Στα προσομοιώματα υπεισέρχεται η απώλεια ενέργειας εισάγοντας τον συντελεστή αποκατάστασης. Η ανάλυση σε κάθε κρούση σταματά και επαναξεκινά με νέες αρχικές συνθήκες που συμπεριλαμβάνουν τη μειωμένη γωνιακή ταχύτητα με βάση τον συντελεστή αποκατάστασης. Μελετήθηκε, επίσης, η περίπτωση εύκαμπτων λικνιζόμενων σωμάτων όπου πρέπει να ληφθούν υπόψη μετακινήσεις λόγω κάμψης και οι οποίες προστίθενται στις μετακινήσεις λόγω κίνησης στερεού σώματος. Η ακρίβεια των αδρομερών μοντέλων που προτάθηκαν και χρησιμοποιήθηκαν στο πλαίσιο της Διατριβής ελέγχθηκε με προσομοιώσεις με εμπορικό πρόγραμμα Πεπερασμένων Στοιχείων όπου χρησιμοποιήθηκαν τετρακομβικά Πεπερασμένα Στοιχεία και στοιχεία επαφής με το έδαφος. Εξετάστηκε, επίσης, η απόκριση προεντεταμένων λικνιζόμενων υποστυλωμάτων. Σε συνέχεια των απλοποιητικών μοντέλων, έγινε επέκταση της προσομοίωσης για την περίπτωση προεντεταμένων σωμάτων με ένα τένοντα που διέρχεται από το κέντρο βάρους του υποστυλώματος. Η επέκταση έγινε με την τροποποίηση των παραμέτρων του προβλήματος και συγκεκριμένα της δυσκαμψίας των ισοδύναμων ελατηρίων.

Στη Διδακτορική Διατριβή μελετήθηκε επίσης το πρόβλημα των λικνιζόμενων πλαισίων που συναντώνται είτε σε λικνιζόμενες γέφυρες είτε σε κιονοστοιχίες αρχαίων ναών. Εξετάστηκαν διαφορετικές περιπτώσεις και μοντέλα τόσο ενός βαθμού ελευθερίας όσο και πιο λεπτομερή, όλα στηριζόμενα σε στοιχεία δοκού που συνδέονται με το έδαφος και με το κατάστρωμα/επιστύλιο με στροφικά ελατήρια. Πραγματοποιήθηκε προσομοίωση των διαφόρων περιπτώσεων λικνιζόμενων πλαισίων με άκαμπτο κατάστρωμα/επιστύλιο και με άκαμπτα ή εύκαμπτα υποστυλώματα. Επίσης, μελετήθηκε η περίπτωση χρήσης προεντεταμένων κατακόρυφων στοιχείων, η περίπτωση των δυο υποστυλωμάτων που μορφώνουν ένα πλαίσιο καθώς επίσης και το πρόβλημα πλαισίων με ανισοϋψή βάθρα.

Σε επόμενο στάδιο, η Διατριβή επικεντρώθηκε στην εκτίμηση της σεισμικής τρωτότητας και της σεισμικής διακινδύνευσης αφενός σε λικνιζόμενα πλαίσια και αφετέρου σε περιεχόμενα κατασκευών. Αρχικά, παρουσιάστηκε το πρόβλημα της σεισμικής τρωτότητας. Διερευνήθηκαν τα διάφορα Μέτρα Έντασης και οι διάφορες Παράμετροι Απόκρισης της κατασκευής ενώ παρουσιάστηκαν οι μέθοδοι με τις οποίες μπορείς να προσεγγίσεις το πρόβλημα. Στόχος ήταν να προταθεί ένα ολοκληρωμένο πλαίσιο για τη σεισμική τρωτότητα πλαισιακών κατασκευών με έμφαση σε περιεχόμενα κατασκευών.

Τα πολυώροφα κτίρια, όπως τα μουσεία, έχουν συχνά περιεχόμενα που είναι πολύτιμα ή αντικείμενα που πιθανές βλάβες τους κατά τη διάρκεια ενός σεισμού προκαλούν σημαντικές συνέπειες. Παρουσιάστηκε ένα νέο πλαίσιο εκτίμησης της αξιοπιστίας και της διακυνδύνευσης δομικών στοιχείων και περιεχομένων που μπορούν να θεωρηθούν άκαμπτα λικνιζόμενα σώματα. Η σεισμική απόκριση των περιεχομένων κατασκευών εξαρτάται από πολλές παραμέτρους όπως η γεωμετρία του αντικειμένου, τα δυναμικά χαρακτηριστικά του κτιρίου και του ορόφου που βρίσκεται τοποθετημένο ένα αντικείμενο. Με βάση το προτεινόμενο πλαίσιο, λαμβάνεται η απόκριση κάθε ορόφου και στη συνέχεια υπολογίζεται η απόκριση των περιεχομένων χρησιμοποιώντας ως εδαφική επιτάχυνση την χρονοϊστορία απόκρισης κάθε ορόφου. Η κατασκευή υποβάλλεται σε πλήθος δυναμικών αναλύσεων με τη βοήθεια μιας τροποποιημένης μορφής της μεθόδου Incremental Dynamic Analysis (IDA) και στη συνέχεια κατασκευάζονται οι καμπύλες τρωτότητας των λικνιζόμενων σωμάτων για κάθε όροφο. Διαφορετικές προσεγγίσεις για την εκτίμηση της σεισμικής τρωτότητας συζητήθηκαν ενώ διερευνήθηκαν οι λεπτομέρειες της επίλυσης του προβλήματος. Παρουσιάστηκε, τέλος, μια απλοποιημένη προσέγγιση, όπου η τρωτότητα των περιεχομένων και της κατασκευής εξετάζεται ξεχωριστά και στη συνέχεια γίνεται συνένωση. Η προτεινόμενη μεθοδολογία συνδυάζει τις υπάρχουσες καμπύλες τρωτότητας και έτσι είναι κατάλληλη για την γρήγορη αξιολόγηση της αξιοπιστίας των περιεχομένων ενός κτιρίου, προσφέροντας επαρκείς εκτιμήσεις της σεισμικής διακινδύνευσης.

Τέλος, κατά τη διάρκεια της Διδακτορικής Διατριβής οργανώθηκαν και πραγματοποιήθηκαν πειραματικές διερευνήσεις σε σεισμικό προσομοιωτήρα που έλαβαν χώρα σε ερευνητικό ινστιτούτο στη Γαλλία και έγινε επεξεργασία των δεδομένων σε συνεργασία με την ερευνητική ομάδα που συμμετείχε σε αυτά.

Λικνιζόμενα σώματα

Στην περίπτωση των λικνιζόμενων σωμάτων, στην παρούσα Διατριβή παρουσιάζονται για πρώτη φορά τέσσερα μοντέλα Πεπερασμένων Στοιχείων, που ονομάζονται *Spring Model* (SM), για την προσομοίωση της σεισμικής απόκρισης ελεύθερα εδραζόμενων σωμάτων, όλα ακολουθώντας το Σχήμα 1α, που θα συζητηθεί αναλυτικά σε επόμενη ενότητα. Οι τρεις πρώτες παραλλαγές προτείνουν έναν μονοβάθμιο ταλαντωτή και η τέταρτη είναι ένα μοντέλο κατανεμημένων μαζών. Αρχικά, παρουσιάζεται η ευρωστία των μοντέλων για άκαμπτα σώματα υπό στατική φόρτιση και απλές παλμικές διεγέρσεις, ενώ στις ενότητες που ακολουθούν εξετάζουμε τη συμπεριφορά κάτω από πραγματικές σεισμικές διεγέρσεις του εδάφους μελετώντας και τα εύκαμπτα σώματα.

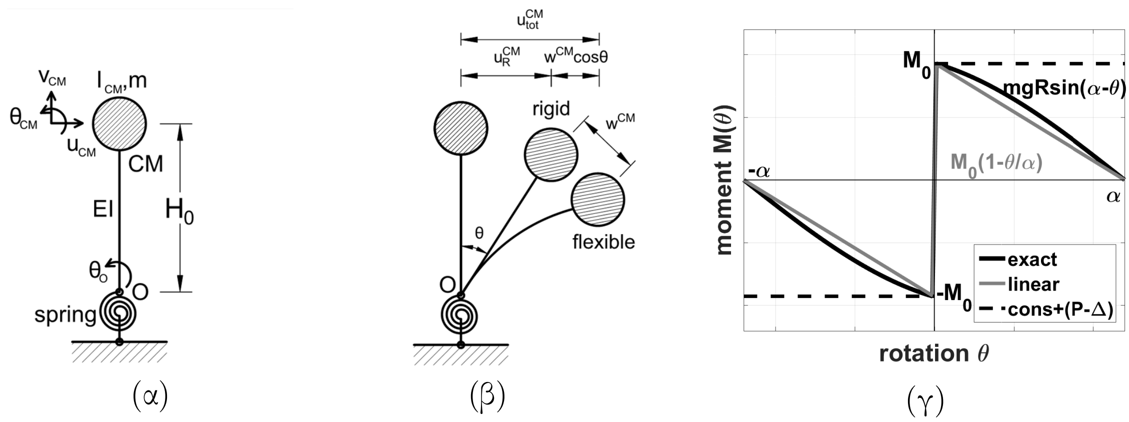

Σχήμα 1: (α) Περιγραφή του προτεινόμενου μοντέλου. (β) Παραμορφωμένη κατάσταση άκαμπτου και εύκαμπτου σώματος. (γ) Καμπύλες ροπής-στροφής ενός λικνιζόμενου σώματος ($M_0 = mgRsin\alpha$).

Το πρώτο μοντέλο συμβολίζεται ως SM1 (Spring Model 1) και φαίνεται στο Σχήμα 2. Το μοντέλο αυτό είναι ένας μονοβάθμιος ταλαντωτής με ύψος ίσο με την απόσταση του

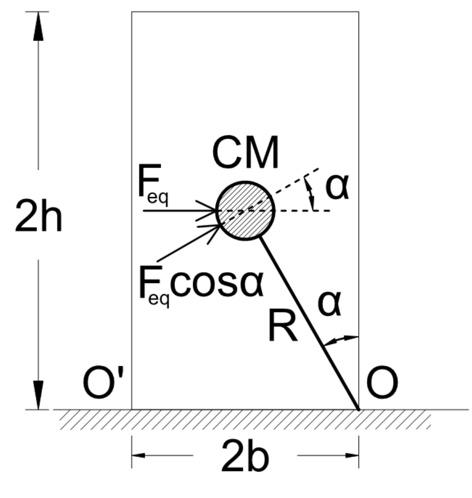

Σχήμα 2: *Spring Model* 1(*SM*1) για την προσομοίωση λικνιζόμενου σώματος.

κέντρου μάζας (CM) από το σημείο περιστροφής, $H_0 = R$. Η σεισμική δύναμη αναλύεται σε δύο ορθογώνιες συνιστώσες. Υποθέτουμε ότι η κάθετη στο R συνιστώσα είναι αυτή που θα εισέλθει στους υπολογισμούς. Επομένως, εάν η σεισμική δύναμη είναι $-m\ddot{u}_g$, μόνο η συνιστώσα $F_{eq} = -m\ddot{u}_g cos\alpha$ θεωρείται στο $SM1$. Χρησιμοποιώντας το μοντέλο του σχήματος 1α, το $SM1$ υλοποιείται αν ορίσουμε: το ύψος του ταλαντωτή ίσο με $H_0 = R = \sqrt{b^2 + h^2}$ και τη στροφική ροπή αδράνειας του κέντρου μάζας CM ίση με $I_{CM} = (1/3)mR^2$ και πολλαπλασιάσουμε την σεισμική καταγραφή με $cos\alpha$.

Το δεύτερο μοντέλο που προτείνεται προσδιορίζεται ως $SM2$ και περιγράφεται εννοιολογικά στο Σχήμα 3. Το ύψος H_0 του μονοβάθμιου ταλαντωτή είναι ίσο με το μισό του ύψους του μπλοκ ($H_0 = h$), ενώ ως πόλος περιστροφής O ορίζεται η προβολή του κέντρου μάζας CM στη βάση, ή ισοδύναμα, ο κόμβος CM βρίσκεται ακριβώς πάνω από το σημείο περιστροφής. Εάν η στροφική ροπή αδράνειας ως προς το CM είναι $I_{CM} = (1/3)mR^2$, αφού το CM μετατοπίζεται οριζόντια σε απόσταση ίση με b, η στροφική ροπή αδράνειας για το μοντέλο $SM2$ θα είναι: $I'_{CM} = (1/3)mR^2 + mb^2$. Με αναφορά στο Σχήμα 1α, το $SM2$ διαμορφώνεται αν ορίσουμε: $H_0 = h$, $I_{CM} = (1/3)mR^2 + mb^2$, ενώ δεν χρειάζεται να πολλαπλασιάσουμε την κίνηση του εδάφους με κάποιο μέγεθος, σε αντίθεση με το $SM1$.

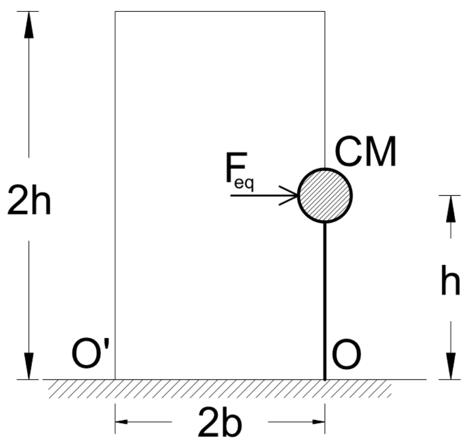

Σχήμα 3: *Spring Model* 2 ($SM2$) για την προσομοίωση λικνιζόμενου σώματος.

Στο μοντέλο $SM3$ ($SpringModel3$), υποθέτουμε ότι η μάζα του σώματος είναι συγκεντρωμένη στο σημείο περιστροφής και ότι η σεισμική φόρτιση εφαρμόζεται απευθείας στον στροφικό βαθμό ελευθερίας του κόμβου στροφής. Η λογική αυτής της προσέγγισης πηγάζει από την άμεση σύγκριση της εξίσωσης κίνησης του άκαμπτου σώματος και της εξίσωσης κίνησης του μονοβάθμιου ταλαντωτή $m\ddot{u} + c\dot{u} + ku = -m\ddot{u}_g$ που λύνει ένα λογισμικό Πεπερασμένων Στοιχείων. Συγκρίνοντας με την εξίσωση κίνησης του άκαμπτου σώματος και υποθέτοντας ότι ο μοναδικός βαθμός ελευθερίας είναι η στροφή θ, αντικαθιστούμε τη μάζα m με την στροφική ροπή αδράνειας I_0 και εφαρμόζουμε τη σεισμική καταγραφή στο στροφικό βαθμό ελευθερίας. Για το άκαμπτο σώμα, το ισοδύναμο του ελαστικού όρου ku ορίζεται μέσω της σχέσης $M - \theta$ του ελατηρίου και, επομένως, πρέπει να προσδιορίσουμε μόνο τον όρο ανατροπής που εκφράζεται ως: $M_{otn}^{SM3} = I_0\ddot{\theta}_g = \lambda I_0\ddot{u}_g$. Η σταθερά λ προκύπτει σε σύγκριση με τον όρο της ροπής ανατροπής του σώματος (Εξ. 2.3):

$$M_{otn}^{RB} - M_{otn}^{SM3} \;=\; 0 \Leftrightarrow m\ddot{u}_g R cos(\alpha-\theta) = \lambda I_0 \ddot{u}_g \Leftrightarrow \lambda = \frac{mRcos(\alpha-\theta)}{I_0} \tag{1}$$

Η έκφραση για το λ περιέχει την στροφή θ που είναι ένα άγνωστος για το πρόβλημα μας. Εφόσον $\theta \in [0, \alpha]$, μπορούμε να αφαιρέσουμε το θ ορίζοντας το ίσο με τις οριακές τιμές του, $\theta = 0$ ή $\theta = \alpha$. Αυτό είναι πάλι μια προσέγγιση, αλλά η ακρίβεια αρκετά καλή. Πιο συγκεκριμένα, εξετάζοντας τη σχέση στατικής δύναμης-στροφής του $SM3$:

$$M_{otn}^{SM3} = M_{res}^{SM3} \Leftrightarrow \lambda I_0 \ddot{u}_g = mgRsin(\alpha-\theta) \Leftrightarrow \lambda I_0 m\ddot{u}_g = m^2 gRsin(\alpha-\theta) \Leftrightarrow \\ \frac{F^{SM3}}{mg} = \frac{mRsin(\alpha-\theta)}{\lambda I_0} \tag{2}$$

Ορίζοντας $\lambda_{\theta=0} = mRcos(\alpha)/I_0$ ή $\lambda_{\theta=\alpha} = mR/I_0$, η σχέση δύναμης-στροφής γίνεται:

$$\frac{F_{\theta=0}^{SM3}}{mg} = \frac{mRsin(\alpha-\theta)}{\lambda_{\theta=0} I_0} = \frac{sin(\alpha-\theta)}{cos(\alpha)} \tag{3}$$

$$\frac{F_{\theta=\alpha}^{SM3}}{mg} = \frac{mRsin(\alpha-\theta)}{\lambda_{\theta=\alpha} I_0} = sin(\alpha-\theta) \tag{4}$$

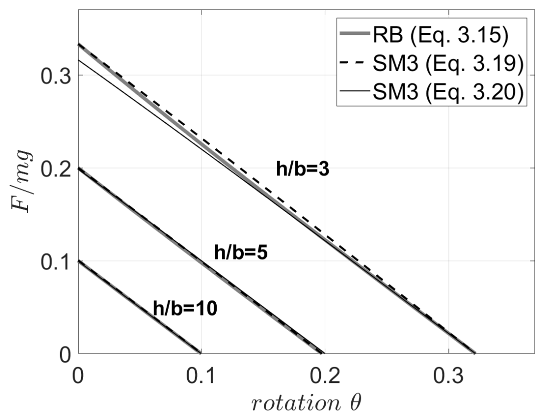

(α)

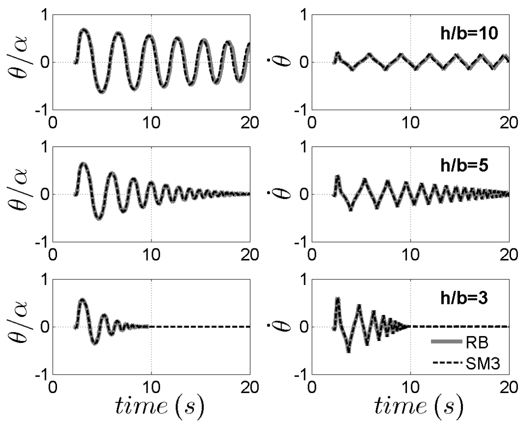

(β)

Σχήμα 4: (α) Σύγκριση καμπυλών δύναμης-στροφής για το μοντέλο $SM3$ χρησιμοποιώντας είτε $\lambda_{\theta=0}$ είτε $\lambda_{\theta=\alpha}$. (β) Σύγκριση των χρονοϊστοριών στροφών (αριστερά), και ταχυτήτων (δεξιά) μεταξύ του RB και του μοντέλου $SM3$ για ένα σώμα με $R = 2m$ και $h/b = 10, 5$ και 3 που υποβάλλεται σε παλμό $Ricker$ $(\alpha_p = 3.6g\tan\alpha,\ \omega_p = 3\pi rad/s)$.

Το σχήμα 4α συγκρίνει τις παραπάνω εκφράσεις με αυτές της λύσης του RB. Και τα δύο $\lambda_{\theta=0}$ και $\lambda_{\theta=\alpha}$ είναι πιθανά, αλλά το $\lambda_{\theta=0}$ είναι ελαφρώς πιο ακριβές και επομένως προτιμάται. Όπως και πριν, το σχήμα 4β συγκρίνει τη χρονοϊστορία απόκρισης των θ και $\dot{\theta}$ για ένα άκαμπτο σώμα με $R = 2m$ και έναν συμμετρικό παλμό $Ricker$ δείχνοντας πως η σύγκλιση με τη λύση RB είναι εξαιρετική για $\lambda_{\theta=0}$.

Το τέταρτο μοντέλο είναι το μοντέλο κατανεμημένων μαζών ($mmSM$) που στηρίζεται ξανά στην ύπαρξη ενός μη-γραμμικού ελατηρίου στη βάση όπως φαίνεται στο Σχήμα 5. Το προτεινόμενο μοντέλο προκύπτει ακολουθώντας μια προσέγγιση παρόμοια είτε με το $SM1$ είτε με το $SM2$. Και στις δύο περιπτώσεις, το μοντέλο αποτελείται από n μάζες που κατανέμονται είτε κατά μήκος της διαγωνίου του σώματος που συνδέει το σημείο περιστροφής με την απέναντι επάνω γωνία του σώματος (Εικόνα 5α) είτε καθ' ύψος του σώματος (Εικόνα 5β). Η δεύτερη προσέγγιση είναι κοντά, αλλά όχι παρόμοια, με το μοντέλο που προτείνουν οι Vassiliou et al., 2016. Στην πρώτη περίπτωση, το σύστημα είναι ένας πρόβολος με ύψος $2R$ και n μάζες στους μεταφορικούς βαθμούς ελευθερίας η καθεμία ίση με $m_i = m/n$ και μηδενικές ροπές αδράνειας, $I_{n,i} = 0$. Ομοίως με το μοντέλο $SM1$, η επιτάχυνση του εδάφους πολλαπλασιάζεται επί $cos\alpha$. Στη δεύτερη περίπτωση, ο πρόβολος έχει ύψος $2h$ και οι κόμβοι έχουν: μάζα $m_i = m/n$, και στροφική ροπή αδράνειας $I_{n,i} = m_i b^2$, όπου b είναι η μετατόπιση κάθε μάζας m_i από μια κατακόρυφη γραμμή που διέρχεται από το σημείο περιστροφής. Για ένα ορθογώνιο σώμα, το b είναι ίσο με το μισό πλάτος του σώματος. Στη δεύτερη περίπτωση, η σεισμική καταγραφή δεν πολλαπλασιάζεται με κάποιον όρο.

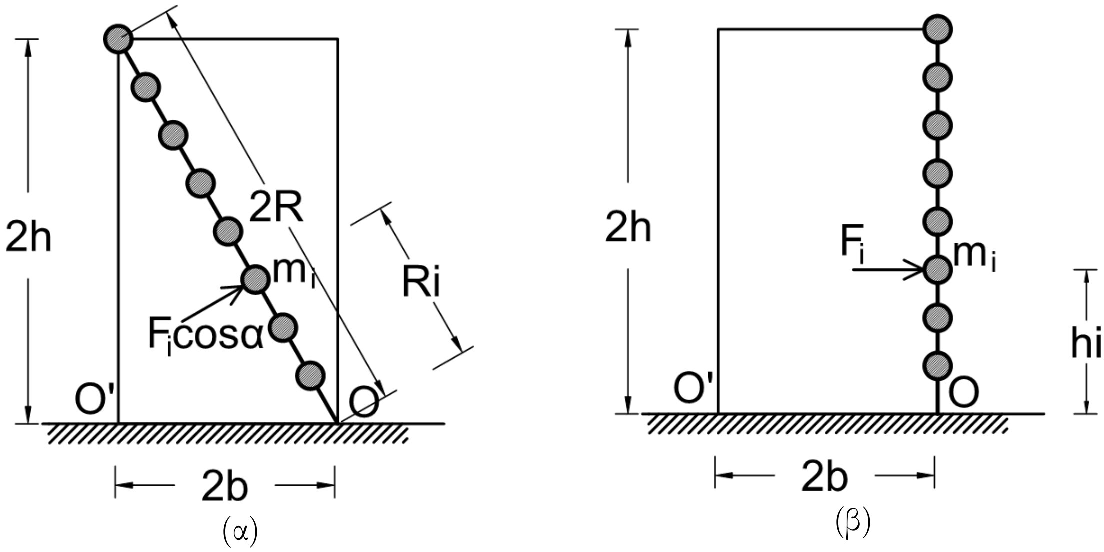

Σχήμα 5: *Multimass Spring Model* ($mmSM$): (α) Η μάζα είναι κατανεμημένη στη διαγώνιο, (β) η μάζα είναι κατανεμημένη καθ' ύψος του σώματος.

Συμπεριφορά λικνιζόμενων πλαισιακών κατασκευών σε σεισμική φόρτιση

Σε συνέχεια των απλοποιητικών μοντέλων για λικνιζόμενα σώματα παρουσιάζεται η προσομοίωση λικνιζόμενων πλαισιακών κατασκευών που αποτελούνται από άκαμπτες ή εύκαμπτες κολώνες που είναι είτε ελεύθερα εδραζόμενες είτε προεντεταμένες. Η μοντελοποίηση επεκτείνεται σε λικνιζόμενα πλαίσια με N κολώνες/κίονες και πλαίσια με υποστυλώματα διαφορετικού ύψους.

Για ένα λικνιζόμενο πλαίσιο με άκαμπτα στοιχεία προτείνεται η προσομοίωση όπως φαίνεται στο Σχήμα 6α. Το προσομοίωμα αυτό είναι μια επέκταση του μοντέλου για άκαμπτα σώματα που προτάθηκε στη Διατριβή και παρουσιάστηκε αναλυτικά και κάποιες γραμμές πιο πάνω. Το προσομοίωμα αποτελείται από μη-γραμμικά στροφικά ελατήρια στις διεπιφάνειες λικνισμού, δηλαδή μεταξύ του υποστυλώματος και του εδάφους και επίσης μεταξύ της κορυφής του υποστυλώματος και του καταστρώματος/επιστυλίου. Εκτός από τις γεωμετρικές παραμέτρους που φαίνονται στο σχήμα 6α, είναι επίσης απαραίτητο να οριστεί: (i) το μητρώο μάζας, δηλαδή η μεταφορική μάζα και η στροφική ροπή αδράνειας, και (ii) η σχέση $M - \theta$ των στροφικών ελατηρίων.

Δεδομένου ότι τα σώματα που συνιστούν το πλαίσιο είναι άκαμπτα, η μάζα μπορεί να συγκεντρωθεί στο μέσο ύψος της κάθε κολώνας όπως φαίνεται στο Σχήμα 6α. Για το λόγο αυτό, εισάγονται δύο βοηθητικοί κόμβοι, C_1, C_2. Αυτοί οι κόμβοι μπορούν να αμεληθούν εάν η μάζα των στύλων θεωρηθεί μηδενική ή εάν προτιμηθεί η προσέγγιση διανεμημένης μάζας, για την οποία γίνεται συζήτηση παρακάτω. Όπως φαίνεται στο Σχήμα 6β, η απόσταση μεταξύ του πάνω και του κάτω σημείων περιστροφής, δηλαδή των κόμβων D_1 (ή D_2), από O_1 (ή O_2), είναι $2R$, όπου $R^2 = b^2 + h^2$. Έτσι, για τους στύλους, το μητρώο μάζας θα σχηματιστεί τοποθετώντας μάζα ίση με m_c στους κόμβους C_1 και C_2 και στροφική ροπή αδράνειας αντίστοιχα ίση με $I_{C1} = I_{C2} = (1/3)m_c R^2 + m_c b^2$. Για την δοκό, οι αντίστοιχοι κόμβοι είναι D_1 και D_2, όπου η μεταφορική μάζα θα είναι $m_b/2$ και η συγκεντρωμένη στροφική $I_{D1s} = I_{D2s} = (m_b/2)(2b)^2$ (Εικόνα 6β).

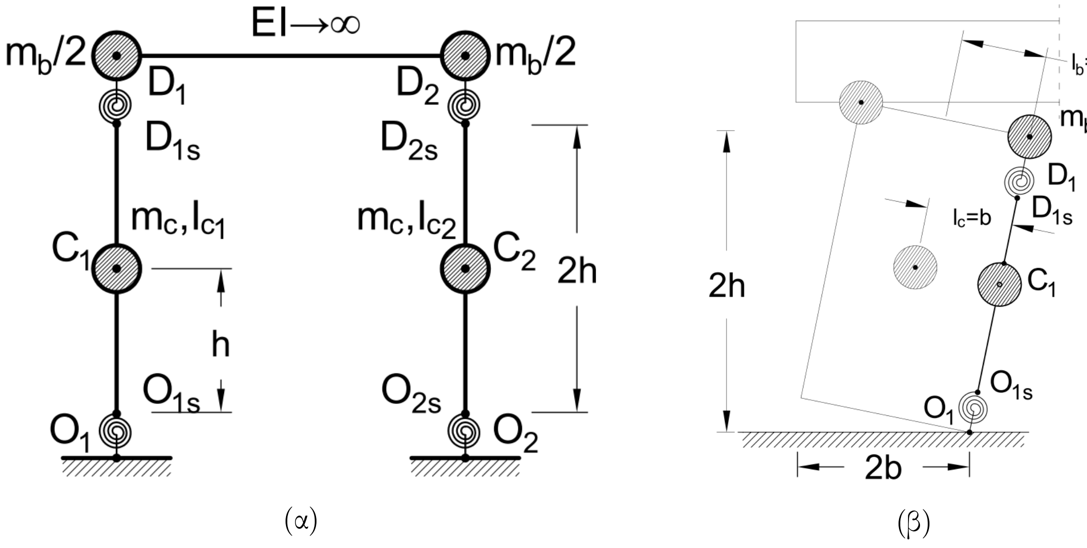

Σχήμα 6: (α) Προτεινόμενο προσομοίωμα για λικνιζόμενα πλαίσια με άκμαπτα μέλη, (β) Λεπτομέρεια του προτεινόμενου προσομοιώματος.

Στο Σχήμα 6α, οι κόμβοι στη διεπαφή εμφανίζονται σε ζεύγη master-slave, όπου ο δείκτης "s" χρησιμοποιείται για τον ορισμό του δευτερεύοντος κόμβου. Κατά γενικό κανόνα, οι ποσότητες που προέρχονται από τους στύλους προστίθενται στους δευτερεύοντες κόμβους D_{1s} (ή D_{2s}), ενώ οι ποσότητες που αναφέρονται στη δοκό (μάζα, φορτία, κλπ.)

τοποθετούνται στους κύριους κόμβους, π.χ D_1 (ή D_2). Τα μη-γραμμικά ελατήρια αρνητικής δυσκαμψίας τοποθετούνται στις επιφάνειες ταλάντωσης κάθε υποστυλώματος, δηλαδή στη βάση, O_1, O_2 και στη σύνδεση στύλου-επιστυλίου, D_1, D_2 (Εικόνα 6).

Η απορρόφηση ενέργειας για το προτεινόμενο προσομοίωμα επίπεδου πλαισίου ακολουθεί την προσέγγιση *"event − based"*, παρόμοια με αυτή που υιοθετήθηκε για το λικνιζόμενο σώμα. Επομένως, απώλεια ενέργειας συμβαίνει μόνο όταν συμβεί κρούση, η οποία λαμβάνει χώρα όταν το πρόσημο της στροφής αντιστρέφεται. Τη στιγμή της κρούσης, η ανάλυση διακόπτεται και στη συνέχεια συνεχίζεται χρησιμοποιώντας ως αρχική ταχύτητα των επόμενων χρονικών βημάτων, το γινόμενο της ταχύτητας πριν από την κρούση κάθε βαθμού ελευθερίας επί τον συντελεστή αποκατάστασης (Εξ.2.14). Απαιτείται προσοχή στη σύνδεση στύλου-επιστυλίου όπου μόνο η μεταφορική ταχύτητα του κύριου κόμβου και η γωνιακή ταχύτητα του υποτελούς κόμβου πρέπει να πολλαπλασιάζονται με η_{frame}. Αυτό οφείλεται στο γεγονός ότι η ροπή επαναφοράς έχει συγκεντρωθεί στον δευτερεύοντα κόμβο.

Στην περίπτωση των πλαισίων με εύκαπτους στύλους, η απλούστερη προσέγγιση είναι να αμεληθεί η μάζα του στύλου, καθώς μπορεί να είναι σημαντικά μικρότερη από αυτή του καταστρώματος/επιστυλίου. Ωστόσο, εάν ληφθεί υπόψη η μάζα, μπορεί είτε να κατανεμηθεί σε n κόμβους καθ' ύψος (Σχήμα 7, αριστερή στήλη) ή αντί αυτού να χρησιμοποιηθεί μια προσέγγιση διανεμημένης μάζας, στην οποία η μάζα κατανέμεται καθ' ύψος του μέλους (Εικόνα 7, δεξιά). Στην πρώτη περίπτωση, η μάζα κατανέμεται σε n κόμβους ίσου διαστήματος που έχουν μάζα $m_i = m_c/n$. Στη δεύτερη περίπτωση, η μάζα κατανέμεται καθ' ύψος, δηλαδή ως $\bar{m} = A\ rho/2h$ και $m_c = A\ rho$, όπου rho είναι η πυκνότητα του υλικού και A η διατομή του στύλου. Οι δύο επιλογές συζητούνται παρακάτω.

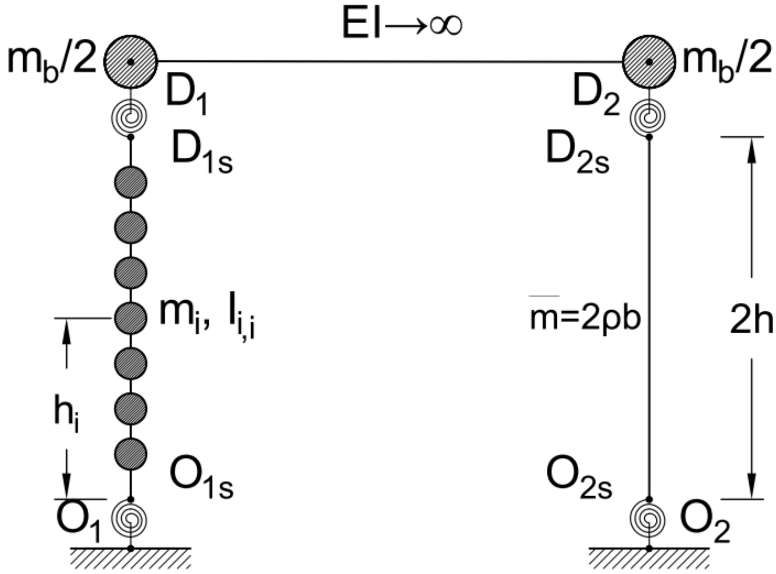

Σχήμα 7: Λικνιζόμενο πλαίσιο με εύκαμπτες κολώνες: η μάζα είναι συγκεντρωμένη σε n κόμβους (αριστερά), ή διαφορετικά μια άλλη παραλλαγή χρησιμοποιείται αναλόγως και την δυνατότητα του λογισμικού (δεξιά).

Η πρώτη επιλογή είναι να συγκέντρωσουμε τη μάζα σε κόμβους ίσης απόστασης n. Επομένως, η μεταφορική μάζα κάθε κόμβου θα είναι $m_i = m_c/n$ και η στροφική ροπή αδράνειας του κόμβου i σε σχέση με έναν άξονα που διέρχεται από το σημείο περιστροφής O είναι $I_{0,i} = m_i h_i^2$. Αυτή η προσέγγιση έχει κάποια, μικρή ευαισθησία, στον αριθμό των μαζών όπως φάνηκε για το ελεύθερα εδραζόμενο σώμα από Diamantopoulos and Fragiadakis, 2019. Επιπλέον, εάν η απόσταση μάζας i από τον πόλο περιστροφής είναι $h_i = (2i/n)Rcos\alpha$, η συνολική ροπή αδράνειας κάθε στύλου ορίζεται ως: $I_0 = \sum m_i h_i^2 = (4/3)m_c R^2 cos^2\alpha$. Ωστόσο, η ακριβής τιμή της συνολικής στροφικής ροπής αδράνειας είναι αυτή της απλά εδραζόμενης κολώνας, δηλαδή $I_0' = (4/3)m_c R^2$. Για να αφαιρεθεί αυτό το μικρό σφάλμα, μια πρόσθετη ποσότητα ίση με $\delta I_{0,i} = (I_0' - I_0)/n = (4/3n)m_c R^2 \sin^2\alpha$ προστίθεται σε καθέναν από τους κόμβους n.

Η προτεινόμενη μεθοδολογία επεκτείνεται σε πλαίσια με προεντεταμένα βάθρα καθώς επίσης σε πλαίσια με υποστυλώματα τα οποία δεν εχουν το ίδιο ύψος, είναι προεντεταμένα ή/και αποτελούνται από περισσότερους από δύο στύλους (N στύλοι). Η διαδικασία επέκτασης περιγράφεται αναλυτικά στο αντίστοιχο κεφάλαιο.

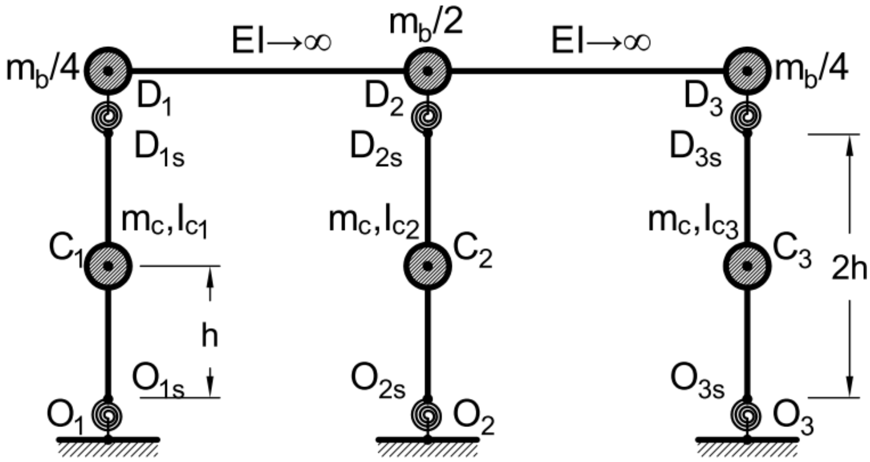

Σχήμα 8: Αναλυτική προσομοίωση λικνιζόμενου πλαισίου με τρία υποστυλώματα ($N = 3$).

Ανάλυση αξιοπιστίας λικνιζόμενων κατασκευών

Οι καμπύλες τρωτότητας είναι ένα πολύτιμο εργαλείο για την εκτίμηση της σεισμικής διακινδύνευσης ενός συστήματος. Η ανάλυση τρωτότητας αναπτύχθηκε αρχικά για την ανάλυση της αξιοπιστίας των πυρηνικών σταθμών σε μια προσπάθεια να διαχωριστεί το τμήμα της στατικής ανάλυσης από την ανάλυση σεισμικού κινδύνου που διενεργείται από Σεισμολόγους. Η ανάλυση τρωτότητας απαιτεί τον υπολογισμό των πιθανοτήτων υπέρβασης ενός αριθμού οριακών καταστάσεων. Επομένως, η σεισμική τρωτότητα ενός συστήματος είναι η πιθανότητα μια παράμετρος απόκρισης (EDP) να υπερβεί μια οριακή τιμή edp και ορίζεται ως:

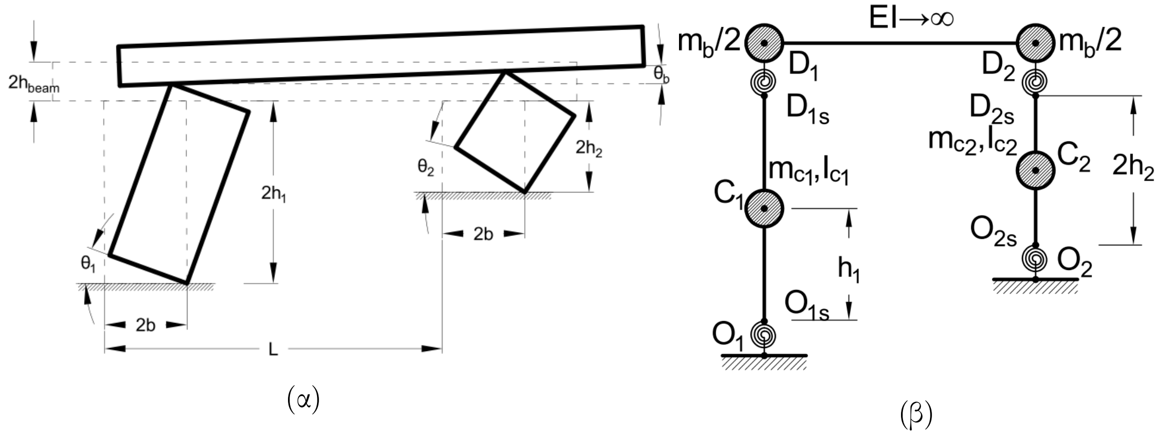

Σχήμα 9: (α) Γεωμετρία ενός πλαισίου με βάθρα διαφορετικού ύψους και (β) προτεινόμενη προσομοίωση ενός λικνιζόμενου πλαισίου με άκμπτα βάθρα διαφορετικού ύψους.

$$F_R(IM) = P(EDP > edp|IM) \tag{5}$$

Για να υπολογιστεί σωστά το ολοκλήρωμα της Εξ. 5 προσδιορίζονται τρεις πιθανοί τρόποι απόκρισης: (i) το σύστημα παραμένει σε ηρεμία κατά τη διάρκεια του σεισμού, (ii) λικνίζεται και (iii) ανατρέπεται. Χρησιμοποιώντας το Θεώρημα Ολικής Πιθανότητας, η τρωτότητα (Εξ. 5) υπολογίζεται ως:

$$F_R = P(EDP|NoUplift)P_{NoUplift} + P(EDP|Uplift)P_{Uplift} + P(EDP|Ovtn)P_{Ovtn} \tag{6}$$

όπου $P(EDP|NoUplift)$, $P(EDP|Uplift)$ και $P(EDP|Ovtn)$ είναι οι πιθανότητες υπέρβασης μιας οριακής κατάστασης όταν υπάρχει ηρεμία, λικνισμός και ανατροπή, αντίστοιχα. Για σώματα που δεν θα λικνίζονται (βρίσκονται σε ηρεμία), $P(EDP|NoUplift) = 0$, ενώ για σώματα που ανατρέπονται $P(EDP|Ovtn) = 1$. Επομένως, ο υπολογισμός της τρωτότητας απλοποιείται σε:

$$F_R = P(EDP \geq edp|Uplift)(1 - P_{Ovtn} - P_{NoUplift}) + P_{Ovtn} \tag{7}$$

Υποθέτοντας ότι τα δεδομένα των περιπτώσεων που λικνίζονται ακολουθούν λογαριθμοκανονική κατανομή, το $P(EDP \geq edp|Uplift)$ μπορεί να υπολογιστεί αναλυτικά μόλις υπολογιστεί ο μέσος όρος και η τυπική απόκλιση των λογαρίθμων των Παραμέτρων Απόκρισης, τα οποία συμβολίζονται ως μ_{logEDP} και σ_{logEDP}, αντίστοιχα. Αν αυτά υπολογιστούν, μπορούν να χρησιμοποιηθούν για τον υπολογισμό της πιθανότητας το EDP να υπερβεί μια τιμή κατωφλίου edp χρησιμοποιώντας την λογαριθμική κατανομή:

$$P(EDP \geq edp|Uplft) = 1 - \Phi\left(\frac{log(EDP) - \mu_{logEDP}}{\sigma_{lnEDP}}\right) \tag{8}$$

όπου edp είναι η τιμή κατωφλίου του EDP που υποδηλώνει υπέρβαση της οριακής κατάστασης που εξετάστηκε και Φ είναι η τυπική κανονική κατανομή.

Η σεισμική διακυνδύνευση εκφράζεται ως υπέρβαση της μέσης ετήσιας συχνότητας (MAF) μιας οριακής κατάστασης. Υιοθετώντας τον τύπο του $PEER$, το MAF μπορεί να υπολογιστεί με τη βοήθεια της έκφρασης:

$$\lambda_{EDP} = \int_{IM} P(EDP|IM) \left| \frac{d\lambda_{IM}}{dIM} \right| dIM \tag{9}$$

όπου λ_{EDP} είναι η μέση ετήσια συχνότητα του EDP και $d\lambda_{IM}$ είναι η κλίση της καμπύλης σεισμικού κινδύνου. Η μέση ετήσια συχνότητα υπέρβασης μιας οριακής κατάστασης λαμβάνεται από την παράγωγο της καμπύλης σειμικού κινδύνου λ_{IM}, εκφρασμένη ως συνάρτηση του IM και την καμπύλη τρωτότητας $P(EDP|IM)$ που λαμβάνεται σε σχέση με το EDP και το IM που εξετάζονται. Στο πλαίσιο της Διατριβής εξετάστηκαν διαφορετικές μέθοδοι προσέγγισης των καμπυλών τρωτότητας οι οποίες συζητώνται διεξοδικά και γίνεται εφαρμογή της προτεινόμενης μεθοδολογίας σε περιπτώσεις λικνιζόμενων σωμάτων, κιονοστοιχιών και πλαισίων με ανισοϋψή βάθρα.

Η προτεινόμενη μεθοδολογία συνδυάζει υπολογιστικά εργαλεία και διαδικασίες αξιολόγησης της αξιοπιστίας προκειμένου να υπολογιστεί η τρωτότητα και η σεισμική διακινδύνευση ενός συστήματος για ένα εύρος οριακών καταστάσεων. Το αποδεκτό επίπεδο βλάβης εξαρτάται από τη σεισμική διέγερση και τη σπουδαιότητα της κατασκευής. Για μονολιθικούς κίονες και κιονοστοιχίες, η κατάρρευση είναι μείζονος σημασίας ζήτημα. Ο καθορισμός των σταθμών βλαβών που είναι αποδεκτές για μνημειακές κατασκευές δεν είναι απλός δεδομένου ότι απαιτεί συναίνεση μεταξύ διαφόρων ειδικοτήτων. Παρόλα αυτά, είναι βέβαιο ότι η πιθανότητα κατάρρευσης πρέπει να είναι όσο το δυνατόν μικρότερη.

Ανάλυση αξιοπιστίας περιεχομένων κατασκευών

Το παραπάνω προτεινόμενο πλαίσιο για την εκτίμηση της αξιοπιστίας σε λικνιζόμενες κατασκευές, γενικά, επεκτάθηκε σε ένα εκτενές πλαίσιο το οποίο παρουσιάζει το πρόβλημα, τα διάφορα Μέτρα Έντασης και τις Παραμέτρους Απόκρισης καθώς και τις διαφορετικές μεθοδολογίες με τις οποίες μπορεί να προσεγγιστεί η σεισμική τρωτότητα και η σεισμική διακινδύνευση σε περιεχόμενα κατασκευών. Η μεθοδολογία που ακολουθήθηκε για την εκτίμηση της σεισμικής απόκρισης των περιεχομένων κτιρίων φαίνεται συνοπτικά στο Σχήμα 10α. Το κτίριο υπόκειται σε μια χρονοϊστορία επιτάχυνσης και αποθηκεύεται η απόκριση του ορόφου ενδιαφέροντος. Η επιτάχυνση των ορόφων χρησιμοποιείται ως επιτάχυνση στη βάση ενός άκαμπτου σώματος και προκύπτει η απόκρισή του. Αυτή η εννοιολογικά απλή διαδικασία απαιτεί δύο μοντέλα, ένα για την προσομοίωση του κτιρίου και ένα δεύτερο για την προσομοίωση των ανεξάρτητων περιεχομένων. Επιπλέον, μετά από κάθε ανάλυση που πραγματοποιείται για το κτίριο η χρονοϊστορία της επιτάχυνσης πρέπει να αποθηκεύεται για κάθε όροφο. Αυτή η διαδικασία χρησιμοποιείται επίσης για την παραγωγή των καμπυλών τρωτότητας των λικνιζόμενων σωμάτων που μας ενδιαφέρουν.

Η αξιολόγηση της σεισμικής απόκρισης απαιτεί τον καθορισμό των Μέτρων Έντασης και των Παράμετρων Απόκρισης τόσο για την κατασκευή όσο και για τα περιεχόμενα. Αυτό το βήμα είναι επίσης σημαντικό για την εκτίμηση της τρωτότητας. Τα Μέτρα Έντασης αντιπροσωπεύουν τη σεισμική ένταση, ενώ οι Παράμετροι Απόκρισης χρησιμοποιούνται για την αξιολόγηση της απαίτησης ή της σεισμικής βλάβης. Για τη διάκριση των μεγεθών που αναφέρονται στην κατασκευή και το λικνζόμενο σώμα, χρησιμοποιούνται οι εκθέτες $''s''$ και $''b''$, αντίστοιχα. Επομένως, $EDP^{(s)}$ και $IM^{(s)}$ είναι το IM και το EDP της κατασκευής, ενώ τα $EDP^{(b)}$ και $IM^{(b)}$ αντιστοιχούν στο άκαμπτο σώμα. Για ένα σώμα στον όροφο j, το $IM^{(b)}$ θα συμπίπτει με (ή θα προέρχεται από) το $EDP_j^{(s)}$ της κατασκευής ή, απλά, την επιτάχυνση του ορόφου η οποία είναι η μέγιστη επιτάχυνση του εδάφους για το λικνιζόμενο σώμα. Επομένως, η επιλογή των $EDP_j^{(s)}$ και $IM^{(b)}$ θα πρέπει να είναι συνεπής.

Για κατασκευές συνήθους ιδιοπεριόδου μια αντισπροσωπευτική επιλογή για το μέτρο έντασης του κτιρίου $IM^{(s)}$, είναι η φασματική επιτάχυνση της πρώτης ιδιομορφής με απόσβεση 5%, $S_a(T_1, 5\%)$. Επιπλέον, το πιο συνηθισμένο Μέτρο Απόκρισης είναι η μέγιστη σχετική μετατόπιση μεταξύ ορόφων. Ωστόσο, δεδομένου ότι η εστιάζουμε σε λικνιζόμενα σώματα, αντί για τη μέγιστη μετατόπιση των ορόφων, θα πρέπει να επιλεγεί μια διαφορετική ποσότητα ως $EDP^{(s)}$, ενώ το μέτρο έντασης $IM^{(s)}$ είναι πάντα $S_a(T_1, 5\%)$, αν και άλλα μέτρα είναι επίσης δυνατά.

Για ένα λικνιζόμενο σώμα, η πιο διαισθητική επιλογή IM είναι η μέγιστη εδαφική επιτάχυνση (PGA), αφού είναι η παράμετρος που καθορίζει τη μέγιστη ροπή ανατροπής, ενώ το PGA καθορίζει, επίσης, εάν θα συμβεί λικνισμός, ολίσθηση ή κανένα από τα δύο. Αν και δεν είναι απαραίτητο, το PGA κανονικοποιείται με $gtan\alpha$ και έτσι το IM του σώματος είναι $IM^{(b)} = PGA/gtan\alpha$, όπου το $IM^{(b)} \leq 1$ υποδηλώνει ότι το σώμα παραμένει ακίνητο. Επιπλέον, παλαιότερες έρευνες έδειξαν ότι το PGV είναι επίσης μια σημαντική Παράμετρος Απόκρισης που παρέχει μια καλή συσχέτιση μεταξύ της σεισμικής απαίτησης και της ανατροπής των σωμάτων. Για λόγους απλότητας, επιλέγουμε να μην κανονικοποιήσουμε το PGV, αν και στη βιβλιογραφία έχει προταθεί η κανονικοποιημένη ποσότητα $pPGV/gtan\alpha$ ως IM κατάλληλο για λικνιζόμενες κατασκευές. Τα αποτελέσματά μας έδειξαν ότι το PGV (ή το PFV) αποδίδει καλά ως IM και ως εκ τούτου επιλέξαμε την απλούστερη δυνατή περίπτωση. Επομένως, το $IM^{(b)}$ για ένα σώμα στον όροφο j που λαμβάνεται υπόψη, είναι είτε η κανονικοποιημένη επιτάχυνση του ορόφου αναφοράς PFA_j, είτε η ταχύτητα ορόφου αναφοράς PFV_j. Η επιλεγμένη παράμετρος θα χρησιμοποιηθεί επίσης ως παράμετρος απαίτησης του κτιρίου $EDP_j^{(s)}$. Η καταλληλότερη παράμετρος απαίτησης $EDP^{(b)}$ για το λικνιζόμενο σώμα είναι η γωνία στροφής θ κανονικοποιημένη από τη ραδινότητα α, δηλαδή $EDP^{(b)} = |\theta|/\alpha$. Τα EDP και τα IM για την κατασκευή και τα ανεξάρτητα περιεχόμενα συνοψίζονται στον Πίνακα 1.

Στα πλαίσια της Διδακτορικής Διατριβής εξετάστηκαν διαφορετικά σώματα, διαφορετικές μέθοδοι για τον υπολογισμό της σεισμικής τρωτότητας και σεισμικής διακινδύνευσης και προέκυψαν σημαντικά συμπεράσματα που καθιστούν τη συμβολή της σημαντική στην επιστημονική κοινότητα.

Πίνακας 1: Ορισμός των *IMs* και *EDPs*.

	IM	EDP
κατασκευή	$S_a(T_1, 5\%)$	$drift$, PFA_j, PFV_j
σώμα	$PGA/gtan\alpha$, PGV	θ / α
σώμα στον όροφο j	$PFA/gtan\alpha$, PFV	θ / α

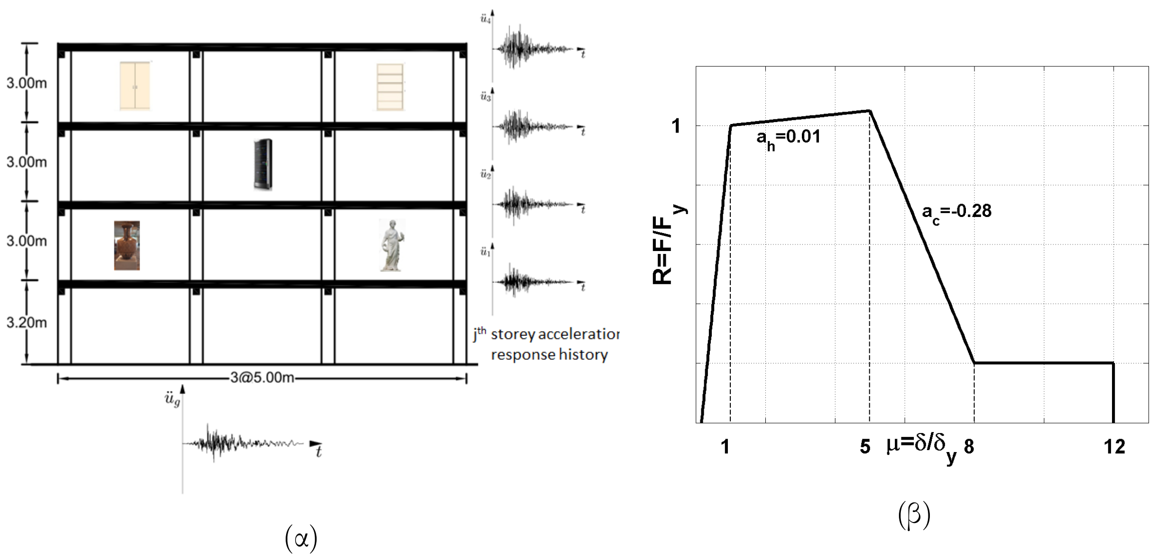

Σχήμα 10: (α) Το τετραόροφο κτίριο αναφοράς, (β) Καμπύλη δύναμης-μετατόπισης ($F - \delta$).

Σεισμική συμπεριφορά μουσειακών εκθεμάτων

Η πειραματική διερεύνηση της λικνιστικής συμπεριφοράς μουσειακών εκθεμάτωντου πραγματοποιήθηκε στα πλαίσια του προγράμματος SEREME και επικεντρώθηκε στη διερεύνηση της σεισμικής συμπεριφοράς μαρμάρινων αγαλμάτων και προτομών πραγματικής κλίμακας που στέκονται σε βήματα/βάθρα. Η επιλογή των αγαλμάτων και προτομών πραγματοποιήθηκε ώστε να έχουν διαφορετική γεωμετρία και βάρη. Πρόκειται για αντίγραφα αρχαίων Ρωμαίων αυτοκρατόρων και χρησιμοποιήθηκαν πέντε προτομές συνολικά. Επιπλέον, τέσσερα αγάλματα επελέγησαν, δύο απλά εδραζόμενα σε μαρμάρινο βάθρο χαμηλού ύψους και δύο απλά γυναικεία αγάλματα. Δεδομένου ότι όλα τα δείγματα είναι κατασκευασμένα από συμπαγές μάρμαρο, το μέσο βάρος των προτομών είναι 250-300 κιλά, ενώ των αγαλμάτων ήταν 500-600 κιλά. Τα αντίγραφα του αγάλματος/προτομής έχουν περίπου την ίδια γεωμετρία, αλλά δεν είναι απολύτως πανομοιότυπα (Εικόνα 11). Εξετάστηκε επίσης η σεισμική απόκριση μιας προθήκης.

(α)

(β)

Σχήμα 11: Περιεχόμενα κατασκευών που θεωρήθηκαν κατά την πειραματική διερεύνηση: (α) Προτομές και προθήκη, (β) αγάλματα γυναικείων μορφών.

Οι προτομές τοποθετήθηκαν σε ένα βάθρο που χρησιμοποιείται για να ανυψώνει τα εκθέματα στο ύψος των ματιών του επισκέπτη. Τρεις διαφορετικοί τύποι βάθρου εντοπίστηκαν και στη συνέχεια υιοθετήθηκαν για τις πειραματικές δοκιμές: (α) συμπαγές βάθρο, με διαστάσεις 45×45×100εκ., (β) κοίλο βάθρο, με διαστάσεις 35×35×100 εκ., και (γ) μοντέρνου τύπου μεταλλικό βάθρο.

Τα παραδοσιακά βήματα ήταν κατασκευασμένα από σκυρόδεμα που έχει ειδικό βάρος κοντά σε αυτό του μαρμάρου. Για την επίτευξη ρεαλιστικών συνθηκών επιτόπιας τριβής, στην επάνω και στην κάτω πλευρά των βάθρων τοποθετήθηκαν μαρμάρινες πλάκες πάχους 3εκ.. Τα συμπαγή βήματα έχουν μεγάλα βάρη (σχεδόν 500 κιλά) και χρησιμοποιούν επίσης μεγάλες βάσεις, επομένως για αυτά τα βήματα δεν αναμενώταν ανύψωση. Από την άλλη πλευρά, τα κοίλα βήματα είναι λεπτά με βάρος 226 κιλά και έχουν βάση με μικρότερο πλάτος ίσο με 35εκ.. Επιπλέον, το κέντρο βάρους τους είναι πολύ υψηλότερο σε σύγκριση με τη συμπαγή περίπτωση. Το μεταλλικό βάθρο έχει μεγάλη τετράγωνη βάση με πλευρά ίση με 85εκ. και ζυγίζει μόλις 85 κιλά. Για την προσομοίωση του δαπέδου των μουσείων, όπου συνήθως φιλοξενούνται προτομές και αγάλματα, τα μη μονωμένα εκθέματα τοποθετήθηκαν σε μαρμάρινη επιφάνεια δαπέδου. Το μάρμαρο έχει πάχος ίσο με 3εκ. και είναι τοποθετημένο σε σκληρό ξύλο επίσης πάχους 3εκ.. Τόσο το μάρμαρο όσο και το ξύλο βιδώθηκαν κατευθείαν στη σεισμική τράπεζα. Όλα τα δείγματα τοποθετούνται πάνω από το μαρμάρινο δάπεδο και το βάθρο χωρίς να παρεμβάλλεται κανένα υλικό σύνδεσης. Για τους μονωτήρες

SMA, μαρμάρινες πλάκες στην επάνω επιφάνεια του σεισμικού μονωτήρα κολλήθηκαν, ενώ τα εκθέματα είναι απλά εδραζόμενα.

Ένας τεράστιος όγκος δεδομένων ελήφθη κατά τη διάρκεια της πειραματικής διερεύνησης που διήρκεσε περίπου δύο μήνες. Ωστόσο, κατά τη διάρκεια της διερεύνησης έγιναν πολύ ενδιαφέρουσες παρατηρήσεις. Λόγω των μέτρων προστασίας δεν σημειώθηκε σημαντική βλάβη στα εκθέματα, ενώ ο πιο χαρακτηριστικός τύπος βλάβης που παρατηρήθηκε είναι η αστοχία στις γωνίες των δειγμάτων. Αυτή η ζημιά φαίνεται στο σχήμα 7.13 τόσο για την προτομή όσο και για τα αγάλματα. Αυτός ο τύπος βλάβης συνέβη σχεδόν σε όλες τις προτομές που εξετάστηκαν ενώ η αστοχία του αγάλματος που φαίνεται στο σχήμα 7.13β συνέβη μία φορά. Επειδή έπρεπε να επαναληφθεί μεγάλος αριθμός δοκιμών, οι μαρμάρινες βάσεις των προτομών αντικαταστάθηκαν, ενώ για το άγαλμα η βλάβη επισκευάστηκε. Δεν σημειώθηκαν αστοχίες (τοπικές ή καθολικές) στα βήματα.

(α)

(β)

Σχήμα 12: Βλάβες στη βάση των εκθεμάτων: (α) προτομή, (β) άγαλμα.

Σημαντικά ευρήματα προέκυψαν από την πειραματική διερεύνηση και συνοψίζονται εν συντομία ως εξής:

- Για δοκιμές με μεγάλη εδαφική επιτάχυνση, τα μη-μονωμένα εκθέματα παρουσίασαν συνδυασμένη κίνηση λικνισμού και ολίσθησης. Η κρούση που προκαλείται από την λικνιστική κίνηση μπορεί να είναι πηγή βλάβης στη βάση των προτομών, ειδικά στις γωνίες.

- Η απόκριση των προτομών στο συμπαγές και στο κοίλο βάθρο είναι ουσιαστικά διαφορετική. Η ανύψωση του κοίλου βάθρου ήταν πάντα μικρή και ήταν δύσκολο να εντοπιστεί οπτικά. Ωστόσο, είναι σαφές ότι επηρέασε σημαντικά τη σεισμική απόκριση. Το αν η προτομή είναι πιο ασφαλής στο συμπαγές ή στο κοίλο βάθρο είναι ένα θέμα που αξίζει περαιτέρω έρευνα. Οι δοκιμές έδειξαν ότι η ασφάλεια εξαρτάται επίσης από το συχνοτικό περιεχόμενο της διέγερσης.

- Δοκιμές όπου ο συντελεστής τριβής μεταξύ της προτομής και του βήματος ήταν χαμηλός έδειξαν ότι η ολίσθηση είναι ένας ευεργετικός τρόπος απόκρισης για την προτομή.
- Στις περισσότερες περιπτώσεις, τα μέτρα προστασίας ήταν αποτελεσματικά. Απαιτήθηκε κάποια προσοχή στην περίπτωση υψηλής κατακόρυφης συνιστώσας της εδαφικής διέγερσης.
- Τα μεταλλικά βάθρα, λόγω της γεωμετρίας τους, δεν ανυψώθηκαν και ως εκ τούτου ήταν εξίσου αποτελεσματικά με τα συμπαγή, με την προϋπόθεση ότι μπορούν να υποστηρίξουν πλήρως το βάρος του έργου τέχνης.
- Η απόκριση των αγαλμάτων ήταν καλά μελετημένη εκ των προτέρων και δεν προέκυψαν μεγάλες εκπλήξεις. Όταν η επιτάχυνση του εδάφους ήταν κάτω από το όριο εκκίνησης λικνισμού, τα αγάλματα έκαναν κάποια ταλάντωση υψηλής συχνότητας λόγω κάμψης.
- Η βάση ορισμένων από τα αγάλματα δεν ήταν εντελώς επίπεδη, λόγω κατασκευαστικών ατελειών. Αυτή η έλλειψη επιπεδότητας επηρέασε την απόκριση και δεν εξασφάλιζε την ασφάλεια των αγαλμάτων. Αυτό το ζήτημα έχει επίσης αναφερθεί σε προηγούμενες έρευνες στη βιβλιογραφία.

Συμπεράσματα

Στην παρούσα Διδακτορική Διατριβή παρουσιάζεται η εκτίμηση της σεισμικής απόκρισης λικνιζόμενων κατασκευών με χρήση απλοποιητικών μοντέλων. Η προσομοίωση αφορά αφενός λικνιζόμενα σώματα/κολώνες και αφετέρου λικνιζόμενα πλαίσια που είναι άκαμπτα ή εύκαμπτα και ελεύθερα εδραζόμενα ή προεντεταμένα. Επιπλέον, διερευνάται η σεισμική τρωτότητα και η σεισμική διακινδύνευση των περιεχομένων κτιρίων που θεωρούνται άκαμπτα και η επίδραση της κατασκευής στη διερεύνηση αυτή εισάγεται στους υπολογισμούς. Στα πλαίσια της παρούσας διατριβής, πλην των υπολογιστικών μοντέλων και προσεγγίσεων, πραγματοποιήθηκε μια πειραματική καμπάνια με έμφαση σε αγάλματα και σε προτομές που στέκονται σε ένα ″βήμα″. Ορισμένα προκαταρκτικά αποτελέσματα παρουσιάζονται εδώ. Τα συμπεράσματα συνοψίζονται παρακάτω σύμφωνα με τα προηγούμενα κεφάλαια.

Αρχικά, συζητείται η χρήση απλών ταλαντωτών ενός βαθμού ελευθερίας για την εκτίμηση της σεισμικής απόκρισης λικνιζόμενων συστημάτων. Το πρόβλημα του λικνιζόμενου σώματος επιλύεται χρησιμοποιώντας μοντέλα που βασίζονται σε στοιχεία δοκού και που συνδέονται στη βάση τους με ένα μη-γραμμικό στροφικό ελατήριο. Αυτή η προσομοίωση, αν και κατ΄ αρχήν προσεγγιστική, έχει αποδειχθεί ικανή να λύσει γρήγορα και με ασφάλεια το πρόβλημα της λικνιστικής συμπεριφοράς είτε για μεμονωμένα σώματα είτε για συστήματα που πραγματοποιούν λικνισμό και τα οποία έχουν περιγραφεί αναλυτικά στην Διατριβή.

Παρά το χάσμα που παρουσιάζεται μεταξύ της λικνιστικής απόκρισης μιας κατασκευής και προτεινόμενων θεωρητικών λύσεων, εντούτοις τα προτεινόμενα μοντέλα μπορούν να θεωρηθούν ως ένα βήμα προς πιο ακριβείς εκτιμήσεις της σεισμικής απόκρισης. Η ευρωστία τους έγκειται στο γεγονός πως επιτρέπουν διάφορες βελτιώσεις χάρη στην ευελιξία της μεθόδου των Πεπερασμένων Στοιχείων. Στην πραγματικότητα, έχουν προταθεί τέσσερα απλά μοντέλα (τέσσερις παραλλαγές). Τα τρία μοντέλα χρησιμοποιούν μια προσέγγιση συγκεντρωμένης μάζας και το τέταρτο είναι ένα μοντέλο κατανεμημένων μαζών. Όλα τα μοντέλα βασίζονται στη θεωρία του λικνισμού λαμβάνοντας υπόψη την "καθαρή" κίνηση συστημάτων που είναι ελεύθερα να ανυψωθούν μερικώς και να λικνιστούν. Η τελική επιλογή μεταξύ των προτεινόμενων μοντέλων, εξαρτάται από το πρόβλημα που παρουσιάζεται, και από τα χαρακτηριστικά του λογισμικού που θα υιοθετηθεί. Πιο συγκεκριμένα, η επιλογή μεταξύ των συγκεντρωμένων και κατανεμημένων μαζών εξαρτάται από το πρόβλημα. Εάν η μάζα μπορεί να θεωρηθεί ως συγκεντρωμένη (π.χ. απλά εδραζόμενο άκαμπτο σώμα, προεντεταμένο άκαμπτο σώμα), τα τρία πρώτα μοντέλα είναι ευκολότερα στην εφαρμογή και επομένως προτιμώνται έναντι της επιλογής του τέταρτου.

Η υπόθεση του εύκαμπτου σώματος εξαρτάται καθαρά από τις ιδιότητες της κατασκευής. Το μοντέλο που παρουσιάζει διανεμημένες μάζες προτιμάται για την προσομοίωση παραμορφώσιμων λικνιζόμενων σωμάτων καθώς οι ανώτερες ιδιομορφές μπορούν να προσεγγιστούν με μεγαλύτερη ακρίβεια. Η επιλογή μεταξύ των τριών μοντέλων εξαρτάται από το λογισμικό που υιοθετείται, καθώς τα δύο πρώτα είναι πρακτικά πανομοιότυπα, ενώ το τρίτο είναι κατάλληλο μόνο για άκαμπτα σώματα.

Επιπλέον, εξετάστηκαν τρεις σχέσεις ροπής-στροφής για τα μη γραμμικά ελατήρια που προσομοιώνουν τη ροπή ευστάθειας ενός συστήματος που πραγματοποιεί λικνιστική κίνηση. Η αποδοτικότητα στα αποτελέσματα κάθε σχέσης σε συνδυασμό με καθένα από τα προτεινόμενα μοντέλα αξιολογήθηκε τόσο υπό στατική όσο και υπό δυναμική φόρτιση. Ο συντελεστής επαναφοράς, μια κρίσιμη παράμετρος για προβλήματα λικνισμού, έχει εξεταστεί άμεσα ως εφαρμογή μιας προσέγγισης που διακόπτει και συνεχίζει την ανάλυση μετά από κάθε κρούση. Η προτεινόμενη προσομοίωση μπορεί να εφαρμοστεί σε κοινά λογισμικά που εφαρμόζουν τη Μέθοδο των Πεπερασμένων Στοιχείων και οι Μηχανικοί είναι συνυφασμένοι με αυτά. Η υλοποίηση είναι δυνατή είτε με το κάποιο ελεύθερο λογισμικό, είτε με κώδικα που μπορεί να στηρίζεται στη μέθοδο. Τέλος, μελετήθηκαν δύο συστήματα: ένα προεντεταμένο λικνιζόμενο σώμα/κολώνα και ένα συζευγμένο σύστημα κάμψης-λικνισμού, όπου το σώμα είναι είτε άκαμπτο είτε εύκαμπτο. Σε όλες τις περιπτώσεις επιτεύχθηκε τέλεια συμφωνία με τα αποτελέσματα από τη βιβλιογραφία.

Επεκτείνοντας την προηγούμενη έρευνα, προτείνεται μια νέα προσέγγιση προσομοίωσης για την εκτίμηση της σεισμικής απόκρισης πλαισιακών κατασκευών. Η μεθοδολογία που παρουσιάζεται μπορεί να εφαρμοστεί ξανά σε ένα πλαίσιο Πεπερασμένων Στοιχείων είτε να υιοθετηθεί κάποιο εμπορικό λογισμικό Πολιτικού Μηχανικού. Η ιδέα βασίζεται στη χρήση στροφικών ελατηρίων με αρνητική ακαμψία στις διεπιφάνειες, πάνω και κάτω, κάθε κολώνας/σώματος που συνιστούν ένα λικνιζόμενο πλαίσιο. Η αποτελεσματικότητα αυτής της προσέγγισης παρουσιάστηκε αρχικά για έναν απλά εδραζόμενο λικνιζόμενο στύλο, επεκτάθηκε σε εύκαμπτες κολώνες και στη συνέχεια σε λικνιζόμενα πλαίσια. Η σύνθεση του προβλήματος συζητείται αρχικά έχοντας ως αναφορά το απλά εδραζόμενο λικνιζόμενο σώμα το οποίο επανεξετάζεται προκειμένου να ληφθούν πιο ακριβείς αρχικές συνθήκες. Αυτό είναι σημαντικό για την αξιολόγηση της σεισμικής απόκρισης εύκαμπτων κολώνων υπό μεγάλη αξονική δύναμη, όπως συμβαίνει συχνά με τα λικνιζόμενα μέλη μιας γέφυρας. Επιπλέον, συζητείται λεπτομερώς η μοντελοποίηση λικνιζόμενων πλαισίων, πρώτα άκαμπτων και στη συνέχεια εύκαμπτων, χρησιμοποιώντας στροφικά ελατήρια αρνητικής δυσκαμψίας που τοποθετούνται στις διεπιφάνειες κρούσης. Οι παράμετροι των ελατηρίων επιλέγονται ανάλογα με τον τύπο ανάλυσης, δηλαδή συμπεριλαμβάνοντας ή όχι τα τα φαινόμενα δευτέρας τάξεως και τη θέση του ελατηρίου. Ωστόσο, είναι επίσης σημαντικό να επιλεγούν σωστά οι όροι στροφικής ροπής αδράνειας που εισέρχονται στο μητρώο μάζας. Μια απλοποιημένη εναλλακτική λύση, κατάλληλη για την περίπτωση άκαμπτων πλαισίων μπορεί να ληφθεί εάν ο μονοβάθμιος ταλαντωτής ταυτιστεί με τη γενικευμένη εξίσωση του προβλήματος λικνισμού. Αντιμετωπίζονται, επίσης, τα προεντεταμένα λικνιζόμενα συστήματα, καθώς η χρήση τενόντων είναι ευρέως αποδεκτή για σύγχρονες γέφυρες. Η μεθοδολογία της προσομοίωσης που παρουσιάζεται μπορεί να επεκταθεί και σε άλλα λικνιζόμενα συστήματα με απλό τρόπο προσφέροντας ακριβείς λύσεις, μειώνοντας το υπολογιστικό κόστος και αποφεύγοντας την ειδική αντιμετώπιση της αλληλεπίδρασης μεταξύ των μελών. Συνολικά, η προτεινόμενη προσέγγιση είναι ένα χρήσιμο και πρακτικό εργαλείο που μπορεί να υιοθετηθεί εκτενώς για την προσομοίωση οποιασδήποτε λικνιζόμενης κατασκευής.

Ακολούθως, η αξιολόγηση της τρωτότητας πλαισιακών κατασκευών συζητείται στην παρούσα Διατριβή. Ένα εκτενές ολοκληρωμένο πλαίσιο το οποίο παρουσιάζει το πρόβλημα, τα διάφορα Μέτρα Έντασης και τις Παραμέτρους Απόκρισης καθώς και τις διαφορετικές μεθοδολογίες για την εκτίμηση της σεισμικής τρωτότητας και της σεισμικής διακινδύνευσης παρουσιάζεται διεξοδικά. Γίνεται εφαρμογή της προτεινόμενης μεθοδολογίας σε περιπτώσεις λικνιζόμενων σωμάτων, κιονοστοιχιών και πλαισίων με ανισοϋψή βάθρα. Η προσέγγιση αυτή είχε στόχο την πρωταρχική διερεύνηση ώστε να επεκταθεί η μεθοδολογία σε περιεχόμενα κατασκευών στη συνέχεια, στα οποία και επικεντρώνεται η Διατριβή παρέχοντας για πρώτη φορά μια πρωτότυπη σύνδεση κτιρίου-σωμάτων που υπόκεινται σε λικνιστική κίνηση.

Στη συνέχεια, η αξιολόγηση της τρωτότητας των περιεχομένων ενός κτιρίου συζητείται στην παρούσα Διατριβή. Τα περιεχόμενα του κτιρίου προσομοιώθηκαν ως άκαμπτα σώματα και έγινε η υπόθεση πως φιλοξενούνται σε ένα τετραώροφο κτίριο από οπλισμένο σκυρόδεμα. Έχει αποδειχθεί ότι το πρόβλημα που αντιμετωπίζεται εδώ είναι πολύπλοκο αφού η απόκριση κτιρίων-περιεχομένων είναι συνδεδεμένη και αλληλοεξαρτώμενη. Τα ευρήματα της μελέτης έχουν ληφθεί χρησιμοποιώντας ένα δισδιάστατο, τετραώροφο κτίριο και ως εκ τούτου δεν μπορούν πάντα να γενικεύονται. Για το λόγο αυτό, απαιτείται περαιτέρω έρευνα προκειμένου να κατανοηθεί πλήρως η επίδραση της κατασκευή στην τρωτότητα των ελεύθερα εδραζόμενων περιεχομένων. Ωστόσο, η εργασία μπορεί να θεωρηθεί ως μια προσπάθεια να προσφερθούν κάποιες πρώτες κατευθυντήριες γραμμές για το πώς μπορεί να αντιμετωπιστεί το πρόβλημα της λικνιστικής κίνησης για ελεύθερα εδραζόμενα αντικείμενα/εκθέματα που φιλοξενούνται σε ένα κτίριο. Μερικά από τα κύρια συμπεράσματα της παρούσας ενότητας συνοψίζονται εν συντομία ως εξής: (*i*) Παρουσιάζεται μια μεθοδολογία εκτίμησης της τρωτότητας που βασίζεται στην Προσαυξητική Δυναμική Ανάλυση, προσαρμοσμένη σε λικνιζόμενα περιεχόμενα κτιρίων. Απεδείχθη ότι ένα ελεύθερα εδραζόμενο σώμα, όταν φιλοξενείται σε μια κατασκευή, μπορεί να είναι περισσότερο ή λιγότερο ευάλωτο από ό,τι στο έδαφος. Αυτό εξαρτάται από τη γεωμετρία των περιεχομένων και τα δυναμικά χαρακτηριστικά της κατασκευής. Επιπλέον, η τρωτότητα των σωμάτων δεν πρέπει να υπολογίζεται ανεξάρτητα από την κατάρρευση ή τις πιθανές βλάβες του κτιρίου. (*ii*) Διερευνάται μια απλοποιημένη προσέγγιση που μπορεί να χρησιμοποιηθεί για την αξιολόγηση της τρωτότητας ενός σώματος όταν είναι γνωστές τόσο η τρωτότητα της κατασκευής όσο και ενός σώματος.

Επιπλέον, αποδεικνύεται ότι είναι σημαντικό να χρησιμοποιείται το μέτρο έντασης της κατασκευής για την αξιολόγηση της σεισμικής διακυνδύνευσης του σώματος, καθώς διασφαλίζει τη συνέπεια μεταξύ του σώματος και της κατασκευής. Μεταξύ των μέτρων έντασης που εξετάστηκαν, βρέθηκε ότι η μέγιστη ταχύτητα ορόφου, γενικά, είναι προτιμότερη. (*iii*) Ανάλογα με τη επεξεργασία των αποτελεσμάτων, τα δεδομένα λαμβάνονται σε μορφή σύννεφου ή πολλαπλών λωρίδων. Θα πρέπει να λαμβάνεται υπόψη η κατάλληλη επεξεργασία προκειμένου να αντιμετωπίζονται με συνέπεια τα λικνιζόμενα σώματα, τα μη λικνιζόμενα σώματα και τα σώματα που ανατράπηκαν. Διαφορετικά, οι καμπύλες τρωτότητας θα υποεκτιμηθούν. (*iv*) Έχει ληφθεί υπόψη ένα σώμα με μεγάλη και ένα σώμα με μικρή ραδινότητα, που δείχνει ότι η γεωμετρία του σώματος είναι κρίσιμη. Διαπιστώθηκε ότι τα πιο στιβαρά σώματα είναι πιο ασφαλή στο ισόγειο ενώ τα λεπτά είναι πιο ασφαλή όταν φιλοξενούνται στο κτίριο. Φυσικά αυτές οι παρατηρήσεις αναφέρονται στην εξεταζόμενη τετραώροφη κατασκευή, αλλά φαίνεται ξεκάθαρα η σημασία τόσο των ιδιοτήτων του κτιρίου όσο και του σώματος και επίσης διαπιστώνεται πως η τρωτότητα των ανεξάρτητων περιεχομένων είναι πολύ διαφορετική από εκείνη των πακτωμένων που αναμένεται να συμπεριφέρονται ως παραμορφώσιμες κατασκευές.

Στο τελευταίο βήμα, παρουσιάζεται μια εκτενής πειραματική διερεύνηση για τη σεισμική απόκριση μουσειακών εκθεμάτων. Η διερεύνηση βασίζεται σε ένα έργο που δίνει έμφαση σε αγάλματα και προτομές και έχει αντιμετωπιστεί σε συνεργασία με ανθρώπους που αποτελούν μια ομάδα. Οι δοκιμές πραγματοποιήθηκαν στο πλαίσιο του Ερευνητικού Έργου σε σεισμική τράπεζα στο Παρίσι. Η πειραματική διερεύνηση στόχευε να βοηθήσει στην κατανόηση της σεισμικής συμπεριφοράς των επιλεγμένων αγαλμάτων και προτομών και στη συνέχεια στην ανάπτυξη νέων και οικονομικά αποδοτικών μέτρων μείωσης του σεισμικού κινδύνου για τη βελτίωση της σεισμικής τρωτότητας πολύτιμων αντικειμένων που φιλοξενούνται σε ευρωπαϊκά μουσεία. Δύο πραγματικής κλίμακας μαρμάρινα (τα αντίγραφα κατασκευάζονται συνήθως από γύψο) ρωμαϊκά αγάλματα και τρεις προτομές τριών Ρωμαίων αυτοκρατόρων που στέκονται σε τρία βάθρα διαφορετικού τύπου και μεγέθους διερευνώνται σχετικά με την απόκρισή τους σε σεισμική φόρτιση. Τα έργα τέχνης θερούνται είτε απλά εδραζόμενα είτε σεισμικά μονωμένα. Στην τελευταία περίπτωση, δοκιμάζονται δύο νέα και εξαιρετικά αποδοτικά συστήματα σεισμικής μόνωσης, προσαρμοσμένα σε έργα τέχνης. Η αποτελεσματικότητα της σεισμικής μόνωσης παρουσιάζει κύριο ενδιαφέρον. Ο πρώτος μονωτήρας είναι ένα σύστημα που βασίζεται σε εκκρεμές, ενώ ο δεύτερος χρησιμοποιεί σύρματα από κράμα μνήμης σχήματος. Για την εξέταση όλων των περιπτώσεων εξετάστηκαν διαφορετικές διαμορφώσεις. Εξετάζεται επίσης η σημασία του κτιρίου που τα φιλοξενεί, δηλαδή ο τύπος του κτιρίου, η ακαμψία και ο όροφος που φιλοξενεί τα έργα τέχνης. Ειδικά προσαρμοσμένα, αριθμητικά μοντέλα ποικίλης πολυπλοκότητας και μοντέλα Πεπερασμένων Στοιχείων για συστήματα που υπόκεινται σε λικνιστική κίνηαη ενός και δύο σωμάτων αναπτύχθηκαν για τις ανάγκες αυτής της μελέτης και αξιολογούνται επίσης σε σχέση με τα πειραματικά αποτελέσματα.

Μερικές πτυχές που αξίζει να ερευνηθούν περαιτέρω είναι:

- Διερεύνηση της αλληλεπίδρασης μεταξύ ολίσθησης και λικνίσματος και πώς θα μπορούσε να πραγματοποιηθεί η προσομοίωση, επεκτείνοντας έτσι τις προτεινόμενες προσεγγίσεις. Η επέκταση μπορεί να βασίστει σε απλοποιητικά προσομοιώματα και πιθανώς σε ένα πρόσθετο ελατήριο που λαμβάνει την ολίσθηση. Σύμφωνα με την πειραματική διερεύνηση, η συζευγμένη κίνηση λικνισμού-ολίσθησης είναι συνήθης σε μουσειακά εκθέματα ή γενικά σε περιεχόμενα κτιρίων.

- Πιο ενδελεχής διερεύνηση της αλληλεπίδρασης μεταξύ λικνισμού και άλλων μη γραμμικών φαινομένων, π.χ. αναπήδηση, παραμόρφωση, ανελαστικότητα και απόσβεση μετά από κρούση. Κατά τη διάρκεια μιας σεισμικής διέγερσης θα πρέπει να λαμβάνονται υπόψη όλα τα παραπάνω αν και κυριαρχεί η λικνιστική κίνηση.

- Επέκταση των προσομοιωμάτων σε τρισδιάστατες κατασκευές. Δισδιάστατες προσεγγίσεις είναι χρήσιμες για την εκτίμηση της τρωτότητας ή για προσεγγιστικές λύσεις του άκαμπτων και εύκαμπτων κατασκευών.

- Μια πιο ενδελεχής διερεύνηση του προβλήματος των δύο σωμάτων χρησιμοποιώντας απλές προσεγγίσεις. Τέτοιες περιπτώσεις είναι συνήθεις για μουσειακά εκθέματα και ειδικά για την περίπτωση του ασύμμετρου άνω σώματος. Επομένως, προσεγγίσεις, απλοποιητικές ή/και πιο σύνθετες, με χρήση λογισμικού Πεπερασμένων Στοιχείων αποτελούν ένα σημαντικό βήμα.

- Επέκταση της διερεύνησης της σεισμικής τρωτότητας και της σεισμικής διακινδύνευσης με χρήση πιο λεπτομερούς προσομοιώματος για το κτίριο και για τα περιεχόμενα είναι επίσης ένα σημείο ενδιαφέροντος που χρήζει περισσότερης διερεύνησης.

- Επέκταση των προσομοιωμάτων Πεπερασμένων Στοιχείων προκειμένου να διερευνηθούν τα σεισμικά μονωμένα αγάλματα και οι προτομές χρησιμοποιώντας τα πειραματικά δεδομένα.

Acknowledgements

The last step of my studies in Structural Engineering at the National Technical University of Athens is this Thesis. Undertaking this PhD has been a truly life-changing experience for me and it would not have been possible to do it without the support and guidance that I received from many people.

First and foremost, I would like to express my deepest gratitude to my supervisor Michalis Fragiadakis, for giving me the opportunity to work with him on such an interesting topic. Our collaboration was exceptional and I can only feel grateful and proud from the whole experience all this years. I would also like to express my appreciation for his support on the decisions I made during this time concerning my future and state that his insight, guidance and patience prepared me for the next step. This fact gives me the strength to continue and I wish to reward him.

Furthermore, I would like to express my deepest thanks to Dr. Ioannis Psycharis, Emeritus professor, NTUA and Dr. Anastasios Sextos, Professor, University of Bristol, UK. Both of them are members of my advisory committee and I had the opportunity to be in collaboration with them either regarding educational or research subjects. I should, also, thank all the members of the examination committee for their contribution to this doctoral thesis.

I would like to express my gratitude to my wife Zmpenti for encouraging and supporting me in every decision relevant to my career and my targets. It would be unfair not to thank my son, George, who's birth changed my whole life almost simultaneously with the completion of the Thesis.

Special thanks to all my friends for their understanding, encouragement, and above all, their friendship.

Contents

List of Figures

List of Tables

Dedicated to my son and my wife

Chapter 1

Thesis outline

In *Chapter 2* the introductory material and literature review on various rocking systems is presented. Previous works on the seismic response assessment of rocking blocks, either rigid or flexible, and rocking frames, with rigid or flexible columns, that are freestanding or restrained are discussed. Some interesting observations on rocking blocks are presented while the case of asymmetric rocking blocks is reviewed. Last but not least the significance of two-block systems and seismic response assessment approaches for handling the equations of motions are discussed.

In *Chapter 3*, a novel modeling approach for the seismic response assessment of free-standing, rigid or flexible, pure rocking single-degree-of-freedom (SDOF) systems is presented. The proposed modeling that refers to rocking columns is based on equivalent single-degree-of-freedom (SDOF) oscillators that can be implemented with common engineering software or user-made structural analysis codes. The proposed SDOF models adopted use beam elements which are connected to a nonlinear rotational spring with negative stiffness that describes the self-centering capacity of the rocking member. Smartly-positioned, negative-stiffness rotational springs are adopted in order to simulate the rocking restoring moment, while all necessary implementation details are presented. Different variations, pertinent to rigid blocks are first presented and then the concept is extended to the flexible case. In case of flexible columns, modified moment-rotation relationships are discussed. The loss of energy which occurs in every impact is treated with an "event-based" approach consistent with Housner's theory. The implementation of the method requires some minor programming skills, while thanks to the versatility of the Finite Element Method it is capable to handle a variety of rocking problems. This is demonstrated with two other applications, i.e. a vertically restrained block equipped with an elastic tendon, and a rocking block coupled with an elastic SDOF oscillator. The efficiency and the accuracy of the proposed modeling is demonstrated with the aid of carefully chosen case studies either using simple wavelets or historical ground motion records.

In *Chapter 4* a novel modeling approach for the seismic response assessment of rocking frames is presented. Rocking frames are systems with columns that are allowed to fully, or partially, uplift. Despite the apparent lack of a mechanism to resist lateral forces, they have a remarkable capacity against earthquake loading. Rocking frames are found in old structures, e.g. ancient monuments, but it is also a promising design concept for modern structures such a bridges, or buildings. The proposed modelling can be implemented in a general-purpose structural analysis software, avoiding the difficulties that come with the need of formulating and solving specifically-tailored differential equations, or the use of detailed computational models. Different configurations of a rocking portal frame problem are examined. Smartly-positioned, negative-stiffness rotational springs are adopted in order to simulate the rocking restoring moment. Both the case of rigid and flexible piers/columns is discussed, while it is shown that frames with restrained columns can be considered in a straightforward manner. A simple alternative based on an equivalent oscillator that follows the generalized rocking equation of motion is also investigated. The efficiency and the accuracy of the proposed modeling is demonstrated with the aid of carefully chosen case studies.

In *chapter 5* a fully performance-based seismic reliability and risk assessment framework for rigid rocking frames is presented for the first time. Different options for fragility assessment are discussed and the underlying details of the problem are investigated. The cases of freestanding blocks, arrays of freestanding columns capped with an architrave and rocking frames with unequal in height columns are investigated. Intensity Measures (IMs) and Engineering Demand Parameters are presented for handling the problem at hand.

In *chapter 6* the Thesis presents a fully performance-based seismic reliability and risk assessment framework for freestanding structural components and contents that can be modelled as rocking rigid blocks. It is generally accepted, that multistorey buildings often have a valuable inventory consisting of objects that their possible damage during an earthquake will cause unacceptable losses. The seismic response of building contents depends on several parameters such as the geometry of the object, the dynamic characteristics of the building and the storey that the object is located. The demand at the storey level is first obtained and then the response of the contents is calculated using the storey acceleration response history. The demand of the structure is obtained with the aid of a modified version of the Incremental Dynamic Analysis method and subsequently the fragility curves of the rocking building contents are derived for every storey of interest. Different options for fragility assessment are discussed and the underlying details of the problem are investigated. A simplified approach, where the fragility of the freestanding components and the structure are derived separately is also presented. The method combines existing fragility curves and thus is suitable for quickly assessing the reliability of a building's inventory offering sufficient risk estimates. Considering that building contents in most cases are not rectangular and homogeneous the proposed framework is extended in the case of asymmetric contents. The extension is based on the different equation of motion of the contents that should be adopted and a comparison with symmetric cases is of interest.

In *Chapter 7* an experimental campaign on museum artifacts is presented. Considering that the protection of cultural heritage structures and also of museums and their treasures against earthquakes is a subject of top priority, in the current Thesis. Large scale shaking table tests are presented on cultural heritage assets emphasizing on the use of computing models in tandem with experimental testing. The tests have been carried out in the framework of SEREME project (Seismic Resilience of Museum Contents) at the AZALEE seismic simulator of CEA in Saclay, Paris under the auspices of the EC funded SERA project. The aim was to understand the seismic response of statues and busts and then to develop novel and cost-effective risk mitigation schemes for improving the seismic resilience of museum valuable contents. The work is focused on the investigation of the seismic response of two real-scale marble roman statues and three busts of three roman emperors standing on pedestals of different types and size. Both non-isolated and seismically isolated artefacts are considered, while two new and highly efficient base isolation systems, tailored to art objects, have been tested. The setting up of the tests and the derivation of preliminary numerical results are presented.

Finally, *Chapter 8* presents the conclusions of the Thesis. This chapter summarizes the key and novel points of the Thesis and proposes future work extensions.

Chapter 2

Rocking Systems

2.1 The freestanding rocking block

Free-standing slender blocks when subjected to an excitation of their base may slide, uplift, rock or overturn. Omitting the uplift and assuming that there is no sliding, the most significant motion is rocking, i.e. the partial uplift of a structure from its base when the center of rotation changes. Rocking during an earthquake is common for free-standing objects and also for many other engineering systems. The seismic response of a solitary rigid block that rocks on a rigid base was first studied more than a century ago by Milne, 1885, while today the problem is typically addressed using the framework proposed by Housner, 1963. Over the years there have been many studies shedding light on the problem, e.g. Yim and Chopra, 1985, Ishiyama, 1982a, Zhang and Makris, 2001, Politopoulos, 2010, Dimitrakopoulos and DeJong, 2012b, Mathey et al., 2016, just to name a few.

The homogeneous rectangular rigid block of Figure 2.1 has dimensions $2b \times 2h$, mass m and its moment of inertia about the pivot point O, or O', is I_0 (Figure 2.1). We assume that the coefficient of friction between the block and its rigid base is always big enough so that the block does not slide. In this simplest case, the rigid block problem has a single-degree-of-freedom, the rotation θ, while $\alpha = atan(b/h)$ is the block *slenderness angle* and $R = \sqrt{b^2 + h^2}$ is its *size parameter*. Parameters α and R fully describe the block's geometry (Housner, 1963), while for a rectangular block the rotational moment of inertia with respect to O is $I_0 = (4/3)mR^2$.

Assuming that there is no jump and as a result the rigid body remains at the same position at the instant of impact, the equation of motion of a free-standing block under a horizontal ground acceleration $\ddot{u}_g$ is obtained from the equilibrium between the seismic resisting and overturning moments about the pivot point "O". The overturning moment M_{otn} due to seismic loading is:

$$M_{otn} = -m\ddot{u}_g\left(t\right)H\left(\theta\right) = -m\ddot{u}_g\left(t\right)R\cos\left[\alpha\text{sgn}(\theta\left(t\right)) - \theta\left(t\right)\right] \tag{2.1}$$

where $H(\theta)$ is the height of the block's center of mass during the rocking motion. When the block is at rest ($\theta = 0$), the height $H(\theta)$ becomes equal to $H_0 = Rcos(\alpha)$. The restoring moment M_{res} resists the overturning of the block and is equal to:

$$M_{res} = mgR \sin\left[\alpha \text{sgn}\left(\theta\left(t\right)\right) - \theta\left(t\right)\right] \tag{2.2}$$

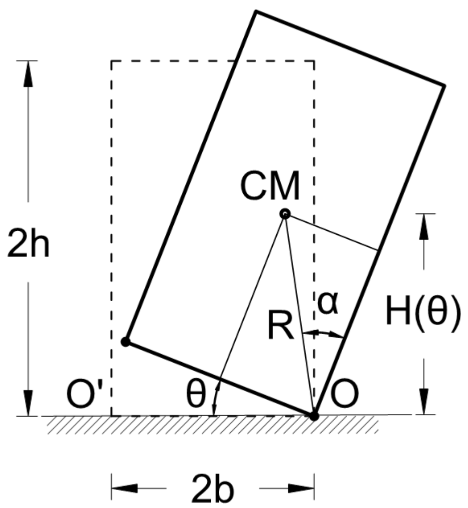

FIGURE 2.1: Geometry of the rocking block.

Assuming that, under dynamic loading, the overturning is also prevented by the inertia term $I_0\ddot{\theta}(t)$, the block's equation of motion will be (Housner, 1963):

$$I_0\ddot{\theta}\left(t\right) + M_{res} - M_{otn} = 0 \Leftrightarrow$$
$$I_0\ddot{\theta}\left(t\right) + mgR \sin\left[\alpha \text{sgn}\left(\theta\left(t\right)\right) - \theta\left(t\right)\right] + m\ddot{u}_g\left(t\right) R \cos\left[\alpha \text{sgn}\left(\theta\left(t\right)\right) - \theta\left(t\right)\right] = 0 \tag{2.3}$$

where g is the acceleration of gravity. The term $sgn(\theta)$ is used to take into consideration that there are two symmetric pivot points, while we assume that an impact occurs and the block continues rocking with a new pivot point when the sign of θ is reversed (Housner, 1963). The equation of motion can be simplified if the angles θ and α are small:

$$I_0\ddot{\theta}\left(t\right) + mgR\left[\alpha \text{sgn}\left(\theta\left(t\right)\right) - \theta\left(t\right)\right] + m\ddot{u}_g\left(t\right) R = 0 \tag{2.4}$$

When the block is at rest ($\theta = 0$), omitting the inertia term in Eq. 2.3, we find that the block will start a rocking motion only if the ground acceleration $\ddot{u}_g$ exceeds a threshold value, i.e. when $\ddot{u}_g \geq (b/h)g$, or $\ddot{u}_g \geq g \tan\alpha$. Furthermore, we often normalize the rotation with the slenderness angle in order to obtain the metric θ/α which is related to the block's overturning. Another way to write the equation of motion is using the *frequency parameter p* of the rocking block. This approach, considering that

$p = \sqrt{3g/4R}$, results to a more compact expression:

$$\ddot{\theta}(t) = p^2 \left[-\sin\left[\alpha \mathrm{sgn}\left(\theta(t)\right) - \theta(t)\right] - \ddot{u}_g(t)/g \cos\left[\alpha \mathrm{sgn}\left(\theta(t)\right) - \theta(t)\right]\right] \tag{2.5}$$

The equation of motion of the block (Eq. 2.3, or one of Eq. 2.4, 2.5) is solved numerically using an Ordinary Differential Equation (ODE) solver. The analysis is initiated at the time instant that the condition $\ddot{u}_g \geq (b/h)g = g\tan\alpha$ is met and continues until an impact is detected. Immediately after impact we assume that the rotation θ is zero and that the sign of the angular velocity changes and becomes equal to $\eta\dot{\theta}$, where η is the *coefficient of restitution*. The coefficient of restitution is obtained with the aid of the principle of conservation of angular momentum as:

$$I_0\dot{\theta}_1 - m\dot{\theta}_1 2bR\sin\alpha = I_0\dot{\theta}_2 \tag{2.6}$$

where $\dot{\theta}_1$ and $\dot{\theta}_2$ is the angular velocity before and immediately after impact, respectively. From Eq. 2.6 and setting $b = Rsin\alpha$, $I_0 = 4/3mR^2$ the ratio of the angular velocity before and after impact defines the coefficient of restitution:

$$\eta = \frac{\dot{\theta}_2}{\dot{\theta}_1} = \frac{I_0 - 2mR^2\sin^2\alpha}{I_0} = 1 - \frac{3}{2}\sin^2\alpha \tag{2.7}$$

In the remaining of this work we refer to the block solutions obtained after directly solving the equation of motion as “rigid block” model, or in short as “RB” solution. All RB solutions were obtained using the ODE23s solver available in Matlab, 2016.

Some interesting observations about the seismic response of rocking blocks can be made with reference to Figure 2.2b. The figure shows results from a large pool of ground motions and blocks of various sizes (Fragiadakis et al., 2016). The results refer to pulse-like ground motions and the data are plotted against the peak ground acceleration (PGA) normalized by the critical acceleration for the initiation of rocking, $gtan\alpha$, versus the normalized pulse period, ω_p/p. Such plots are referred as “overturning spectra”, since the horizontal axis measures frequency and the vertical axis measures PGA which is a possible ground motion intensity measure. The red points correspond to blocks that overturned and the green points to blocks that did not overturn. Furthermore, for comparison, the solid blue lines show the closed-form solution of Dimitrakopoulos and DeJong, 2012a that define the safe-unsafe threshold for full, symmetric sine pulses.

Simulations of a large pool of ground motion records and blocks of various sizes (Fragiadakis et al., 2016) (blue lines: closed-form solution (Dimitrakopoulos and DeJong, 2012a) and red curve: approximately separates the safe from the overturning data) are presented in Figure 2.2. Moving horizontally to the right side of Figure 2.2,

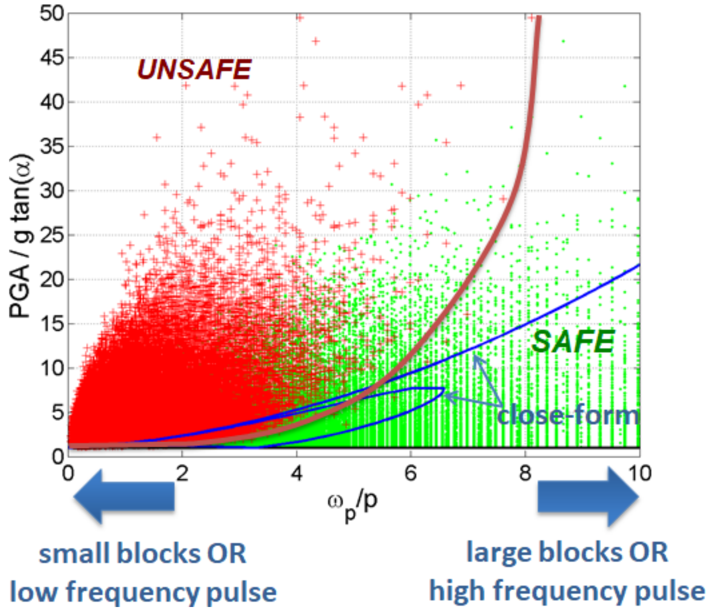

FIGURE 2.2: Simulations of a large pool of ground motion records and blocks of various sizes (Fragiadakis et al., 2016) (blue lines: closed-form solution (Dimitrakopoulos and DeJong, 2012a) and red curve: approximately separates the safe from the overturning data.)

.

the points refer to blocks that are either large (large R and small p) or are subjected to high frequency ground motions (large ω_p values). Therefore, towards the right (increasing ω_p/p), the possibility of overturning reduces, while for ω_p/p larger than 8, the blocks are safe regardless of the acceleration level. Towards the left side (decreasing ω_p/p), either the ground motions contain long-period pulses (small ω_p values), or the blocks have a small size (large p values). Especially for $\omega_p/p \leq 2$, overturning occurs for all ground motion records that are capable to initiate rocking. It is interesting to note, that the apparent limit between the safe and the unsafe region implies only that the blocks on the safe side do not overturn. In other words, there are many blocks on the "unsafe" region that did not overturn. In this sense, the threshold between the safe and the unsafe region corresponds to the minimum normalized ground acceleration $PGA/g \tan \alpha$ for each value of ω_p/p that could topple the block; this does not mean that all excitations with larger $PGA/g \tan \alpha$ values will cause overturning.

2.2 The asymmetric rocking block

Considering the dynamics of a symmetric freestanding block, that have been previously discussed, the extension of the theory to asymmetric cases is here presented.

The asymmetric rocking block of Figure 2.3b is assumed. The asymmetric bust of Figure 2.3a can be modeled using the simplification of Figure 2.3b. The block's width is $b = b_1 + b_2$, the center's of mass height is h while the total mass and the rotational moment of inertia with respect to the center of mass are m and I_{CM}, respectively. The

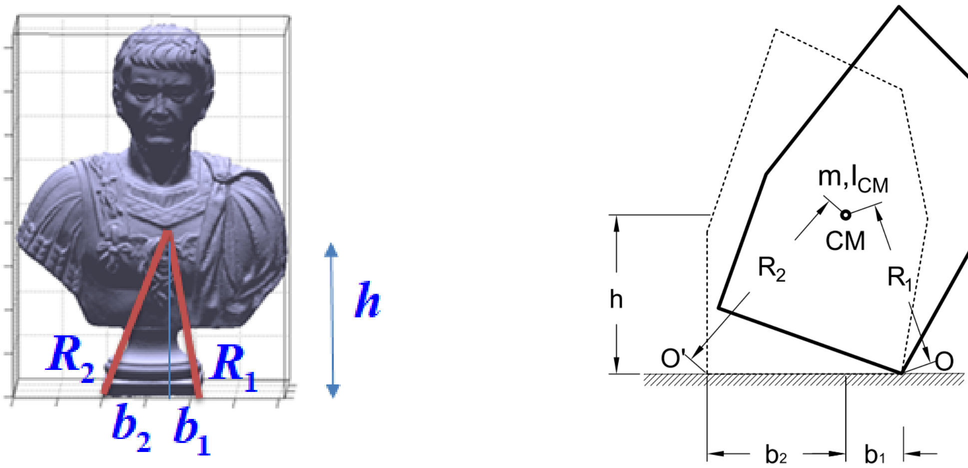

FIGURE 2.3: (a) implementation of the asymmetric rocking block theory to a freestanding bust, (b) Geometry of an asymmetric rocking block.

.

rocking motion of an asymmetric rocking block, that is assumed as rigid, is described by a modified equation of motion as discussed by Wittich and Hutchinson, 2015:

$$\left(I_{CM} + mR_i^2\right)\ddot{\theta}\left(t\right) + mgR_i \sin\left[\alpha_i \mathrm{sgn}\theta\left(t\right) - \theta\left(t\right)\right] = -m\ddot{u}_g\left(t\right)R_i \cos\left[\alpha_i \mathrm{sgn}\theta\left(t\right) - \theta\left(t\right)\right] \tag{2.8}$$

where the subscript i denotes the positive or negative rotation of the block and $sgn(\theta)$ is the signum function that corresponds to rocking motion with respect to the critical or the noncritical side. Therefore, when $i = 1$, the block rotates with respect to O and when $i = 2$ the pivot point is the O'.

When impact occurs, the kinetic energy is reduced and this reduction is derived through conservation of momentum with reference to the rocking point immediately before and just after the impact. This yields to a velocity ratio, known as the coefficient of restitution, which for the rigid block of interest is given by the following formulas for the positive to negative and the negative to positive transition, respectively:

$$\eta_1 = \frac{1}{I_{CM} + mR_1^2}\left[I_{CM} + mR_2^2 - m(b_1 + b_2)R_2 sin\alpha_2\right] \tag{2.9}$$

$$\eta_2 = \frac{1}{I_{CM} + mR_2^2}\left[I_{CM} + mR_1^2 - m(b_1 + b_2)R_1 sin\alpha_1\right]. \tag{2.10}$$

2.3 Rocking frames

Frames with columns that are allowed to uplift and then pivot during a seismic excitation can be found in various systems. A notable example is the case of ancient monuments in which freestanding columns support an epistyle (Figure 2.4a). Although rocking systems lack a mechanism in order to resist lateral forces, they have survived many strong earthquakes during their long history. Based on the rocking principle, a relatively recent “damage avoidance design” concept (Mander and Cheng, 1997) that allows a partial/controlled rocking motion of the columns offers a promising seismic design procedure. Remarkable examples of modern rocking bridges are the Rangitikei Railway Bridge (Figure 2.4b) and the Deadman’s Point bridge at Cromwell, both in New Zealand (Skinner et al., 1980; Priestley et al., 1996). Rocking can be seen as a form of seismic isolation (Chen et al., 2006; Di Egidio and Contento, 2009) that reduces transient deformations and column damage (Giouvanidis et al., 2015), while it results to reduced moment demand at the foundation. Moreover, the residual displacements can be controlled using a self-centering system (ElGawady and Sha’lan, 2011).

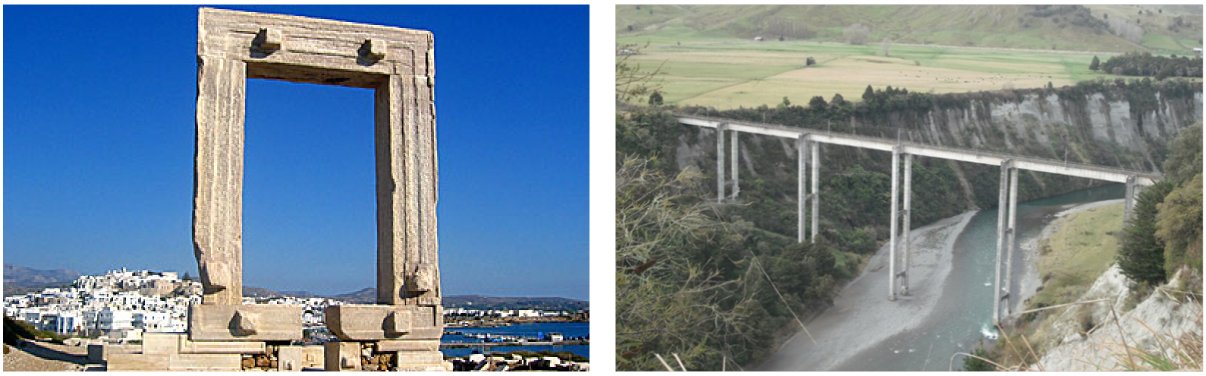

(a) (b)

FIGURE 2.4: Examples of rocking frames: (a) Portara monument, Naxos island, Greece. A massive marble entrance of an unfinished temple that faces directly toward Delos island, the birthplace Apollo. Portara survived more than 2500 years. (b) The Rangitikei railway bridge in New Zealand.

The dynamics of the freestanding rocking block can be easily extended to the study of rocking frames. Among others, Makris and Vassiliou, 2013, DeJong and Dimitrakopoulos, 2014 and Dimitrakopoulos and Giouvanidis, 2015a, expressed the equation of motion of a simple rocking frame using principles of analytical dynamics. The beneficial effect of rocking in critical structures (e.g. bridges) has been confirmed by Cheng, 2008, and has been also shown by Palermo et al., 2007 and Wacker et al., 2005, among others. Giouvanidis and Dimitrakopoulos, 2016b worked on the modeling of bridges, and specifically on precast frame structures, equipped with vertical restrainers. Dar et al., 2018 first investigated the seismic response of rocking frames when the contact edge is allowed to reside anywhere between the center of the pier and its extreme edge, while recently they examined the seismic response of rocking frames with unsymmetrical piers (Dar et al., 2019). Thomaidis et al., 2020 studied the influence of the abutment-backfill system on rocking bridges, while Zhou et al., 2019 presented an experimental study on the seismic response and rocking isolation of a bridge with post-tensioned rocking piers exhibiting negative stiffness.

The rigid block, referred also as "freestanding column", is the simplest rocking structure. The rocking frame can be seen as an extension of the solitary block and hence the fundamentals of the rocking problem are quickly repeated. The freestanding block of Figure 2.1 has dimensions $2b \times 2h$, mass m_c and is subjected to a horizontal seismic excitation $\ddot{u}_g(t)$. This is a nonlinear single-degree-of-freedom (SDOF) problem described by the equation of motion (Eq. 2.3) proposed by Housner, 1963:

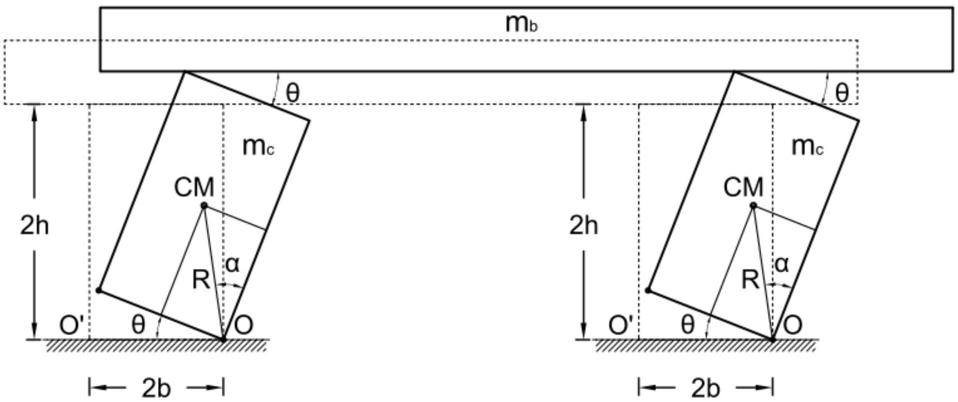

FIGURE 2.5: Rocking frame with two rigid columns and a rigid beam.

The right-hand side of the Equation 2.3 is the seismic demand and it is equal to the overturning moment (Eq. 2.1): The left-hand side term is the resistance (or capacity) which is equal to the inertia term plus the restoring moment M_{res} produced by the selfweight if the problem was static:

$$I_0\ddot{\theta}(t) + M_{res} = I_0\ddot{\theta}(t) + m_c g R \sin\left[\alpha sgn\theta(t) - \theta(t)\right] \tag{2.11}$$

The simplest rocking frame problem consists of two freestanding columns that are capped with a rigid beam (Figure 2.5). The columns are identical, i.e. they have the same size parameter R, equal slenderness α and mass m_c, while the properties of each column are equal to those of the freestanding block of Figure 2.1. The mass of the beam is denoted as m_b and the ratio of the deck/epistyle mass over the sum of the mass of the two columns is the *mass ratio* γ, equal to $\gamma = m_b/(2m_c)$. The rocking frame of Figure 2.5 is also a SDOF system since the rotation $\theta(t)$ is the only degree-of-freedom.

The equation of motion of the two-column rocking frame is (Makris and Vassiliou, 2013):

$$\ddot{\theta}(t) = \frac{1+2\gamma}{1+3\gamma} p^2 \left[-\sin\left[\alpha sgn\theta(t) - \theta(t)\right] - \frac{\ddot{u}_g(t)}{g} \cos\left[\alpha sgn\theta(t) - \theta(t)\right] \right] \tag{2.12}$$

The above equation of motion (Eq. 2.12) is similar to that of the rigid block (Eq. 2.5) if the p^2 term is multiplied by $(1+2\gamma)/(1+3\gamma)$. Thus, Eq. 2.12 can be solved assuming that the rocking frame is a rigid block with modified frequency parameter $\tilde{p}^2 = p^2(1+2\gamma)/(1+3\gamma)$ and slenderness $\tilde{\alpha} = \tan^{-1}(b/h)$, same to that of the rocking block α. The size parameter is given by the expression $\tilde{R} = \big((1+3\gamma)/(1+2\gamma)\big)R$. Moreover, setting $p^2 = 3g/4R$ and multiplying Eq. 2.12 with $(4/3)m_c R^2 \times (1+3\gamma)/(1+2\gamma)$, the equation of motion becomes:

$$\frac{1+3\gamma}{1+2\gamma} I_0 \ddot{\theta}(t) + m_c g R \sin[\alpha sgn\theta(t) - \theta(t)] = -m_c \ddot{u}_g(t) R \cos[\alpha sgn\theta(t) - \theta(t)] \tag{2.13}$$

Eqs. 2.12 and 2.13 are equivalent and known as the *generalized* equation of motion of the rocking frame problem. When $\gamma = 0$ Eqs. 2.12 and 2.13 reduce to the equation of motion of the rocking block, while if the frame has N freestanding columns that are capped with a rigid beam, the same equation can be used setting $\gamma = m_b/(Nm_c)$. The generalized equation of motion offers a convenient tool for solving rocking frames; in our work it will be used as the basis of an alternative simplified modelling approach. For the rocking frame, the uplift acceleration is equal to $\ddot{u}_{g,min}(t) = g tan\alpha$, and the coefficient of restitution is given by the expression (Makris and Vassiliou, 2013; Dimitrakopoulos and Giouvanidis, 2015a):

$$\eta_{frame} = \frac{\dot{\theta}_2}{\dot{\theta}_1} = \frac{1 - 1.5\sin^2\alpha + 3\gamma\cos 2\alpha}{1+3\gamma} \tag{2.14}$$

As expected, when $\gamma = 0$, Eq. 2.14 reduces to that of the solitary block (Eq. 2.7).

2.4 Two-block systems

Following the observations on the dynamics of the freestanding block, Psycharis, 1990 extended the problem to the rocking response assessment of two-block systems. This concerns the rocking response of stacked blocks, consisting of freestanding blocks placed one on top of the other. Psycharis, 1990 examined the simplest case of two symmetric blocks. This work was later revisited by Spanos et al., 2001 who formulated again the equations of motions trying to facilitate the development of multi-block structural models (i.e. pillars). From all the above studies it is evident that special care is required for the assessment of the energy dissipation. Chatzis et al., 2017 investigated analytically the loss of energy in two-body systems providing an alternative way to assess such a non-linear dynamic phenomenon. Recently, Anagnostopoulos et al., 2019 presented a compact mathematical formulation in order to describe the dynamic rocking response of two-block systems subjected to ground excitation. Their work aims to derive a unified system of governing equations capable of describing all possible rocking and impact modes of two-stacked rigid blocks, based on the Euler-Lagrange approach and the principle of the conservation of angular momentum. Kounadis et al., 2012 studied the overturning instability of a freely standing two-rigid block system, focusing on the determination of the minimum amplitude ground excitation.

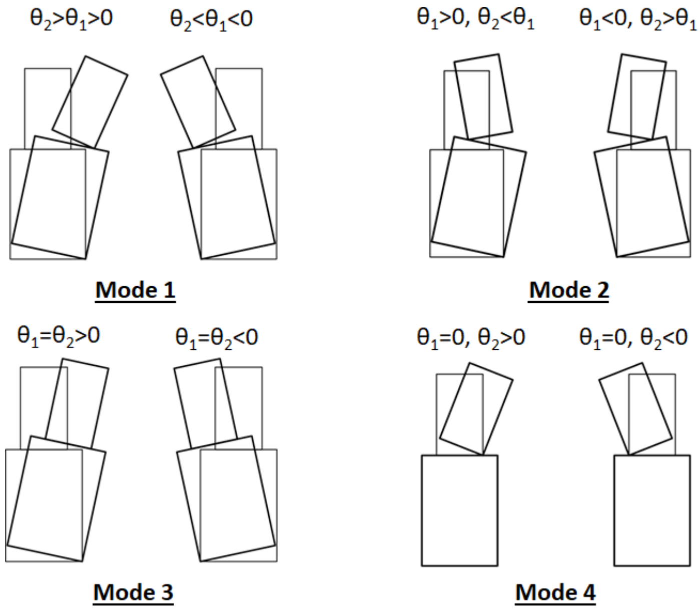

FIGURE 2.6: Four different modes in two-block assemblies considering symmetric upper block (Psycharis, 1990).

Psycharis, 1990 addressed the two-block problem proposing the corresponding equations of motion. Applying Newton's second law to each block separately and considering the equilibrium of restoring and overturning moments, e.g. Diamantopoulos and Fragiadakis, 2019, about the appropriate pivot point, the equations of motion can be written in a form equivalent with the approach proposed by Housner, 1963 for the single block case. The free-standing block can oscillate under a seismic excitation and hence, the equation of motion is changed when the angle of rotation changes sign. That means that the problem has only one "mode" and is governed by one set of equations. The analytical formulation of the non-linear two-block problem is complicated enough, because of the four possible "modes" (Fig. 2.6) of vibration, each being governed by a different set of equations of motion.

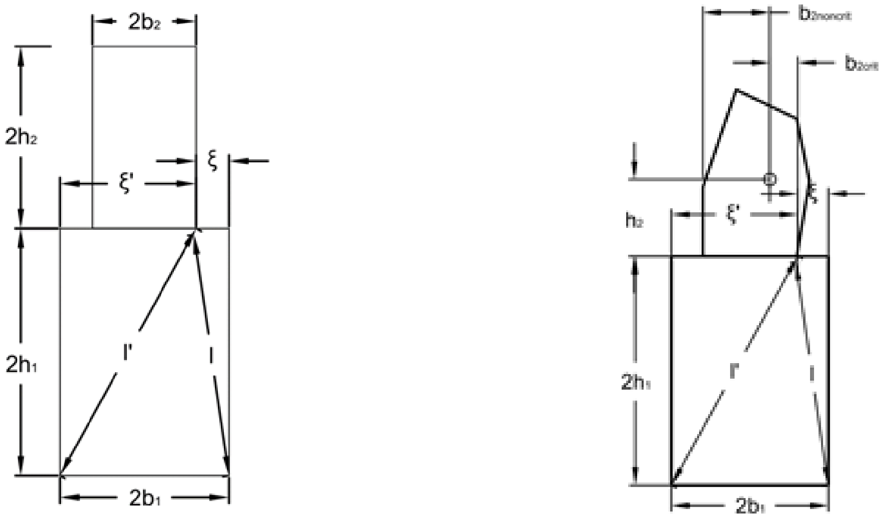

(a) (b)

FIGURE 2.7: Geometrical properties: (a) symmetric two-block system, (b) asymmetric two-block system considered.

In two-block assemblies (Fig. 2.7) it is assumed that there are two degrees of freedom, the rotations of the lower and upper block, respectively, while the four possible modes of oscillation (Fig. 2.6) are independent. For each of the four different modes, the equation of motion is implemented with the aid of the equivalent matrices presented below. Supposing that each mode has two sub-cases, then there are eight cases and hence eight equations of motion. The eight equations are simplified to four using the sign function in order to define the restoring moments M_{res}. The four equations are defined as:

$$I_0 + M_{res} = M_{otn} \tag{2.15}$$

and the corresponding matrices, are as follows:

Mode 1:

$$I_0 = \begin{bmatrix} I_{01} + m_2 l'^2 & m_2(2h_1h_2 + b_2\xi) \\ m_2(2h_1h_2 + b_2\xi) & I_{02} \end{bmatrix} \tag{2.16}$$

$$M_{res} = \begin{bmatrix} -(m_1h_1 + 2m_2h_1)g & 0 \\ 0 & m_2h_2g \end{bmatrix} \begin{Bmatrix} \theta_1 \\ \theta_2 \end{Bmatrix} + \begin{bmatrix} \pm(m_1b_1 + m_2\xi)g \\ \pm(m_2b_2)g \end{bmatrix} \tag{2.17}$$

$$M_{otn} = \begin{bmatrix} -(m_1h_1 + 2m_2h_1)\ddot{x_g} \\ -m_2h_2\ddot{x_g} \end{bmatrix} \tag{2.18}$$

Mode 2:

$$I_0 = \begin{bmatrix} I_{01} + m_2 l'^2 & m_2(2h_1h_2 - b_2\xi') \\ m_2(2h_1h_2 - b_2\xi) & I_{02} \end{bmatrix} \tag{2.19}$$

$$M_{res} = \begin{bmatrix} -(m_1h_1 + 2m_2h_1)g & 0 \\ 0 & m_2h_2g \end{bmatrix} \begin{Bmatrix} \theta_1 \\ \theta_2 \end{Bmatrix} + \begin{bmatrix} \pm(m_1b_1 + m_2\xi')g \\ \mp(m_2b_2)g \end{bmatrix} \tag{2.20}$$

$$M_{otn} = \begin{bmatrix} -(m_1h_1 + 2m_2h_1)\ddot{x_g} \\ -m_2h_2\ddot{x_g} \end{bmatrix} \tag{2.21}$$

Mode 3:

$$I_0 = \begin{bmatrix} I_0 & 0 \\ 0 & I_0 \end{bmatrix} \tag{2.22}$$

$$M_{res} = \begin{bmatrix} -mhg & 0 \\ 0 & -mhg \end{bmatrix} \begin{Bmatrix} \theta_1 \\ \theta_2 \end{Bmatrix} + \begin{bmatrix} \pm(mb_1)g \\ \pm(mb_1)g \end{bmatrix} \tag{2.23}$$

$$M_{otn} = \begin{bmatrix} -mh\ddot{x_g} \\ -mh\ddot{x_g} \end{bmatrix} \tag{2.24}$$

Mode 4:

$$I_0 = I_{02} \tag{2.25}$$

$$M_{res} = m_2h_2g\theta_2 \pm m_2b_2g \tag{2.26}$$

$$M_{otn} = -m_2h_2\ddot{x_g} \tag{2.27}$$

where m_1, m_2 are the masses of lower (block 1) and upper (block 2), respectively, I_{01}, I_{02} are the moments of inertia of blocks with respect to their pivot points, $m = m_1 + m_2$ is the total mass of the system, I_0 is the moment of inertia of the system about any of the two pivot points and h is the height of the center of mass of the two-block system:

$$h = \frac{m_1h_1 + m_2(2h_1 + h_2)}{m} \tag{2.28}$$

The study extended to the case of an asymmetric upper block and a symmetric, solid pedestal, which is typically the case of museum artefacts, as shown in Figure 2.8. This requires to modify the matrices above in order to define the critical and the non-critical sides of the upper asymmetric body (Fig. 2.7b). As shown below, the geometrical properties of the upper block need to be distinguished in the sub-cases included in each mode. Two significant modifications are needed for the transition from the simple symmetric case to the asymmetric. Initially, the width b_2 should be replaced with b_{2crit} (modes 1a, 2a, 4a) when the upper block rocks with respect to the right pivot point or $b_{2noncrit}$ (modes 1b, 2b, 4b) when the block rocks with respect to the

FIGURE 2.8: Example of two-block systems.

left pivot point assuming that the critical side is the right one. In mode 3 where both blocks oscillate around the pivot point of the lower block b_{2crit} and $b_{2noncrit}$ should be defined. Also, the moment of inertia in I_0 (i.e Eqs.2.16, 2.19, 2.22, 2.25,) matrices should be calculated for every mode according to the above b values.

Chapter 3

Modeling of rocking blocks

In this chapter, the modeling of rigid/flexible rocking blocks that are freestanding/restrained is presented. It has to be noted that, the notation was partially changed with respect to the original corresponding paper Diamantopoulos and Fragiadakis, 2019 in order to be consistent with the notation used throughout the Thesis.

3.1 Introduction

Rocking of rigid, or flexible, bodies/systems is a fundamental problem in earthquake engineering. The most common option for handling a 2D rocking problem is directly solving the equation of motion proposed by Housner, 1963. However, there have been attempts to develop "equivalent" solutions based on the dynamics of the single-degree-of-freedom (SDOF) oscillator, since structural engineers are more comfortable with elastically deforming structures and software. Priestley et al., 1978 proposed an equivalent SDOF oscillator with a constant damping ratio whose period depends on the amplitude of the rocking angle; this approach was latter adopted by ASCE/SEI 41-06, 2007. Makris and Konstantinidis, 2003 revisited the approach of Priestley et al., 1978 showing that in many cases it fails to produce accurate response estimates. Another equivalent SDOF approach is that found in ASCE 43-05, 2005 where the SDOF oscillator has constant damping but its period depends on the amplitude of rocking. This method was also recommended for the seismic loss assessment of unanchored objects in the FEMA P-58-1, 2012 guidelines but it also has serious limitations, as shown in Dar et al., 2016. On the other hand, there are different modeling approaches for solving numerically the problem as shown in Figure 3.1. The first three models of Figure 3.1a,b,c are essentially SDOF systems equipped with tension-only springs, dashpots or a curved base. These models are conceptually simple but often lack computational stability, or have a limited purpose, e.g. are suitable only for rigid blocks. A full finite (FEM) (Figure 3.1d), or discrete element (DEM) modeling, is also possible but again there are various computational shortcomings, e.g. large computing cost for handling a simple problem, difficulty to define energy loss and damping, difficulty to define the interaction surface either through springs, or through proper boundary conditions.

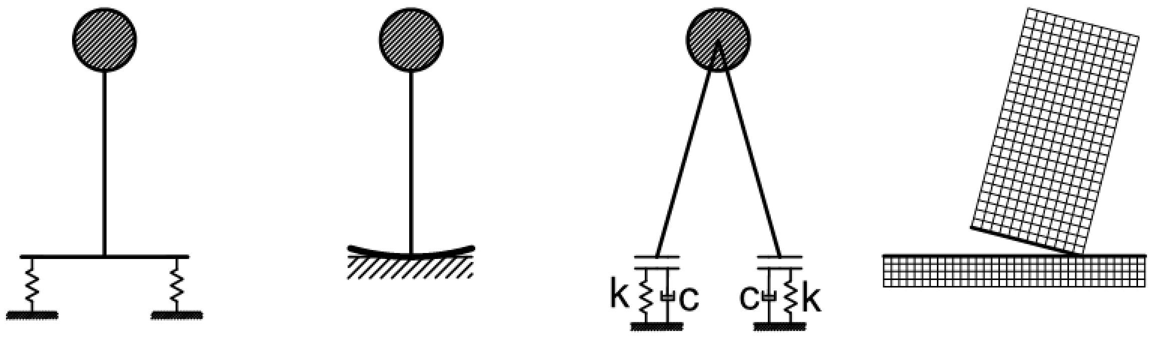

(a) (b) (c) (d)

FIGURE 3.1: Existing numerical models for the rocking block problem in the literature.

Due to the apparent difficulties of simple modeling methods, several fundamentally different approaches have been proposed in the literature for solving the rocking block problem. Prieto et al., 2004 introduced an approach based on a Dirac-delta type interaction for the impact mechanism. Chatzis and Smyth, 2012 proposed two models: a concentrated spring model and a Winkler model for the simulation of a rigid body experiencing a 2D rocking motion on a moving deformable base. Vassiliou et al., 2014 and Vassiliou et al., 2016 developed a versatile finite element model for the seismic response analysis of solitary blocks based on elastic multimass oscillators. Giouvanidis and Dimitrakopoulos, 2016a solved the problem following a nonsmooth approach that consistently treats the contact/impact phenomenon during the rocking motion, while Acikgoz and DeJong, 2012 and Acikgoz and DeJong, 2016 proposed analytical models and studied the dynamics of flexible rocking structures. Recently, Kakouris et al., 2018 solved the problem using the Material Point Method (MPM) which is a method where the continuum is represented by a set of moving material points.

The initial motivation of the work presented in the Thesis stems from the need for simple, robust and fast models necessary for studying the dynamic/seismic behaviour of rocking structures. Centered around the equation of motion of Housner, 1963, a rocking modeling that for rigid blocks has a single degree-of-freedom, the rotation, is presented. Rocking is simulated with a negative-stiffness rotational spring at the base of a beam element with properties consistent with the geometry of the block. Depending on the problem at hand, a single (lumped) mass, or an array of masses is introduced, resulting to a system that can be easily solved with the direct stiffness method and thus with common matrix analysis methods. The proposed method allows also to easily calculate the seismic response of flexible rocking bodies and can be extended to many other applications avoiding specifically tailored analytical solutions, or costly finite element simulations.

3.2 Proposed rigid block modeling

3.2.1 SDOF oscillator vs Rocking Block

The proposed rigid block model is essentially a single-degree-of-freedom (SDOF) system connected at its base with a nonlinear rotational spring (Figure 3.2a) that has a negative stiffness moment-rotation relationship. The proposed model is conceptually explained comparing the equation of motion of the SDOF oscillator against that of the rigid block. Structural analysis software solve the equation of motion of a SDOF oscillator that consists of the sum of the inertia F_I, the damping F_D and the elastic F_E forces resisting the externally applied load P, i.e.:

$$F_I(t) + F_D(t) + F_E(t) = P(t) \Leftrightarrow m\ddot{u} + c\dot{u} + F_E = -m\ddot{u}_g \tag{3.1}$$

where m is the mass, c the damping, $\ddot{u}$, $\dot{u}$ the acceleration and the velocity of the SDOF, respectively. We can tune a software that has been programmed to solve Eq. 3.1 so that it solves the equation of motion of the block (e.g. Eq. 2.3) by smartly adjusting the input parameters. For this purpose, we can rewrite Eq. 3.1 replacing u with θ, the force F with the moment M and the mass m with the rotational inertia of the block I_0. The elastic term F_E is determined from the $M - \theta$ relationship of the spring at the base of the oscillator and is denoted $M_{res}(\theta)$. Furthermore, the external force term $P(t)$ is replaced by the overturning moment M_{otn}, which is equal to the seismic force $F_{eq} = -m\ddot{u}_g$ times its leverarm $H(\theta)$. For the moment, the damping term F_D is omitted, since it will be considered with an event-based approach that is discussed in the section that follows. With these replacements, the SDOF equation of motion (Eq. 3.1) is rewritten as:

$$M_I + M_{res} = M_{otn} \Leftrightarrow I_0\ddot{\theta}(t) + M_{res}(\theta) = -m\ddot{u}_g H(\theta) \tag{3.2}$$

where M_{res} is the restoring moment under static loading (Eq. 2.2). Comparing with Eq. 2.3, we have arrived at the equation of motion of the block starting from the SDOF oscillator's equation (Eq. 3.1). In the sections that follow, we show that if we choose appropriately the SDOF's height H, the rotational moment of inertia I and the $M - \theta$ relationship of the spring, we can solve quickly and accurately any rigid block problem using a structural analysis software, e.g. OpenSees (McKenna and Fenves, 2001).

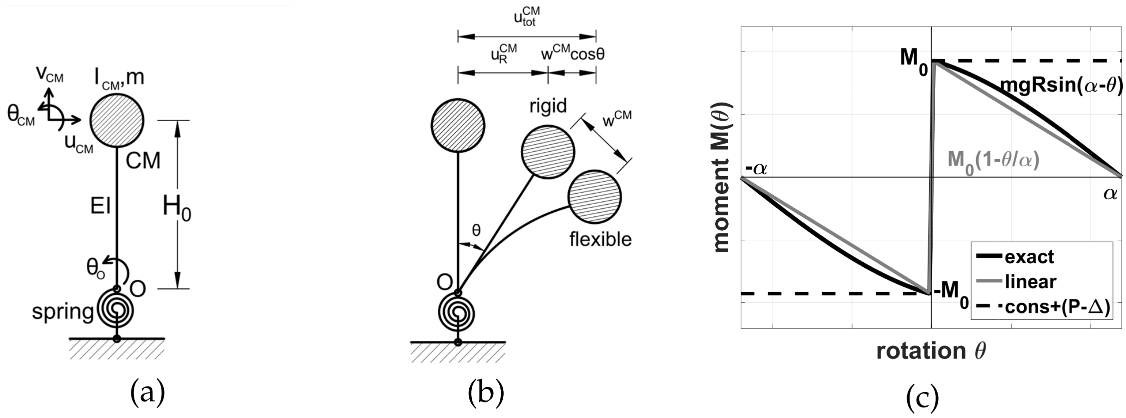

FIGURE 3.2: (a) Conceptual description of the proposed rigid block modeling. (b) Deformed shape of rigid and flexible rocking blocks. (c) Moment-rotation relationships of the nonlinear rotation spring ($M_0 = mgRsin\alpha$).

The proposed modeling of the rocking block problem is shown schematically in Figure 3.2a where we model the SDOF oscillator assuming two nodes connected with a beam element and having a distance H_0. The top node corresponds to the center of mass "CM" of the block and the bottom node is denoted as "O" and loosely corresponds to the pivot point. The elastic beam element that connects the two nodes can be rigid, or flexible, depending on the properties of the block, while in the simplest of our models we assume that all the mass m is lumped at the CM node. The lumped mass also has a rotational moment of inertia I_{CM}; the subscript implies that it is calculated with respect to an axis that passes from the center of mass CM. Moreover, the bottom node O is connected to the ground with a rotational spring that has a $M - \theta$ relationship describing the block's restoring moment under static loading. Assuming that the SDOF oscillator is rigid, the rotations θ_{CM} and θ_0 are equal ($\theta_{CM} = \theta_0 = \theta$), while the horizontal and the vertical displacements u_R^{CM}, v_R^{CM} of the CM node are always function of θ, since $u_R^{CM} = H_0 sin\theta = H_0\theta$ and $v_R^{CM} = H_0(1 - cos\theta)$. Therefore, for the rigid case, the four degrees-of-freedom (dof) are reduced to one, the rotation of the spring θ; similar to the rocking block equation of Eq. 2.3. When the block is flexible, there is an additional degree-of-freedom the displacement w, while the total horizontal displacement of the center of mass can be decomposed to a rocking and a bending part $u_{tot}^{CM} = u_R^{CM} + w^{CM}cos\theta$ (Figure 3.2b).

The analogy between the SDOF oscillator and the rocking block (RB) problem allows adopting a modeling based on the SDOF oscillator, but, more importantly, this analogy allows to easily solve rocking problems that are more complicated or have more degrees-of-freedom. Below we outline the fundamental components of the proposed modeling based on the SDOF oscillator of Figure 3.2a, while in the sections that follow we give more details on how the various parameters are derived.

3.2.2 Properties of the $M - \theta$ relationship

The self-centering capacity of the block depends on the $M - \theta$ relationship of the rotational spring. Vassiliou et al., 2016 and Kalkan and Graizer, 2007 have shown that it is possible to use an elastic-perfectly plastic spring combined with a modeling that takes into consideration second-order effects. The "yield" moment of the nonlinear spring should be equal to $M_0 = mgb = mgR \sin \alpha$, which is the moment required for setting a rectangular block from its rest position to a rocking motion. This option may not be always stable and its efficiency depends on the software used. In our work, we propose to omit the geometric nonlinearity and to use a negative stiffness $M - \theta$ relationship, as shown in Figure 3.2c. The moment at $\theta = 0$ is M_0, but once the block is set to rocking motion the restoring moment decreases (negative stiffness) reaching a zero moment at $\theta = \alpha$ (overturning). This mildly nonlinear moment-rotation relationship follows the expression of the restoring moment $M(\theta) = mgRsin(\alpha - \theta)$ of Eq. 2.2 and can be inserted in a FE (finite element) code using a piecewise linear approximation. Another option is to use the linearized relationship $M(\theta) = mgRsin\alpha(1 - \theta/\alpha) = M_0(1 - \theta/\alpha)$ which stems from the simplified equation of motion of Eq. 2.4. The three $M - \theta$ options are shown in Figure 3.2c. In all cases unloading and reloading should follow the same path, while the behaviour in the opposite direction is symmetric about the origin.

The choice among the three $M - \theta$ relationships of Figure 3.2c depends on the options available in the software adopted. All three options are possible in OpenSees (Mazzoni et al., 2006) which offers pertinent material models and can be used for large displacement and small strain problems. The differences between the two negative stiffness options of Figure 3.2c are negligible, while the perfectly plastic model may produce errors, or it may not be stable. In the remaining of this work, unless otherwise specified, our results have been obtained using the "exact" option of Figure 3.2c. The linear $M - \theta$ relationship is more easy to implement, while, in terms of accuracy, it produces some very minor differences when the slenderness angle α becomes large. Furthermore, typically in most FE codes the first branch of the available material models is linear elastic, followed by a hardening (or a softening) branch. Since our $M - \theta$ relationship is not zero at $\theta = 0$, we assume a very small "yield" rotation, typically of the order of 10^{-5}.

The case of *flexible* rocking columns deserves further attention. Especially in the case of a large axial load or very flexible systems the properties of negative-stiffness nonlinear springs should be properly adjusted in order the accuracy to be improved. This situation is common in rocking frames with flexible columns, which typically correspond to modern structures, e.g rocking bridges, where the axial load is larger than the column's self-weight.

A deformable rocking column with height $2h$ and axial load N is shown in Figure 3.3. Depending on the problem examined, the mass of the column can be assumed lumped at the center of mass or it can be neglected (e.g. Acikgoz and DeJong, 2012; Avgenakis and Psycharis, 2017). Unless otherwise specified and the for the sake of simplicity, the self-weight of the column will be neglected while other axial loads, are lumped at the column top and are denoted as N. When the lateral seismic force F_{eq} is

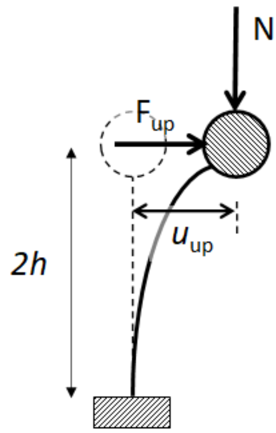

FIGURE 3.3: Freebody diagram of flexible rocking column before uplift.

not strong enough to uplift the column, the column will deform as a cantilever. At the instant that the column uplifts, the horizontal displacement at the column top is u_{up} and the *equation of equilibrium* of the cantilever is:

$$F_{eq} = k_e u_{up} \tag{3.3}$$

If the weight of the column W_c is not neglected, a more accurate expression for k_e can be obtained assuming that the resultant horizontal force (base shear) is applied at height z measured from the base of the frame:

$$z = \frac{W_c + 2N}{W_c + N} h \tag{3.4}$$

where setting $W_c = 0$ the expression gives $z = 2h$. Using the force method, the elastic stiffness k_e of a cantilever with a force acting at height z is:

$$k_e = \frac{3EI}{z^3(1 + 3(2h - z)/2z)} \tag{3.5}$$

where setting $z = 2h$ we obtain $k_e = 3EI/(2h)^3$. The *uplift condition* requires that the restoring and the overturning moment should be equal, thus:

$$M_{otn} = M_{res} \Leftrightarrow F_{eq} z = N(b - u_{up}) + W_c(b - 0.5u_{up}) \tag{3.6}$$

where the leverarm of the axial load is $b - u_{up}$ and the leverarm of W_c is equal to $b - 0.5u_{up}$ [1]. Combining Eq. 3.3 and Eq. 3.6, the critical displacement u_{up} at the instant of uplift is:

$$u_{up} = \frac{Nb + W_c b}{k_e z + N + 0.5W_c} \tag{3.7}$$

Omitting the self-weight of the column, Eq. 3.7 becomes:

$$u_{up} = \frac{Nb}{k_e z + N} \tag{3.8}$$

If $b - u_{up} \approx b$, Eq. 3.8 can be further simplified:

$$u_{up} = \frac{Nb}{k_e 2h} \tag{3.9}$$

The above expression (Eq. 3.9) is in agreement with that proposed by other researchers, e.g Acikgoz and DeJong, 2012 while Eq. 3.8 has been adopted by Caliò and Greco, 2016. For typical values of k_e and N, Eq. 3.8 and Eq. 3.9 will yield practically the same uplift displacement u_{up}.

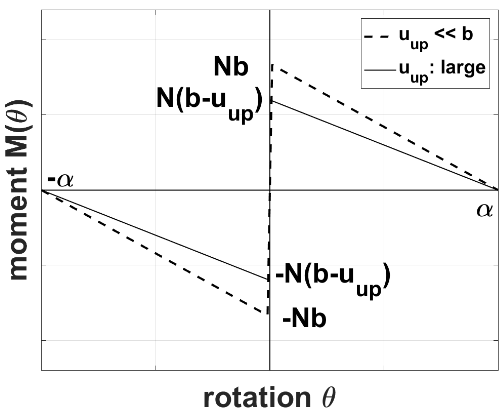

(a)

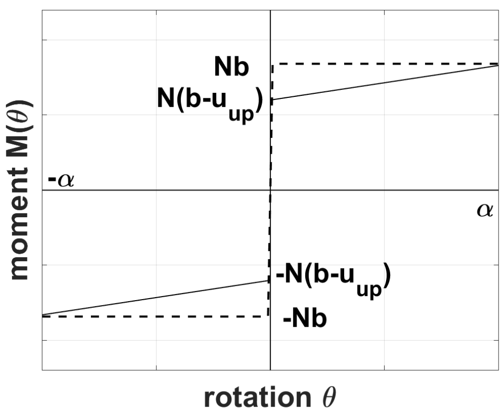

(b)

FIGURE 3.4: (a) Negative stiffness spring, (b) moment-rotation relationship of the spring when the $P - \Delta$ effects are introduced to the model.

The parameters of the base spring of Figure 3.2b should be also adjusted. The spring should be fully rigid prior uplift so that the total stiffness of the system is k_e (Eq. 3.5). The maximum moment of the spring at the onset of uplift should be equal to $M_0 = N(b - u_{up})$. If the column is perfectly rigid, or when u_{up} is small, then $b - u \approx b$ and $M_0 = Nb$. Depending on the analysis method chosen, there are two

[1] assuming a linear triangular distribution of the displacements along the height of the column

options: (i) The analysis does not include $P-\Delta$ effects and therefore, the spring should have negative stiffness (Figure 3.4a), and (ii) the analysis explicitly accounts for $P-\Delta$ effects. The two variants are shown in Figure 3.4, where it shown that in both cases the maximum rotation is the overturning rotation equal to the column slenderness angle α. The two approaches produce results that are very close, but not perfectly identical, as shown in the paragraph that follows. The similarity of the two approaches is due to the fact that, when the moment-rotation relationship has a horizontal, or a hardening branch (Figure 3.4b), the stiffness that is assigned internally by the software is augmented with a $P-\Delta$ term which is approximately equal to $k_{P\Delta} = -N/2h$ [2]. Thus, the total stiffness of the column will be approximately equal to $k_t = k_e - N/2h$. In other words, due to the presence of the axial force, the actual slope of the force-displacement curve will be negative after the uplift, although the $M-\theta$ curve does not soften.

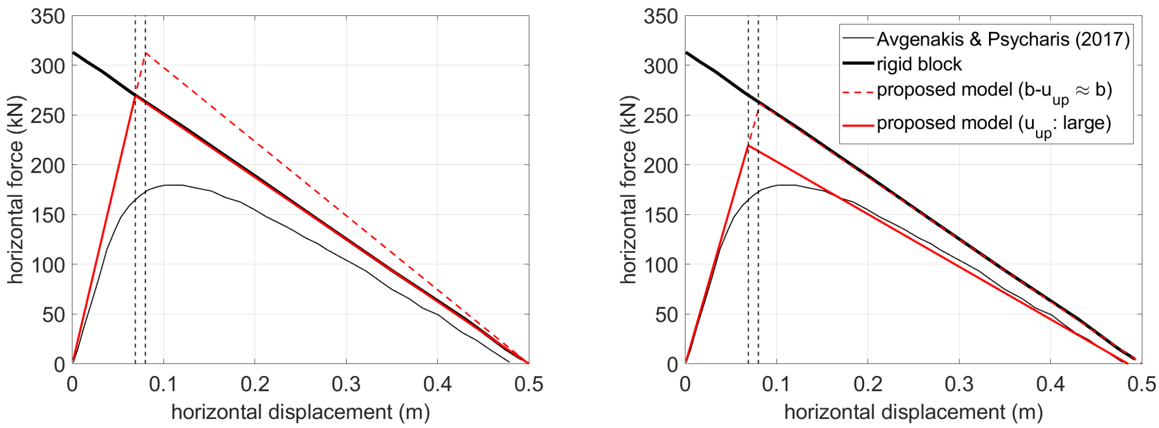

(a) (b)

FIGURE 3.5: Comparison of force displacement curves for a flexible column ($2h = 4m$, $2b = 1m$, $N = -2500kN$) with $E = 1GPa$: (a) using negative stiffness $M-\theta$ spring and (b) analysis including $P-\Delta$ effects.

Figure 3.5 and 3.6 compare the two models with the results presented in Avgenakis and Psycharis, 2017 who proposed a macroelement for modelling rocking members resting on a deformable base. For comparison purposes, a very small modulus of elasticity ($E = 1GPa$) has been assumed in Figure 3.5a, while in Figure 3.6 the differences tend to disappear for ordinary values of the modulus ($E = 10GPa$). In all cases, the response is initially linear elastic and when the uplift condition is met, a negative stiffens branch is initiated. In the model of Avgenakis and Psycharis, 2017 the transition is smooth since a fiber model is used to model the deformability of the column base. The black thick solid line corresponds to the rigid case which is shown here for

[2] this term corresponds to the "geometric stiffness"

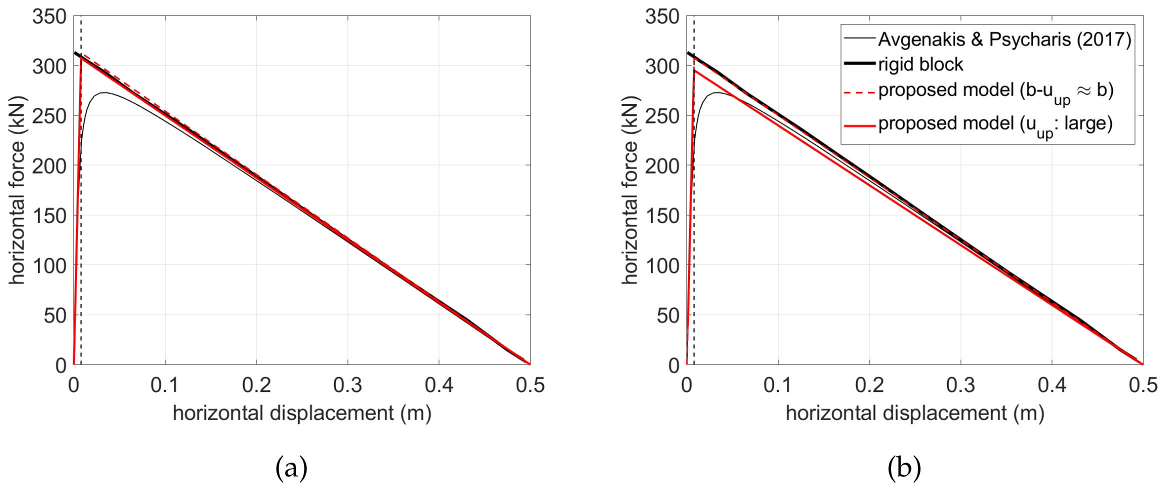

FIGURE 3.6: Comparison of force displacement curves for a flexible column ($2h = 4m$, $2b = 1m$, $N = -2500kN$) with $E = 10GPa$: (a) using negative stiffness $M - \theta$ spring and (b) analysis including $P - \Delta$ effects.

reference. The red solid curves in Figure 3.5a and Figure 3.6a were obtained assuming that the maximum restoring moment is $M_{res} = N(b - u_{up})$, while the dashed red lines correspond to $M_{res} = Nb$. Figures 3.5b and Figure 3.6b were obtained using the moment-rotation relationship of Figure 3.4b for the base spring and explicitly including $P - \Delta$ effects. Again, the difference of the red solid and the red dashed lines is due to the uplift moment, i.e. $N(b - u_{up})$ and Nb, respectively. Based on the experience of the authors, the sensitivity between the two approaches for introducing negative stiffens and/or of using the approximation $b - u_{up} \approx b$ is trivial. Therefore, either Eq. 3.8 or 3.9 can be safely adopted, especially for small axial loads, or large values of the modulus of elasticity (e.g. concrete or steel structures).

3.2.3 Energy dissipation and time integration

When a FE software is used for solving rocking problems (e.g. Figure 3.1d), the damping force is assumed continuous and proportional to the velocity, i.e. $F_D = c\dot{u}$, where c is a percentage of the critical damping. For rigid blocks, a possible value can be obtained using concepts of dimensional analysis as shown by Vassiliou et al., 2016, where the following expression was proposed:

$$c = 0.02 \left(\frac{\alpha}{0.1}\right)^2 mg^{0.5}R^{1.5} \tag{3.10}$$

The damping coefficient c can be introduced in the model with the aid of a simple dashpot element in parallel with the rotational spring. However, rocking bodies dissipate energy primarily when impact occurs and thus damping is "event-based" and energy is mainly lost after every impact (Housner, 1963).

As already discussed in Section 2.1, when solving Eq. 2.3 an impact is detected if the sign of the rotation is reversed. If the time step is sufficiently small, at the exact instant of impact, the rotation is practically zero and the velocity is reversed and multiplied by the coefficient or restitution η given by Eq. 2.7. Since η is always less than one, energy is damped out at every impact. The same practice is also followed with our modeling, where the coefficient of restitution is introduced by pausing the analysis once an impact is detected, or simply when the sign of rotation is reversed. The analysis is then resumed using as "initial" velocity of the subsequent time steps the product of the pre-impact angular velocity of every degree-of-freedom (dof) of the FE model with the coefficient of restitution. The same procedure is repeated for every impact/event until the analysis is completed. As we will show, the results obtained with this practice, match perfectly the results obtained after solving directly the rigid block's equation of motion as derived by Housner's theory (Eq. 2.3).

For the flexible block, a more general definition of the impact model is adopted since, upon impact, the displacements of the block may not follow the rotation of the base as in the rocking block case. Again we distinguish two phases: the rocking phase, where impacts are assumed instantaneous, and the full contact phase where the base of the block is in full contact with the supporting ground for a finite duration just prior and right after the impact. When the block is at rest, rocking is initiated when the overturning moment exceeds the resisting moment. However, when the block is in the rocking phase and $\theta = 0$, in order to decide whether a rocking phase will start or the block will remain for some time in full contact with the ground, we need to check the sign of the *total angular momentum* $\mathcal{L}_{tot}$:

$$\mathcal{L}_{tot} = \Sigma \mathcal{L}_i = \Sigma I_{0,i} \dot{\theta}_i \tag{3.11}$$

where the subscript "i" implies that $\mathcal{L}$ is measured at every node of the structure. Therefore, in order to initiate a new rocking phase, the conditions that should be met are: (i) the angular momentum $\mathcal{L}_{tot}$ should have the same sign with the angular velocity of the base $\dot{\theta}_0$ at the instant of impact (e.g. Acikgoz and DeJong, 2012; Acikgoz and DeJong, 2016), and (ii) the overturning moment about the impending pivot point must exceed the resisting moment. Otherwise, full contact should be assumed since the transition to a new rocking phase occurs smoothly. This approach is rather intuitive since, according to several researchers (e.g. Psycharis, 1983; Yim and Chopra, 1985; Acikgoz and DeJong, 2012; Acikgoz and DeJong, 2016), the actual response of the flexible rocking block at impact is unvalidated; examining the validity of our assumption is beyond the purpose of our study while different approaches can be easily handled. Furthermore, we detect an impact when the product of the rotations of two subsequent time steps is negative and we set the current (last) time as the time of impact. This simple assumption was found adequate in practice, but if more accuracy is desired, the exact instant of impact can be easily found, e.g. using a bisection method.

All results obtained with the proposed modeling were produced with the aid of a standard Newmark algorithm. It is, therefore, possible to obtain accurate response estimates for the rocking problem using an implicit integration scheme allowing for large time steps of the order of $10^{-2}sec$. Otherwise, an explicit time integration scheme can be easily implemented, avoiding the need for corrective iterations but requiring a smaller time-step; this option was not further examined. Different tolerance values are used for RB and the SM models, while as a rule of thumb, we've left the tolerances to their default values in Matlab and OpenSees. Specifically, the (default) tolerance of the ODE23s algorithm is 10^{-3} for the relative error and 10^{-6} for the absolute error. For the SM models, the convergence test for the corrective iterations was based on a displacement-based norm with a tolerance equal to 10^{-6}. Although, in principle, it is possible to adjust the two approaches and compare them in terms of speed, this comparison is not straightforward. Therefore, our comparisons are based primarily on accuracy and not on computing speed (although the proposed SM models are quite fast).

A minimum threshold on the rotational velocity $\dot{\theta}_{min}$ should be also considered. Below this threshold, the block is assumed at rest (full contact) and the analysis is paused, i.e. the rotation θ and the velocity $\dot{\theta}$ are set equal to zero, until the next time step that the overturning moment exceeds the resisting moment. In our RB solutions this threshold was assumed equal to $10^{-4}rad/s$, while Acikgoz and DeJong, 2016 recommend $\dot{\theta}_{min} = 10^{-2}rad/s$. In the proposed modeling the same procedure is followed using the same threshold value. Hence, the cases of excitations with a spike after the instant of the theoretical termination of rocking are correctly modelled. Although this practice adds both accuracy and stability, our models produced sufficient response estimates for most cases examined even without this threshold. On the other hand, standard ODE solvers, such as those of Matlab, typically increment automatically the time step and are often trapped in an effort to exactly locate the instant of impact. Implementing the threshold in the later case is critical when the seismic loading is a ground motion record.

3.3 Proposed block models

We present four models, called *spring models* (SM), for simulating the seismic response of blocks, all following the concept of Figure 3.2a, discussed in section 3.2. The first three variations assume a single lumped mass SDOF oscillator and the fourth is a multimass model. We first demonstrate the capacity of the models for the rigid case under static loading and simple wavelets, while in the sections that follow we examine the behaviour under ground motion records and we also study the flexible case.

3.3.1 Spring Model 1 (SM1)

The first model is denoted SM1 (Spring Model 1) and is shown in Figure 3.7. SM1 is a SDOF oscillator with height equal to the distance of the center of mass (CM) from the pivot point, $H_0 = R$. The seismic force is analyzed into two orthogonal components; we assume that only the component perpendicular to R is of interest. Therefore, if the seismic force is $-m\ddot{u}_g$, only the component $F_{eq} = -m\ddot{u}_g cos\alpha$ is considered in SM1. Using the SDOF model of Figure 3.2a, SM1 is implemented if we set: the oscillator's height equal to $H_0 = R = \sqrt{b^2 + h^2}$, the rotational moment of inertia of the CM node equal to $I_{CM} = (1/3)mR^2$ and the record timehistory is multiplied times $cos\alpha$.

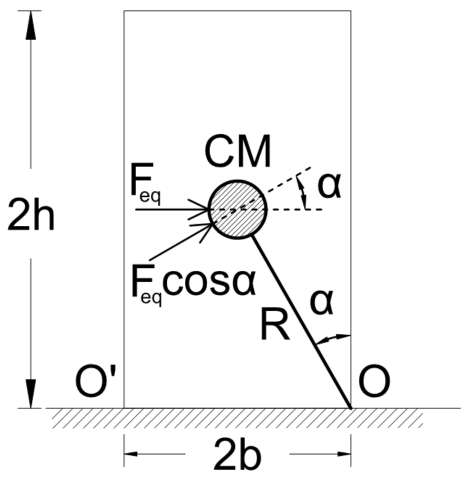

FIGURE 3.7: Spring Model 1 (SM1) for rocking block modeling.

In theory, the results of this model do not exactly coincide with the block's equation of motion of Eq. 2.3, but as we show below the error is always negligible. In order to investigate the error of SM1, we first look at the force-rotation curves under static loading, i.e. neglecting the inertia term $I_0\ddot{\theta}$. The seismic force is equal to $F_{eq} = -m\ddot{u}_g cos\alpha$ and the overturning moment is the seismic force F_{eq} times the leverarm $H_0 = R$:

$$M_{otn}^{SM1} = F_{eq} H_0 = -m\ddot{u}_g\left(t\right) R \cos\alpha \tag{3.12}$$

The restoring moment M_{res} depends on the $M - \theta$ relationship adopted. For the non-linear spring it is equal to $M(\theta) = mgRsin(\alpha - \theta)$ (Figure 3.2c, solid line). Therefore, for the SM1 model, the block's force-rotation relationship becomes:

$$M_{res}^{SM1} = M_{otn}^{SM1} \Rightarrow mgRsin(\alpha - \theta) = -m\ddot{u}_g\,(t)\,R\cos\alpha \Rightarrow \frac{F^{SM1}}{mg} = \frac{\sin(\alpha - \theta)}{\cos\alpha} \tag{3.13}$$

If instead we choose a constant $M - \theta$ relationship combined with second order analysis ($P - \Delta$), the expression of the restoring moment is different and the force-rotation relationship becomes:

$$F_{P-\Delta}^{SM1} = \frac{mgR\sin\alpha - mgR\sin\theta}{R\cos\alpha\cos\theta} \Rightarrow \frac{F_{P-\Delta}^{SM1}}{mg} = \frac{\sin\alpha - \sin\theta}{\cos\alpha\cos\theta} = \frac{\tan\alpha}{\cos\theta} - \frac{\tan\theta}{\cos\alpha} \tag{3.14}$$

The two force-rotation relationships are compared to that of the rigid block (RB) equation (Eq. 2.3). From Eq. 2.1, the overturning moment is known and it can be calculated as $M_{otn}^{RB} = -m\ddot{u}_g\,(t)\,R\cos\left[\alpha\mathrm{sgn}\left(\theta\left(t\right)\right) - \theta\left(t\right)\right]$, while the distance of CM from the ground during the rocking motion is $H(\theta) = R\cos\left[\alpha\mathrm{sgn}\left(\theta\left(t\right)\right) - \theta\left(t\right)\right]$. Thus, the force-rotation curve of the rigid block (RB) equation is:

$$F^{RB} = \frac{M_{res}^{RB}}{H(\theta)} \Rightarrow F^{RB} = \frac{mgR\sin(\alpha - \theta)}{Rcos(\alpha - \theta)} \Rightarrow \frac{F^{RB}}{mg} = \tan(\alpha - \theta) \tag{3.15}$$

The linear option of Figure 3.2c is also possible, but its difference with the exact expression is small and thus is not further examined.

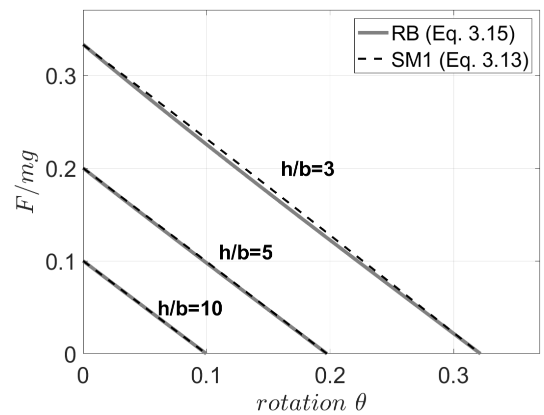

(a)

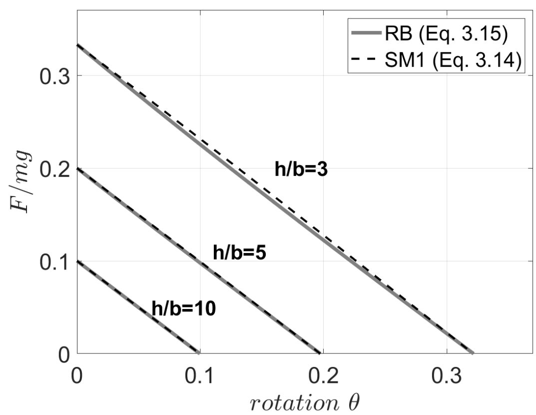

(b)

FIGURE 3.8: Force-rotation curves for the spring model SM1 vs the rocking block (RB), obtained with: (a) Eq. 3.13, and (b) Eq. 3.14.

Figure 3.8a compares the force-rotation curves of Eq. 3.13 and 3.15 for three slenderness values $h/b = 3, 5$ and 10. The same comparison is shown Figure 3.8b but the SM1 curve is that of Eq. 3.14. Overall, for both variations of SM1, the errors are small and increase slightly for more stocky blocks (smaller h/b ratio), as shown in the

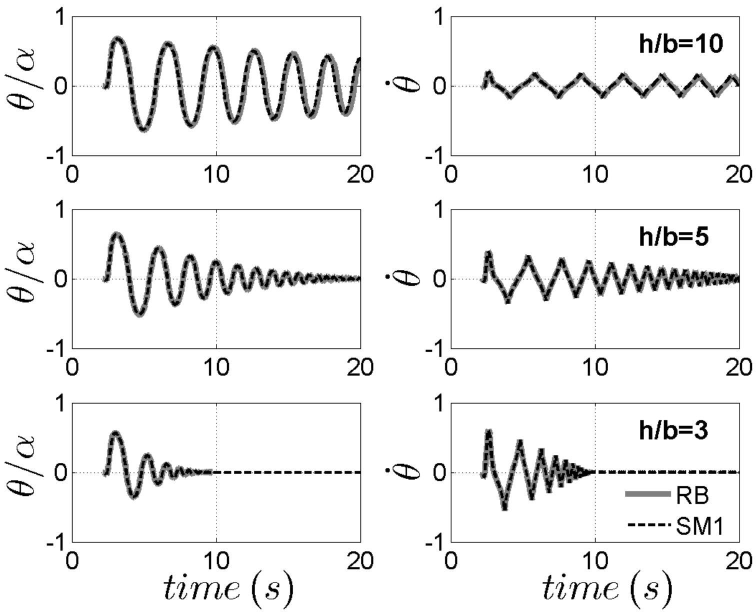

FIGURE 3.9: Comparison of rocking rotation (*left column*) and velocity (*right column*) response histories between the rocking block RB and SM1. The results refer to a block with $R = 2m$ and $h/b = 10, 5$ and 3 subjected to a symmetric Ricker pulse ($\alpha_p = 3.6g \tan \alpha$, $\omega_p = 3\pi$ rad/s).

static results. Figure 3.9 shows also the response estimates of the SM1 model under dynamic analysis. We compare the response history of the rotation θ and the angular velocity $\dot{\theta}$ of a rigid block with $R = 2m$ and slenderness values equal to $h/b =$ 3, 5 and 10 ($tan\alpha = 0.33, 0.2, 0.1$, respectively). The block is subjected to a symmetric Ricker pulse with pulse amplitude $\alpha_p = 3.6g \tan \alpha$ and frequency $\omega_p = 3\pi$ rad/s and the coefficient of restitution is obtained using Eq. 2.7. The results of Figure 3.9 are compared against the solution of the equation of motion of the rocking block (RB) and show perfect agreement for all three h/b values considered.

3.3.2 Spring Model 2 (SM2)

The second rigid block model is identified as SM2 and is conceptually shown in Figure 3.10. The height H_0 of the SDOF is equal to half the height of the block ($H_0 = h$), while the pivot point O is the projection of the center of mass CM to the base, or equivalently, the CM node is located right above the pivot point. If the rotational moment of inertia around the CM is $I_{CM} = (1/3)mR^2$, since the CM is displaced horizontally at an offset distance equal to b, the rotational moment of inertia for the SM2 model will be: $I'_{CM} = (1/3)mR^2 + mb^2$. With reference to Figure 3.2a, SM2 is realized if we set: $H_0 = h$, $I_{CM} = (1/3)mR^2 + mb^2$, while there is no need to multiply the ground motion with a scalar factor (contrary to SM1).

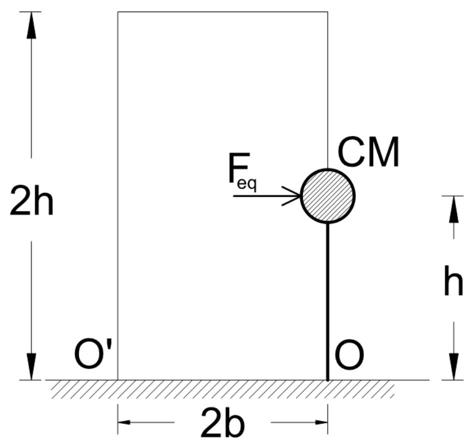

FIGURE 3.10: Rigid block Spring Model 2 (SM2).

Similarly to SM1, the SM2 model is also approximate but again the error is always small. For the static case, the force-rotation relationships are similar to that of SM1, since $H_0 = R\cos\alpha$ and thus $M_{otn}^{SM2} = F_{eq}H_0 = F_{eq}Rcos\alpha$, while the restoring moment depends always on the $M-\theta$ relationship chosen. However, it is interesting to show that when we combine the SM2 model with a nonlinear spring that combines a constant moment M_0 and $P-\Delta$ effects, instead of Eq. 3.14 we obtain the expression:

$$F_{P-\Delta}^{SM2} = \frac{M_0 - mgh\sin\theta}{R\cos\alpha\cos\theta} = \frac{mgR\sin\alpha - mg(R\cos\alpha)\sin\theta}{R\cos\alpha\cos\theta} \Leftrightarrow$$
$$\frac{F_{P-\Delta}^{SM2}}{mg} = \frac{\tan\alpha}{\cos\theta} - \tan\theta \tag{3.16}$$

Figure 3.11a compares the static response of the SM2 to that of the rigid block (RB) solution of Eq. 3.15. The errors are overall small, with the exception of small values of the h/b ratio (small slenderness), e.g. $h/b = 3$ (Figure 3.11a). Therefore, SM2 is also accurate unless the $M-\theta$ relationship of the spring is defined with a constant relationship. The validation of the SM2 model under wavelet pulses is shown in Figure 3.11b. Again we compare the response history of the rotation θ and the angular velocity $\dot{\theta}$ of a rigid block with $R = 2m$ and slenderness values equal to $h/b = 3$, 5 and 10 using the symmetric Ricker pulse used also in Figure 3.9. The $M-\theta$ relationship adopted is the nonlinear negative (exact) stiffness expression of Figure 3.2c. Excellent agreement with the results of the RB solution is again observed.

3.3.3 Spring Model 3 (SM3)

In the SM3 (Spring Model 3) model, we assume that the mass of the block is lumped at the pivot point and that the seismic loading is applied directly on the rotational

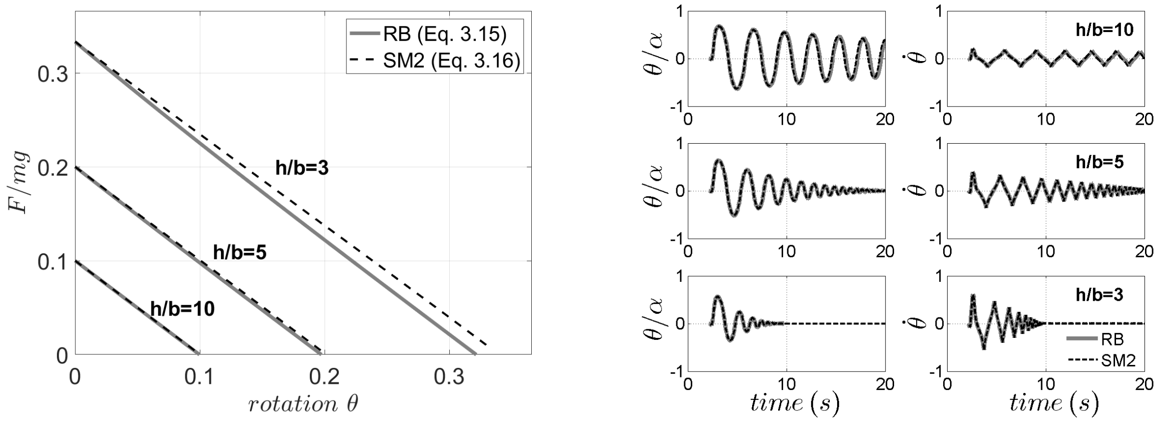

(a) (b)

FIGURE 3.11: (a) Force-rotation curves for the rocking block (RB) and the SM2 model when a perfectly-plastic $M-\theta$ relationship is adopted. (b) Comparison of rocking rotation (left column) and velocity (right column) response histories between the rocking block RB and SM2. The results refer to a block with $R = 2m$ and $h/b = 10, 5$ and 3 subjected to a symmetric Ricker pulse ($\alpha_p = 3.6g \tan\alpha$, $\omega_p = 3\pi$ rad/s).

degree-of-freedom of the base node. The rationale of this approach stems from the direct comparison of the equation of motion of the rigid block (Eq. 2.3) and the equation of motion of the SDOF oscillator $m\ddot{u} + c\dot{u} + ku = -m\ddot{u}_g$ that structural analysis software solve. Comparing with the equation of motion of the rigid block (Eq. 2.3) and assuming that the only dof of interest is the rotation θ, we replace the mass m with the rotational mass I_0 and we apply the record on the rotational dof. For the rigid block, the equivalent of the elastic term ku is defined through the $M-\theta$ relationship of the spring and, therefore, we need to determine only the overturning term which is written as: $M^{SM3}_{otn} = I_0\ddot{\theta}_g = \lambda I_0 \ddot{u}_g$. The constant λ is obtained comparing with overturning moment term of the rocking block (Eq. 2.3):

$$M^{RB}_{otn} - M^{SM3}_{otn} = 0 \Leftrightarrow m\ddot{u}_g Rcos(\alpha-\theta) = \lambda I_0 \ddot{u}_g \Leftrightarrow \lambda = \frac{mRcos(\alpha-\theta)}{I_0} \quad (3.17)$$

The expression for λ contains the rotation θ which is a problem unknown. Since $\theta \in [0, \alpha]$, we can remove θ setting it equal to its bounding values, $\theta = 0$ or $\theta = \alpha$. This is again an approximation, but the loss of accuracy is small. More specifically, looking into the static force-rotation relationship of SM3:

$$M^{SM3}_{otn} = M^{SM3}_{res} \Leftrightarrow \lambda I_0 \ddot{u}_g = mgRsin(\alpha-\theta) \Leftrightarrow \lambda I_0 m \ddot{u}_g = m^2 gRsin(\alpha-\theta) \Leftrightarrow$$
$$\frac{F^{SM3}}{mg} = \frac{mRsin(\alpha-\theta)}{\lambda I_0} \quad (3.18)$$

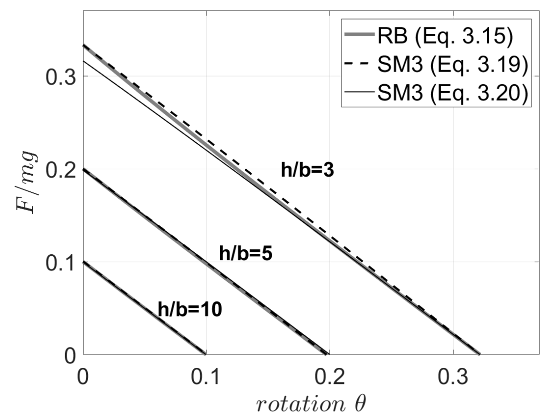

(a)

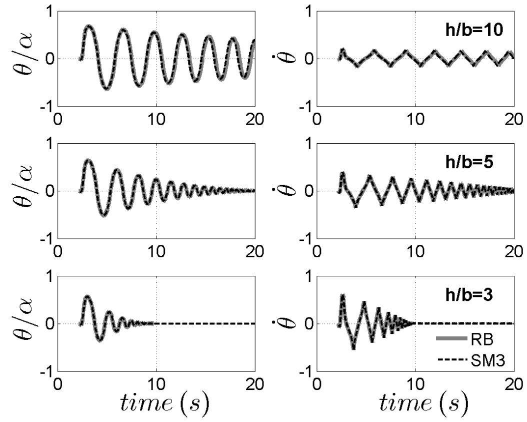

(b)

FIGURE 3.12: (a) Comparison of force-rotation curves for the SM3 model using either $\lambda_{\theta=0}$ or $\lambda_{\theta=\alpha}$. (b) Comparison of rocking rotation (*left column*), and velocity (*right column*) response histories between the RB and the SM3 model for a block with $R = 2m$ and $h/b = 10, 5$ and 3 subjected to a Ricker pulse ($\alpha_p = 3.6g \tan\alpha$, $\omega_p = 3\pi$ rad/s).

Setting $\lambda_{\theta=0} = mRcos(\alpha)/I_0$, or $\lambda_{\theta=\alpha} = mR/I_0$, the force-rotation relationship becomes:

$$\frac{F^{SM3}_{\theta=0}}{mg} = \frac{mRsin(\alpha-\theta)}{\lambda_{\theta=0}I_0} = \frac{sin(\alpha-\theta)}{cos(\alpha)} \tag{3.19}$$

$$\frac{F^{SM3}_{\theta=\alpha}}{mg} = \frac{mRsin(\alpha-\theta)}{\lambda_{\theta=\alpha}I_0} = sin(\alpha-\theta) \tag{3.20}$$

Figure 3.12a compares the above expressions with that of the RB solution (Eq. 3.15). Both $\lambda_{\theta=0}$ and $\lambda_{\theta=\alpha}$ are possible, but $\lambda_{\theta=0}$ is slightly more accurate and therefore is preferred. As before, Figure 3.12b compares the response history of θ and $\dot{\theta}$ for a rigid block with $R = 2m$ and the symmetric Ricker pulse of Figure 3.9 showing perfect agreement with the RB solution for $\lambda_{\theta=0}$.

To summarize, with reference to the model of Figure 3.2a, the SM3 model can be implemented in a structural analysis code if we set $H_0 = 0$, $I_0 = (4/3)mR^2$ and we apply the record timehistory on the rotational dof of the base node multiplied times λ, where $\lambda = 3\cos\alpha/(4R)$ for a rectangular block. Note that obviously, the option of using a constant $M-\theta$ relationship is not possible with the SM3 model. Moreover, since flexible blocks have at least one more degree-of-freedom, the SM3 model is pertinent only for rigid blocks, unless a second rotational spring is introduced.

3.3.4 Multimass Spring Model (mmSM)

The fourth model is the multimass Spring Model (mmSM) shown in Figure 3.13. The multimass spring model is obtained following an approach similar to either SM1, or SM2. In both cases, the model consists of n masses distributed either along the block's diagonal that connects the pivot point with the block's opposite upper corner (Figure 3.13a), or along the height of the block (Figure 3.13b). The second approach is close, but not similar, to the model proposed by Vassiliou et al., 2016. In the first case, the SDOF system is a cantilever with height $2R$ and n nodes with lumped masses at the horizontal translational dofs equal to $m_i = m/n$ and zero rotational moment inertia, $I_{n,i} = 0$. Similarly to the SM1 model, the ground motion record is multiplied times $cos\alpha$. In the second case, the cantilever has height $2h$ and the nodes have: mass $m_i = m/n$, and rotational moment inertia $I_{n,i} = m_i b^2$, where b is the offset of each mass m_i from a vertical line that passes from the pivot point. For a rectangular block, b is equal to the block's half width. In the second case, the ground motion record is left unscaled.

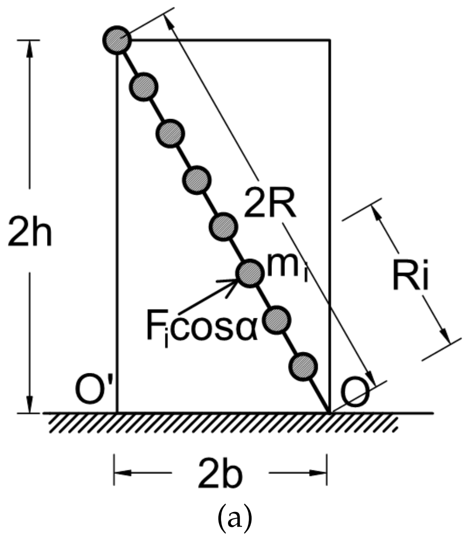

FIGURE 3.13: Multimass Spring Model (mmSM): (a) the mass is distributed along the block's diagonal, (b) the mass is distributed along the block's height.

For the mmSM, initially, we investigate the horizontal force-rotation pushover response under static loading. In the first case (Figure 3.13a) the seismic force of the i^{th} mass is equal to $F_{eq}^i = -(\Sigma m_i)\ddot{u}_g cos\alpha$ and its leverarm is $H_i = R_i$ with $R_i = 2R(i/n)$. If the second approach is preferred, the seismic force is equal to $F_{eq}^i = -(\Sigma m_i)\ddot{u}_g$ and the leverarm is $H_i = h_i$ with $h_i = 2h(i/n)$. Since both variations of Figure 3.13 are possible, we focus on the first option and we find that the total overturning moment is equal to:

$$M_{otn}^{mmSM} = -\sum_i (m_i \ddot{u}_g \cos\alpha H_i) = -\sum_i \left(\frac{m}{n}\ddot{u}_g R_i \cos\alpha\right) = -m\ddot{u}_g 2R\cos\alpha \sum_i \left(i/n^2\right) \tag{3.21}$$

The restoring moment M_{res} depends on the $M-\theta$ relationship adopted for the nonlinear spring (Figure 3.2c); if the base shear is $F_b^{mmSM} = \sum F_{eq}^i = -m\ddot{u}_g$, the force-rotation relationship of the mmSM model becomes:

$$M_{res}^{mmSM} = M_{otn}^{mmSM} \Leftrightarrow F_b^{mmSM} = \frac{M_{res}^{mmSM}}{2R\cos\alpha\sum_i(i/n^2)} \Leftrightarrow$$
$$\frac{F_b^{mmSM}}{mg} = \frac{\sin(\alpha-\theta)}{2\cos\alpha\sum_i(i/n^2)} \tag{3.22}$$

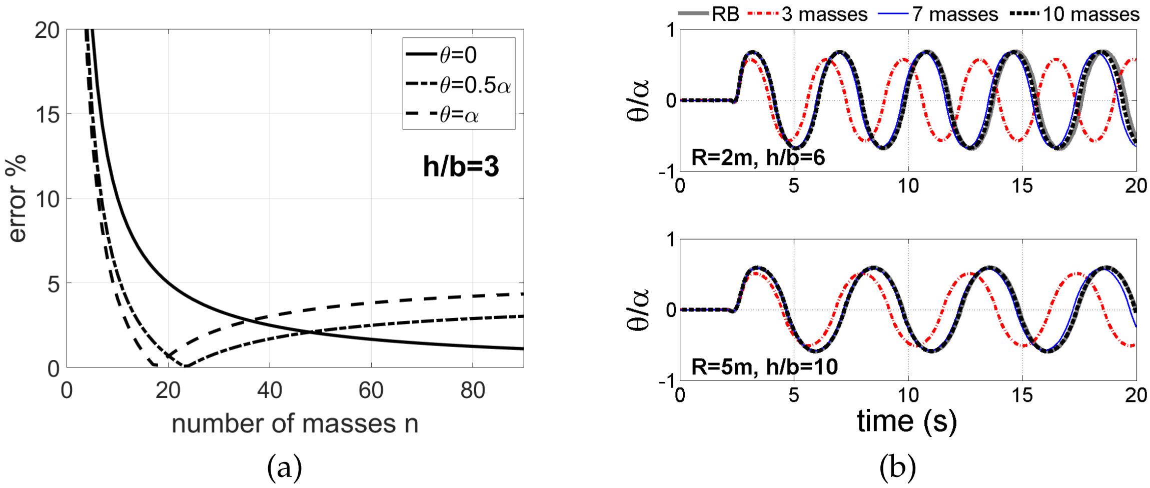

FIGURE 3.14: (a) Convergence of the error term of Eq. 3.23 as function of the number of masses and the rotation angle for a rigid block with $h/b = 3$, (b) Sensitivity of mmSM model to the number of masses for blocks with: (*up*) $R = 2m$, $h/b = 6$, Ricker pulse ($\omega_p = 3\pi$ rad/s), (*down*) $R = 5m$, $h/b = 10$, Ricker pulse ($\omega_p = 2\pi$ rad/s).

When the quantity $2\cos\alpha\sum\left(i/n^2\right)$ in the denominator of Eq. 3.22 converges to $\cos(\alpha-\theta)$, then Eq. 3.22 converges to the exact solution $F^{RB}/mg = \tan(\alpha-\theta)$ of Eq. 3.15. Therefore, the accuracy of Eq. 3.22 depends on the number of masses and on θ. To further investigate the sensitivity of the mmSM model, we define the error of the denominator of equation Eq. 3.22 as:

$$error = \left|\left[\cos(\alpha-\theta) - 2\cos\alpha\sum\left(i/n^2\right)\right]\right| / \cos(\alpha-\theta) \tag{3.23}$$

As shown in Figure 3.14a, the error quickly decreases as the number of masses increases; for more than 7 masses it becomes less than 10% and is always less than 5% as the number of masses increases. For θ values other than zero, it is practically zero when $n \approx 20$. Moreover, Figure 3.14b compares the sensitivity of the response to the number of masses for two blocks with $R = 2m, h/b = 6$ and $R = 5m, h/b = 10$. The blocks are subjected to a symmetric Ricker pulse with $\omega_p = 3\pi$ rad/s and $\omega_p = 2\pi$ rad/s, respectively, while the coefficient of restitution is equal one in order to facilitate the comparison. For both blocks when $n = 3$ there is both amplitude and period elongation error, obviously stemming from the different eigenfrequency properties of the system. Both oscillators produce results equivalent to that of the RB solution when more than 7 masses are adopted and perfect agreement is obtained for approximately 10 masses.

It is interesting to note that in the work of Vassiliou et al., 2016, the authors recommend the use of a rotational spring with a constant $M - \theta$ relationship combined with second order analysis ($P - \Delta$). Their formulation follows the second multimass variation of Figure 3.13b. Our investigations have shown that, a constant M_{res} may overestimate the restoring moment, which is not observed when the first variation of Figure 3.13a is preferred. Nevertheless, the problem is fully amended if the model of Figure 3.13b is combined instead with a negative stiffness $M - \theta$ law.

3.4 Validation using acceleration time-histories

The accuracy of the proposed simplified models is further investigated using natural ground motion records. We have extracted the set of twenty ground motion records shown in Table 3.1 from the far-field set of FEMA P695 Federal Emergency Management Agency, 2009. Among the full list of the FEMA P-695 records, the 20 records chosen have M_w over 6.5 and their PGAs cover a wide range from 0.15g to 0.73g.

Figures 3.15a,b show the response history of a block with $R = 2m$ and $\tan\alpha = 0.16$ ($h/b = 6$) subjected to records #2 and #11 of Table 3.1. Specifically, Figure 3.15a shows the response history of a block that was modeled using the SM1 model subjected to record #11, where excellent agreement for the whole range of the response history is obtained compared to the RB model of Eq. 2.3. A similar comparison, is shown in Figure 3.15b for record #2 which overturns the block. The analyses were repeated with the SM2 and the SM3 models and similar results were obtained and hence are not repeated.

Figures 3.16 and 3.17 show a wide comparison, where the accuracy of each of the four models is obtained in terms of the maximum rotation demand normalized by the slenderness angle of the block $|\theta|/\alpha$. The figures show the maximum demand for two blocks with $R = 2m, tan\alpha = 0.16$ and $R = 5m, tan\alpha = 0.10$ subjected to the 20

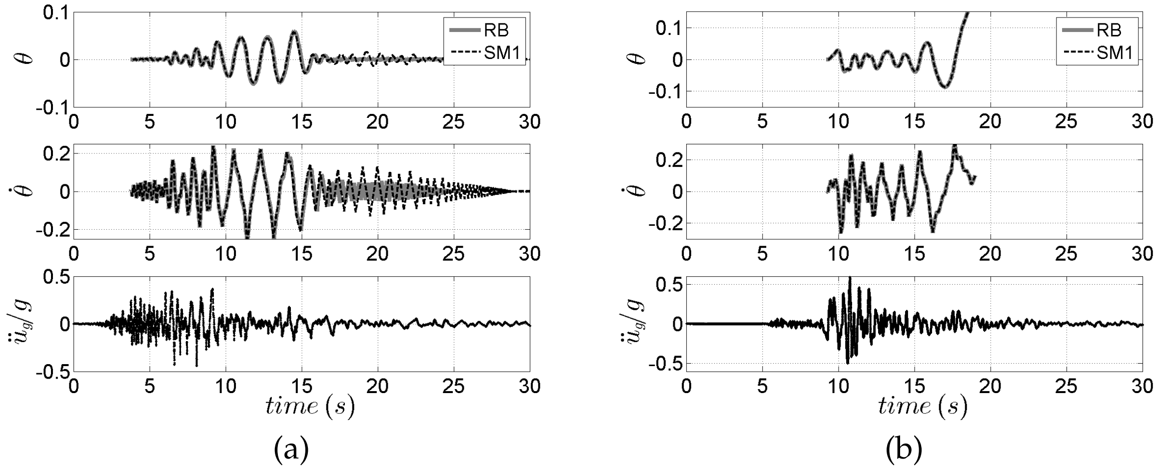

FIGURE 3.15: Comparison of rocking rotation and angular velocity response history for a block with $R = 2m$ and $\tan\alpha = 1/6$: (a) response history to record #11, (b) response history to record #2, the block overturns.

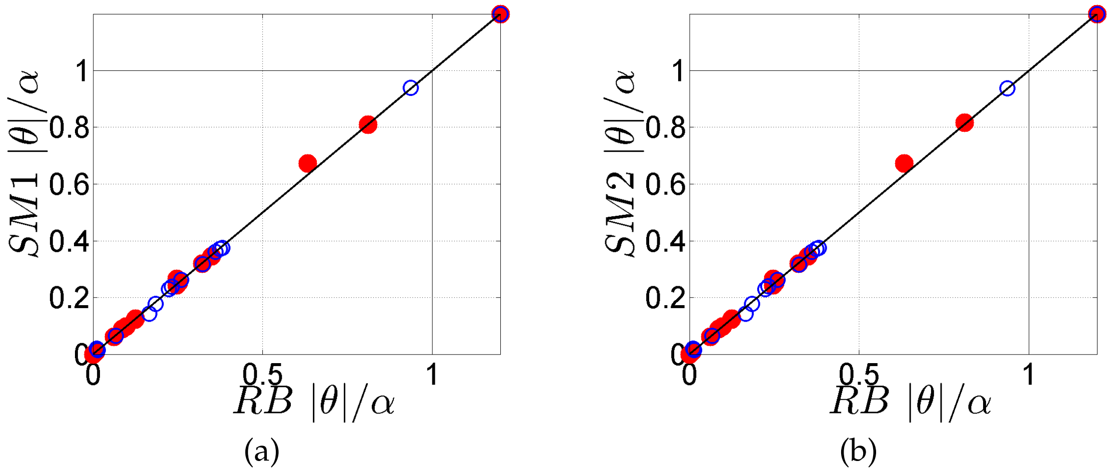

FIGURE 3.16: Comparison of the maximum response rotation between the RB and the proposed models for the 20 ground motions of Table 3.1: (a) SM1, (b) SM2.

ground motions of Table 3.1. The dimensions of the blocks were chosen so that they either rock or overturn when subjected to the 20 records (i.e. rocking always initiates). The agreement is very good practically for all four models (Figure 3.16 and 3.17). More specifically, with the sole exception of one simulation modeled with the mmSM model (Figure 3.16d), all four models successfully captured overturning, while, overall, the differences with the RB solution are minor and less than 5% regardless of the peak ground acceleration of the ground motion record. Moreover, the maximum values obtained are not biased, since none of the models systematically under- or over-estimates the demand.

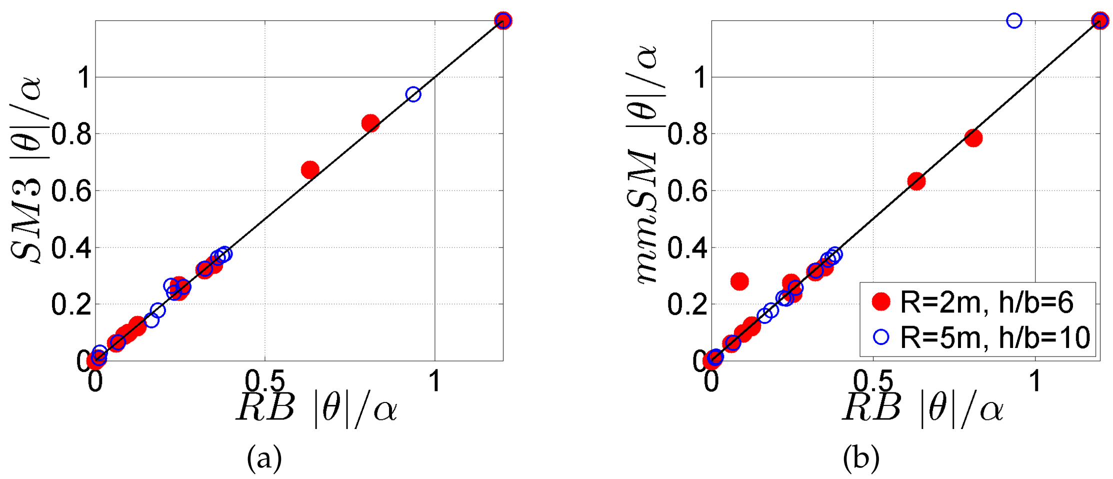

FIGURE 3.17: Comparison of the maximum response rotation between the RB and the proposed models for the 20 ground motions of Table 3.1: (a) SM3, (b) mmSM model of Figure 3.13a.

TABLE 3.1: The twenty ground motion records adopted.

No	Event	Station	ϕ°	Soil	M	PGA(g)
1	Northridge, 1994	Beverly Hills-14145 Mulh	279	D	6.7	0.52
2	Duzce, 1999	LA, Bolu	000	D	7.1	0.73
3	Hector, 1999	Hec	000	C	7.1	0.27
4	Imperial Valley, 1979	El Centro Array 11	140	D	6.5	0.36
5	Imperial Valley, 1979	Hollister Diff. Array 11	230	D	6.5	0.38
6	Kobe, 1995	LA, Shin-Osaka	090	D	6.9	0.21
7	Kocaeli, 1999	Duzce	180	D	7.5	0.31
8	Kocaeli, 1999	Duzce	270	D	7.5	0.36
9	Kocaeli, 1999	Arcelik	000	C	7.5	0.22
10	Kocaeli, 1999	Arcelik	090	C	7.5	0.15
11	Loma Prieta, 1989	Capitola	090	D	6.9	0.44
12	Manjil, 1990	Manjil	000	C	7.4	0.51
13	Superstition Hills, 1987	El Centro Imp. Co. Center	090	D	6.5	0.26
14	Cape Mendocino, 1992	Rio Dell Overpass FF	270	D	7.0	0.39
15	Cape Mendocino, 1992	Rio Dell Overpass FF	360	D	7.0	0.55
16	Chi-Chi, 1999	Chy101	000	D	7.6	0.35
17	Chi-Chi, 1999	Chy101	090	D	7.6	0.44
18	Chi-Chi, 1999	Tsu045	000	C	7.6	0.47
19	Friouli, 1976	Tolmezzo	000	C	6.5	0.35
20	Friouli, 1976	Tolmezzo	270	C	6.5	0.31

3.5 Flexible blocks

Real structures, or structural members, when designed to resist seismic loading through rocking, are usually made from concrete or other structural materials and thus have some flexibility, especially when their size is large. The proposed modeling can be easily extended to the case of flexible blocks simply modifying the properties of the beam element of Figure 3.2a and adopting the rocking conditions discussed in Section 3.2.3 when impact is detected. We study systems with both lumped and distributed mass, the former using the SM1, SM2 models and the latter with the mmSM model. Both lumped and distributed mass modeling are useful and the choice depends on the problem at hand. For example, for rocking bridge piers, a lumped mass modeling may be preferable, while for a tall, slender system the multimass model may be preferred.

For the flexible block, our node of interest is usually the top node instead of the center of mass. The flexibility of the block is modeled through the flexibility of the beam element connecting the top with the base of the oscillator. Therefore, if the lateral stiffness of the beam is $k = 3EI/h^3$, the rigidity EI is defined according to the properties and the geometry of the rigid block. Moreover, although rocking is still the major source of energy dissipation, viscous damping needs to be considered in order to damp out the pure bending motion. Therefore, we introduce some mild mass (or stiffness) proportional viscous damping of the order of $\zeta = 0.5 \div 2\%$ calculated using the properties of the equivalent fixed SDOF system.

Some attention is required when post-processing the results. The analysis software outputs the total displacement of every node, e.g. u_{tot}^{CM} for the CM node (Figure 3.2b). Focusing at the top node, the total displacement u_{tot}^{top} is broken down to the *rigid rocking* displacement u_R and the *pure bending* displacement w. Assuming that w is perpendicular to a coordinate system that follows the rocking rotation (Figure 3.2b), the total displacement u_{tot} is:

$$u_{tot}^{top} = u_R^{top} + w^{top}\cos\theta \Leftrightarrow u_{tot}^{top} = (2R\cos\alpha)\sin\theta + w^{top}\cos\theta \Leftrightarrow$$
$$w^{top} = \frac{1}{\cos\theta}(u_{tot}^{top} - 2R\cos\alpha\sin\theta) \tag{3.24}$$

where $h = 2R\cos\alpha$ is the height of the block. Similarly, for the CM node the bending displacement is obtained if we set $h = R\cos\alpha$ instead. Furthermore, when the SM1 or the mmSM model of Figure 3.13a is adopted, the nodal displacements u_{tot}^{top}, u_{tot}^{CM} should be multiplied times $cos\alpha$ before inserted in Eq. 3.24.

When the block is at rest and the acceleration level is below $gtan\alpha$, the system responds as a SDOF (or MDOF) oscillator, until the combined rocking-bending motion begins when $\ddot{u}_g \geq gtan\alpha$. As discussed by Psycharis, 1983 and Acikgoz and DeJong, 2012, the first mode interacts with rocking and its effect becomes important as the block becomes more flexible. Specifically, the effect of flexibility is significant when either the ratio $E/\rho g$ is small, or when the size parameter R of the block is large. This is better understood from the expression of the first eigenperiod of flexible homogeneous

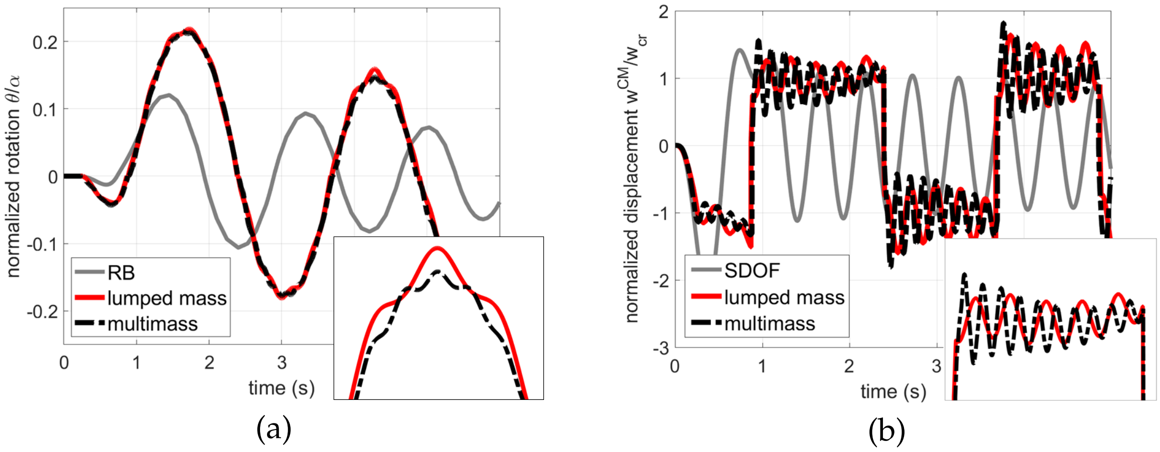

FIGURE 3.18: Response of flexible block vs rigid blocks (Acikgoz and DeJong, 2012): (a) response history of rotation θ, (b) response history of bending displacement w. The block is subjected to a sinusoidal pulse excitation ($\alpha_p = 1.3g \tan\alpha$, $\omega_p = 5.1 rad/s$). The figure also compares the lumped vs the multimass (7 masses) modelling using SM2 and the model of Figure 3.13a, respectively ($\alpha = 0.20$, $\zeta = 0.005$, $p = 1 rad/s$ and $\omega_{SDOF} = 11.9 rad/s$).

rectangular blocks with a fixed base(Vassiliou et al., 2016):

$$T_1 = \frac{12.38h}{\tan\alpha}\sqrt{\frac{\rho}{E}} \tag{3.25}$$

where ρ is the mass density of the block and E is the modulus of elasticity. The block becomes more flexible as E decreases which results to higher overturning accelerations and rotation demand due to the transformation of rotational kinetic energy to bending vibrations. Another interesting aspect is the vibration period of the uplifted rocking body. According to Chopra and Yim, 1985 the vibration frequency of the uplifted structure is given, approximately, by the following equation:

$$\omega_{n,up} \approx \frac{R}{b}\omega_n \tag{3.26}$$

where ω_n is the frequency of the fixed-based structure. Since $R/b > 1$, $\omega_{n,up}$ is higher than ω_n. As also discussed by Vassiliou et al., 2015, for a rocking problem with two degrees-of-freedom $\omega_{n,up}$ corresponds to the second, the rotational, eigenmode of the system. In the proposed models, the first eigenfrequency is equal to zero, since the uplifted block is a mechanism and the first eigenmode represents a rigid body rotation around the pivot point(s).

In order to further examine the response of flexible blocks, Figure 3.18 compares the response of a block subjected to a sinusoidal pulse when it is either rigid or flexible. The problem was first examined by Acikgoz and DeJong, 2012 in a dimensionless form, assuming a single lumped mass. We extent the comparison examining also the possibility of having a "distributed" mass system. For this problem, Eq. 3.26 gives $\omega_{n,up} = 60 rad/sec$, while when the SM and the mmSM models are used the period was found equal to $49.44 rad/sec$ and $50.24 rad/sec$, respectively. The two values are in reasonable agreement with the approximate estimate of Eq. 3.26. According to Figure 3.18a, the differences when the block is rigid or flexible are significant, since the flexible system is shown to produce considerably larger rocking rotations (Figure 3.18a). Figure 3.18b shows the pure bending displacements of the SDOF system, normalized by w_{cr}, the displacement at the instant of rocking initiation, obtained as $w_{cr} = gB/(\omega_{SDOF}^2)H$ (Acikgoz and DeJong, 2012). For the flexible block, after every impact there are sudden and large "jumps" of the displacement (Figure 3.18a points of the left plot that the curves cross the $y = 0$ line). This indicates that the mass is not in phase with the rocking motion and that the bending oscillations resist the rocking motion producing larger rotations. Furthermore, both plots of Figure 3.18 show the existence of higher mode effects which are coupled with the rocking oscillations. This is shown at the two zoom windows at the lower right side of each plot. Looking at the lumped and the distributed mass case, although the rocking motion is sufficiently captured by both models, as expected, the distributed mass system is more sensitive to higher modes. Figure 3.18b shows also the response of the corresponding linear SDOF oscillator, which has a substantially different frequency content and damping than the rocking system. The response of the SDOF oscillator follows the sinusoidal shape of the seismic loading which is not the case for the rocking structure.

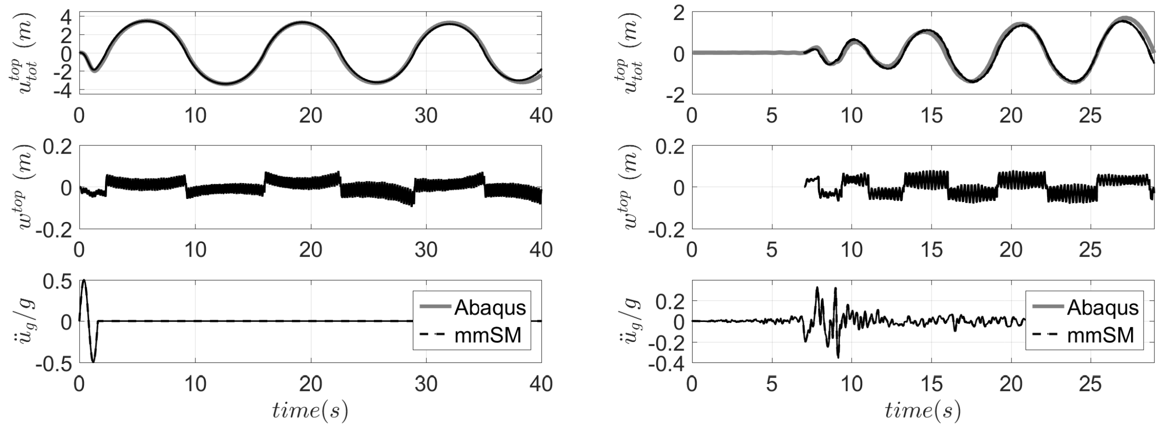

(a) (b)

FIGURE 3.19: Response histories of total displacement u_{tot}^{top} (*upper row*) and pure bending displacement w^{top} (*lower row*) between a flexible block modelled in ABAQUS and modelled using the mmSM model (7 masses): (a) response to a sine pulse excitation, (b) response to record #8.

In Figure 3.19 we compare the results of our models against response estimates obtained with the aid of ABAQUS, 2011. Figure 3.19a shows the response of a block with total height $2h = 50m$ and $\tan\alpha = 0.1$ subjected to a sine pulse ($T_p = 1.6sec$, $a_p = 5g\tan\alpha = 4.905m/sec^2$), while Figure 3.19b shows the response of the same block subjected to record #8. In both cases the block was assumed from concrete with modulus of elasticity $E = 30GPa$ and density $\rho = 2.5Mg/m^3$ and was solved using the model of Figure 3.13a (7 masses). In ABAQUS we created a model with a full mesh of quadrilateral elements and a 2D planar base. We've assumed a surface-to-surface contact between the base and the bottom of the block and we've set the friction formulation as rough in order to omit the effect of sliding. The dynamic explicit analysis option with automatic time step was also adopted. The first row of Figures 3.19a, b compare the total displacements u_{tot}^{top} at the top of the block, showing close agreement for the examples shown. The plots immediately below depict the pure bending displacements w^{top} produced by our model.

3.6 Restrained blocks

All four models can be easily adopted for the study of vertically restrained rocking blocks. A vertically restrained rocking block is equipped with an elastic tendon that passes through its centerline, as shown in Figure 3.20a. The tendon has axial stiffness EA and is prestressed with a force P_0. This problem can be solved with all of the proposed models by appropriately adjusting the $M-\theta$ relationship of the spring. According to Vassiliou and Makris, 2015 the condition for the initiation of rocking is $\ddot{u}_g \geq g\tan\alpha(1 + P_0/mg)$ while the restoring moment M_{res} of a restraint block depends on EA and P_0 and is given by the expression:

$$M_{res}(\theta) = mgR\left[\sin(\alpha-\theta) + sin\alpha\sin\theta\left(\frac{\tan\alpha}{2}\frac{EA}{mg} + \frac{P_0}{mg}\frac{1}{\sqrt{2}\sqrt{1-cos\theta}}\right)\right] \tag{3.27}$$

Figure 3.20b shows the modified $M-\theta$ relationship for the restraint block case, where the slope of the $M-\theta$ law depends on the axial stiffness EA and the prestressing force P_0. When the stiffness EA of the restrainer is small compared to the weight, the restoring moment M_{res} will have negative stiffness once rocking initiates. As EA increases, the restoring moment increases and may become positive. Figures 3.21a and b compare the response of a block with negative, zero and positive stiffness against the block's equation of motion proposed by Vassiliou and Makris, 2015. The numerical results presented were obtained using the SM3 model, where the $M-\theta$ relationship is that of Eq. 3.27 and refer to a block with $R = 2m, h/b = 6$ subjected to the Duzce 1999 record (#2) and to a second block with $R = 5m, h/b = 10$ subjected to the Imperial Valley 1979 record (#4). Moreover, in Figure 3.20b we examine the influence of

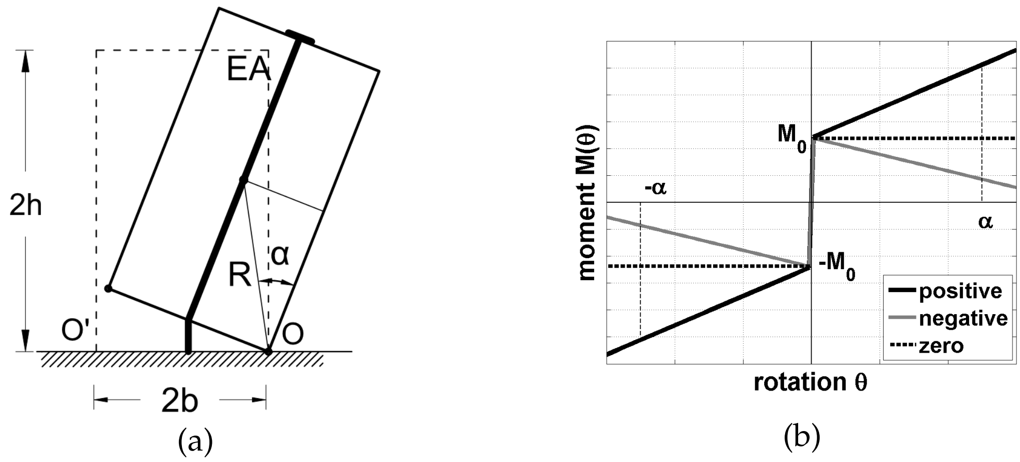

FIGURE 3.20: (a) Restrained rocking block geometry, (b) Moment-rotation relationship for restrained blocks. Adjusting the properties of the tendon, the restoring moment can have a positive or negative slope.

EA and P_0 on the response history assuming (from top to bottom): (*i*) negative $M-\theta$ stiffness, setting $EA/mg = 40$, $P_0 = 0$ (both blocks), (*ii*) zero $M-\theta$ stiffness, setting $EA/mg = 73$, $P_0 = 0.1mg$ for the first block and $EA/mg = 201$, $P_0 = 0.1mg$ for the second block, and (*iii*) positive $M-\theta$ stiffness setting $EA/mg = 120$, $P_0 = 0.2mg$, and $EA/mg = 250$, $P_0 = 0.2mg$, respectively. For all cases examined, the results match perfectly the analytical solution for both ground motions and for all EA and P_0 combinations.

Furthermore, in Figure 3.22a,b we show the maximum normalized rotation demand as function of the block's size parameter and we compare against the analytical solution. For both cases examined, the results using either the solution of Vassiliou and Makris, 2015, or the proposed modeling are very close. For some simulations there is a small error (e.g. Figure 3.22b, $R = 2.5m$), which is attributed to the Matlab ODE (ODE23s) solver, while the solution using the proposed model is always stable and accurate. Notice that for simulations with $|\theta|/\alpha > 1$, the blocks continue their rocking motion since the systems have either positive or zero moment-rotation relationship. A possible straightforward extension of the proposed modeling is the study of flexible blocks with linear or nonlinear behaviour.

Vertical restrainers are used to improve, in general, the restoring capacity of a system. This technology is commonly implemented in modern structures, but it can be used for any rocking system. Prior the initiation of the rocking motion, the column behaves elastically with elastic stiffness k_e which does not include the contribution of the restrainers. If u_{up} is much smaller than the width of the column (e.g. Zhou et al., 2019), the lateral displacement prior uplift is obtained according to Eq. 3.9 where the axial load N is set equal to $N + P_0 cos\phi$, i.e.:

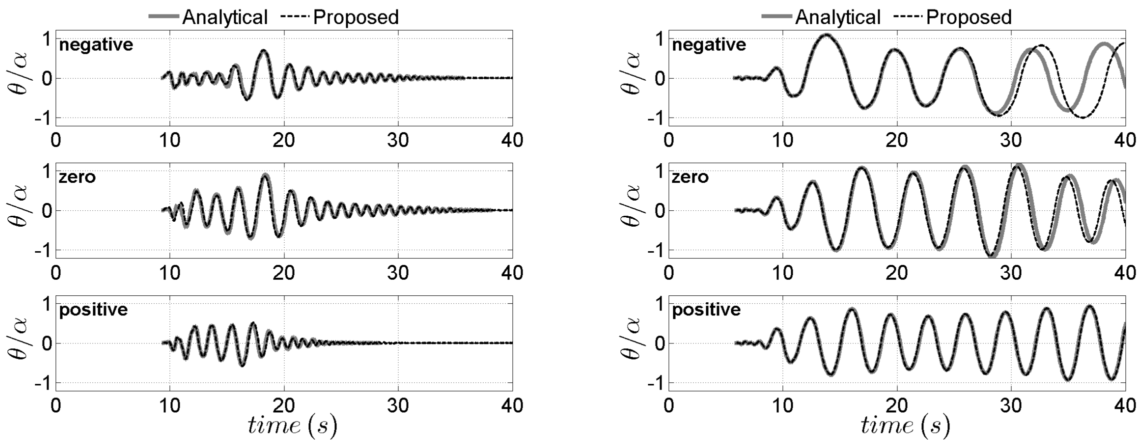

(a) (b)

FIGURE 3.21: Comparison of rotation response history between the analytical solution (Vassiliou and Makris, 2015) and the proposed model: (a) $R = 2m$, $h/b = 6$, record #2, (b) $R = 5m$, $h/b = 10$, record #4. *Upper row*: negative stiffness $M - \theta$, *middle row*: $M - \theta$ zero stiffness $M - \theta$, *lower row*: positive stiffness $M - \theta$.

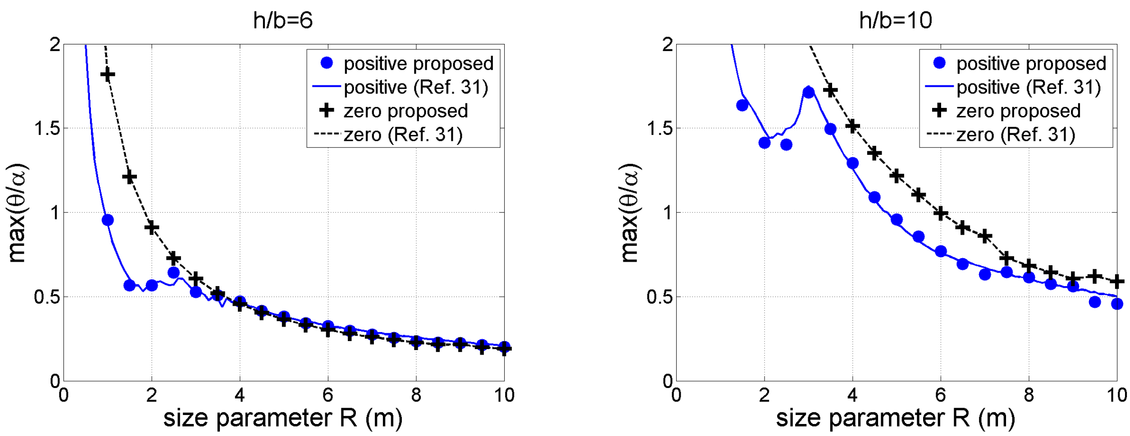

(a) (b)

FIGURE 3.22: Rocking spectra of restrained rocking systems subjected to earthquake records: (a) record #2, block slenderness: $h/b = 6$ and (b) record #4, block slenderness: $h/b = 10$.

$$u_{up} = \frac{(N + P_0 cos\phi)\, b}{k_e 2h} \tag{3.28}$$

where ϕ is the top rotation of the cantilever due to bending and P_0 is the force of the restrainer. The equation above omits the mass of the column, while the component of the pre-stressing force P_0 that is parallel to the axis of the column (Figure 3.23a) is added to the axial force N. With minor loss of accuracy, it can be assumed that $cos\phi \approx 1$, especially for slender blocks. This simplifies Eq. 3.28 and allows to directly calculate u_{up}. Otherwise, u_{up} can be calculated through an iterative process, where $\phi = F_{eq}4h^2/2EI$.

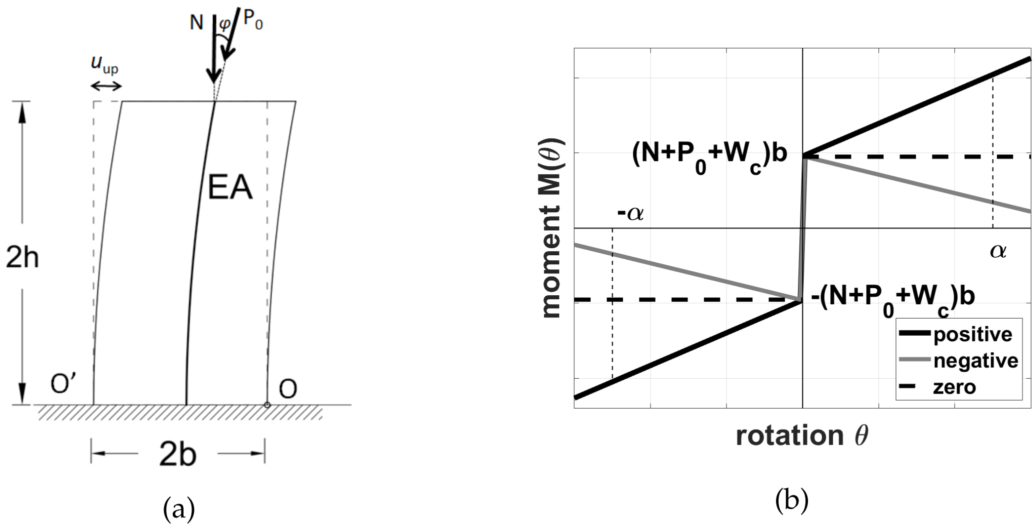

FIGURE 3.23: a) Restraint freestanding block, (b) Spring moment-rotation relationship for restraint blocks.

In the general case, where the mass of the column is not neglected, the uplift displacement is obtained from Eq. 3.9 considering that at $\theta = 0$ the moment is $M_0 = (N + P_0 + W_c)b$, while the stiffness k_e is calculated from Eq. 3.5 assuming that $b - u_{up} \approx b$. The spring $M - \theta$ relationship follows approximately the equation of the rigid restrained column and is thus equal to (Diamantopoulos and Fragiadakis, 2019):

$$M_{res}(\theta) = (W_c + N)R\sin(\alpha sgn\theta - \theta) + R\sin\alpha\sin\theta\left(\frac{EA\tan\alpha}{2} + \frac{P_0}{\sqrt{2-2\cos\theta}}\right) \tag{3.29}$$

According to the expression above, the moment-rotation relationship can be either negative or positive depending on the second term of Eq. 3.29. This approach allows to easily implement and solve a restraint rocking block using a structural analysis software. The simplifications introduced cause some minor error but in most cases examined it is small and the resulting models are accurate enough. From the experience of the author there are many sources of error, e.g. the ODE solver, or the integration method that can produce considerably larger errors.

3.7 Blocks connected to a SDOF oscillator

The second system example is a SDOF oscillator rigidly connected to a rocking wall. The coupling of a bending and a rocking member has several applications, e.g. in a moment frame, a rocking wall can be used to suppresses the dynamic response of the SDOF oscillator.

Makris and Aghagholizdeh, 2017 investigated the dynamic response of a SDOF rigidly connected with a rocking wall as shown in Figure 3.24a and they also studied

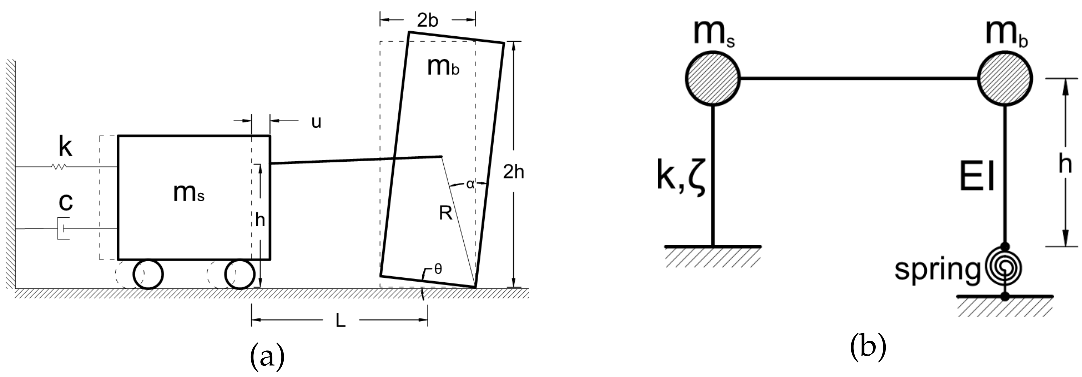

FIGURE 3.24: (a) Rocking block coupled with a SDOF oscillator, (b) Equivalent rocking block coupled with a SDOF oscillator.

the case of having an inelastic SDOF instead (Aghagholizadeh and Makris, 2018). According to Figure 3.24a, the SDOF oscillator has mass m_s, stiffness k, damping c and is connected with a rectangular rocking wall via a rigid link (arm) with length L. The wall is rigid, with dimensions $2b \times 2h$, size parameter $R = \sqrt{b^2 + h^2}$, slenderness α and mass m_b. It is assumed that the rigid link is articulated at the center of mass of the rocking wall at height, h, from the rigid base and also that the length L is large enough so that the displacements of the SDOF and the rigid block are the same. Therefore, since the displacements are equal, the system has only one degree-of-freedom, the rotation of the rocking wall, θ. The equation of motion of this coupled system is (Makris and Aghagholizdeh, 2017):

$$\left[\tfrac{4}{3} + \gamma\cos^2(\alpha \mp \theta)\right]\ddot{\theta} \pm \gamma\cos(\alpha \mp \theta)$$
$$\left[\omega_0^2(\sin\alpha - \sin(\alpha \mp \theta)) \pm 2\zeta\omega_0\dot{\theta}\cos(\alpha \mp \theta) + \dot{\theta}^2\sin(\alpha \mp \theta)\right]$$
$$= \mp\tfrac{g}{R}\left[\pm(\gamma + 1)\tfrac{\ddot{u}_g}{g}\cos(\alpha \mp \theta) + \sin(\alpha \mp \theta)\right] \tag{3.30}$$

where m_s, m_b is the mass of the SDOF and of the wall, respectively, and $\gamma = m_s \,/\, m_b$, $\zeta = c \,/\, 2m_s\omega_0$, $\omega_0 = \sqrt{k/m_s}$. The signs of Eq. 3.30 are either positive or negative, depending on the sign of the angle θ, i.e. $\mp$ implies that the sign is negative when $\theta > 0$. Furthermore, the condition for starting the rocking motion is: $\ddot{u}_g \geq (g\tan\alpha/(\gamma + 1))$ (Makris and Aghagholizdeh, 2017).

We can solve this problem coupling a SDOF oscillator with a rocking block as shown conceptually in Figure 3.24b. We assume that the link is articulated at the center of mass of the block and that the mass and the moment of inertia is lumped at the block's center of mass, as shown in Figure 3.2b. In OpenSees the SDOF oscillator can be simply implemented with a zeroLength element of given stiffness and damping, while a 2-node model of the SDOF is also possible (Figure 3.24b). The non-linear $M - \theta$ relationship of the rocking wall is one of those of Figure 3.2c with $M_0 = m_b g R\sin\alpha$.

We also examine the case of having a flexible rocking wall; a more pertinent assumption for real-world applications. For the flexible wall we've used the mmSM model of Figure 3.13b, assuming that the mass is distributed along the height of the wall. The time instant that the wall starts its rocking motion can be found with the condition provided a few lines above, while the SDOF's displacements begin as soon as the earthquake starts. In the general case, when it is necessary to identify the instant that rocking initiates, a simple pushover analysis can be performed. The acceleration that initiates rocking is found from the overturning moment at the pushover time increment that the rotation of the rocking member exceeds zero for the first time.

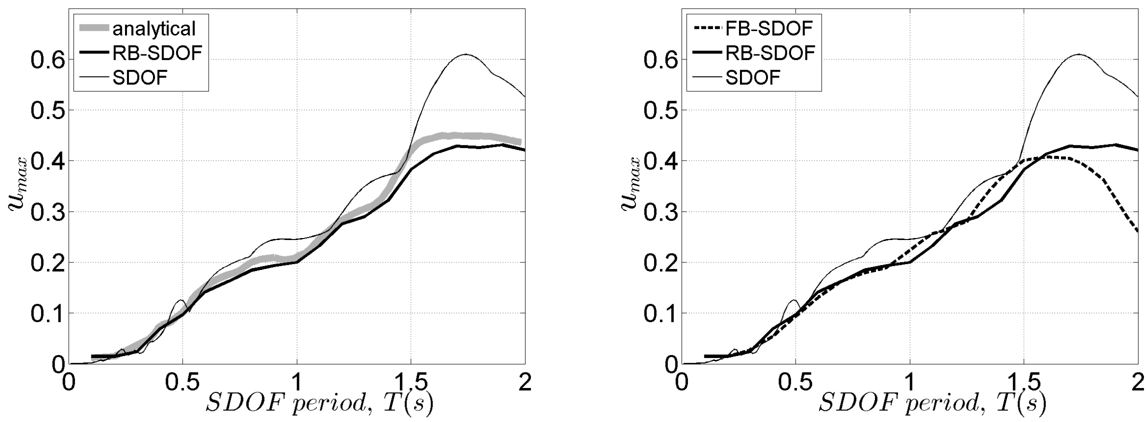

(a) (b)

FIGURE 3.25: Rocking spectra of the coupled rocking-bending system: (a) SDOF oscillator coupled with a rigid wall, (b) SDOF oscillator coupled with a flexible rocking wall.

Figure 3.25a shows the response of the coupled rocking-bending system, adopted from Makris and Aghagholizdeh, 2017 with parameters: $\gamma = m_s \,/\, m_b = 5$, $\eta = 0.90$, $\zeta = c \,/\, 2m_s\omega_0 = 0.03$, $\omega_0 \,/\, p = 15$ and $\tan\alpha = 1/6$. The figure compares the response for period values in the range of $0 \div 2$ sec when the system is subjected to the "Takarazuka, Kobe 1995" (Makris and Aghagholizdeh, 2017) earthquake. For modeling the rigid block we've used the SM2 model (Figure 3.10) and we compare our modeling with the response obtained after solving Eq. 3.30. For the sake of comparison we also plot the displacement spectrum of the record which provides the displacement demand of the SDOF, without the rocking wall. Figure 3.25a shows the excellent agreement of the proposed model with the analytical solution. Furthermore, the rocking wall considerably reduces the displacement demand when the SDOF is flexible ($T > 1.5sec$), however for stiffer systems its effect is small.

With the aid of the proposed modeling we can also easily investigate cases where the SDOF is inelastic, or the wall is flexible. To demonstrate the versatility of our models, we've considered also a SDOF oscillator coupled with a flexible rocking wall with properties: $E = 20GPa$ and $\rho = 2.5Mgr/m^3$. Figure 3.25b compares the response of the coupled system when the wall is either rigid, or flexible. A further reduction of the displacement demand is observed for period values above 1.7sec. In brief, Figure 3.25 validates the accuracy of the proposed modeling, but most importantly, it demonstrates its capacity to handle rocking problems other than the solitary block.

Chapter 4

Rocking frames

In this chapter, the modeling of rocking frames that consist of rigid/flexible columns that are freestanding/restrained is presented. The modeling is extended to rocking frames with N columns and frames which columns are unequal in height. It has to be noted that, the notation was partially changed with respect to the original corresponding paper (Diamantopoulos and Fragiadakis, 2022) in order to be consistent with the notation used throughout the Thesis.

4.1 Introduction

Previous research, as discussed in the above paragraph, examine different variations of the rocking frame problem. It can be seen that the solution of the problem requires to formulate and then solve the equation of motion using an ODE (Ordinary Differential Equation) solver. This practice requires a specifically-tailored equation of motion and lacks the comfort of a general-purpose finite element software. As a result, few, well-trained engineers will be able to handle the numerical solution of rocking frame problems, while solving more complex structural configurations becomes cumbersome, or is possible only after several simplifying assumptions. The Thesis aims to fill this gap and provide a generic and robust modeling. The work is motivated by the need to develop simple models that are suitable for a variety of rocking frame systems. The proposed models follow the work of Diamantopoulos and Fragiadakis, 2019 who have shown that the solitary block can be modeled using an equivalent-single-degree-of-freedom oscillator, equipped with a negative stiffness rotational spring at their base. This modeling can be extended to rocking frames showing that this simple and efficient modeling approach is suitable for a variety of rocking frame structures.

The idea of using springs for modeling the rocking problem is not new. There have been several publications in the past that introduce support springs in order to model rocking. For example, Psycharis and Jennings, 1983 and Chopra and Yim, 1985 used vertical springs at the pivot points in order to consider the soil conditions, while more recently Ma and Butterworth, 2012 examined a combination of two vertical springs for solving the rocking block problem. However, these solutions usually are not robust enough, especially when the base is rigid, while the applications on rocking frames are few. In our work, a novel alternative with a minimum number of rotational, instead of vertical, negative-stiffness springs is discussed. This approach has practical advantages and it can be easily extended to other rocking problems (Diamantopoulos and Fragiadakis, 2019). This simple modeling is suitable for frames with either rigid or flexible columns, while vertical column restrainers can be introduced by appropriately modifying the properties of the rotational springs. The consistent derivation of the properties of the springs from first principles is explained in detail while an extensive discussion on how to chose the entries of the mass matrix is presented. The proposed numerical scheme is fast and robust, while the results obtained match closely those of detailed FE models and/or the solutions obtained by other researchers in the literature.

4.2 Detailed modeling

Monolithic columns can be simulated with the aid of software based on the Finite Element Method (FEM), or the Discrete Element Method (DEM). Other modeling based on multi-body dynamics is also possible, but it is more complicated and, to some extent, is covered by the discussion that follows. FEM methods have the advantage that there is a large variety of powerful software that can be adopted, while engineers are already comfortable with the method. The main disadvantage is that the method is considerably more time consuming compared to the DEM. Examples of FE models created with ABAQUS software (ABAQUS, 2011) are shown in Figures 4.1 and 4.2. The modeling of a simple column requires the definition of two "areas". The first represents the ground, and the second the column. Furthermore, the user has to define the mass, the center of mass and the moment of inertia of every body. With the aid of a CAD environment, it is straightforward to define the exact dimensions and all required properties of each body. Since, a common assumption is that the column is freestanding and therefore the ground-structure interaction is obtained through a friction-contact condition. For marble-marble interfaces, the coefficient of friction takes values in the range 0.6-1.15 (different assumptions are adopted in the literature). Since rocking impacts is the major mechanism for energy absorption, the critical damping coefficient (material damping) can be set equal to zero. However, some mild viscous damping of the order of 1% can help to damp out the low amplitude vibrations and also adds some numerical stability.

The Discrete (or Distinct) Element Method (DEM) offers an efficient and perhaps a suitable alternative for studying the dynamic behaviour of columns and colonnades.

(a) (b)

FIGURE 4.1: (a) A freestanding column in Aphaia Temple, Greece and and (b) detailed modelling of a rocking monolithic column.

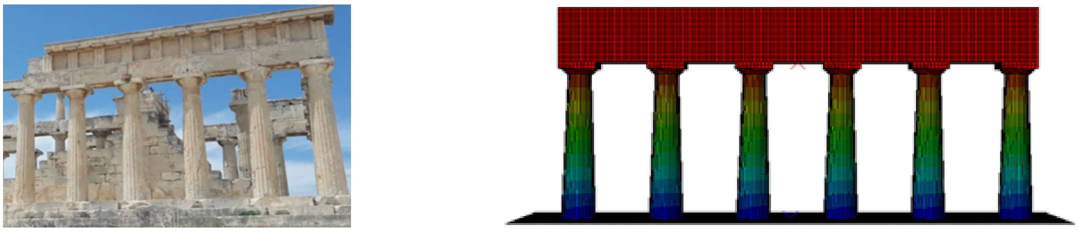

(a) (b)

FIGURE 4.2: (a) Array of freestanding columns in Aphaia Temple, Greece and (b) detailed modelling of an array of freestanding columns that are capped with an architrave.

The Molecular Dynamics (smooth-contact) approach (e.g. Cundall & Strack Cundall and Strack, 1979) offered by the three dimensional DEM code 3DEC (i.e. Itasca Group, 1998) is a suitable choice that was also adopted in Papantonopoulos et al., 2002 and Psycharis et al., 2013a, among others studies. The method models the structure as a system of blocks which may be either rigid, or deformable. For the problem at hand, assuming rigid blocks is a sufficient approximation that reduces substantially the computing time. The system deformation is concentrated at the joints (soft-contacts), where frictional sliding and/or complete separation may take place (dislocations and/or disclinations between blocks). As discussed in detail by Papantonopoulos et al., 2002, the discrete element method employs an explicit algorithm for the solution of the equations of motion, taking into account large displacements and rotations.

For the numerical analysis using DEM models, it is important to appropriatelly select the constitutive laws that govern the mechanical behaviour of the joints. A Coulomb-type failure criterion can be adopted for this purpose. The selection of the properties of the springs is not a straightforward. One way to calculate the appropriate values is by calibrating the model against ambient vibration measurements (e.g. see Ambraseys and Psycharis, 2012). The reader who seeks more information, may consult the work of Psycharis and his co-workers, i.e Papantonopoulos et al., 2002 and Toumbakari and Psycharis, 2010.

4.3 Equivalent single-degree-of-freedom oscillators

The SDOF oscillator model proposed by Diamantopoulos and Fragiadakis, 2019 can be also adopted to obtain a simple solution for rigid frames based on the generalized equation of motion of the rocking block (Eq. 2.12 and 2.13). Modifying either the size parameter R, or the moment of inertia I, an equivalent rocking system can be obtained. The properties of the modified SDOF oscillator are summarized in Table 4.1 and are compared against the SDOF model adopted for solving the solitary freestanding column. The reasoning behind the values of Table 4.1 is explained below.

TABLE 4.1: Properties of the equivalent SDOF oscillator.

			$M(\theta)$	I_{CM}	mass
block	R	α	$m_c g R\sin(\alpha sgn\theta-\theta)$	$(1/3)m_c R^2+m_c b^2$	m_c
modified R	$\widehat{R}$	α	$m_c g\widehat{R}\sin(\alpha sgn\theta-\theta)$	$(1/3)m_c\widehat{R}^2+m_c\widehat{b}^2$	m_c
modified I	R	α	$m_c g R\sin(\alpha sgn\theta-\theta)$	Eq. 4.4	m_c

The first option is to modify the *size parameter* R in order to obtain a block that follows Eq. 2.12. Thus the rotational moment of inertia should be equal to $\widehat{I}_0 = (4/3)m_c\widehat{R}^2$, where $\widehat{R} = \big((1+3\gamma)/(1+2\gamma)\big)R$ and the slenderness should be equal to that of a freestanding column: $\widehat{\alpha}=\alpha$. Therefore, a block with dimensions $\widehat{h}=\widehat{R}\cos\alpha$, $\widehat{b}=\widehat{R}\sin\alpha$ and slenderness α is assumed. For the proposed SDOF oscillator, the rotational moment of inertia with respect to the center of mass is $\widehat{I}_{CM}=(1/3)m_c\widehat{R}^2+m_c\widehat{b}^2$. The equivalent moment-rotation relationship of the rotational spring will be $\widehat{M}(\theta) = m_c g\widehat{R}\sin(\alpha sgn\theta-\theta)$. This expression indicates that the rocking motion will initiate when $\widehat{M}_0 = m_c g\widehat{R}\sin\alpha$ and $\ddot{u}_{g,min} = gtan\alpha$. The resulting equation of motion will become:

$$\widehat{I}_0\ddot{\theta}(t) + m_c g\widehat{R}\sin[\alpha sgn\theta(t)-\theta(t)] = -m_c\ddot{u}_g(t)\widehat{R}\cos[\alpha sgn\theta(t)-\theta(t)] \tag{4.1}$$

It is also possible to modify *the rotational moment of inertia*. Setting $p^2 = 3g/4R$ and multiplying Eq. 2.12 with $(4/3)m_cR^2\times(1+3\gamma)/(1+2\gamma)$. The equation of motion is rewritten as follows:

$$\frac{1+3\gamma}{1+2\gamma}I_0\ddot{\theta}(t) + m_c gR\sin[\alpha sgn\theta(t)-\theta(t)] = -m_c\ddot{u}_g(t)R\cos[\alpha sgn\theta(t)-\theta(t)] \tag{4.2}$$

Comparing Eq. 4.2 with the block's equation of motion, the modified rotational moment of inertia I' is:

$$I_0' = \frac{1+3\gamma}{1+2\gamma} I_0 \Leftrightarrow I_0' = \frac{4}{3} m_c R^2 + \frac{4}{3} \frac{\gamma}{2\gamma+1} m_c R^2 \tag{4.3}$$

while the rotational moment of inertia with respect to the block's center of mass I'_{CM} is (Diamantopoulos and Fragiadakis, 2019):

$$I'_{CM} = \frac{1}{3} m_c R^2 + m_c b^2 + \frac{4}{3} \frac{\gamma}{2\gamma+1} m_c R^2 \tag{4.4}$$

In this case, the mass of the equivalent block should be set equal to the mass of the column m_c and the $M - \theta$ relationship is defined according to the geometry of the frame columns, where $M'(\theta) = m_c g R \sin(\alpha sgn\theta - \theta)$.

4.4 Single-bay rocking frame

4.4.1 Rocking frames with rigid members

A single-bay rocking frame with rigid columns is modeled as shown in Figure 4.3a. The model is an extension of the rigid block model of Diamantopoulos and Fragiadakis, 2019 that was briefly summarized in Section 4.3. It consists of nonlinear rotational springs at the rocking interfaces, i.e. between the rocking column and the ground and also between the column top and the deck. Apart from the geometric parameters shown in Figure 4.3a, it is also necessary to define: (i) the entries of the mass matrix, i.e. the translational mass and the rotational moment of inertia, and (ii) the $M - \theta$ relationship of the rotational springs.

Since the columns are rigid, the mass can be lumped at the midheight of the columns as shown in Figure 4.3a. For this reason, two auxiliary nodes, C_1, C_2, are introduced. As shown in Figure 4.3b, the distance between the top and the bottom pivot points, i.e., nodes D_1 (or D_2), from O_1 (or O_2), is $2R$, where $R^2 = b^2 + h^2$. Thus, for the columns, the mass matrix will be formed by lumping the mass at C_1 and C_2, assuming translational mass equal to m_c and rotational mass equal to $I_{C1} = I_{C2} = (1/3)m_c R^2 + m_c b^2$. For the deck, the corresponding nodes are D_1 and D_2, where the translational mass will be $m_b/2$, and the rotational $I_{D1s} = I_{D2s} = (m_b/2)(2b)^2$ (Figure 4.3b).

The rotational springs are introduced as zero-length springs which define the restraints between the dofs of two nodes. In OpenSees (Mazzoni et al., 2006) additional nodes are required in order to define the rotational springs, while the same principle, more or less, is followed by most software. In Figure 4.3a, the nodes at the rocking interface appear in master-slave pairs, where the subscript "s" is used to define the slave node. As a rule of thump, quantities due to the columns are added to the slave nodes D_{1s} (or D_{2s}), while the quantities that refer to the deck (mass, loads, etc) are placed on the master nodes, e.g. D_1 (or D_2). The negative stiffness nonlinear springs are placed

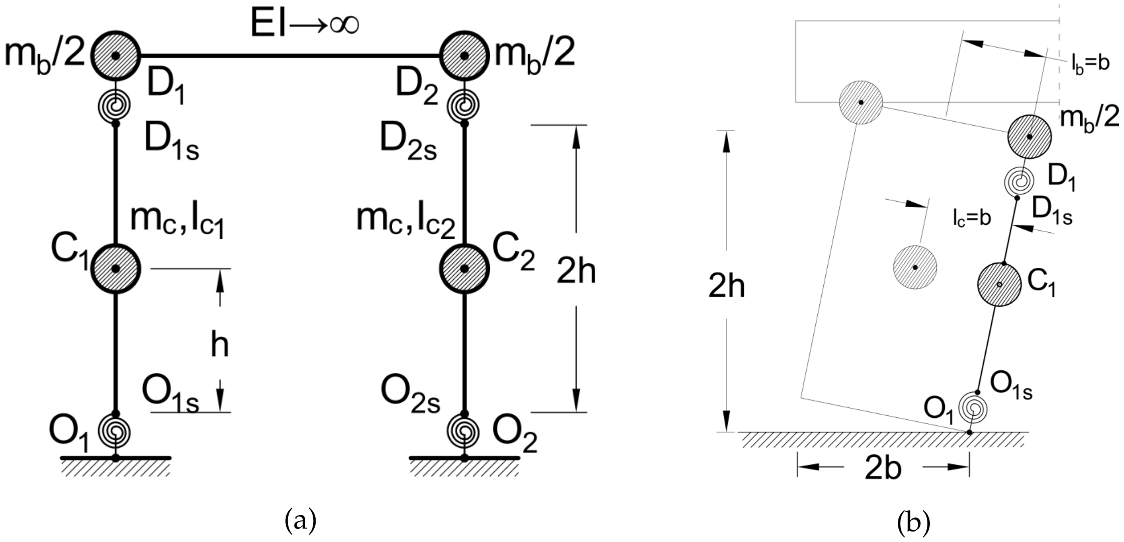

FIGURE 4.3: (a) Proposed model of rocking frame with rigid columns, (b) detail of the proposed model.

at the rocking surfaces of each column, i.e. at the base, O_1, O_2 and at the column-deck connection, D_1, D_2 (Figure 4.3). In the simple case of a symmetric frame, all springs have moment-rotation relationships that have a form similar to that of the rigid block shown in Figure **??**b. The restoring moment $M(\theta)$ of each spring is equal to the axial load times the corresponding leverarm. The axial load that stems from the deck is $W_b = 0.5m_b g$ and the load due to the column weight is $W_c = m_c g$. The corresponding leverarms are $l_c = R\sin[\alpha sgn\theta(t) - \theta(t)]$ and $l_b = l_c$, respectively (Figure 4.3b). Thus, the restoring moment of the top and the bottom spring of each column will be:

$$\begin{aligned} M^{top}(\theta) &= W_b l_b = 0.5W_b R\sin[\alpha sgn\theta(t) - \theta(t)] \\ M^{btm}(\theta) &= W_c l_c + W_b l_b = (W_c + 0.5W_b)R\sin[\alpha sgn\theta(t) - \theta(t)] \end{aligned} \tag{4.5}$$

Eqs. 4.5 can be implemented with a piecewise linear approximation, or for simplicity, they can be linearized (Diamantopoulos and Fragiadakis, 2019). Notice that, compared to the rocking block problem, m_b adds stability to each column of the frame, while if $m_b = 0$ the single freestanding column problem is retrieved. For $\theta = 0$ the maximum restoring moment at the top and the bottom spring is $M_0^{top} = 0.5m_b gb$ and $M_0^{btm} = (0.5m_b + m_c)gb$, respectively. When $\theta = a$ the moment is zero for each of the four springs.

In order to further examine the proposed model, the restoring moment $M_{res}^{frm}(\theta)$ and the overturning moment $M_{res}^{otn}(\theta)$ of the whole structure are calculated and the resulting equation is compared to the equation of motion of the rocking frame (Eq. 2.13). The frame restoring moment $M_{res}^{frm}(\theta)$ with respect to the pivot point is:

$$\begin{aligned} M_{res}^{frm}(\theta) = 2M^{top}(\theta) + 2M^{btm}(\theta) = 2\left(W_c + W_b\right) R \sin\left[\alpha sgn\theta(t) - \theta(t)\right] \Leftrightarrow \\ M_{res}^{frm}(\theta) = 2(1+2\gamma) W_c R \sin\left[\alpha sgn\theta(t) - \theta(t)\right] \end{aligned} \tag{4.6}$$

Furthermore, the overturning moment of the frame M_{ovtn}^{frm} is defined as (Diamantopoulos and Fragiadakis, 2019):

$$M_{ovtn}^{frm}(\theta) = 2\left(m_c l_c + m_b l_b\right) \ddot{u}_g = 2(1+2\gamma) m_c \ddot{u}_g R \cos\alpha \tag{4.7}$$

and the total moment of inertia of the system with respect to the pivot point(s) is:

$$I_0^{frm} = 2\left(\frac{4}{3} m_c R^2 + \frac{m_b}{2} 4R^2\right) = 2(1+3\gamma) I_0 \tag{4.8}$$

Inserting Eqs. 4.6, 4.7 and 4.8 into the equation of equilibrium (i.e. 2.3), yields:

$$\frac{1+3\gamma}{1+2\gamma} I_0 \ddot{\theta}(t) + m_c g R \sin[\alpha sgn\theta(t) - \theta(t)] = -m_c \ddot{u}_g(t) R \cos\alpha \tag{4.9}$$

The equation above is practically equivalent to the equation of motion (Eq. 2.13). Comparing Eq. 2.13 with 4.9, there is a difference at the overturning term, i.e. it is $Rcos\alpha$ instead of $R\cos\left[\alpha sgn\theta(t) - \theta(t)\right]$. This difference is minor as has been shown in Diamantopoulos and Fragiadakis, 2019 and thus can be neglected. Note also that having a bottom and a top spring that follow Eqs. 4.5 is not the only possibility for the rigid frame. For example, one could have chosen to insert a hinge at top and a rotational spring at the bottom. For a frame with rigid piers, this practice can also produce accurate results, provided that the proper $M-\theta$ relationships are chosen.

Energy dissipation for the planar frame model follows the "event-based" approach, similar to that adopted for the block. Therefore, energy is dissipated only when an impact occurs, which is simply detected when the sign of rotation is reversed. At the instant of impact, the analysis is paused and then resumed using as "initial" velocity of the subsequent time steps, the product of the pre-impact velocity of each dof of the FE model times the coefficient of restitution η_{frame} (Eq. 2.14). Attention is required at the pier-deck connection where only the master node translational velocity and the slave node angular velocity should be multiplied with η_{frame}. This is due to the fact that the rotational moment has been lumped on the slave node.

4.4.2 Rocking frames with flexible columns

Modern rocking structures, e.g. rocking RC bridges, should be modeled as flexible systems. The model of Figure 4.3 can be extended to flexible rocking frames in a straightforward manner. However, in this case it is not advisable to lump the column mass at the column midheight, since the system eigenmodes may not be captured correctly. Therefore, compared to the rigid rocking frame, there are minor differences in the mass matrix and the spring M-θ relationship, which both depend on the column mass modeling. The mass of the deck is again lumped at the two ends of the deck, similar to the rigid frame. Energy dissipation follows an "event-based" scheme, as in the rigid block case. Other sources of energy dissipation, e.g. viscous damping, are here omitted. However, one may wish to consider some mild Rayleigh damping of the order of $0.5 - 2\%$.

In the case of flexible frames, the simplest approach is to neglect the column mass since it may be considerably less than that of the deck. However, if the column mass is taken into consideration, it can be either distributed to n nodes along the height of the columns (Figure 4.4, left column), or instead a consistent mass matrix approach, where the mass is continuously distributed along the member can be adopted (Figure 4.4, right column). In the first case, the column mass is distributed to n equally-spaced nodes that have mass $m_i = m_c/n$. In the second case, the mass is continuously distributed along the pier's height, i.e. $\bar{m} = A\rho/2h$ and $m_c = A\rho$, where ρ is the material density of the column and A the column cross-section. The two options are discussed below.

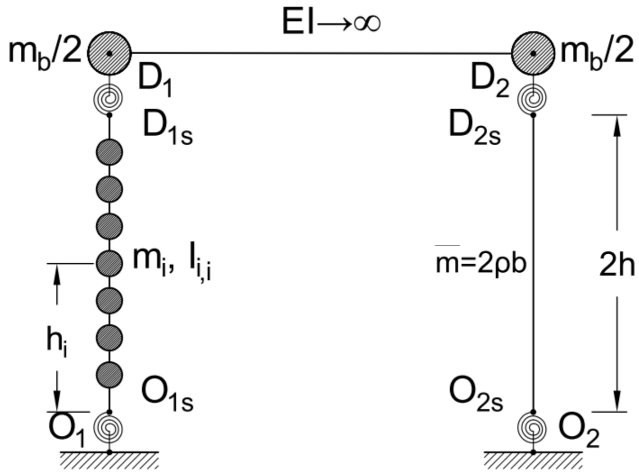

FIGURE 4.4: Rocking frame with flexible columns: the mass is lumped on n nodes (left column), or a consistent mass matrix approach can be used (right column).

The first option is to *lump the mass on n equally-spaced nodes*. Therefore, the translational mass of each node will be $m_i = m_c/n$ and the rotational moment of inertia of node i with respect to an axis that passes from the pivot point O is $I_{0,i} = m_i h_i^2$. This approach has some, small sensitivity, to the number of masses as was shown for the solitary block by Diamantopoulos and Fragiadakis, 2019. Furthermore, if the distance of mass i from the pivot point is $h_i = (2i/n)Rcos\alpha$, the total rotational moment of inertia of each column is defined as: $I_0 = \sum m_i h_i^2 = (4/3)m_c R^2 cos^2\alpha$. However, the exact value of the total rotational moment of inertia is that of the solitary column, i.e. $I_0' = (4/3)m_c R^2$ (Eq. 2.11). In order to remove this small error, an additional quantity equal to $\delta I_{0,i} = (I_0' - I_0)/n = (4/3n)m_c R^2 \sin^2\alpha$ is added to each of the n nodes and the final expression for the rotational moment inertia of each node becomes:

$$I_{0,i} = (4m_c/n)R^2[cos^2\alpha(i/n) + (1/3)\sin^2\alpha] \tag{4.10}$$

The $M-\theta$ expressions of the top and the bottom spring will differ due to the column mass. At zero rotation ($\theta = 0$), the $M-\theta$ expressions will have values equal to M_0^{top} and M_0^{btm} for the top and the bottom spring, respectively. Both expressions terminate at rotation equal to α. Note that in this case we do not obtain a close-form expression for $M(\theta)$ as in Eq. 4.5. A straight line between M_0^{top} and M_0^{btm} ($\theta = 0$) and $M^{top}(\alpha) = M^{btm}(\alpha) = 0$ ($\theta = \alpha$) is drawn to obtain the $M-\theta$ relationship. Moments M_0^{top} and M_0^{btm} at $\theta = 0$ are obtained from the uplift condition similarly to the freestanding column case (Eq. 3.6):

$$M_0^{top} = 0.5W_b(b - 0.5u_{up}) \tag{4.11}$$

$$M_0^{btm} = (0.5W_b + W_c)(b - 0.5u_{up}) \tag{4.12}$$

The uplift displacement, u_{up}, is calculated from Eq. 3.8 (or Eq. 3.9) setting $N = W_c + W_b$. A more accurate expression for u_{up} can be obtained from Eq. 3.8 assuming that the resultant horizontal force (base shear) is applied at height z, measured from the base of the frame. The height z is equal to:

$$z = \frac{2\sum m_i h_i + m_b 2h}{2\sum m_i + m_b} \Leftrightarrow z = \frac{4m_c h \sum i/n^2 + 2m_b h}{2m_c + m_b} \Leftrightarrow z = \frac{2m_c + 2m_b}{2m_c + m_b}h \tag{4.13}$$

where $\sum i/n^2 \approx 0.5$ (Diamantopoulos and Fragiadakis, 2019). Using the force method, the expression of the elastic stiffness k_e of a double curvature column with a force acting at height z is:

$$k_e = \frac{12EI}{2z^2(6h - z) - 6hz^2} \tag{4.14}$$

The total overturning moment is thus calculated as:

$$M_0 = 2\sum W_i(b-u_i) + W_b(2b-u_{up}) = 2W_c\sum(b-(i/n)u_{up}) + W_b(2b-u_{up}) \Leftrightarrow$$
$$M_0 = 2(W_c+W_b)(b-0.5u_{up}) \tag{4.15}$$

where W_i is the weight of each of the n-nodes and W_b is the weight of the deck. If u_i is the horizontal displacement of node i and h_i is the corresponding height from the base, then $u_i = (h_i/2h)u_{up} = (i/n)u_{up}$. With the aid of Eqs. 4.11, 4.12 and 4.15 it is shown that $M_0 = 2M_0^{top} + 2M_0^{btm}$. Furthermore, if the column mass is neglected, then all system mass is on the deck, i.e. it is lumped at D_1 and D_2. All the above expressions can be used in this case setting $m_c = 0$ and $z = 2h$. Specifically, the $M-\theta$ relationship will be the same for each of the four springs and equal to $M_0 = 0.5W_b(b-0.5u_{up})$. The member stiffness will be $k_e = 12EI/(2h)^3$.

Most software offer the *consistent or distributed mass* matrix option. The expression of the mass matrix for beam-column elements can be found in textbooksPrzemieniecki, 1968. Note that, this mass matrix is no longer diagonal, as in the lumped mass case. The lack of diagonality causes the loss of the sparsity of the effective stiffness matrix which makes the solution process too costly for problems with many degrees of freedom. However, for the rocking frame problems here examined, the number of degrees-of-freedom is small and hence the problem is not noticeable. Moreover, since the are no intermediate column nodes, the column rotational moment of inertia has to be lumped at the top and the bottom nodes. At nodes D_1 and D_2 (Figure 4.4), the translational mass will be $m_b/2$. The rotational inertia should consider also the inertia of the columns, thus: $I_{D1} = I_{D2} = 0.5(4m_c/3)R^2\sin^2\alpha + (m_b/2)(2b)^2$. The rotational moment at the base node should be $I_{O1} = I_{O2} = \Delta I_0^c/2 = 0.5(4m_c/3)R^2\sin^2\alpha$. The $M-\theta$ relationship is that of Eq. 4.15, setting $W_c = \bar{m}g2h$.

4.5 Column restraining

Structures designed to behave as rocking systems will be most likely restrained in order to maintain some control of the rocking motion. Following the work of Diamantopoulos and Fragiadakis, 2019 and the previous discussion for the freestanding block, it can be shown that the models already presented (Figure 4.3 and 4.4) for unrestrained frames can be extended to frames with rigid, or flexible, restrained columns maintaining the same mass and rotational moment of inertia values. The restrainers affect only the $M-\theta$ relationship which describes the self-centering restoring moment. Therefore, the required modifications concern the $M-\theta$ relationship of the rotational spring(s), while the uplift displacement u_{up} is obtained with the aid of Eq.

3.28 and Eq. 4.14. The equation of motion of a rigid rocking frame with vertical restrainers that pass from the column axis is (Makris and Vassiliou, 2015):

$$\ddot{\theta}(t) = -\tfrac{1+2\gamma}{1+3\gamma} p^2 \left[\sin\left[\alpha sgn\theta(t) - \theta(t)\right] + \tfrac{\ddot{u}_g(t)}{g} \cos\left[\alpha sgn\theta(t) - \theta(t)\right] \right] - \\ \tfrac{2}{1+3\gamma} p^2 \sin\alpha \sin\theta(t) \left[\tfrac{EA}{m_c g} \tan\alpha + \tfrac{P_0}{m_c g} \tfrac{1}{\sqrt{2-2\cos\theta(t)}} \right] \tag{4.16}$$

where P_0 is the pre-stressing force and EA the axial stiffness of the restrainers. Compared to the generalized frame equation of motion (Eq. 2.12), the second term in the right hand-side accounts for the restrainers. Moreover, when the frame is at rest, the first uplift will occur when the threshold acceleration $\ddot{u}_{g,min}$ is exceeded:

$$\ddot{u}_{g,min} = g \tan\alpha \left(1 + \frac{2}{2\gamma + 1} \frac{P_0}{m_c g} \right) \tag{4.17}$$

For a frame with *rigid* columns, if $M^{top/btm}(\theta)$ is the $M - \theta$ relationship of the top, or the bottom, springs without the restrainer (Eq. 4.5), the corresponding $M - \theta$ relationships for the restraint frame is denoted as $\widetilde{M}$ and will be:

$$\widetilde{M}^{top/btm}(\theta) = M^{top/btm}(\theta) + R \sin\alpha \sin\theta \left[EA \tan\alpha + \frac{P_0}{\sqrt{2 - 2\cos\theta}} \right] \tag{4.18}$$

The additional term, is the extra stability provided by the restrainer and is obtained

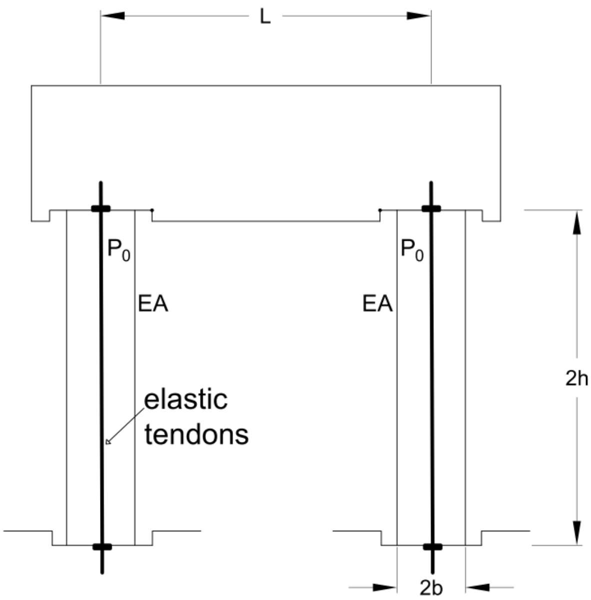

FIGURE 4.5: Rocking frame with two symmetric restrained columns.

from the second right-hand side term of Eq. 4.16. The extension to *flexible* rocking columns is straightforward following the previous sections. For $\theta = 0$, the maximum moment of the spring for which the rocking motion starts will be:

$$\begin{aligned} \widetilde{M}_0^{top} &= 0.5 m_b g R sin\alpha + P_0 R \sin\alpha \\ \widetilde{M}_0^{btm} &= 0.5 m_b g R sin\alpha + m_c g R sin\alpha + P_0 R \sin\alpha \end{aligned} \tag{4.19}$$

Furthermore, from Figure 4.5b and Eq. 4.18, it is clear that the restoring moment $\widetilde{M}(\theta)$ may have positive (stiffening) or negative (softening) hardening, depending on the axial stiffness EA and the force P_0 of the restrainer. When the piers are flexible, the uplift displacement is obtained using Eq. 3.28, setting $N = W_b/2 + W_c$ and using Eq. 4.14 to obtain k_e. The $M - \theta$ relationships are that of the rigid case assuming the M_0^{top} and M_0^{btm} values of Eq. 4.19. Tables 4.2 and 4.3 summarize the properties of the proposed frame models with either rigid or flexible columns. For frames with restrained columns, Table 4.3 can be applied as it is, while the $M - \theta$ relationships of Table 4.2 require a minor adjustment according to Eqs. 4.19. Eqs. 4.19 are considered for both rigid and flexible case, i.e. neglecting the cases in which u_{up} is large.

TABLE 4.2: Spring properties for freestanding rocking frames.

	moment at $\theta = 0$ (M_0)
rigid frame, column top	$0.5 m_b g b$
flexible frame, column top	$0.5 m_b g (b - 0.5 u_{up})$
rigid frame, column bottom	$(m_c + 0.5 m_b) g b$
flexible frame, column bottom	$(m_c + 0.5 m_b) g (b - 0.5 u_{up})$

TABLE 4.3: Moment of inertia of rocking frames.

	column-deck I_{D1s}, I_{D2s}	column-ground I_{01s}, I_{02s}	at nodes i I_i
rigid frame (Fig. 4.3)	$\frac{m_b}{2}(2b)^2$	-	$\frac{1}{3} m_c R^2 + m_c b^2$ *
flexible frame (Fig. 4.4, left)	$\frac{m_b}{2}(2b)^2 + \frac{4m_c}{3n} R^2 sin^2\alpha$	-	$\frac{4m_c}{3n} R^2 sin^2\alpha$ **
flexible frame (Fig. 4.4, right)	$\frac{m_b}{2}(2b)^2 + 0.5 \frac{4m_c}{3} R^2 sin^2\alpha$	$0.5 \frac{4m_c}{3} R^2 sin^2\alpha$	-

* at column midheight, ** at n nodes

A simple alternative is to use the generalized rocking equation of motion, using a "modified R", or a "modified I", system similar to that of Table 4.1. The additional term due to restraining is inserted into the $M - \theta$ relationship of the spring and thus the model remains similar to that of the freestanding frame, but with different spring properties. Table 4.4 summarizes the properties of the equivalent SDOF oscillator and also compares the properties of the equivalent frame with the modelling of a restrained rigid block (Vassiliou and Makris, 2015).

TABLE 4.4: Properties of the equivalent SDOF oscillators for rocking frames with restrained columns.

			$M(\theta)$	I_{CM}
block (restraint)	R	α	$m_c g R \sin(\alpha sgn\theta - \theta) + R\sin\alpha\sin\theta\left(\frac{EA\tan\alpha}{2} + \frac{P_0}{\sqrt{2-2\cos\theta}}\right)$	I_{CM}
modified R	$\widehat{R}$	α	$m_c g \widehat{R} \sin(\alpha sgn\theta - \theta) + \frac{2}{1+2\gamma}\widehat{R}\sin\alpha\sin\theta\left(EA\tan\alpha + \frac{P_0}{\sqrt{2-2\cos\theta}}\right)$	$\widehat{I_{CM}}$
modified I	R	α	$m_c g R \sin(\alpha sgn\theta - \theta) + \frac{2}{1+2\gamma}R\sin\alpha\sin\theta\left(EA\tan\alpha + \frac{P_0}{\sqrt{2-2\cos\theta}}\right)$	I'_{CM}

4.5.1 Column array capped with a rigid beam (epistyle)

The extension to an array of N-symmetric columns can be achieved either with one of the equivalent SDOF beam models (modified R or modified I model) that solves the generalized equation of motion, or with an extension of the detailed model of Figure 4.3 or Figure 4.4. The generalized equation of motion (Eq. 2.12) can be modified to include an array of N freestanding columns by adjusting γ, i.e. the ratio of the mass of the deck over the total mass of the columns (Makris and Vassiliou, 2013). Since the total mass of the N-columns is Nm_c the parameter γ of the array is set equal to $\gamma = m_b/Nm_c$. Therefore, the extension to N-columns is straightforward using the parameter values summarized in Tables 4.1 and 4.4.

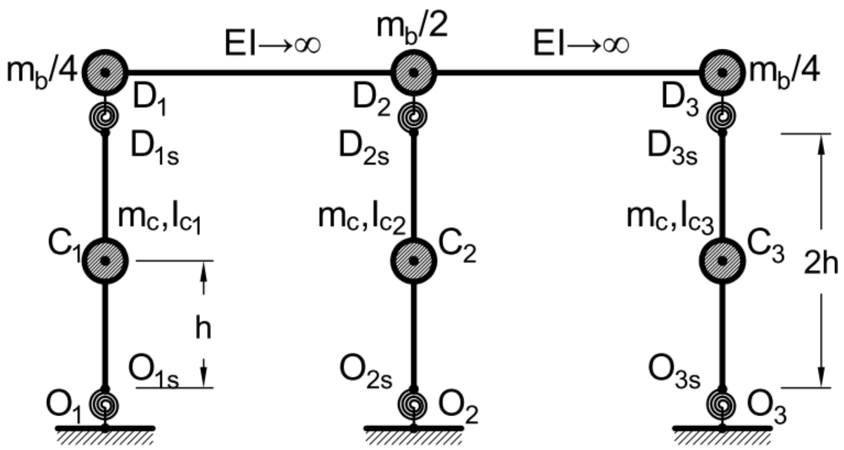

FIGURE 4.6: Detailed modelling of a rocking frame with three columns ($N = 3$).

The model of Figure 4.3a can be also extended to an array of N-symmetric columns as shown in Figure 4.6 ($N = 3$). The mass of the deck is lumped at the top of each supporting column (points D_1, D_2, D_3, Figure 4.6). In the general case of N columns, the deck mass at the internal nodes/columns is $m_b/(N-1)$ and $m_b/(2(N-1))$ at the two end nodes/columns. Therefore, when $N = 3$, the mass at nodes D_1 and D_3 will be $m_b/4$ (external nodes) and the mass of middle node will be $m_b/2$. The rotational moment of inertia at the column midheight ($C_1, C_2, \ldots C_N$, Figure 4.6) will be $(1/3)m_c R^2 + m_c b^2$. Furthermore, at the top nodes, the rotational moment of inertia will differ for the external and the internal columns. More specifically, at the external nodes D_{1s} and D_{Ns} it will be equal to $[0.5m_b/(N-1)](2b)^2$ and at the internal nodes $D_{2s}, \ldots, D_{(N-1)s}$ it will be $[m_b/(N-1)](2b)^2$. The moment-rotation relationship of the springs will differ for the external and the internal columns. Therefore the equivalent $M-\theta$ relationship of each spring at the bottom and the top of each column will be:

$$M^{top}(\theta) = \frac{m_b}{k(N-1)} gR \sin\left[\alpha sgn\theta(t) - \theta(t)\right]$$
$$M^{bot}(\theta) = m_c gR \sin\left[\alpha sgn\theta(t) - \theta(t)\right] + \frac{m_b}{k(N-1)} gR \sin\left[\alpha sgn\theta(t) - \theta(t)\right] \tag{4.20}$$

where $k = 1$ for the internal and $k = 2$ for the two external columns. Note that the $M-\theta$ relationship is the same for all columns. Moreover, for a frame with N piers which is at rest the maximum restoring moment is obtained assuming $\theta = 0$ and $\gamma = m_b/(Nm_c)$ in Eq. 4.20.

The extension to the restrained case is straightforward and the moment-rotation relationship of each spring is given from the expression:

$$\widetilde{M}^{top/btm}(\theta) = M^{top/btm}(\theta) + 2R\sin\alpha\left(EA\tan\alpha\sin\theta(t) + P_o\frac{\sin\theta(t)}{\sqrt{2-2\cos\theta(t)}}\right) \tag{4.21}$$

Column flexibility can be also taken into consideration simply adopting the model of Figure 4.4. The moment-rotation relationship is introduced according to Eq. 4.20 and/or Eq. 4.21 for freestanding and restrained columns, respectively. The rotational moment of inertia at the top of the external and the internal columns is the same with the rigid case as described above for N columns, while the rest of the model properties are these discussed in Section 4.4.2 and summarized in Table 4.3.

4.5.2 Rocking frame with asymmetric piers

Asymmetric rocking frames is a special case of rocking frames with piers of different heights that may be found in the transverse direction of bridges. The problem has been studied in detail by Dimitrakopoulos and Giouvanidis, 2015a. Following their work, the asymmetric frame examined has two piers of different size parameter R but same width b, connected with a rigid beam. The main difference between the symmetric and the asymmetric rocking frame is that in the latter case a three-block rocking mechanism should be studied (DeJong and Dimitrakopoulos, 2014). This results to a structure with three degrees of freedom, i.e. the rotations of the two piers and the deck. The problem can be further simplified if the rotation of the deck is related to the rotations of the columns.

Figure 4.7a shows the free-body diagram of the asymmetric frame, while Figure 4.7b shows a detailed model with beam elements and negative-stiffness rotational springs, similar to the model of Figure 4.3. The rotation of the deck θ_b depends on the rotation of the two columns θ_1, θ_2 and approximately can be calculated as: $\theta_b = \Delta v/L = (2b/L)(sin\theta_2 - sin\theta_1)$, where L is the horizontal distance of the two pivot points and Δv is the difference of the vertical displacements of the tips of the two piers. If the difference of the pier heights h_1 and h_2 is small and/or the length of the deck is large, it can be assumed that the deck remains approximately horizontal during the ground motion. Furthermore, since $b_1 = b_2 \Leftrightarrow R_1 sin\alpha_1 = R_2 sin\alpha_2$ and assuming that the deck is horizontal, it is found that the rotations θ_1, θ_2 are approximately related as follows:

$$\frac{sin\theta_2}{sin\theta_1} = \frac{R_1\cos\alpha_1}{R_2\cos\alpha_2} = \frac{sin\alpha_2\cos\alpha_1}{\sin\alpha_1 cos\alpha_2} \Leftrightarrow \frac{sin\theta_1}{sin\theta_2} = \frac{tan\alpha_1}{tan\alpha_2} \Leftrightarrow \frac{\theta_1}{\alpha_1} \approx \frac{\theta_2}{\alpha_2} \tag{4.22}$$

For the model proposed, the mass of the columns is concentrated at the column mid-height (C_1 and C_2), the mass of the deck is lumped at the two ends D_1 and D_2, while negative-stiffness rotational springs are inserted at the rocking surfaces. Due to the different height of the columns, the moment-rotation relationships are calculated with Eq. 4.5, but adopting the size parameter R and the rotation θ of the column considered. Furthermore, the rotational moment of inertia of each node is obtained using the equations discussed in the detailed model of a frame with rigid columns and presented in Table 4.3 for the freestanding rigid case, i.e. $I_{C1} = (1/3)m_{c1}R_1^2 + m_{c1}b^2$, $I_{C2} = (1/3)m_{c2}R_2^2 + m_{c2}b^2$, $I_{D1s} = I_{D2s} = (m_b/2)(2b)^2$.

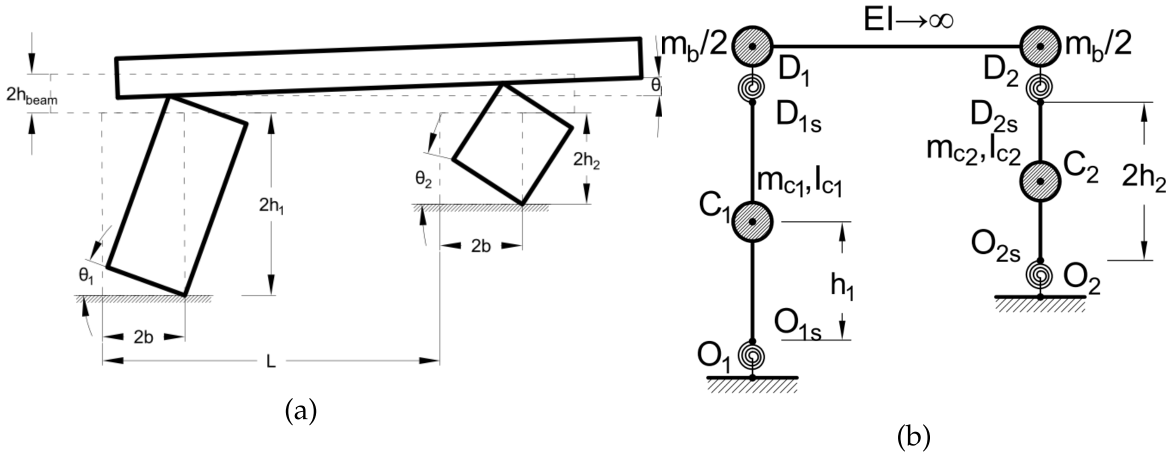

FIGURE 4.7: (a) Geometry of an asymmetric frame, and (b) proposed modelling of a rocking frame with asymmetric rigid columns.

The asymmetric frame has two major differences compared to the symmetric frame. The first is related to the coefficient of restitution, η_{asym}, and the second to the uplift acceleration, $u_{g,min}$. The coefficient of restitution differs depending on the pivot point as discussed in the work of Dimitrakopoulos and Giouvanidis, 2015a. Due to length limitations the equation are not here repeated; instead the reader can find them in paper of Dimitrakopoulos and Giouvanidis, 2015a (Eq. 36, Appendix II). It is worth mentioning that the η_{asym} values obtained will have as upper and lower bound the two values obtained with Eq. 2.14 using the geometry of each pier. For example, for $\tan\alpha_1 = 0.15$ and $\tan\alpha_2 = 0.20$, the coefficient of restitution will be 0.955 and 0.923. Assuming $L = 5m$ and $2h_{beam} = 1m$, an asymmetric frame with the same α_1, α_2 values will result to η_{asym} values equal to 0.948 and 0.934.

It is also interesting to mention that the minimum acceleration $\ddot{u}_{g,min}$ required for the initiation of rocking motion of a frame with columns of the same b, depends on the sign of the record and it is given by the equation below (Dimitrakopoulos and Giouvanidis, 2015a) :

$$\frac{\ddot{u}_{g,min}}{g} = \mp\frac{b}{h_1}\frac{m_{c1} + m_b[1 + \bar{h} - 2\bar{b}(\pm\bar{h} \mp 1)] + m_{c2}\bar{h}}{m_{c1} + 2m_b[\frac{\bar{b}h_{beam}}{h_1}(\pm\bar{h} \mp 1) + 1] + m_{c2}} \tag{4.23}$$

where $2h_{beam}$ is the beam's height, $\bar{h} = h_1/h_2$, $\bar{b} = b/L$ and L is the length of the beam. Alternatively, the minimum acceleration required for the initiation of rocking can be determined through a static pushover analysis using the proposed model and avoiding the expression of Eq. 4.23.

4.6 Numerical results

Different rocking frame examples are examined in order to validate the accuracy of the models proposed. The first example concerns two *rigid frames* with properties: $2h$=5m, $2b$=0.75m, γ=1 (Frame 1) and $2h$=8.4m, $2b$=1.4m, γ=5 (Frame 2). Frame 1 is representative of an ancient monument with monolithic columns that support an epistyle (e.g. Figure 2.4a), while the properties of Frame 2 are representative of a modern rocking bridge. Note that in the case of a bridge, the mass ratio γ is usually larger than 4, as opposed to the case of monuments where this ratio is much lower, e.g. $\gamma \approx 1$. The records adopted are the *Loma Prietta (1989), Saratoga - Aloha Ave* ($PGA = 0.36g$) and the *Northridge (1994), MUL279 component* ($PGA = 0.52g$). The acceleration time histories are shown in Figure 4.8; the first is a near-fault record, while the second is a far-field ground motion.

The model of Figure 4.3 is adopted first. Figure 4.9 and Figure 4.10 show the normalized rotation response history (θ/α) for Frames 1 and 2, respectively. The results for the records of Figure 4.9 and Figure 4.10 are compared to the solution obtained solving directly the differential equation (Eq. 2.12) using Matlab ODE23s solver. Close agreement between the two solutions is found in all cases examined. Furthermore,

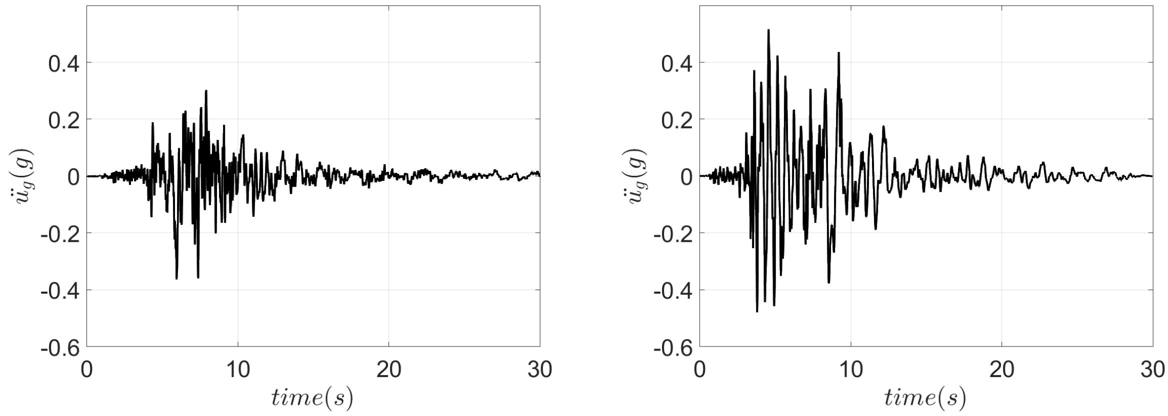

(a) (b)

FIGURE 4.8: (a) Near-fault excitation (1989 Loma Prietta, Saratoga - Aloha Ave), and (b) far-field excitation (1994 Northridge, MUL279 component).

Figure 4.11 shows the response obtained using the simplified models of sections 4.3. The Figure 4.11 shows the results of Frame 1 and 2 under the near and far-field record, respectively considering the two simplified rocking frame models, i.e. the modified R and the modified I. The results of both modified R and modified I approaches coincide almost perfectly with the solution of the generalized equation of motion of the rocking frame.

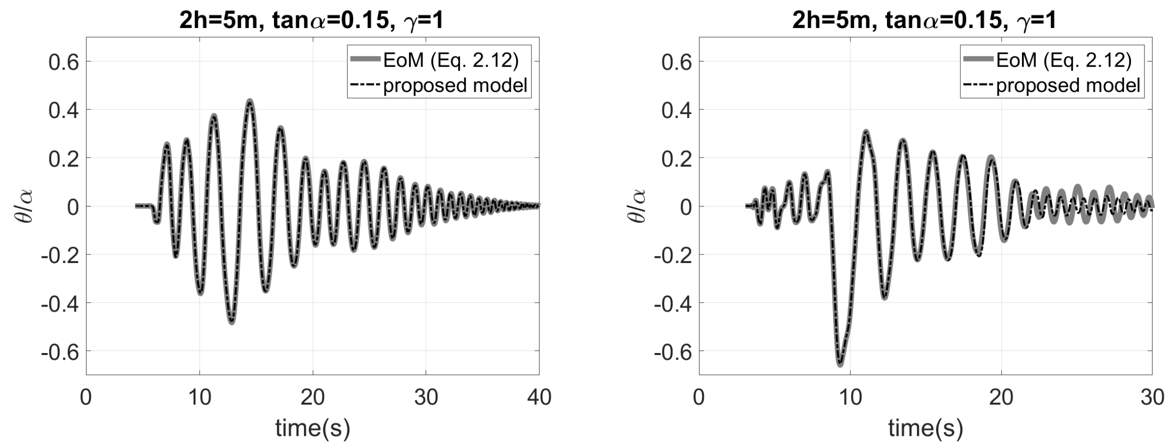

(a) (b)

FIGURE 4.9: Rocking response history obtained using the detailed model of Figure 4.3: (a) Frame 1, subjected to the near-field record (Figure 4.8a), (b) Frame 1, subjected to the far-field record (Figure 4.8b).

The flexible rocking frame model of Figure 4.4 is examined assuming a frame with two symmetric columns ($2h = 12m$, $2b = 1.2m$) and mass ratio $\gamma = 4$ (Frame 3). Compared to the previous two frames, this frame has larger height and smaller slenderness and thus the dynamic response is affected significantly by the column flexibility. The

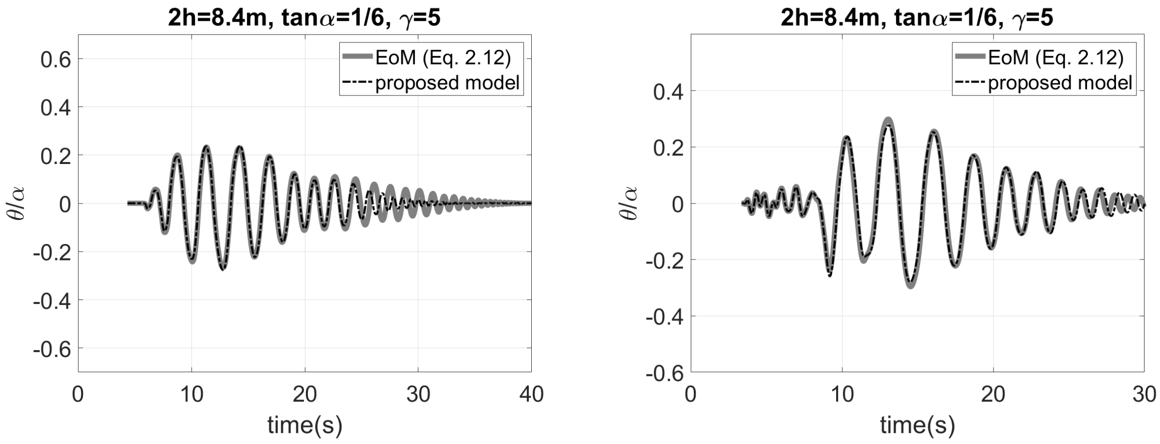

(a) (b)

FIGURE 4.10: Rocking response history obtained using the detailed model of Figure 4.3: (a) Frame 2, subjected to the near-fault record (Figure 4.8a), (b) Frame 2, subjected to the far-fault record (Figure 4.8b).

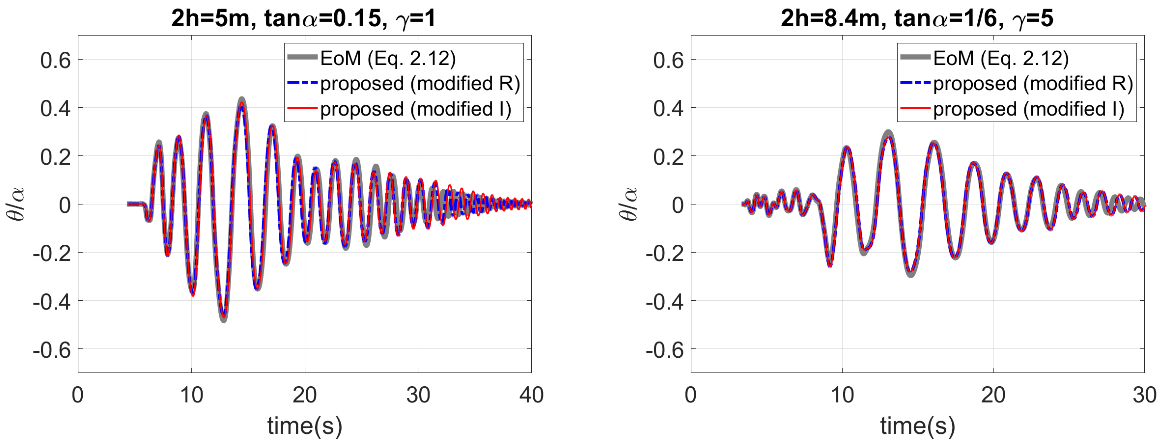

(a) (b)

FIGURE 4.11: Rocking response history of Frame 1, simulated with the "modified R" and "modified I" approach. (a) Near-fault record, (b) far-field record.

columns are made of concrete and have properties E=30GPa and ρ=2.5Mg/m^3. Figure 4.12 compares the response of the proposed flexible rocking frame models of Figure 4.4 against the response of the rigid rocking frame. Clearly, the rigid column assumption is not suitable for the frame examined. Furthermore, the agreement of the two models is almost perfect for both the near and the far-field ground motion. The choice of assuming eight masses ($n = 8$) is based on a previous investigation (Diamantopoulos and Fragiadakis, 2019), where it was shown that there is a small sensitivity of the results to the number of nodes n assumed. Reduced rotation demand is observed for the flexible frame, although this is not a general rule. Furthermore, Figure 4.13 compares the response of the proposed flexible rocking frame model of Figure 4.4 against

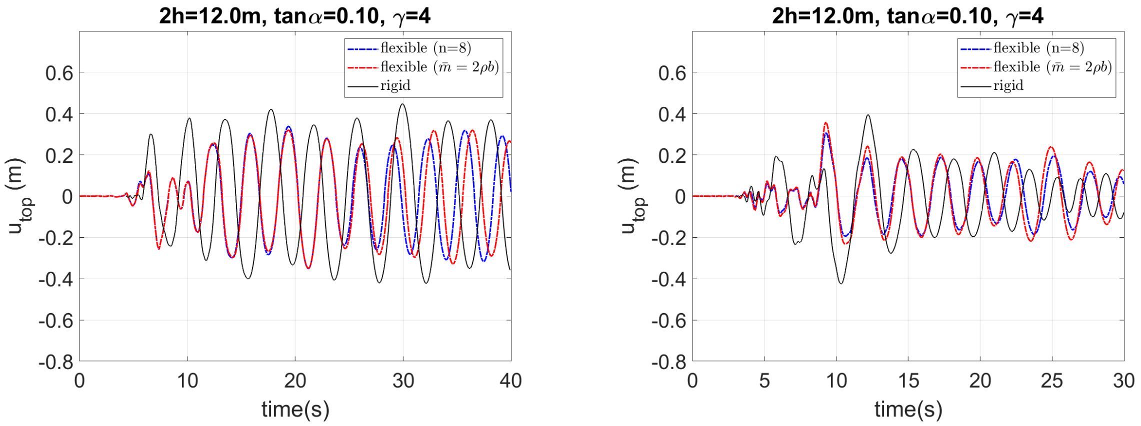

(a) (b)

FIGURE 4.12: Seismic response history of a single-bay rocking frame with flexible columns (E=30GPa and ρ=2.5Mg/m^3) when it is subjected to: (a) the near-fault ground motion, and (b) the far-field ground motion.

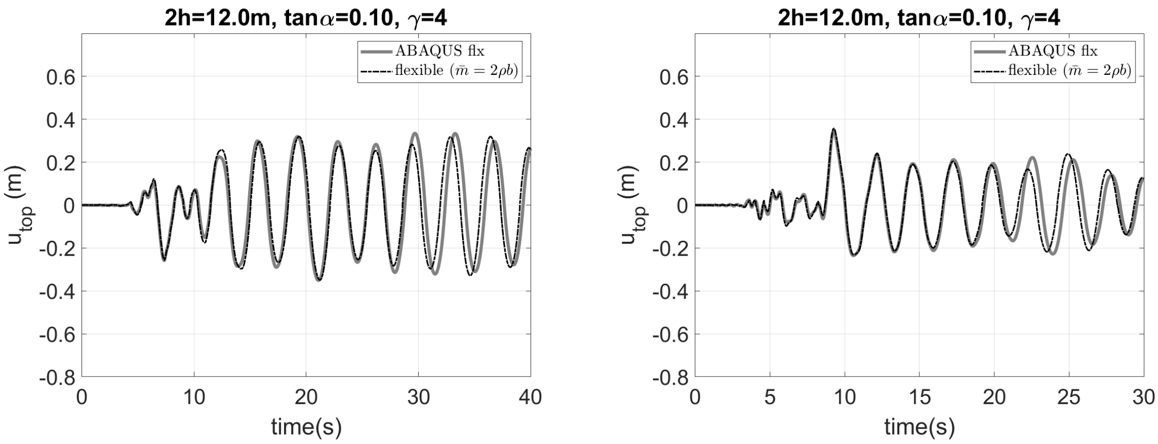

(a) (b)

FIGURE 4.13: Seismic response history of a single-bay rocking frame with flexible columns (E=30GPa and ρ=2.5Mg/m^3) when it is subjected to: (a) the near-fault ground motion, and (b) the far-field ground motion. The plot compares the response of the proposed model assuming that the mass is distributed along the height of the columns with the solution obtained using Abaqus.

the solution obtained with Abaqus software; the agreement is practically perfect in both cases. For the Abaqus model, surface-to-surface interaction with zero damping and a rough friction coefficient was assumed while the dynamic analysis is explicit. Moreover, the bodies were assumed flexible, the model was 2D and the material was linear elastic with E=30GPa and ρ=2.5Mg/m^3. For the proposed model, the coefficient of restitution was set equal to one in order to allow a fair comparison with the Abaqus model that uses only continuous damping while a three-point backward Euler numerical integration scheme (TRBDF2 integrator in OpenSees) was adopted since

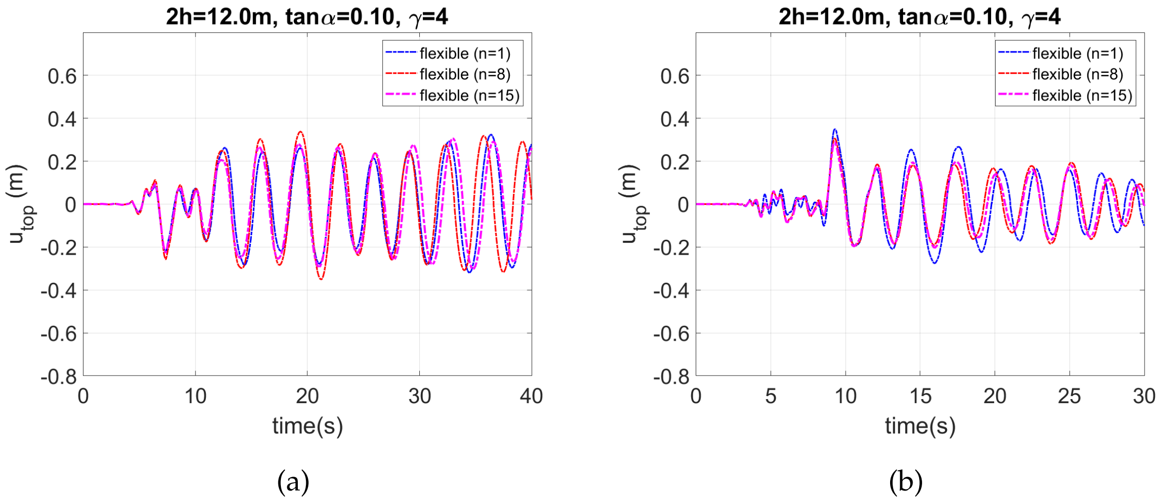

FIGURE 4.14: Seismic response history of a single-bay rocking frame with flexible columns (E=30GPa and ρ=2.5Mg$/m^3$). The plot compares the response when $n = 1$, $n = 8$ and $n = 15$ equally spaced masses are adopted and the frame is subjected to: (a) the near-fault ground motion, and (b) the far-field ground motion.

it was found to be more accurate and efficient.

Figure 4.14 further investigates the sensitivity of the response prediction to the number of equally spaced masses. Three different values ($n = 1, 8$ and 15) are compared. The case of $n = 1$ leads to the model of Figure 4.3, while for $n = 8$ and $n = 15$ the model of Figure 4.4 (left column) is adopted. For $n = 1$ the seismic response does not agree well with the solution of Abaqus due to the flexibility of the columns, while for $n = 15$ the agreement is practically perfect. Since the difference between $n = 8$ and $n = 15$ is small, $n = 8$ can be adopted without loss of accuracy for columns up to 12m. In any case, it is concluded that the larger the number of equally spaced nodes, the more accurate the model response prediction.

The third example examines the seismic response of a rocking bridge with vertical restrainers at the piers. Frame 2 is considered for this example since it has dimensions that can be assumed representative to those of a contemporary rocking bridge. The columns are equipped with restrainers pre-tensioned to axial force $P_0/m_c g = 0.5$, while two types of restrainers with $EA/m_c g = 80$ and 250 are considered. The first EA value results to springs with negative $M - \theta$ relationship and the second to springs with a positive stiffness. Figure 4.15 shows the response of the structure subjected to the far-field excitation (Figure 4.8) and is compared against the direct solution of the equation of motion (Eq. 4.16) using the ODE23s solver. Perfect agreement is obtained for both restrainer types when the proposed model is adopted.

Figure 4.16 compares the rigid response against a version of Frame 2 with flexible columns (E=30GPa, ρ=2.5Mg/m^3) and rigid deck. In this case, the flexible response

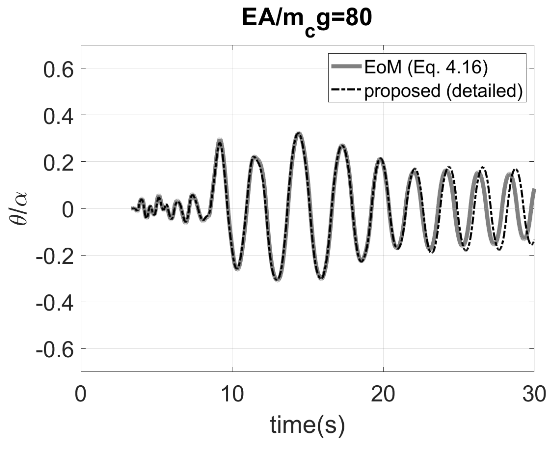

(a) (b)

FIGURE 4.15: Comparison of the response obtained for the solution of the equation of motion of Frame 2 with pre-stressed rocking columns and the proposed modelling when it is subjected to Northridge (Figure 4.8b) earthquake and the springs have: (a) negative ($EA/m_cg = 80$) or (b) positive stiffness ($EA/m_cg = 250$).

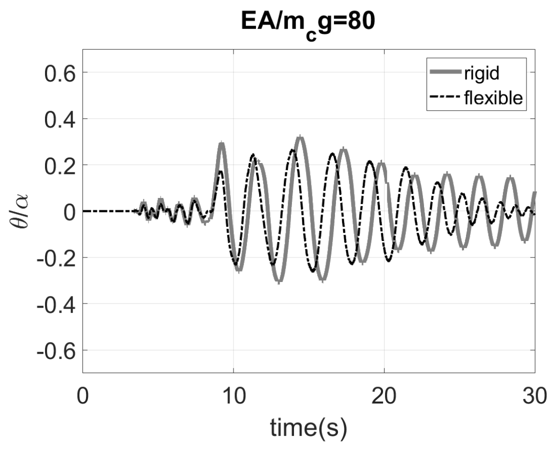

(a) (b)

FIGURE 4.16: Comparison of the response obtained for the solution of the equation of motion of Frame 2 with pre-stressed rocking columns and the proposed modelling (Figure 4.4) when the columns are assumed flexible (E=30GPa and ρ=2.5Mg/m^3), the frame is subjected to Northridge (Figure 4.8b) earthquake and the springs have: (a) negative or (b) positive stiffness.

starts at time zero as opposed to the rigid frame where the motion initiates at the instant of the first uplift. Moreover, it is seen that the rotation at the base of the columns is smaller than that of the rigid frame since the flexibility acts beneficially for both restrainer types considered.

The first example considered for the case of an array of freestanding columns capped with a beam is an array of $N = 3$ columns. Two frames with properties:

$2h$=5m, $2b$=0.75m, γ=1 (Frame 1) and $2h$=8.4m, $2b$=1.4m, γ=5 (Frame 2) are considered. The two frames have been adopted for the two different ground motions with different dimensions and different γ values. The colonnades are capped with a rigid epistyle and are subjected to a near-field and a far-field ground motion record. The same example frames were adopted in Diamantopoulos and Fragiadakis Diamantopoulos and Fragiadakis, 2022 and are used as reference frames for the validation of the modeling.

Figure 4.17 presents the results obtained using the model of Figure 4.6 and is compared against the solution of the equation of motion of the problem. In Figure 4.17a the Frame 1 is subjected to the *Loma Prietta (1989), Saratoga - Aloha Ave* ($PGA = 0.36g$) which is a near-fault ground motion, while in Figure 4.17b Frame 2 is subjected to the *Northridge (1994), MUL279 component* ($PGA = 0.52g$) which is a far-field signal. In both cases, excellent agreement is obtained confirming that the proposed model is accurate and stable.

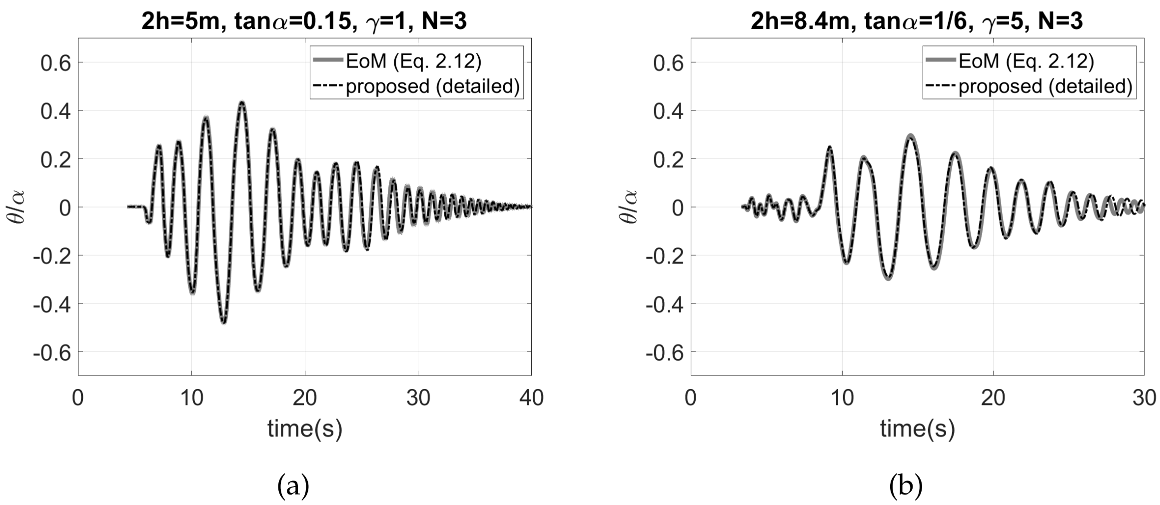

FIGURE 4.17: Rocking response history of a two-bay rocking frame modeled with the detailed model (Fig. 4.6), when subjected to (a) *Loma Prietta (1989), Saratoga - Aloha Ave* (far-field with $PGA = 0.36g$) and (b) *Northridge (1994), MUL279 component* (near-fault with $PGA = 0.52g$).

The next numerical example refers to the modeling of frames with columns of unequal height. Such a frame is not common in ancient structures. However, it can be assumed as a case when an imperfection is considered in the ground or when the monuments is located on a downhill terrain. In order to validate the results of the proposed model for asymmetric columns, an ABAQUS finite element model was employed (Fig. 4.18). Details about the FE modeling using ABAQUS can be found in Diamantopoulos and Fragiadakis, 2019 and Diamantopoulos and Fragiadakis, 2022.

Figure 4.19a shows the results of an asymmetric rocking frame with $2h_1 = 5.0m$, $2h_2 = 3.75m$, $tan\alpha_1 = 0.15$, $tan\alpha_2 = 0.20$ (Frame 3). The mass of the epistyle is equal to the sum of the masses of the two columns, i.e. $m_b = m_{c1} + m_{c2}$. It is reminded that

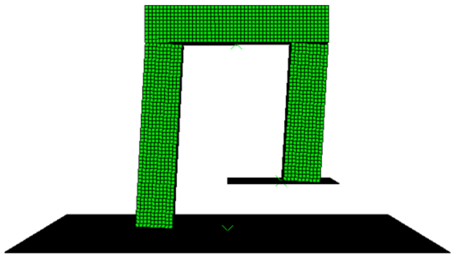

FIGURE 4.18: Asymmetric rocking frame modeled with ABAQUS, 2011 ($2h_1 = 5.0m$, $2h_2 = 3.75m$, $tan\alpha_1 = 0.15$, $tan\alpha_2 = 0.20$).

γ can not be defined for the asymmetric case. Figure 4.19b shows the same results but for another asymmetric rocking frame with $2h_1 = 8.4m$, $2h_2 = 7.0m$, $tan\alpha_1 = 0.16$, $tan\alpha_2 = 0.20$ and $m_b = 5 \times (m_{c_1} + m_{c_2})$ (Frame 4). The difference between the two frames is that the second is higher than the first and has a larger mass ratio $m_b/\Sigma m_c$. In both frames considered here the taller column is equal to that of Frame 1 and Frame 2, respectively and always the columns have the same width $2b$. The first frame is subjected to the near-field record and the second to the far-field ground motion, respectively. As shown in Figure 4.19, the accuracy of the proposed model is satisfactory, although it has been assumed that the deck remains always horizontal. More specifically, for the first frame (Fig. 4.19a), the results perfectly coincide up to $t \approx 20$sec, while the agreement for the second frame is good for the whole response history duration. Note that the vertical axes of the plots show the ratio of the rotation normalized by the column slenderness which is, approximately, equal for both columns as explained in Eq. 4.22.

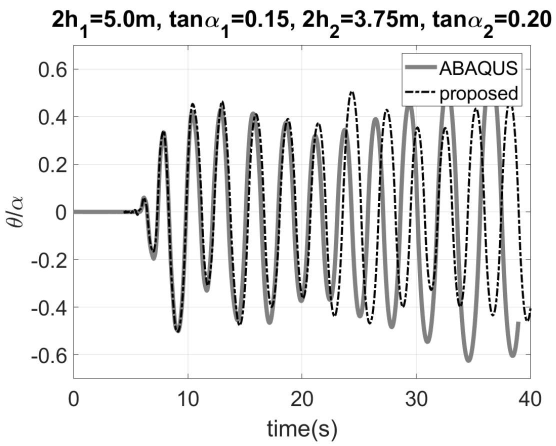

(a)

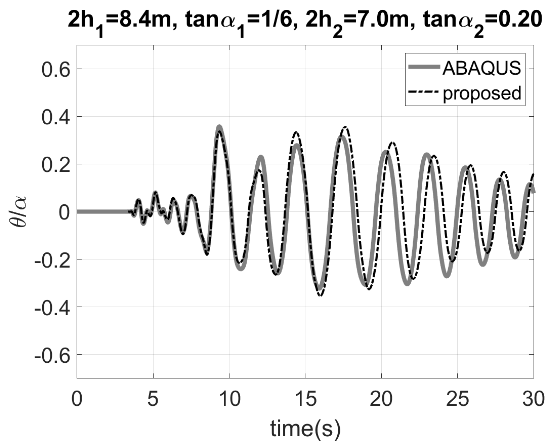

(b)

FIGURE 4.19: Rocking response history of asymmetric frames subjected to reference ground motion records: (a) first asymmetric frame ($2h_1 = 5m, 2h_2 = 3.75$), subjected to near-field record, (b) second asymmetric frame ($2h_1 = 8.4m, 2h_2 = 7m$), subjected to the far-field record.

Chapter 5

Fragility and risk assessment

In this chapter, a fragility and risk assessment framework for rocking frames is presented. It has to be noted that, the notation was partially changed with respect to an original corresponding paper which is under review in order to be consistent with the notation used throughout the Thesis.

5.1 Performance-based assessment framework

Performance-Based Earthquake Engineering (PBEE) combines computational tools and reliability assessment procedures in order to obtain the system fragility and risk for a range of limit-states. According to PBEE, the acceptable level of damage depends on the level of ground shaking and the significance of the structure considered. These concepts are today well understood among earthquake engineers, but when monuments are considered the criteria differ (Psycharis et al., 2013a). For freestanding monolithic columns and colonnades, the collapse damage state is primarily of interest. Determining what risk level is acceptable for monuments is not straightforward since it requires a consensus among various experts, i.e. archaeologists, experts in monument preservation and engineering. Nevertheless, it is certain that the risk of collapse should be as low as possible.

5.1.1 Engineering Demand Parameters and Intensity Measures

The work of the Thesis is concentrated on monolithic columns and colonnades. Therefore, the Engineering Demand Parameter (EDP) considered is the normalized rotation θ of the column over its slenderness angle α, where α is defined as the ratio of the column height over the width of the base. The normalized rotation θ/α provides a measure of column deformation during the ground shaking and also shows how close to collapse a column or a colonnade was brought during the earthquake. This EDP has a clear physical meaning and allows to identify various damage states and to set empirical performance objectives. For example a value of θ/α equal to $1/3$ indicates that the maximum rotation was 1/3 of the slenderness and thus there was no danger of collapse, while values of θ/α larger than one imply intense shaking, large deformations of the column and most probably collapse.

Although the critical performance level of interest is collapse, intermediate performance levels, in some cases, can be also of importance. Lower performance levels are related to secondary damage indicators, e.g. minor fracture of a wedge, that do threaten the stability of the system but may still damage the monument. Therefore, three performance levels have been considered in this chapter. The first level (damage limitation) corresponds to weak shaking with small or no rocking at all. At this level of shaking, no damage, and no residual deformations are expected. The second level (significant damage) corresponds to intense shaking with significant rocking of the column; however, the column is not brought close to collapse. The third performance level (near collapse) corresponds to very intense shaking with significant rocking. The column does not necessarily collapse at this level but it is brought close to collapse and its safety is critically threatened. Possible EDP threshold values are: 0.15, 0.35 and 1.00. These values are based on engineering judgment and also on experience from past earthquakes and the literature. Although it is clear that, in general, strong ground motions lead to large rotations during an earthquake there is a significant scatter of the results indicating that intense rocking does not necessarily imply large rotations and also that large rotations can occur for relatively weak shaking of the column. This is due to the complexity of the problem.

The selection on an appropriate Intensity Measure (IM) is also a point of interest. For rocking systems, the most intuitive IM choice is the peak ground acceleration (PGA), since it is the parameter that defines the maximum overturning moment, while it also defines whether rocking, sliding or none of the two will occur. The PGA can be normalized with $gtan\alpha$ in order to be dimensionless and thus the block's IM is $IM = PGA/gtan\alpha$, where $IM \leq 1$ implies that the block does not start rocking. Past research papers, e.g. Ishiyama, 1982b and Dimitrakopoulos and Giouvanidis, 2015b, have shown that also the PGV is an important response parameter that correlates the seismic demand with the block's overturning. A third IM considered in this work is the average spectral acceleration S_a^{avg} (Eads et al., 2015; Kohrangi et al., 2017). S_a^{avg} is defined for a range of periods (or frequencies) and is calculated as:

$$S_a^{avg} = \left(\prod_{i=1}^{N} S_a(c_i) \right)^{(1/N)} \tag{5.1}$$

where N is the number of discrete period values considered and c_i defines the period range of interest, that typically varies from 0.50 to 1.50sec, as it is discussed in the

Numerical Results section.

In summary, the three IMs considered are the Peak Ground Acceleration over the tangent of the slenderness value ($PGA/gtan\alpha$), the Peak Ground Velocity (PGV) and the average spectral acceleration (S_a^{avg}). All three IMs have the desired IM properties, i.e. "practicality", "efficiency" and "sufficiency", as discussed by Giouvanidis et al., 2017.

5.1.2 Fragility and Risk assessment

Fragility curves are a valuable tool for the seismic risk assessment of a system. Fragility analysis was initially developed for the reliability analysis of nuclear plants in an effort to separate the structural analysis part from the hazard analysis performed by engineering seismologists. Fragility analysis requires the calculation of the probabilities that a number of monotonically increasing limit-states are exceeded. Therefore, the seismic fragility F_R is defined as the limit-state probability conditioned on seismic intensity. Therefore, the fragility of a system is the probability that an engineering demand parameter (EDP) exceeds a threshold value edp and is defined as:

$$F_R(IM) = P(EDP > edp|IM) \tag{5.2}$$

In order to properly calculate the integral of Eq. 5.2 three possible response states are identified: (*i*) the system remains at rest during the earthquake, (*ii*) it uplifts and rocks and (*iii*) it overturns. Using the total probability theorem, the fragility function (Eq. 5.2) is calculated as:

$$F_R = P(EDP|NoUplift)P_{NoUplift} + P(EDP|Uplift)P_{Uplift} + P(EDP|Ovtn)P_{Ovtn} \tag{5.3}$$

where $P(EDP|NoUplift)$, $P(EDP|Uplift)$ and $P(EDP|Ovtn)$ are the limit-state exceedance probabilities when there is *no-uplift*, there is *uplift* and there is *overturning*, respectively. $P_{NoUplift}$, P_{Uplift} and P_{Ovtn} are the corresponding probabilities. For columns that will not uplift, $P(EDP|NoUplift) = 0$, while for the overturning columns $P(EDP|Ovtn) = 1$. Therefore, the calculation of fragility is simplified to:

$$F_R = P(EDP \geq edp|Uplift)(1 - P_{Ovtn} - P_{NoUplift}) + P_{Ovtn} \tag{5.4}$$

Assuming that rocking data are lognormally distributed, $P(EDP \geq edp|Uplift)$ can be calculated analytically once the mean and the standard deviation of the logs of the EDP are calculated, which are denoted as μ_{logEDP} and σ_{logEDP}, respectively. Once they are known they can be used to calculate the probability that the EDP exceeds a threshold value edp using the lognormal distribution:

$$P(EDP \geq edp|Uplft) = 1 - \Phi\left(\frac{log(EDP) - \mu_{logEDP}}{\sigma_{lnEDP}}\right) \tag{5.5}$$

where edp is the EDP's threshold value that denotes that the limit-state examined is exceeded and Φ is the standard normal distribution. For example, if the fragility that corresponds to normalized rotation of the column's capital θ/α is larger than 0.3, $log(edp)$ would be equal to log(0.3).

The risk is expressed as the mean annual frequency (MAF) of a limit-state being exceeded. Adopting the PEER's formula, the limit-state MAF can be calculated with the aid of the expression:

$$\lambda_{EDP} = \int_{IM} P(EDP|IM) \left|\frac{d\lambda_{IM}}{dIM}\right| dIM \tag{5.6}$$

where λ_{EDP} is the mean annual frequency of the EDP and $d\lambda_{IM}$ is the slope of the seismic hazard curve. The limit-state MAF is obtained convolving the slope of the site hazard curve λ_{IM}, expressed as function of the IM, with the fragility curve $P(EDP|IM)$ obtained with respect to the EDP and the IM of interest.

5.2 Fragility analysis methods

5.2.1 Multiple-stripe analysis

The limit-state fragilities of rocking systems can be calculated using different approaches. The Incremental Dynamic Analysis (IDA) method is a common tool for such problems. IDA involves subjecting the system to a suite of ground motion records, each scaled to multiple levels of intensity. After incrementally scaling every ground motion, single record capacity curves are produced in terms of demand versus seismic intensity. IDA has conceptual similarities to the Multiple Stripe Analysis (MSA) method (Jalayer, 2003; Baker, 2015), where instead of scaling up every ground motion, the records are scaled to the same IM level (Fig. 5.1). Since for every scaling level the ground motions have the same IM value, the EDP values form a "stripe" (Fig. 5.1) which allows to directly calculate the median (50% percentile) and the 16% and 84% percentile capacity curves conditional on the IM. Strictly speaking, in IDA the scaling factors will be different, but stripped data can be easily obtained with interpolation (Vamvatsikos and Cornell, 2004). For the sake of simplicity, in this work MSA was performed (i.e. scaling the records to a common IM level), but loosely speaking the "term" IDA could have been also used since it is more widespread and the difference is merely lie on the implementation.

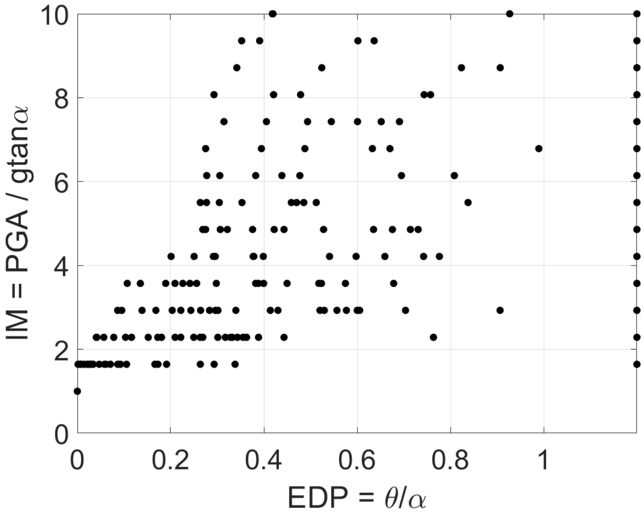

FIGURE 5.1: EDP - IM plot: multiple stripe analysis.

Eq. 5.4 can be directly solved using a multiple stripe analysis approach when the EDP values form stripes conditional on the IM value. For every stripe, the mean and standard deviation conditional on the IM, are calculated. Assuming that the data follow the lognormal distribution, the fragility conditioned on the IM level is obtained as:

$$F_R = \Phi\left(\frac{\mu_{logEDP} - log(edp)}{\sigma_{logEDP}}\right)\left(1 - P_{Ovtn} - P_{NoUplift}\right) + P_{Ovtn} \tag{5.7}$$

$P_{NoUplift}$ and P_{Ovtn} are obtained, for every stripe, as the percentage of simulations where no-uplift and overturning was observed, respectively. In other words, $P_{NoUplift}$ and P_{Ovtn} are calculated following the equations:

$$P_{NoUplift} = \frac{number\ \ of\ \ simulations\ \ NoUplift}{total\ \ number\ \ of\ \ simulations} \tag{5.8}$$

$$P_{Ovtn} = \frac{number\ \ of\ \ simulations\ \ Ovtn}{total\ \ number\ \ of\ \ simulations} \tag{5.9}$$

5.2.2 Cloud analysis

If the data are not stripped (Fig. 5.1) then they will form a "cloud" (Fig. 5.2) and the "cloud analysis" has to be adopted instead. Therefore, the cloud analysis is a common method when the data are scattered in the EDP-IM plane. This occurs when the ground motions are left unscaled, or when they have all been scaled with the same factor. A linear fit (Fig. 5.3) provides the mean of the logarithms (μ_{logEDP}) and a single constant value for the dispersion σ_{logEDP}. Knowing μ_{logEDP} and σ_{logEDP}, it is possible to calculate the fragility of the rocking simulations using Eq. 5.7. Eq. 5.7 requires the

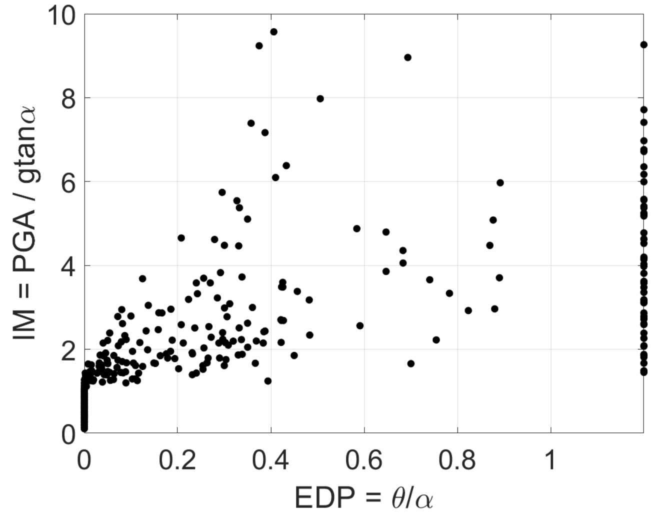

FIGURE 5.2: EDP - IM plot: cloud analysis.

knowledge of P_{NoRock} and P_{Ovtn} over the whole IM range. These probabilities can be calculated (Fragiadakis and Diamantopoulos, 2020; Jalayer et al., 2017) using a logistic regression model (logit) which yields a probability estimate that is function of the IM (Jalayer et al., 2017). Therefore, for the NoUplift and Overturning cases:

$$P_{NoUplift} = \frac{1}{1 + e^{-(b_1 + b_2 log(IM))}} \tag{5.10}$$

$$P_{Ovtn} = \frac{1}{1 + e^{-(b_3 + b_4 log(IM))}} \tag{5.11}$$

where the constants b_1, b_2, b_3, b_4 are the parameters of the logistic regression model, obtained with binomial-based, generalized linear model (GLM) regression.

5.2.3 Maximum-Likelihood (MLE) fitting

A maximum-likelihood (MLE) fitting can be also adopted both when the data are striped, or form a cloud in the $EDP - IM$ plane (Baker, 2015). The MLE fitting approach fits the CDF (Cumulative Distribution Function) of a lognormal distribution on the EDP-IM data and thus the fragility function is simply a lognormal CDF of the form:

$$F_R = P(EDP \geq edp) = \Phi \left(\frac{log(EDP/\theta_a)}{\beta_a} \right) \tag{5.12}$$

where θ_a and β_a are the median and the dispersion that have to determined by maximizing the likelihood function (Baker, 2015).

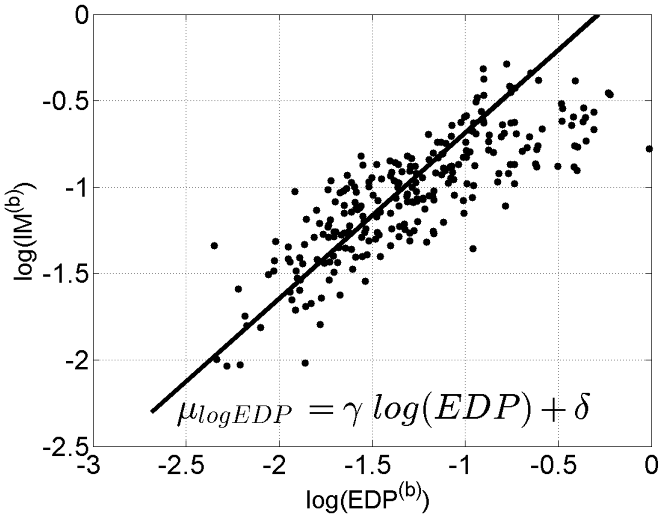

FIGURE 5.3: Cloud analysis: Linear fitting in the log-log space.

Multiple-stripe analysis provides, at discrete IM levels (stripes), the number of successes n_{suc}, i.e. the number of simulations that the limit-state has been exceeded after n_{tot} total simulations. Using the binomial distribution on the data of a single stripe, the probability of having exactly n_{suc} successes after n_{tot} simulations, will be:

$$P(Success = n_{suc}) = \begin{pmatrix} n_{tot} \\ n_{suc} \end{pmatrix} P(EDP^{(s)})^{n_{suc}}(1 - P(EDP^{(s)}))^{n_{tot}-n_{suc}} \tag{5.13}$$

If there are k stripes, substituting Eq. 5.12 to Eq. 5.13, we obtain the MLE function as:

$$\mathcal{L} = \prod_{i=1}^{k} \begin{pmatrix} n_{tot,i} \\ n_{suc,i} \end{pmatrix} \Phi \left(\frac{log(EDP/\theta_a)}{\beta_a} \right)^{n_{suc,i}} \left(1 - \Phi \frac{log(EDP/\theta_a)}{\beta_a} \right)^{n_{tot,i}-n_{suc,i}} \tag{5.14}$$

The only unknowns are θ_a and β_a which are found as the values that maximize the likelihood function $\mathcal{L}$ of Eq. 5.14, or preferably its natural logarithm. This can be achieved easily with a spreadsheet or with a simple computer script. Note that the fit is performed on the whole data, avoiding the partitioning of Eqs. 5.3 and 5.4. If the EDP-IM pairs form a cloud, each simulations is assumed as a stripe. Therefore, k is the number of simulations, n_{tot} is equal to one ($n_{tot} = 1$) and n_{suc} is equal to one, or zero, depending whether the simulation exceeds the limit-state threshold or not.

The fragility curves of Figure 5.4 have been obtained using the above modeling approach. Figure 5.4a compares smooth and chainsaw-like fragility curves, i.e. the fragility that comes from the multiple-stripe analysis and the fragility considering the Baker's method (Baker, 2015). Figure 5.4b compares the multiple-stripe and the cloud analysis for the same $IM = PGA/gtan\alpha$ and the same structure. The proposed results shed light on the fact that the methods presented have limitations especially related to

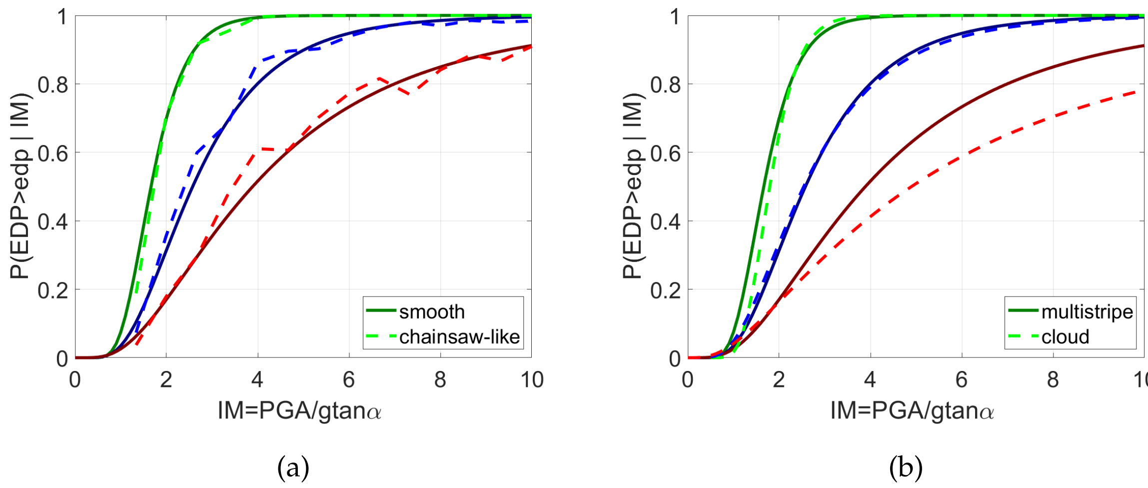

FIGURE 5.4: (a) Chainsaw-like vs smooth fragility curves, (b) multiple stripe vs cloud analysis. The limit-states considered correspond to θ/α = 0.15, 0.35 and 1.00.

the fitting of the fragilities in the tails of the distribution. For example, a large number of simulations may be required to properly assess the correct values of the median and percentiles that are used in the formulation or convergence analysis may be needed.

5.3 Numerical results

5.3.1 Rocking columns

A rectangular freestanding rocking block with dimensions $2h \times 2b = 5.00m \times 0.75m$ is assumed. The IMs considered are the $PGA/g \tan\alpha$ and the PGV (Peak Ground Velocity). This is the first step for the application of the previous framework on the simplest rocking case, i.e. a freestanding rocking block. The suite of thirty, non-pulse, like ground motion records are used again. The ground motions are listed in Vamvatsikos and Fragiadakis, 2010 and are also adopted in Figure 5.4. Figure 5.5a presents the smooth fragility curves. The three limit-states are considered in the current results, i.e. θ/α = 0.15, 0.35, 1.00 (Psycharis et al., 2013b). Figure 5.5b presents the same results using as IM the PGV. In the following subsection the same plots are used for comparison purposes with a more complicated rocking system, a rocking colonnade.

5.3.2 Rocking colonnade

Figure 5.6 compares the response of a column with a colonnade of symmetric columns. For the freestanding column and for comparison purposes the rectangular block $2h \times 2b = 5.00m \times 0.75m$ is assumed. For the columns of the colonnade it is assumed again

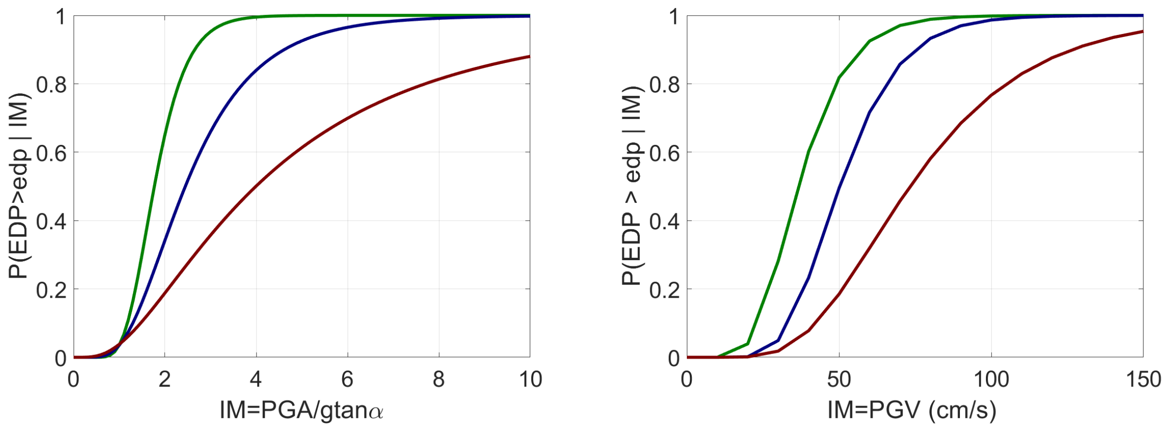

(a) (b)

FIGURE 5.5: Fragility curves of a rocking block: (a) $IM = PGA/gtan\alpha$ and (b) $IM = PGV$.

that $2h \times 2b = 5.00m \times 0.75m$ while quantity $\gamma = m_b/Nm_c$ is equal to one. The IMs are either $PGA/g \tan\alpha$ or PGV. It is clear that colonnades are more stable compared to the corresponding column dimensions. In both plots, the probability of exceedance of all IMs is larger for the freestanding column compared to that of the colonnade.

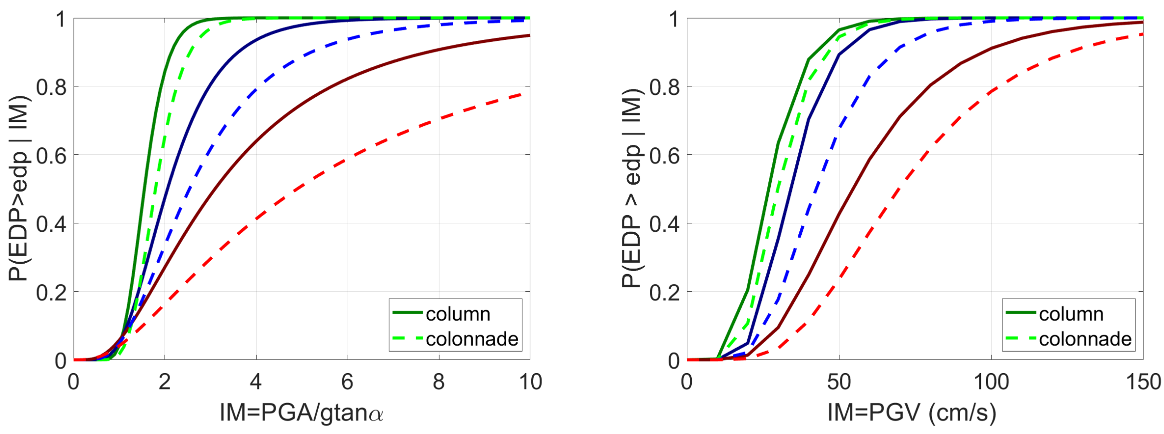

(a) (b)

FIGURE 5.6: Fragility curves of a column vs the corresponding colonnade with $\gamma = 1$: (a) $IM = PGA/gtan\alpha$ and (b) $IM = PGV$.

In order to adopt as IM the average spectral acceleration (S_a^{avg}), in Figure 5.7 the Fourier spectra of the records have been calculated. The spectra are used in order to decide the c_i values of Eq.5.1 which corresponds to the frequencies of interest. S_a^{avg} needs a careful handling in order the fragilities to be usable. In general, the lower period ordinates affect early damage, similar to the effect of peak ground acceleration to uplift, while longer periods have been found to be correlated to overturning. Based on Figure 5.7 the period range of interest is $T_1 = 0.5s$ to $T_N = 1.5s$ and is shown as a black thick line.

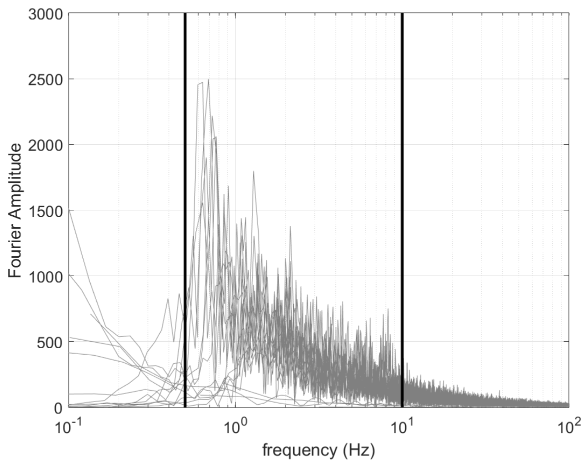

FIGURE 5.7: Fourier spectra of the rocking response of the colonnade adopted.

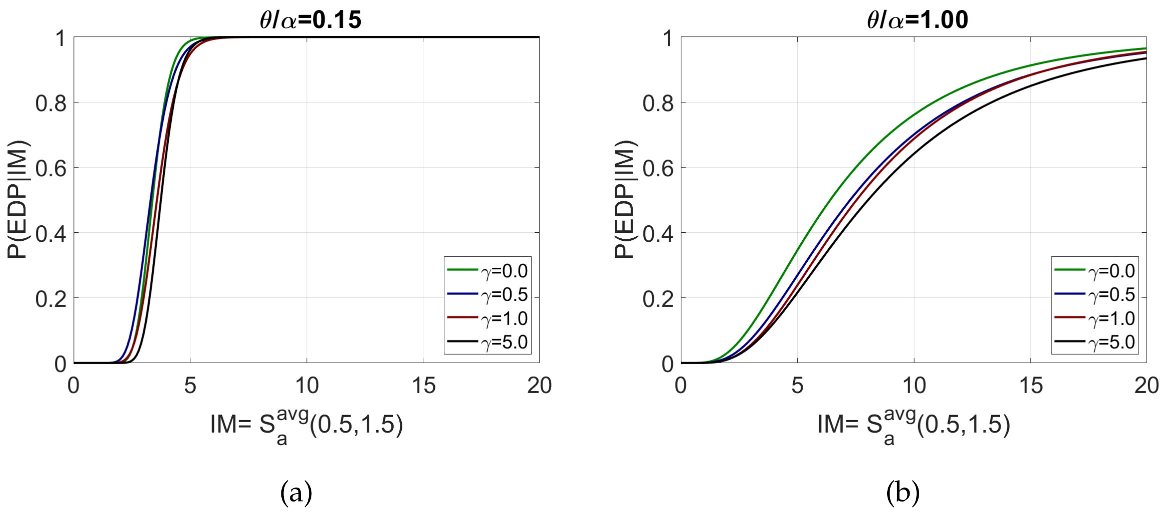

FIGURE 5.8: Fragility assessment for different values of the epistyle's weight (γ =0.0, 0.5, 1.0, 5.0) for: (a) $\theta/\alpha = 0.15$ and (b) $\theta/\alpha = 1.00$.

Figure 5.8 presents the smooth fragilities obtained using $IM = S_a^{avg}(0.5, 1.5)$ for different values of beam to column mass ratio γ. This investigation shows the effect of the epistyle's weight on the fragility of the colonnade. It is observed that the larger the γ values the more stable the rocking frame. It is clearly shown for the case of overturning fragility curves, i.e. $\theta/\alpha = 1.00$. However, the effect of γ can not be assumed straightforward or proportional, as it affects not only the equation of motion but also the coefficient of restitution.

In order to calculate the limit-state MAFs of the block, we adopt a hazard curve that corresponds to a site in the island of Crete, Greece (5.9). As discussed above, the

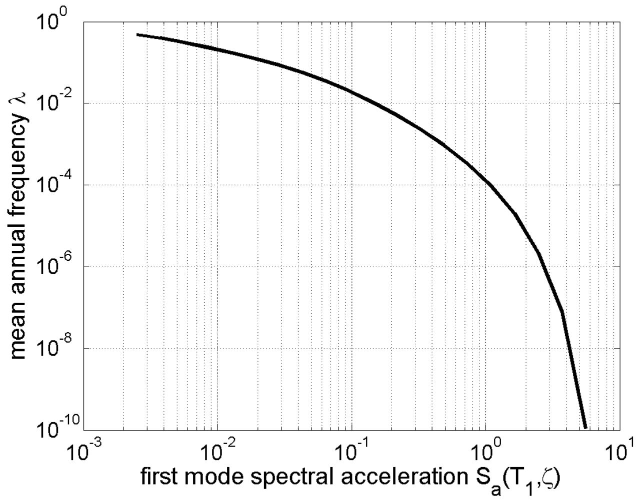

FIGURE 5.9: Hazard curve adopted for the risk assessment.

	$(\theta/\alpha \leq 0.15)$	$(\theta/\alpha \leq 0.35)$	$(\theta/\alpha \leq 1.0)$
$\gamma = 0.0$	434 years	552 years	801 years
$\gamma = 0.5$	399 years	642 years	1122 years
$\gamma = 1.0$	478 years	648 years	1327 years
$\gamma = 5.0$	549 years	739 years	1429 years

TABLE 5.1: Limit-state return periods for the colonnade.

limit-state MAFs are calculated using Equation 6.7. Table 6.2 presents the limit-state MAFs obtained for the colonnade and for different values of parameter γ.

5.3.3 Frame with columns of unequal height

For the fragility assessment, both cases consider that $2h_1 = 5.00m$, $2b_1 = 0.75m$ and the intensity measure adopted is the average spectral acceleration S_a^{avg}. Figure 5.10a considers that $2h_2 = 3.75m$, $2b_2 = 0.75m$, while in Figure 5.10b it is assumed that the second column's height is equal to the 95% of the first column's height, i.e. $2h_2 = 4.75m$, $2b_2 = 0.75m$. Both cases consider $m_b = m_{c1} + m_{c2}$. The Engineering Demand Parameter (EDP), as in all the previous plots, is the rotation over the slenderness of the columns, i.e. θ/α and the limits states follow the recommendations of Psycharis et al., 2013b.

It can be observed that the fragility curves are not affected considerably by the asymmetry. The difference in the initiation of rocking and the coefficient of restitution affect the response histories but considering the fragility assessment it can not be decided if the asymmetric frame is more or less stable. Further parametric investigation is proposed considering all the input parameters. However, the fragility assessment

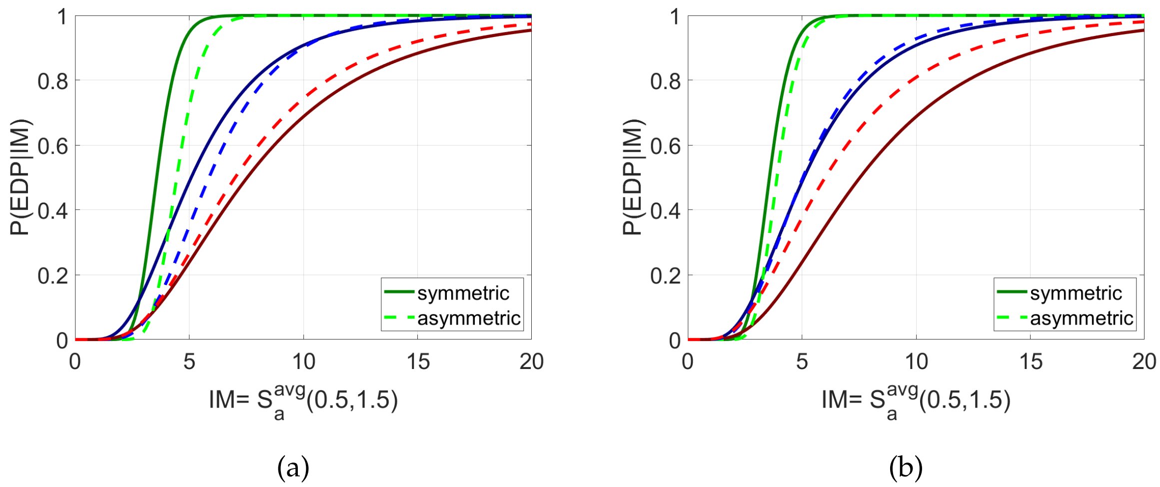

FIGURE 5.10: Comparison of the fragility curves of a symmetric and an asymmetric rocking frame using as $IM = S_a^{avg}$. Asymmetric frame's height is: (a) 75% and (b) 95% of the corresponding symmetric.

procedure presented, is an efficient approach for handling ancient structures while it can be extended in a straightforward manner to a variety number of more complicated rocking systems.

Chapter 6

Fragility and risk assessment of rocking building contents

In this chapter, the fragility and risk assessment of freestanding building contents is presented. The framework of handling the problem of rocking contents and the effect of the structure was examined. It has to be noted that, the notation was partially changed with respect to the original corresponding paper (Fragiadakis and Diamantopoulos, 2020) in order to be consistent with the notation used throughout the Thesis.

6.1 Introduction

6.1.1 Past research

Earthquake losses may be due to structural damage, damage of non-structural components (e.g. infills, piping system) and also due to the damage of the structure's contents. Recent guidelines (e.g. FEMA, 2012b, FEMA, 2012a, NIST, 2017) address the problem of the seismic response of building contents, acknowledging that the losses are comparable, or may exceed, those of structural damage. Non-structural damage can be due to damage of components attached, or anchored, to the hosting building, or due to damage on the freestanding inventory of the building. In the latter case, there is a huge variability of systems and configurations hampering the systematic study of the problem and the recommendation of generally-applicable guidelines. The risk assessment of building contents is a complicated task since the response of the contents depends also on the behaviour of the hosting structure. As a result, there may be cases where a strong earthquake does not overturn an object but strongly damages the structure, while more benign ground motions may leave the structure intact however causing losses due to damage on the building's contents. The current work focuses on the seismic performance, fragility and risk assessment of freestanding building contents. Some common examples of such contents are shown in Figure 6.1. Freestanding building contents are treated as rocking rigid blocks and are modelled using

Housner's theory (Housner, 1963). A specifically tailored version of the Incremental Dynamic Analysis (IDA) method is proposed in order to assess the structure and its contents considering that the structural collapse implies also collapse/overturning of the contents. A second point of interest is the derivation of fragility curves and the calculation of the Mean Annual Frequency (MAF) of the rocking building contents.

FIGURE 6.1: Examples of building contents (left to right: an artefact, a sculpture and a computer server).

Despite the significance of the problem at hand, there are relatively few past studies on the seismic response assessment of freestanding contents, especially compared to the case of anchored non-structural components and anchored building equipment. Recent research examines, for example, the seismic behaviour of artefacts (Spyrakos et al., 2016), or hospital equipment (DiSarno et al., 2015; Petrone et al., 2017). Spyrakos et al., 2016 proposed predictive models for artefacts assuming that they form systems of one, or two, rocking blocks, while DiSarno et al., 2015 performed shake table tests on hospital equipment. In this direction, Wittich and Hutchinson, 2017 and Wittich and Hutchinson, 2015 studied the seismic response of human-formed artefacts that are either standing on a pedestal (Wittich and Hutchinson, 2017) or are asymmetric (Wittich and Hutchinson, 2015). Both configurations are very common for freestanding building contents and therefore the numerical tools developed are quite useful for their seismic performance assessment.

One of the first studies that focus on the fragility of rocking systems, is the work of Purvance et al., 2008. The authors derived overturning fragilities for both symmetric and asymmetric freestanding blocks and they compared the overturning fragilities with shake table experiments. They also showed that objects with multiple rocking points are more fragile than predicted. Furthemore, Konstantinidis and Makris, 2009, studied the seismic response of laboratory equipment using analytical solutions and experimental results, while Konstantinidis and Nikfar, 2015 studied the sliding motion of stocky freestanding equipment and contents located at base-isolated buildings. Bakhtiary and Gardoni, 2016 presented a probability model that predicts the rotation demand of rocking bodies. Their fragility-assessment approach is based on identifying the approximate period and equivalent damping ratio for the rocking object. Dimitrakopoulos and Paraskeya, 2015 proposed dimensionless fragility curves for the rocking response of rectangular blocks under near-fault excitations of their base. Their work was the first that proposed dimensionless Intensity Measures (IMs) for rocking blocks, while Giouvanidis et al., 2017 discussed the fragility assessment of rocking frames. Petrone et al., 2017 focused on the efficiency of different intensity measures in predicting the damage states of the rigid block, while alternative intensity measures for rocking systems were also investigated in Purvance et al., 2008, Pappas et al., 2017, Kavvadias et al., 2017a and Kavvadias et al., 2017b. Psycharis et al., 2013a developed a fragility assessment framework for mutidrum ancient columns that consist of rigid marble pieces that are stacked one on top of the other. The work of Contento et al., 2019 studies the seismic response and the fragility of rocking objects that are paired with two different protective devices. The work uses a logistic regression model calibrated with a Bayesian approach in order to construct the fragility curves as function of the block properties.

In this Thesis a performance-based seismic fragility and risk assessment framework for freestanding building contents is presented. Contrary to previous works on the seismic fragility assessment of rocking contents, the proposed methodology discusses how the response of the hosting building and that of the contents are coupled and also the effect of different stories and different block geometries. In order to consistently study the effect of increasing seismic intensity in a performance-based setting, a modified version of the well-known Incremental Dynamic Analysis (IDA) method is presented. It is shown that the EDP that should "drive" the IDA simulations is that of the building rather than that of the contents and also that the collapse of the building should not be neglected. Moreover, the calculation of fragility and risk are discussed. Existing fragility assessment methodologists are adopted showing that the IM of the building should be adopted (instead of that of the contents), while a procedure that uses the total probability theorem in order to calculate the MAFs combining fragilities that were separately generated for the structure and for the contents is investigated. Overall it is shown that the problem is not as simple, as it may initially seem, and that various tools should be appropriately combined in order to accurate and efficiently calculate the risk of freestanding contents.

6.1.2 Building contents as rigid blocks

In order to study the seismic response of freestanding bodies to an earthquake ground motion, it is assumed that the bodies are orthogonal blocks. Following the pioneering work of Housner, 1963, the problem of rocking and overturning of freestanding blocks to earthquakes has been the subject of intense analytical and experimental research. Despite its apparent simplicity, the rocking problem has been proven difficult, since the blocks behave nonlinearly and also due to the occurrence of many impacts between the rocking bodies and their base. Previous studies have revealed the complex response, including certain counter-intuitive trends. Some important remarks are (Fragiadakis et al., 2016): (*i*) the stability of a block subjected to a specific ground motion does not depend monotonically on the size or the slenderness of the block, (*ii*) the overturning of a block under a certain ground motion does not necessarily imply overturning for an increase of the base excitation amplitude, (*iii*) the amplitude of the response does not always decrease as the coefficient of restitution increases. A planar model is adopted in this work. This is an often made approximation, which leads to unconservative results when applied to three-dimensional objects such as those shown in Figure 6.1. Nevertheless the two-dimensional, planar modelling adopted offers some simplicity and was found adequate for the purpose of this work.

The fundamentals of rocking block's theory have been summarized in the previous subsections. In is worth noting that following Figure 2.1, in the static case, when $\theta \geq \alpha$ the block will overturn since the self-weight becomes an overturning force instead of a restoring force. Under dynamic loading, this is not strictly true since there may be cases where the block does not overturn for θ/α values that slightly exceed one. Therefore, we often normalize the rotation with the slenderness angle in order to obtain the metric θ/α that provides an estimate of how close to overturning is the block. Moreover, when the block is at rest ($\theta = 0$), omitting the inertia term in Eq. 2.3, we find that it will start a rocking motion only if the ground acceleration $\ddot{u}_g$ exceeds a threshold value, i.e. when:

$$|\ddot{u}_g| \geq (b/h)g \Leftrightarrow |\ddot{u}_g| \geq g \tan\alpha \tag{6.1}$$

On the other hand, a body will slide if the seismic force $F_{eq} = m\ddot{u}_g$ exceeds the static friction:

$$F_{eq} \geq \mu_{st} W \Leftrightarrow |\ddot{u}_g| \geq \mu_{st} g \tag{6.2}$$

where μ_{st} is the static coefficient of friction, that typically receives values above 0.65. Therefore, the inequality of Eq. 6.2 implies that typically an acceleration above $0.65g$ is required for sliding to occur. Comparing Eq. 6.1 to Eq. 6.2, sliding will precede rocking only if $tan\alpha$ is less than μ_{st}. This is possible for small friction conditions, or for stocky blocks, i.e. for small μ_{st} or for large $tan\alpha$ values. Interestingly, when neither conditions of Eq. 6.1 or Eq. 6.2 are met, the body will remain at rest in its initial position. The equation of motion is solved numerically using standard Ordinary Differential Equation (ODE) solvers available in Matlab's (Matlab, 2016) library or considering the various alternative ways to model the seismic response of rocking systems which are discussed in Diamantopoulos and Fragiadakis, 2019. Considering the coefficient of friction, it typically receives values between $0.7 \div 1.0$.

6.2 Performance assessment

6.2.1 Definition of IMs and EDPs

The procedure followed for the seismic response assessment of freestanding building contents is shown schematically in Figure 6.5a. The building is subjected to an acceleration timehistory and the total acceleration response history of the storey of interest is stored. The stored storey acceleration response history is used as the input acceleration time history for the rigid block assessment. This, conceptually simple, cascading procedure requires two models, one for simulating the building and a second for simulating the freestanding contents. Moreover, after every building simulation the complete acceleration, or velocity, response history has to be stored for every storey. This workflow is used also for developing the fragility curves of the rocking objects of interest.

Seismic response assessment requires to define pertinent Intensity Measures (IM) and Engineering Demand Parameters (EDP) for both the structure and the contents. This step is also important for the fragility assessment. IMs represent seismic intensity, while the EDPs are used to measure the demand, or the "damage". In order to distinguish the quantities that refer to the "structure" and the "block', the superscripts "s" and "b" ' are used, respectively. Therefore, $EDP^{(s)}$ and $IM^{(s)}$ are the IM and the EDP of the structure, while $EDP^{(b)}$ and $IM^{(b)}$ refer to the rigid block. For a block at storey j, $IM^{(b)}$ will coincide with (or be derived from) the structure's $EDP_j^{(s)}$, or, simply, the peak floor acceleration of the storey is the peak ground acceleration for the rocking body. Therefore, the selection of $EDP_j^{(s)}$ and $IM^{(b)}$ should be consistent.

For moderate-period structures with no near-fault activity, an appropriate choice for the intensity measure of the building $IM^{(s)}$, is the 5%-damped, first-mode spectral acceleration, $S_a(T_1, 5\%)$. Moreover, the most common EDP for moment frames is the maximum interstorey drift. However, since our focus is on freestanding components, instead of the maximum interstorey drift, a consistent quantity should be chosen as the $EDP^{(s)}$, while the intensity measure $IM^{(s)}$ is always $S_a(T_1, 5\%)$, although other measures are also possible.

For a rocking block, the most intuitive IM choice is the peak ground acceleration (PGA), since it is the parameter that defines the maximum overturning moment, while according to Eqs. 6.1 and 6.2 the PGA defines whether rocking, sliding or none of the two will occur. Although it is not necessary, the PGA is normalized with $g\tan\alpha$ and thus the block's IM is $IM^{(b)} = PGA/g\tan\alpha$, where $IM^{(b)} \leq 1$ implies that the block does not start rocking. Furthermore, past research (Ishiyama, 1982b; Dimitrakopoulos and Giouvanidis, 2015b) has shown that the PGV is also an important response parameter that provides a good correlation between seismic demand and block overturning. For simplicity, we choose not to normalize the PGV, but researchers (e.g. Dimitrakopoulos and Paraskeya, 2015) have also proposed the normalized quantity $pPGV/g\tan\alpha$ as an IM suitable for rocking blocks. Our results have shown that the PGV (or PFV) performs well as an IM and hence we have chosen the simplest IM possible. Therefore, the $IM^{(b)}$ for a rocking block at storey j considered, is either the normalized peak floor acceleration PFA_j, or the peak floor velocity PFV_j; the parameter chosen will be also used as the demand parameter of the building $EDP_j^{(s)}$. The most suitable engineering demand parameter $EDP^{(b)}$ for the rocking block is the rotation angle θ normalized by slenderness angle α, i.e. $EDP^{(b)} = |\theta|/\alpha$. The EDPs and IMs for the structure and the freestanding contents are summarized in Table 6.1.

TABLE 6.1: Definition of IMs and EDPs.

	IM	**EDP**
building	$S_a(T_1, 5\%)$	drift, PFA_j, PFV_j
block	PGA/g tanα, PGV	θ / α
block at storey j	PFA/g tanα, PFV	θ / α

In order to assess a system's capacity, meaningful performance objectives related with the system's modes of failure or damage have to be identified. For rocking systems, overturning is the primary limit-state of interest, while rocking initiation is also of interest but it can be easily identified from the PGA. Depending on the freestanding component, (e.g. its purpose, its material, etc), "limited" damage can be identified for normalized rotation values $\theta/\alpha \approx 0.1 \div 0.3$, "moderate" damage for $\theta/\alpha \approx 0.3 \div 0.5$ and "overturning" is assumed for $\theta/\alpha \geq 1$. Recommendations of limit-state thresholds for rocking bodies can be found in various publications, e.g. Dimitrakopoulos and DeJong, 2012a, Psycharis et al., 2013a and Kavvadias et al., 2017b. In practice, these limits vary considerably and it is not possible to decide threshold values that are generally applicable. For example, for sensitive mechanical equipment a rotation $\theta/\alpha \geq 0.1$ may result to permanent damage and thus in terms of loss the outcome will be the same with overturning. Another important aspect is the geometry of the block. Slender blocks start rocking for smaller acceleration values, while stocky blocks require higher acceleration values to start rocking and are more stable.

6.2.2 Fragility assessment

Past research on fragility assessment focuses on the risk assessment of the structure itself (e.g. Fragiadakis et al., 2015), while the contents are examined separately and, usually, neglecting the effect of the hosting structure. Independent, and often generic, fragility curves for various building contents can be found in guidelines (e.g. FEMA, 2012b) and the literature. Such fragility curves are empirical and are targeted to specific component types (e.g. cladding panels, masonry parapets). The direct fragility calculation that is here proposed through simulations allows to consider additional sources of uncertainty (e.g. related to the shape of the object, its mass distribution) and hence is preferable. The fragility function is the conditional limit-state exceedance probability, it has been discussed in the previous subsection and is given by Eq. 5.2. The fragility calculation of the building and of the contents are discussed separately following the framework of Chapter 5.

Structure: There will be simulations that the building collapses (denoted as "C") and simulations where no collapse occurs (denoted as "NC"). Making this separation and dropping the conditioning term in order to simplify the notation, i.e.: $P(EDP) = P(EDP > edp|IM)$, the probability of Eq. 5.2 is calculated using the total probability theorem (TPT) as follows:

$$\begin{aligned} F_R^{(s)} &= P(EDP^{(s)}|NC)P_{NC} + P(EDP^{(s)}|C)P_C \Leftrightarrow \\ F_R^{(s)} &= P(EDP^{(s)}|NC)(1 - P_C) + P_C \end{aligned} \tag{6.3}$$

where $P(EDP > edp^{(s)}|C)$ is equal to 1 since the inequality is always satisfied and $P_{NC} = 1 - P_C$.

Rocking body: When an object is subjected to a seismic ground motion there are three possible types of response: (*i*) the object may not rock and remain at rest, (*ii*) it may rock, or (*iii*) it may overturn. Using the total probability theorem for the block, the fragility function becomes:

$$F_R^{(b)} = P(EDP^{(b)}|NoRock)P_{NoRock} + P(EDP^{(b)}|Rocking)P_{Rocking} + P(EDP^{(b)}|Ovtn)P_{Ovtn} \tag{6.4}$$

where $P(EDP^{(b)}|NoRock)$, $P(EDP^{(b)}|Rocking)$ and $P(EDP^{(b)}|Ovtn)$ are the probabilities that $EDP^{(b)} = \theta/\alpha$ exceeds a threshold value $edp^{(b)}$ and P_{NoRock}, $P_{Rocking}$ and P_{Ovtn} are the corresponding probabilities of no rocking, rocking and overturning, respectively. Blocks that will not rock, will not exceed any $edp^{(b)}$ value and consequently $P(EDP|NoRock) = 0$, while the overturning blocks always exceed the limit-state threshold and thus $P(EDP|Ovtn) = 1$. The conditional limit-state probability (fragility) is further simplified to:

$$F_R^{(b)} = P(EDP^{(b)} \geq edp|Rocking)(1 - P_{Ovtn} - P_{NoRock}) + P_{Ovtn} \tag{6.5}$$

The calculation of Eq. 6.5 is discussed in the sections that follow. A fundamental assumption of our derivation is that *the simulations that collapse the building also overturn/collapse the freestanding contents*.

Seismic risk can be expressed as the mean annual frequency (MAF) of a limit-state being exceeded. Adopting PEER's formula, the limit-state MAF for the structure and for a rigid block can be calculated with the aid of the expressions below:

$$\lambda_{EDP}^{(s)} = \int_{IM^{(s)}} P(EDP^{(s)}|IM^{(s)})\ |d\lambda_{IM^{(s)}}| \tag{6.6}$$

$$\lambda_{EDP}^{(b)} = \int_{IM^{(b)}} P(EDP^{(b)}|IM^{(b)})\ |d\lambda_{IM^{(b)}}| \tag{6.7}$$

where $\lambda_{EDP}^{(s)}$, $\lambda_{EDP}^{(b)}$ is the mean annual frequency of the engineering demand parameter ($EDP^{(s)}$ or $EDP^{(b)}$) exceeding threshold level and $d\lambda_{IM}^{(s)}$, $d\lambda_{IM}^{(b)}$ is the slope of the seismic hazard curve. The limit-state MAFs are obtained convolving the site hazard curve, expressed as function of the IM, with the fragility curve obtained with respect to any of the EDPs of interest. For the structure, the IM of interest is always available, e.g. spectral acceleration $S_a(T_1, 5\%)$, but for the block this information is available only at the ground floor. For assets located at a storey, the calculation of $d\lambda_{IM}^{(b)}$ has no meaning and thus their fragility should be calculated as function of $IM^{(s)}$ instead of $IM^{(b)}$:

$$\lambda_{EDP}^{(b)} = \int_{IM^{(s)}} P(EDP^{(b)}|IM^{(s)})\ |d\lambda_{IM}| \tag{6.8}$$

Conditioning the block's fragility to $IM^{(s)}$, i.e. using Eq. 6.8 instead of Eq. 6.7, is also conceptually preferable since the MAF is directly calculated from the site's hazard. Note that we have dropped the superscript "s" from $d\lambda_{IM^{(s)}}$, since $d\lambda_{IM}$ will refer to the site.

A simplified and more generic methodology for the seismic risk of structure's contents is possible if we apply the total probability theorem (TPT), using the block's intensity measure $IM^{(b)}$ as an intermediate variable. This allows to expand Eq. 6.8

and obtain the MAF using the expression:

$$\lambda_{EDP}^{(b)} = \int_{IM^{(s)}} \int_{IM^{(b)}} P(EDP^{(b)}|IM^{(b)}) \, dP(IM^{(b)}|IM^{(s)}) \, |d\lambda_{IM}| \tag{6.9}$$

where $P(IM^{(b)}|IM^{(s)}) = P(EDP^{(s)}|IM^{(s)})$ is the building's fragility curve. Eq. 6.9 can be used in order to calculate separately the fragilities using Eqs. 6.6 and 6.7, thus bypassing the need for performing building simulations and storing the response acceleration histories for the stories of interest. The use of this formula does not implement the interaction between the building and the contents and thus is appealing but not always suitable.

6.3 Handling of the structure and the contents

Below we first discuss how the multiple stripe method is applied for the cascading problem at hand. We first examine the structure since the ground motions are applied at the base of the building and in the subsection that follows we discuss how the fragilities of the freestanding contents are obtained from the floor response histories.

6.3.1 Hosting structure

Following the discussion of Chapter 5 every IDA curve is plotted in the EDP-IM plane (Fig. 6.6) for the structure considered. The building adopted is discussed a few lines below, in the numerical results subsection. The median curve (50% percentile) provides an estimate of the expected value and the fractile curves can be used to measure the dispersion (Vamvatsikos and Fragiadakis, 2010). The IDA capacity curve of Figure 6.6 is the most common form of IDA where $EDP^{(s)}$ is the maximum interstorey drift ratio. However, a different EDP has to be adopted for studying building contents which leads to the representation of Figure 6.2, where the $EDP^{(s)}$ is either the normalised peak floor acceleration (PFA), or the peak floor velocity (PFV). The summarized EDP-IM plots (Figure 6.2a or b) allow to directly calculate $P(EDP_j^{(s)}|NC)$ and P_C (Eq. 6.3) for every IM stripe. If the $EDP_j^{(s)}$ values are lognormally distributed, the buildings fragility for the j^{th} storey is calculated as follows:

$$P(EDP^{(s)} \geq edp^{(s)}) = 1 - P(EDP^{(s)} < edp^{(s)}) = 1 - \Phi\left(\frac{edp^{(s)} - \mu_{logEDP}}{\sigma_{logEDP}}\right) \Rightarrow$$

$$P(EDP^{(s)} \geq edp^{(s)}) = \Phi\left(\frac{\mu_{logEDP} - edp^{(s)}}{\sigma_{logEDP}}\right) \tag{6.10}$$

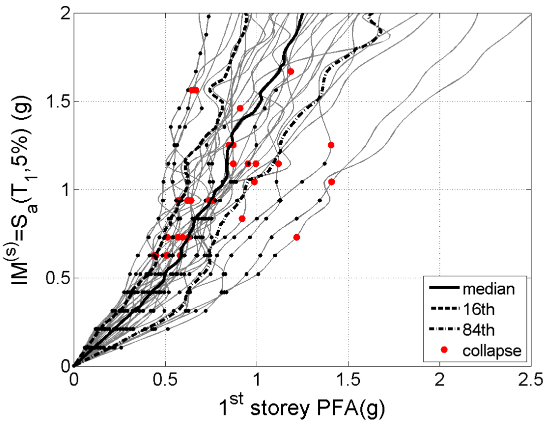

(a)

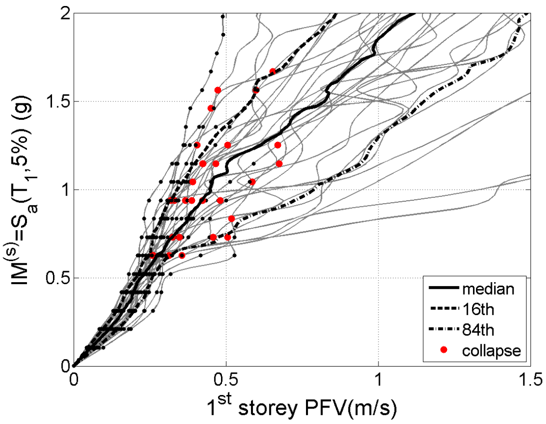

(b)

FIGURE 6.2: Storey capacity curves for the four-storey RC building considered, using as EDP: (a) the Peak Floor Acceleration (PFA), and (b) the Peak Floor Velocity (PFV).

where μ_{logEDP} and σ_{logEDP} are the mean and the standard deviation of the logarithm of the demand, always conditional on the $IM^{(s)}$. The mean μ_{logEDP} and the dispersion σ_{logEDP} of the logarithms can be also calculated as (Vamvatsikos and Fragiadakis, 2010):

$$\begin{aligned} \mu_{logEDP} &\approx log(EDP_{50\%}) \\ \sigma_{logEDP} &\approx \frac{1}{2}(log(EDP_{84\%}) - log(EDP_{16\%})) \end{aligned} \tag{6.11}$$

where $EDP_{x\%}$ is the $x\%$ percentile values of EDP-demand. Regardless the IM, the fragility of the building should be obtained combing Eq. 6.10 with Eq. 6.3:

$$F_R^{(s)} = \Phi\left(\frac{\mu_{logEDP} - edp^{(s)}}{\sigma_{logEDP}}\right)(1 - P_C) + P_C \tag{6.12}$$

where P_C is the percentage of collapsed simulations. Obviously different fragilities will be obtained depending on the EDP of interest. Figure 6.2 and Eq. 6.10 allow for two important observations:

- The calculation of Eq. 6.10 using Eqs. 6.11, is not efficient when the drift is used as the EDP. This is understood looking at Figure 6.6 and Eq. 6.11, where it is evident that the median (or the 16, 84% fractile) curves, conditional on the IM, cannot be calculated above the IM level where more than 50% (or the 16, 84% fractile, respectively) of the single-record IDAs become horizontal. On the contrary, when the PFA, or the PFV, is adopted, the median and the 16, 84%

fractiles can be easily calculated due to the practically monotonic increase of the IDA curves.

- Although the drift is not the primary EDP of interest, the IDAs should be driven by the drift, or any other EDP that is related with the structural damage. This is because when structural collapse occurs, the freestanding contents are also considered collapsed (overturned). In the single-record capacity curves of Figure 6.6, the solid dots indicate when the building collapses, i.e. either when the analysis structurally fails, or when the maximum drift threshold is exceeded. The dots are transferred in Figure 6.2 indicating the occurrence of structural failure. This is done merely for visualization purposes since all simulations after the dots are assumed collapsed. This visualization shows that even for relatively low PFA, or PFV values, structural damage may have already occurred.

A very efficient alternative for calculating the fragilities using IDA, is to fit the CDF (cumulative distribution function) of a lognormal distribution on the striped EDP-IM data as discussed by Baker, 2015. The fragility function can be simply seen as the lognormal CDF:

$$F_R^{(s)} = P(EDP^{(s)} \geq edp) = \Phi\left(\frac{log(EDP^{(s)}/\theta_a)}{\beta_a}\right) \tag{6.13}$$

where θ_a and β_a are the parameters that we need to determine. θ_a is the "median" of the fragility function, i.e. the IM value corresponding to limit-state probability equal to 0.5 and β_a is the dispersion (standard deviation of log(IM)). The values of θ_a and β_a are obtained from the whole data using a Maximum Likelihood Estimation (MLE) approach (Baker, 2015) presented in Chapter 5.

6.3.2 Rocking contents

Figure 6.3 shows the EDP-IM plots of a freestanding block with $R = 1.0m$ and $\alpha = 0.2$. The hosting structure was subjected to the IDA simulations of Figs. 6.6 and 6.3 and then the simulations (shown as black dots in Figure 6.6) are transferred to the $EDP^{(b)} - IM^{(b)}$ (Figure 6.3a), or the $EDP^{(b)} - IM^{(s)}$ plane (Figure 6.3b). In both plots the collapsed simulations appear as dots just right to the vertical line at $EDP^{(b)} = 1$. The dots below the horizontal line at $IM^{(b)} = 1$ (Figure 6.3a) correspond to the no rocking simulations. As already discussed in Section 6.2.2, the $EDP^{(b)} - IM^{(b)}$ representation is the natural EDP-IM choice, but is not the easiest choice when it comes to the calculation of MAF $\lambda_{EDP}^{(b)}$. Moreover, as shown in Figure 6.3a, the data in the

$EDP^{(b)} - IM^{(b)}$ form a cloud, while if they are plotted in the $EDP^{(b)} - IM^{(s)}$ place they are already conditional on the $IM^{(s)}$.

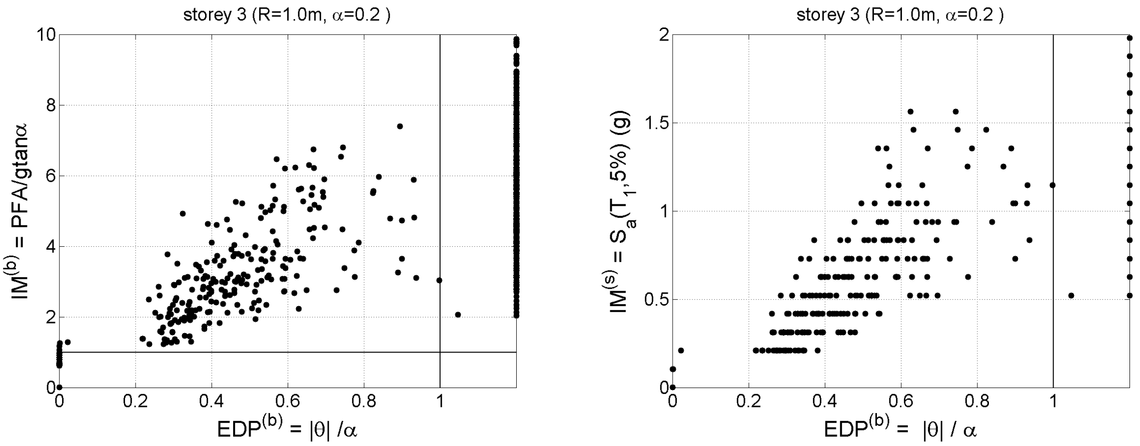

(a) (b)

FIGURE 6.3: Seismic response of a freestanding building object with $R = 1.0m$ and $\alpha = 0.2$: (a) plotting $EDP^{(b)} - IM^{(b)}$ results to cloud data, (b) plotting $EDP^{(b)} - IM^{(s)}$ results to data in stripes.

Both EDP-IM representations allow to calculate the fragility of the blocks, but with respect to a different IM. Defining the fragility conditional on the IM of the structure, i.e. $F_R^{(b)} = P(EDP^{(b)}|IM^{(s)})$ can be used for directly calculating the MAF using Eq. 6.8. On the other hand, the intuitive definition $F_R^{(b)} = P(EDP^{(b)}|IM^{(b)})$ provides the storey fragilities with respect to the block's IM and always for the storey of interest. Another major difference is that when $IM^{(b)}$ is adopted, the EDP-IM data appear as a "cloud" (Figure 6.3a), while when $IM^{(s)}$ is adopted instead, they appear in stripes (Figure 6.3b). The IDA method can be directly applied to the striped data, while the cloud data require a different post-processing in order to derive the fragility curve. In the case of Figure 6.3b, the data form stripes and hence they can be post processed as was already shown in Section 6.3.1 for the building:

$$F_R^{(b)} = \Phi\left(\frac{\mu_{logEDPb} - edp^{(b)}}{\sigma_{logEDPb}}\right)(1 - P_{Ovtn} - P_{NoRock}) + P_{Ovtn} \qquad (6.14)$$

Since the $F_R^{(b)}$ is calculated at every stripe P_{NoRock}, P_{Ovtn} are simply obtained as the percentage of simulations where no-rocking and overturning was observed, respectively. The fitting of Eq.6.13 is also very efficient in the case of the freestanding contents. If the data are not stripped, as in Figure 6.3a, the cloud analysis method should be used instead.

6.3.3 Cloud analysis

Cloud analysis is a common method when the data are scattered in the EDP-IM plane (e.g. Figure 6.3a). This occurs when the ground motions are left unscaled, or when they have all been scaled with the same factor. Cloud analysis is shown schematically in Figure 5.3, where a least-squares straight line is fitted on the $log(EDP^{(b)})$ - $log(IM^{(b)})$ data. The linear fit provides the mean of the logarithms (μ_{logEDP}) and a single constant value for the dispersion σ_{logEDP}. Knowing μ_{logEDP} and σ_{logEDP}, it is possible to calculate the fragility of the rocking simulations using Eq. 6.14. This requires the knowledge of the no-rocking P_{NoRock} and overturning P_{Ovtn} probabilities over the whole IM range. These probabilities are calculated using a logistic regression model (logit) which yields a probability estimate that is function of the $IM^{(b)}$ (Jalayer et al., 2017). Therefore, for the overturning case:

$$P_{Ovtn} = \frac{1}{1 + e^{-(b_1 + b_2 log(IM^{(b)}))}} \tag{6.15}$$

where the constants b_1, b_2 are the parameters of the logistic regression model, obtained with binomial-based, generalized linear model (GLM) regression.

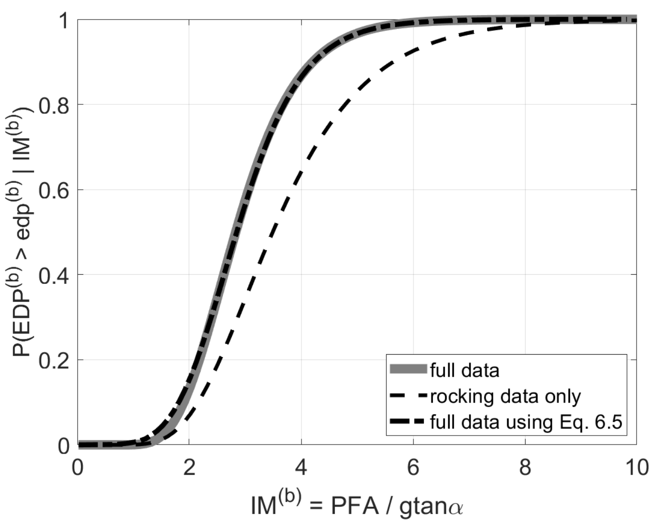

FIGURE 6.4: Cloud analysis: Derivation of the fragility curves using the cloud method (Eq. 6.13) on the whole set of data, i.e. including rocking, overturning and no rocking simulations. If Eq.6.13 is applied only on the rocking data, it is necessary to add the overturning and no-rocking curves obtained with Eq. 6.5 ($R = 1.0m$, $\alpha = 0.2$, θ/α=0.5, 3^{rd} storey).

A third option for post-processing the cloud data is the "running mean" method (e.g. Psycharis et al., 2013a and Zentner et al., 2017). The method allows to obtain stripes conditional on the IM. The response data are plotted in EDP-IM ordinates and the conditional probabilities are calculated dividing the IM axis into stripes. If IM_m is the central IM value of the stripe, the conditional probability $P(EDP \geq edp|IM_m)$ can be calculated according to Eq. 6.14 using the response data that are found within the stripe. Thus, the mean μ_{logEDP} and the dispersion σ_{logEDP} are obtained from the stripe data, and $P(EDP \geq edp|IM_m)$ is approximated with Eq. 6.14 resulting to a procedure that is equivalent to that of multiple-stripe analysis.

The methods presented above have several limitations especially related to the fitting of the fragilities in the tails of the distribution. In the case of the pointwise fragility of Eq. 6.12 a high number of simulation is required to properly assess the correct values of the median and percentiles that are used in the formulation and convergence analysis may be needed. Furthermore, in the case of the fragility presented in Eq. 6.13, which is obtained fitting a probit model, the behavior of the tail is constrained by the assumption of lognormal distribution. Nevertheless, various other possible fragility calculation methods could have been adopted for both stripped and cloud data. For example, Lallemant et al., 2015 and Zentner et al., 2017 discuss possible alternative approaches that could be applied for both the structure and the block. Moreover, the Bayesian approach (e.g. Singhal and Kiremidjian, 1998 and Jalayer et al., 2017) can be also adopted. A Bayesian approach will allow to easily update the parameters of the fragilities when more simulations become available which would be very useful for simulation-based curves.

6.4 Numerical Results

6.4.1 Example of four-storey reinforced concrete building adopted

The case-study building adopted is the four storey RC building shown in Figure 6.5a. The building has been designed for a site in Greece following the Greek seismic code which results to designs close to those of Eurocode 2 and 8, assuming Ductility Class High (DCH). This planar building should be considered as a simplification, since the reality is more complex, i.e. the model omits the bidirectional effect of the earthquake, the torsional coupling and the direction of the earthquake. The columns of the first two storeys have a rectangular section of $40cm$ and those of upper two stories of $35cm$. The cross section of the beams is $30 \times 60cm$ for all stories apart from the last where a $30 \times 50cm$ cross-section has been assumed instead. The concrete and steel quality were assumed C20/25 and B500C, respectively. The mass of every storey is 50, 50, 40 and 40 Mgr (first to last) and the first two periods are $T_1 = 0.60sec$ and $T_2 = 0.24sec$. Every storey has the force-displacement ($F - \delta$) relationship shown in Figure 6.5b, while the elastic stiffness k_j of the j^{th} storey was calculated according to the formula (Chopra, 1995):

$$k_j = \frac{\sum 12EI_{c_j}}{h_j^3}\frac{12\rho_j+1}{12\rho_j+4} \tag{6.16}$$

where $S_b = \sum EI_b/L_b$, $S_c = \sum EI_c/L_c$, $\rho_j = S_b/S_c$. L_b, L_c are the lengths of the beams and the columns of the storey considered, respectively. The formula assumes that there is a shear building with beams that have finite stiffness. The stiffness values of each storey were obtained as follows: $k_1 = 78612kN/m$, $k_2 = 94459kN/m$, $k_3 = 59370kN/m$ and $k_4 = 55257kN/m$. The storey stiffnesses were subsequently reduced by 50% in order to consider the effective stiffness according to EC8. Furthermore, section analysis was performed in order to obtain the moment capacities of the columns. The storey yield strengths F_{y_j} were found equal to: $F_{y,1} = 450kN$, $F_{y,2} = 420kN$, $F_{y,3} = 360kN$ and $F_{y,4} = 240kN$. The remaining parameters of the storey capacity curves are shown in Figure 6.5b. More specifically, the capping ductility was set equal to 5, the ultimate ductility equal to 12, and the post-capping slope was assumed equal to -28%. The building's model was implemented in OpenSees (Mazzoni et al., 2006) and the cyclic degradation follows the modified Ibarra-Medina-Krawinkler deterioration model with bilinear hysteretic response (Bilin material in OpenSees (Mazzoni et al., 2006)). The total mass is 180Mgr and the building yields approximately at a normalized base shear equal to $F_b/W = 0.26$, while the roof drift at yield is 0.33%.

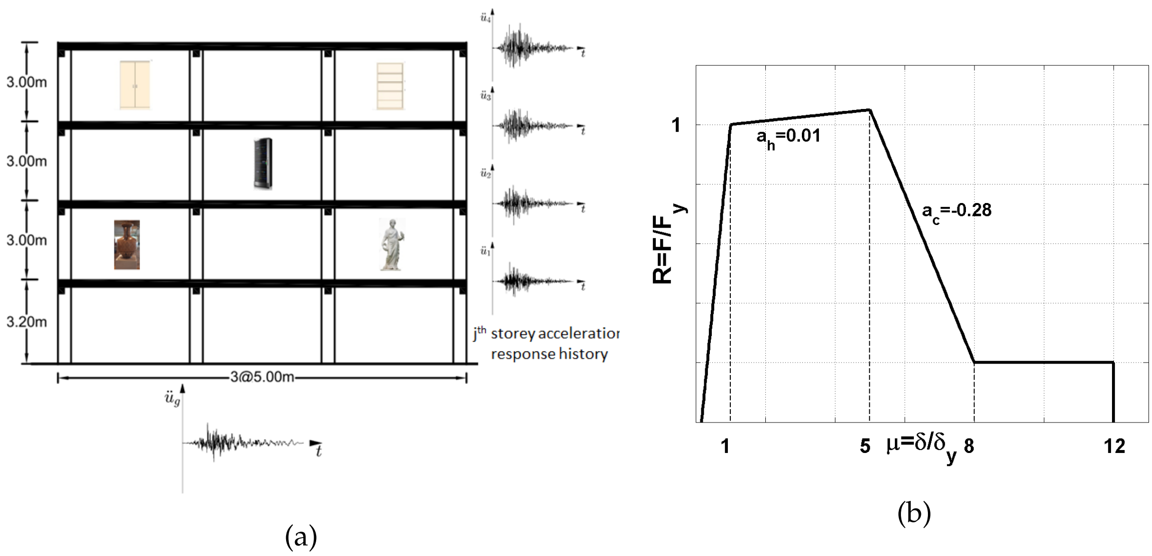

FIGURE 6.5: (a) The four-storey RC building considered, (b) Storey force-displacement ($F-\delta$) relationship with in-cycle degradation.

The building's capacity curve (Figure 6.6) is obtained with the aid of the IDA method (Incremental Dynamic Analysis). IDA was performed using a suite of thirty

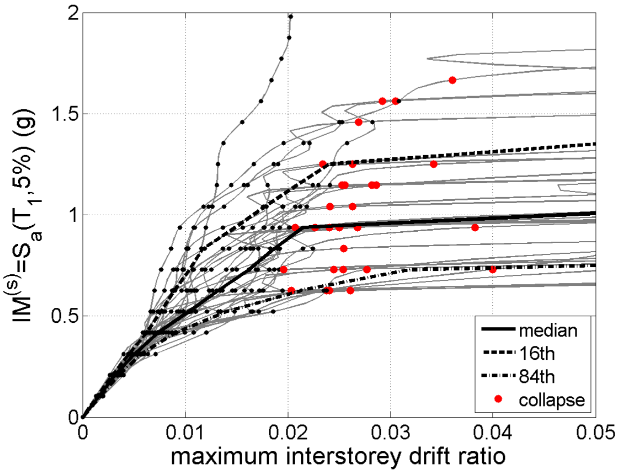

FIGURE 6.6: IDA capacity curve, i.e. plot of the maximum interstorey drift ratio vs the 5%-damped, first mode spectral acceleration, $IM^{(s)} = S_a(T_1, 5\%)$. The red large dots indicate simulations where first collapse occurs, beyond this point the single-record curve is assumed that has reached collapse.

non-pulse like ground motion records representing a scenario earthquake. The properties of the ground motions can be found in elsewhere (Vamvatsikos and Fragiadakis, 2010), where the same records were adopted. These ground motions belong to a bin of relatively large magnitudes of 6.5–6.9 and moderate distances, all recorded on firm soil and bearing no marks of directivity. The gray lines correspond to the 30 single-record IDA curves, the black solid line is the median IDA curve, while the black dashed lines show the 16^{th} and 84^{th} percentile capacities, respectively. According to Figure 6.6, the median capacity of the structure is approximately $S_a(T_1, 5\%) = 1g$. The median capacity is calculated as the median of the maximum drift demands over time (in absolute values) of every ground motion. In the IDA plot of Figure 6.6, the IM adopted is the 5%-damped, first mode spectral acceleration, i.e. $S_a(T_1, 5\%)$ and the $EDP^{(s)}$ is the maximum interstorey drift ratio. This is the most common IM choice, typically used for assessing the capacity of a structure and thus differs from the IM adopted in the rest of the thesis.

6.4.2 Symmetric building contents

Figure 6.7 shows the mean acceleration spectra at $S_a(T_1, 5\%)$= 0.4g and 1.0g. According to the capacity curve of Figure 6.6, the first $S_a(T_1, 5\%)$ value corresponds to elastic behaviour of the building, while for $S_a(T_1, 5\%)$= 1.0g the building is inelastic. The ground spectra, indicated as *ground*, refer to the mean acceleration spectra of the originally recorded timehistories scaled so that all records have the same $S_a(T_1, 5\%)$. The spectra at the j^{th} storey refer to the acceleration response histories of the corresponding storey. The spectra of the "ground" records have a different shape than those measured at each storey, while the spectra of the storey response histories have all a similar shape but different amplification. The similar shape of the storey spectra is possible due the uniform distribution of mass, stiffness and strength along the height of the structure. When the building is elastic (Figure 6.7a) all storey spectra are amplified at $T_1 = 0.6s$ and $T_2 = 0.24s$, i.e. the first and the second eigenmodes of the structure. The resonance shows that the building strongly filters the ground motions, while the amplification depends on the storey of interest. In general, the maximum amplification is expected for the upper stories, which is also here verified. For the inelastic case (Figure 6.7b) at $S_a(T_1, 5\%)$=1.0g, the amplification spans all period values between T_2 and T_1. Another interesting observation is that the building beneficiary filters down seismic accelerations at periods beyond 1sec regardless of the $S_a(T_1, 5\%)$ level. Similar conclusions are offered by the 5%-damped velocity spectra, but the amplification at the first and the second mode is stronger and more clear compared to the acceleration spectrum. Also, the ground velocity spectrum exceeds the storey spectra at slightly longer periods, at 1.5s instead of 1.2s.

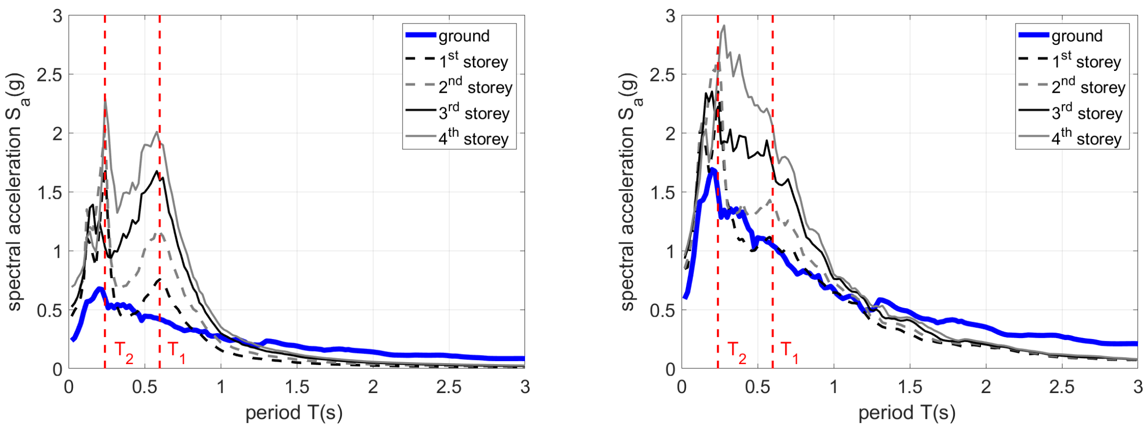

(a) (b)

FIGURE 6.7: 5%-damped acceleration spectra $S_a(T, 5\%)$: (a) $IM^{(s)} = 0.4g$, and (b) $IM^{(s)} = 1.0g$.

Figure 6.9a shows the mean storey PFAs, normalized with the peak ground acceleration (PGA). As shown in the acceleration and velocity spectra of Figures 6.7 and 6.8, the floor demands increase monotonically as the intensity increases, while the maximum demand appears always at the top storey. In Figure 6.9a, the PFAs have been normalized in order to allow understanding the propagation of PGA along the height of the building. For small values of the IM, the first storey has the smallest values of PFA/PGA which is equal to 2, as opposed to the top storey where the ratio is around

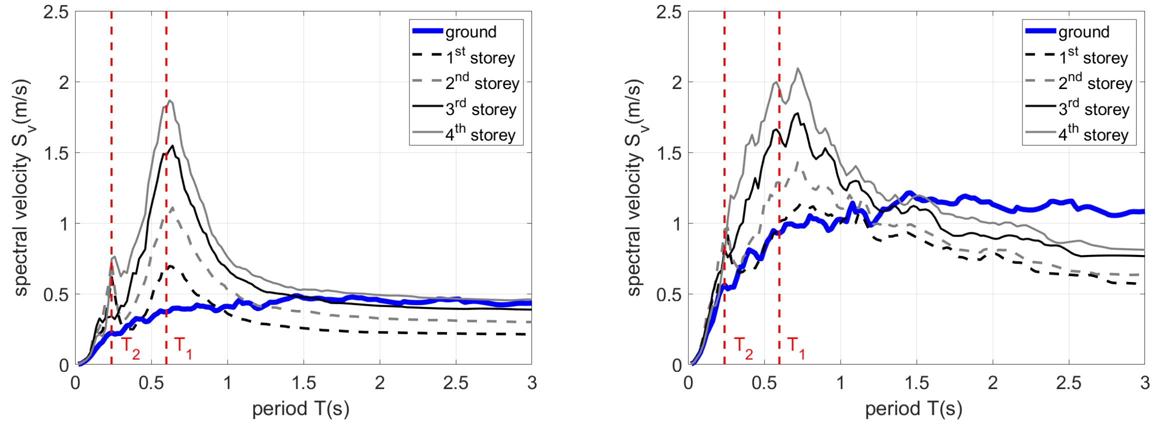

(a) (b)

FIGURE 6.8: 5%-damped velocity spectra $S_v(T, 5\%)$: (a) $IM^{(s)} = 0.4g$, and (b) $IM^{(s)} = 1.0g$.

3.4. However, as the IM increases, the PFA/PGA ratio tends to one for all stories of the building. Furthermore, Figure 6.9b shows the structure's fragility curves using as EDP the PFA of the 3^{rd} storey. Three threshold values were assumed for the PFAs, i.e.: $edp^{(s)}$ = 0.50, 0.70 and 0.90g. The structure's fragilities were obtained using the IM-stripes extracted from the IDA curves of Figure 6.2a and with the MLE fitting. In the former case the curves are monotonic but not smooth, as in the latter case where the fragility is obtained as the CDF of Eq. 6.13. As it is possible to observe from Figure 6.9b when the two kinds of fragilities are compared, considerable difference may be seen at the tails.

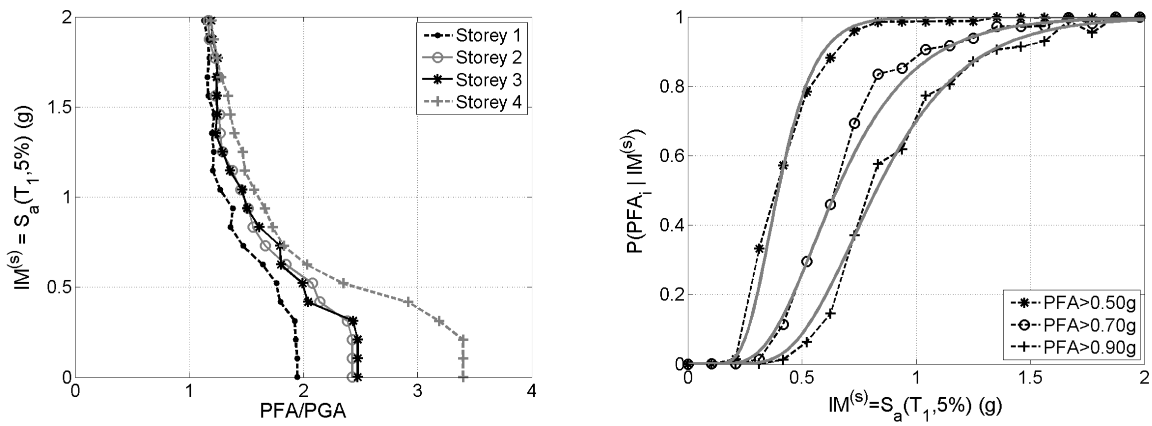

(a) (b)

FIGURE 6.9: (a) Mean storey PFA/PGA demand capacities as function of $S_a(T_1, 5\%)$, and (b) Fragility curves of the 3^{rd} storey assuming $IM^{(s)}$ = PFA. The smooth curves correspond to the fitting of Eq. 6.13.

The acceleration and the velocity response spectra of Figures 6.7 and 6.8 allow to understand how the structure filters the record, i.e. they show the modes that are amplified and those that are filtered out. However, rocking structures do not have modes of vibration in the classical sense, i.e. like an elastically deforming body. For this reason, Figure 6.10 shows the mean rotation demand for two rigid blocks with the same size parameter $R = 1m$ and varying slenderness angle α. A smaller slenderness α value implies a more slender block, hence the block is more sensitive to overturning and keen to larger rotations. Having set overturning simulations to $\theta/\alpha = 1$, very interesting findings are offered by Figure 6.10. At $S_a(T_1, 5\%)$=0.4g (Figure 6.10), the mean rotations of the scaled ground motions are very close to that of the top storey, while the demand is considerably smaller at lower stories. When the building is inelastic ($S_a(T_1, 5\%)$=1.0g, Figure 6.10b), the blocks that are subjected to the storey response histories have smaller rotation demand compared to the "ground" records. Therefore, regardless of the $S_a(T_1, 5\%)$ level, the building alters the frequency content of the ground motions reducing the fragility of the block for any slenderness angle α.

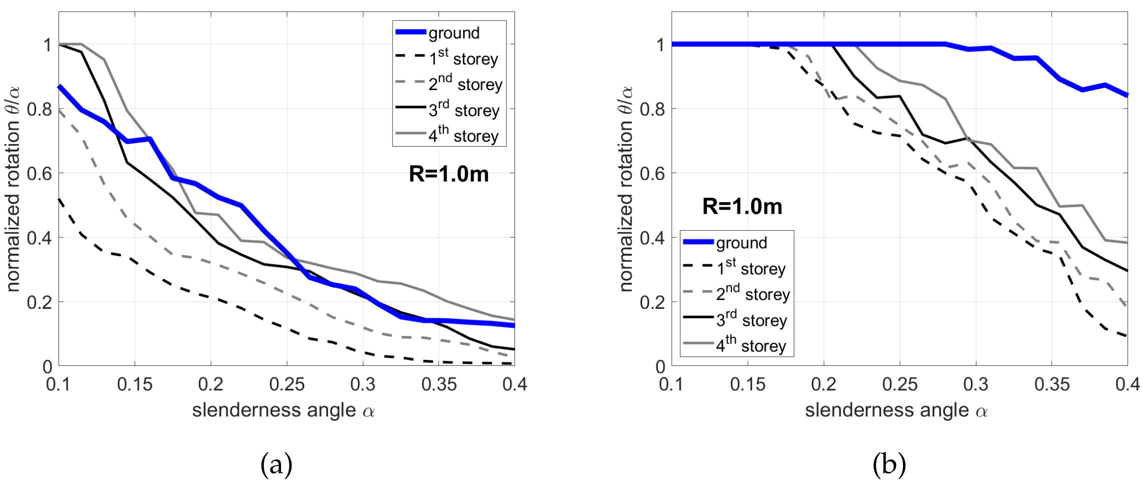

FIGURE 6.10: Mean rotation demands for rigid blocks with $R = 1m$ as function of the slenderness angle. The spectra were produced for building response histories scaled at: (a) $IM^{(s)} = 0.4g$ (elastic structure), and (b) $IM^{(s)} = 1.0g$ (inelastic structure).

The remaining of the thesis is focused on the seismic fragility assessment of the freestanding contents. We isolate two freestanding rocking blocks with $R = 1m$. The first has a slenderness angle $\alpha = 0.20$ and is considered as "slender", while the second has $\alpha = 0.35$ and is referred as "stocky". Three limit-states are identified for each block. For the slender block, the corresponding $EDP^{(b)} = \theta/\alpha$ threshold values are assumed as 0.3, 0.5 and 1, respectively, while for the stocky block the values are 0.1, 0.3 and 1. Different threshold values are used for each block due to their very different dynamic behaviour (e.g. see Fig 6.10). For example, $\theta/\alpha = 0.1$ is easily exceeded for the slender block and thus it is not a reasonable threshold, while for a stocky block

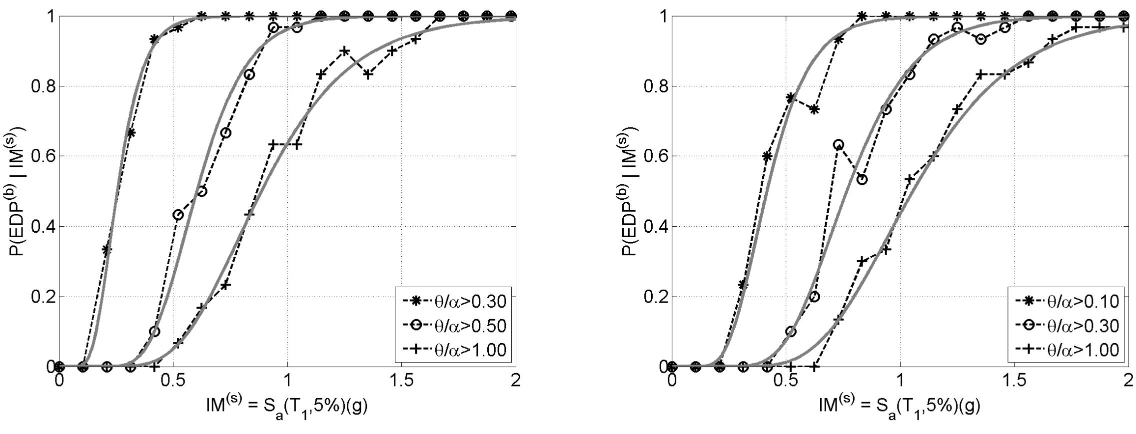

(a) (b)

FIGURE 6.11: Fragility curves for a block located at the 3^{rd} storey of the building: (a) slender block ($R = 1.0m, \alpha = 0.2$), (b) stocky block ($R = 1.0m, \alpha = 0.35$).

the limit-state fragility of $\theta/\alpha = 0.5$ will, practically, coincide with that of overturning ($\theta/\alpha \geq 1$). This is reasonable also for blocks of the same geometry, since they may have a different use or other operational restrictions. For example, a computer server may not be able to operate at all after a very small rocking rotation. On the other hand, for another type of freestanding equipment, e.g. furniture, this rotation would have been negligible. Figure 6.19 shows the fragility curves of the two rectangular blocks on the 3^{rd} storey of the RC building considered. The curves were produced with respect to $IM^{(s)} = S_a(T_1, 5\%)$, a practice that allows convolving the fragility curve with the hazard curve in order to obtain the mean annual frequencies (MAF) (Eq. 6.8). As shown in Figure 6.19, both chainsaw-like and smooth fragilities can be obtained depending on the post-processing method. Both curve types are acceptable, although intuitively the reader will be more comfortable with the smooth curves offered by the MLE fitting of Eq. 6.13. The smooth fragility curves are shown in rest of the manuscript.

Figure 6.20 shows the block overturning fragilities using PFA as the intensity measure $IM^{(b)}$ of the block. The solid lines refer to the block subjected to the original ground motions, while the dashed lines were obtained using the response history of the fourth storey. Also, the dark lines correspond to the slender block and the grey to the stocky. As expected, the slender block is always more vulnerable, while the building reduces its fragility (Figure 6.20a). On the contrary, the building fragility overall increases for the stocky block. This is in agreement with the rocking spectra of Figure 6.10. In order to better understand the importance of considering the collapse of the structure, Figure 6.20b, repeats the fragility curves of Figure 6.20a, but this time ignoring the coupling between the structure and the block. In other words, in Figure 6.20b,

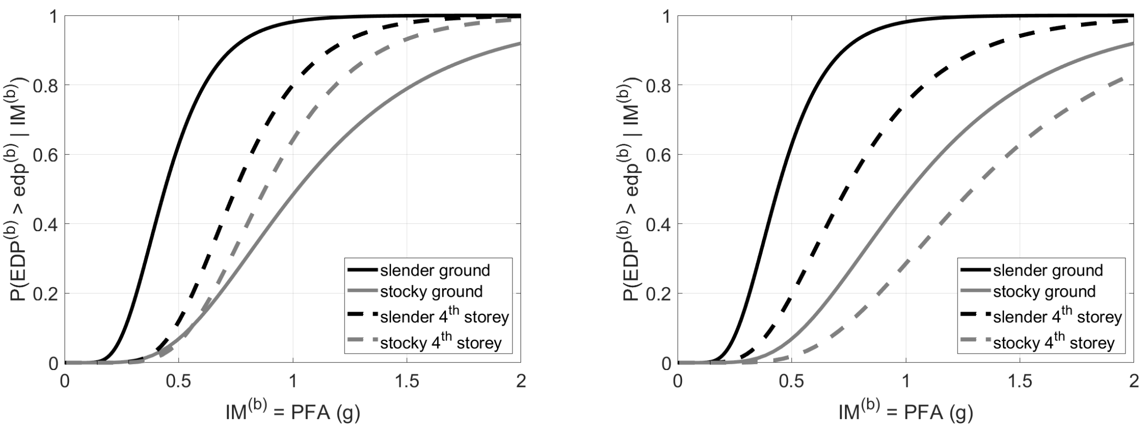

(a) (b)

FIGURE 6.12: Overturning fragility curves of a slender ($R = 1.0m$, $\alpha = 0.2$) and a stocky block ($R = 1.0m, \alpha = 0.35$) assuming $IM^{(b)} = PFA$: (a) the block is considered overturned when the structure collapses, (b) the collapse of the structure is omitted.

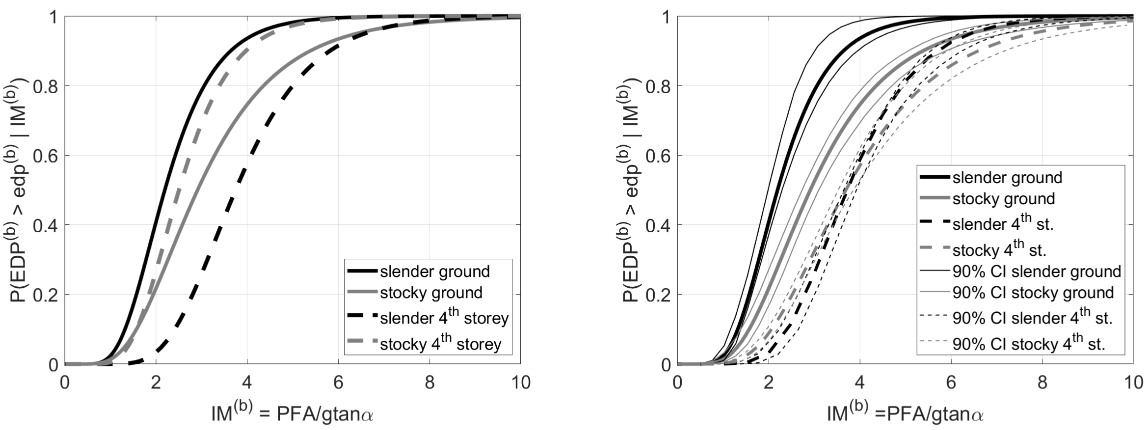

(a) (b)

FIGURE 6.13: Overturning fragility curves of a slender ($R = 1.0m$, $\alpha = 0.2$) and a stocky block ($R = 1.0m, \alpha = 0.35$) assuming $IM^{(b)} = PFA/gtan\alpha$: (a) the block is considered overturned when the structure collapses, (b) the collapse of the structure is omitted.

we do not assume that the block overturns when structural collapse occurs. As before, for the slender block the fragilities are only slightly affected, but for the stocky block the fragility is very different. According to Figure 6.20a and b, when the coupling is neglected, the building is beneficial also for the stocky block.

The results of Figure 6.20 are repeated in Figure 6.13 but with $IM^{(b)} = PFA/gtan\alpha$, instead of PFA. Since the blocks have a different slenderness angle α, the normalized $IM^{(b)}$ affects the fragilities obtained. Qualitatively the results are the same compared

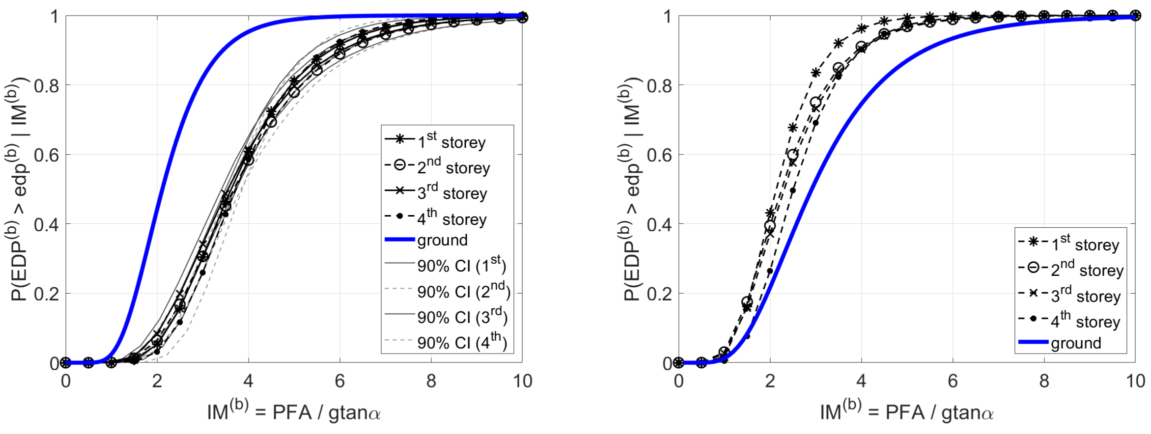

(a) (b)

FIGURE 6.14: Storey overturning fragility curves: (a) slender block ($R = 1.0m, \alpha = 0.2$), (b) stocky block ($R = 1.0m, \alpha = 0.35$).

to those of Figure 6.20a and b, but the fragilities curves are less dispersed, bringing closer the slender and the stocky block fragilities. Figure 6.13b also shows the 90% bootstrap confidence intervals around each fragility curve. The narrow confidence intervals obtained, verify that the comparison is statistically significant. Figure 6.21 presents for all stories of the structure the block overturning fragilities assuming $IM^{(b)} = PGA/gtan\alpha$. For both blocks, the storey fragilities practically coincide, while the "ground" fragilities differ considerably from those of the four stories. In principle, the fragility curves should coincide since they provide a property of the system that should not be sensitive to the ground motion set. However, due to the substantially different frequency content of the ground motions (see the spectra of Figure 6.7) this in not the case here. Of interest is also to show the fragilities obtained using as $IM^{(b)}$ the PGV (or PFV) instead of the PGA (Figure 6.22). Adopting the PGV, the storey fragilities appear more dispersed compared to the $PFA/gtan\alpha$, which is more profound for the stocky block. Quantitatively, as before, the stocky block is more vulnerable on the ground, while the slender block is less affected by the structure compared Figure 6.20a. As a general conclusion, although qualitatively our conclusions are not affected by the $IM^{(b)}$, the fragility curves will differ and their interpretation requires attention. Furthermore, Figures 6.21a and 6.22a show the 90% confidence intervals which again verify the statistical significance of the fragilities obtained.

In order to calculate the limit-state mean annual frequencies (MAF) of the block, we adopt the hazard curve shown in Figure 6.16a and corresponds to a site in the island of Crete, Greece. As discussed in Section **??**, the limit-state MAFs are "exactly" calculated with Eq. 6.8. Alternatively, the MAFs can be calculated with Eq. 6.9 finding separately the fragility of the block and of the structure. The calculation of Eq. 6.9 requires the

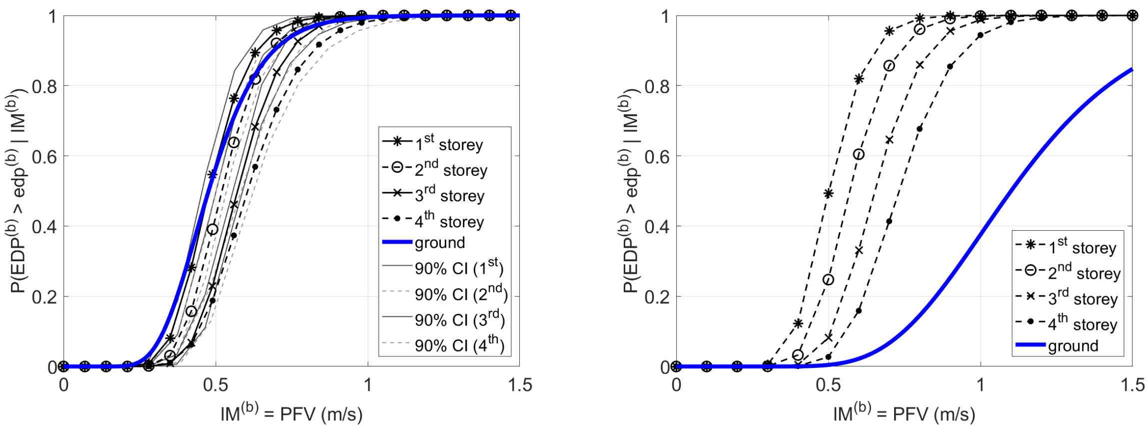

(a) (b)

FIGURE 6.15: Storey overturning fragility curves using PFV as the IM of the block: (a) slender block ($R = 1.0m, \alpha = 0.2$), (b) stocky block ($R = 1.0m, \alpha = 0.35$).

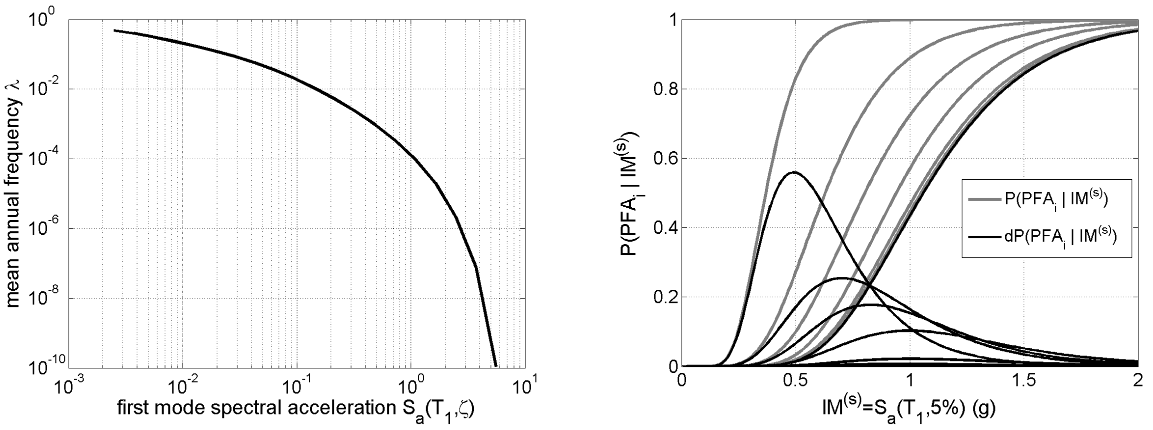

(a) (b)

FIGURE 6.16: (a) Hazard curve for a site located in Southern Greece, (b) Calculation of $dP(PFA|IM^{(s)})$.

derivative of the block's fragility, which essentially is the probability density function (PDF) for a number of discrete limit-states, as shown in Figure 6.16b. For the example considered, the MAFs of Eq. 6.8 and Eq. 6.9 are shown in Table 6.2 for the first and the fourth storey of the RC building considered. In Eq. 6.9 two $IM^{(b)}$ were considered, $PGA/gtan\alpha$ and PFV. Sufficient accuracy between the MAFs of the two approaches is achieved when the PFV is used as the intermediate variable in Eq. 6.9, while significant errors are observed for $IM^{(b)} = PFA/gtan\alpha$. Although not shown, poor results were observed when the PFA was used as $IM^{(b)}$. Moreover, the simplified method of Eq. 6.9 produces slightly better estimates for the slender block. The cloud data should be handled carefully, since the associated dispersion is naturally large. The main reason for the large variation of the MAFs in Table 6.2 is the biased fragilities of the blocks when the IM considered is the PFA. However, we have observed that using the PFV as IM, the approximate evaluation tends to produce smaller errors.

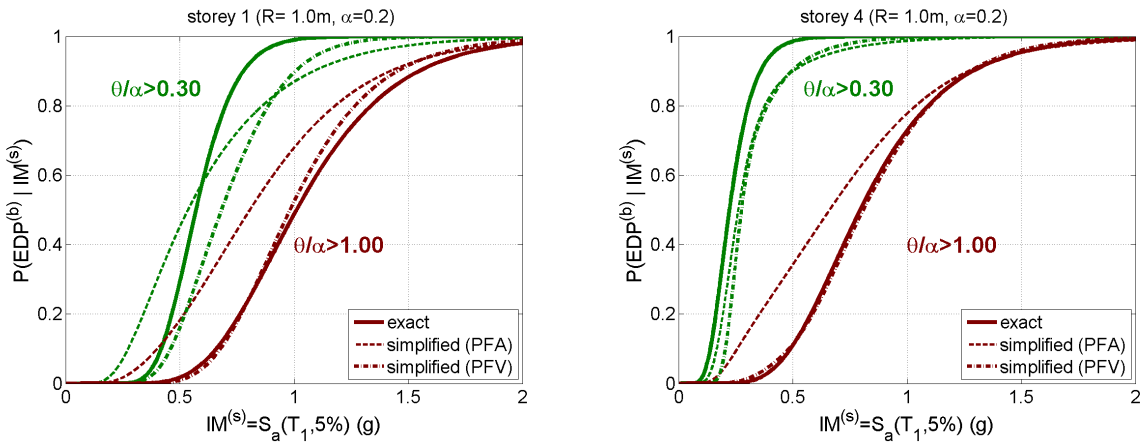

(a) (b)

FIGURE 6.17: Fragility curves using the exact (Eq. 6.8) and the simplified approach (Eq. 6.9) for the slender block ($R = 1.0m, \alpha = 0.2$): (a) first storey, (b) forth storey.

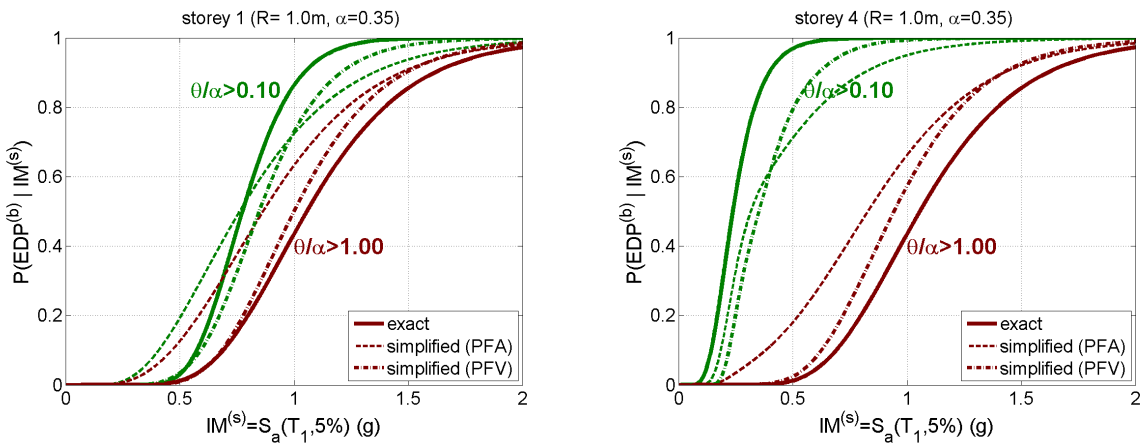

(a) (b)

FIGURE 6.18: Fragility curves using the exact (Eq. 6.8) and the simplified approach (Eq. 6.9) for the stocky block ($R = 1.0m, \alpha = 0.35$): (a) first storey, (b) forth storey.

The comparison of the MAF estimates is better understood looking at the fragilities of Figures 6.17 and 6.18. The fragility $P(EDP^{(b)}|IM^{(s)})$ is calculated as $P(EDP^{(b)}|IM^{s}) = \int_{IM^{(b)}} P(EDP^{(b)}|IM^{(b)})\, dP(IM^{(b)}|IM^{(s)})$ and is compared with the direct calculation, i.e. without an intermediate variable. Essentially the calculation of Eq. 6.9 is repeated leaving out the slope of the hazard curve $d\lambda_{IM^{(s)}}$, which is common for both MAF equations. Figures 6.17 and 6.18 show the good performance of PFV as opposed to $PFA/gtan\alpha$, while better agreement is shown for the overturning limit-state and for the slender block.

Accepting that the choice of the $IM^{(b)}$ is important, it is necessary to investigate where do the errors shown in Figures 6.17, 6.18 come from. This is understood comparing Figure 6.21 and Figures 6.17,6.18. Figure 6.21 shows that the fragility curves of the block at the building and at the ground will differ for the stocky block but not for the slender block. Since the collapse of the building does not affect the overturning fragility of the slender block (Figure 6.21a), the overturning fragility of the slender block is almost the same regardless, if the structure's collapse is neglected or not, hence the overturning MAF of Figure 6.17 is closely estimated. On the other hand, for the slender block, the building and the ground fragilities differ and this is transfered to Figure 6.18. However, even for the stocky block, the solution provided is acceptable given the many sources of uncertainty on the problem at hand. Another important remark is that the block used in this example were obtained including the building's collapse. Therefore, when the building's collapse does affect the fragilities, as in the case of the slender block, Eq. 6.9 is accurate. This hampers the use of Eq. 6.9 when generic fragility curves are to be adopted.

6.4.3 Asymmetric building contents

The case of asymmetric building contents is also examined here. The asymmetry of a rocking block leads to different equation of motion and the energy dissipation depends on the pivot point. Also, it has been shown in Vlachos et al., 2019 that the sign of the ground motion also affects the response.

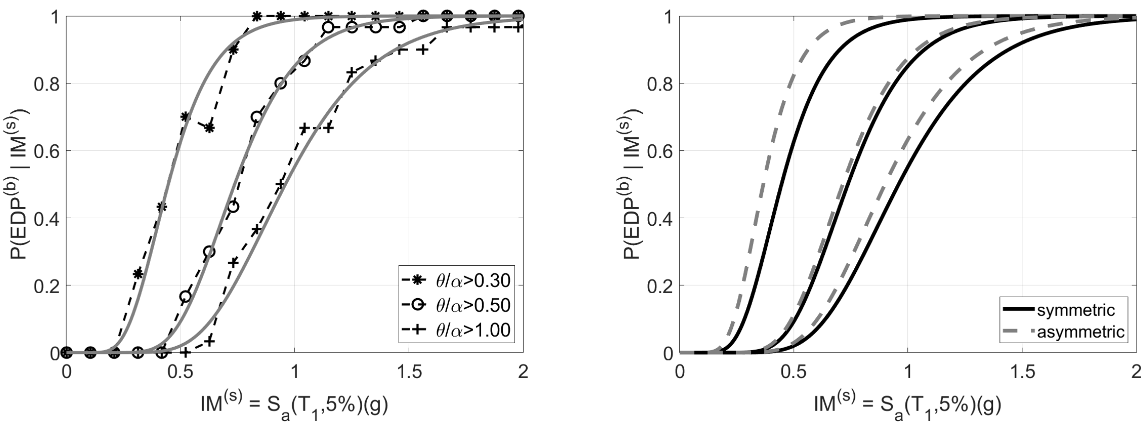

FIGURE 6.19: Fragility curves for a block located at the 2^{nd} storey of the building: (a) slender block ($R = 1.0m, \alpha = 0.2$), (b) comparison between the symmetric and the asymmetric block considered.

Two blocks, a symmetric and an asymmetric, are compared. The symmetric block has slenderness angle $\alpha = 0.20$ and size parameter $R = 1m$ and the asymmetric slenderness angles $\alpha_1 = 0.212$, $\alpha_2 = 0.182$ and size parameters $R_1 = 1.003m$, $R_2 = 0.997m$. Three limit-states are identified for each block. The corresponding $EDP^{(b)} = \theta/\alpha$ threshold values are assumed as 0.3, 0.5 and 1, respectively. Figure 6.19a shows the fragility curves of a rectangular block on the 2^{nd} storey of the RC building considered and Figure 6.19b compares the fragility curves of the symmetric and the asymmetric block in each limit-state. The curves were produced with respect to $IM^{(s)} = S_a(T_1, 5\%)$, a practice that allows convolving the fragility curve with the hazard curve in order to obtain the mean annual frequency (MAF) (Eq. 6.8). As shown in Figure 6.19, both chainsaw-like and smooth fragilities can be obtained depending on the post-processing method. Both curve types are acceptable, although intuitively the reader will be more comfortable with the smooth curves offered by the MLE fitting of Eq. 6.13. The smooth fragility curves are shown in rest of the section. Figure 6.20 shows

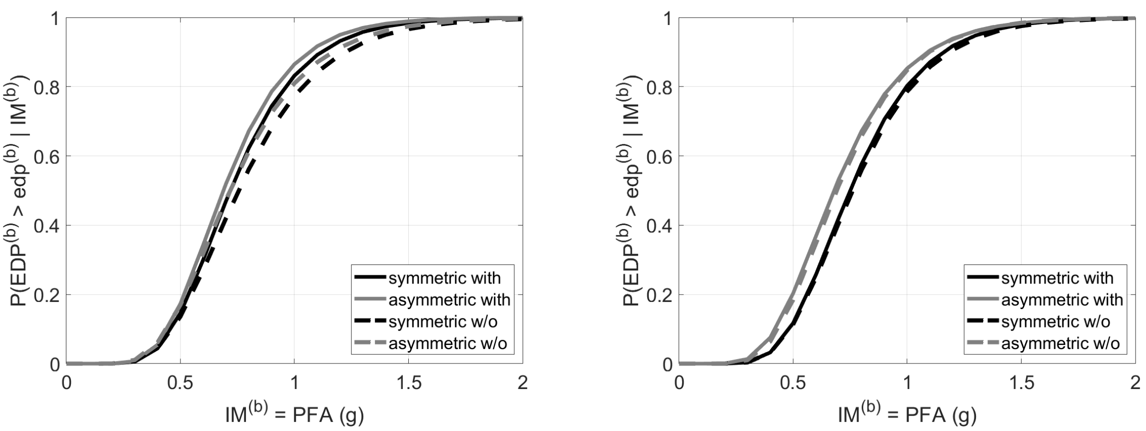

FIGURE 6.20: Overturning fragility curves of a slender block assuming it as symmetric or asymmetric: (a) the block is considered at the 1^{st} storey of the structure, (b) the block is considered at the 4^{th} storey of the structure.

the block overturning fragilities using PFA as the intensity measure $IM^{(b)}$ of the block. The solid lines refer to the block subjected to the storey response time-history and assuming that the structure's collapse means overturning of the blocks, while the dashed lines were obtained omitting the structure's collapse. Also, the dark lines correspond to the symmetric block and the grey to the asymmetric. As expected, the asymmetric block is always more vulnerable, while the building affects the fragilities especially when the block is hosted in the lower storeys of the building (Fig. 6.20a vs Fig. 6.20b). Figure 6.21 presents for all stories of the structure the block overturning fragilities assuming $IM^{(b)} = PFA/gtan\alpha$. For both blocks, the storey fragilities practically coincide. In principle, the fragility curves should coincide since they provide a property of the system that should not be sensitive to the ground motion set. However, due to the

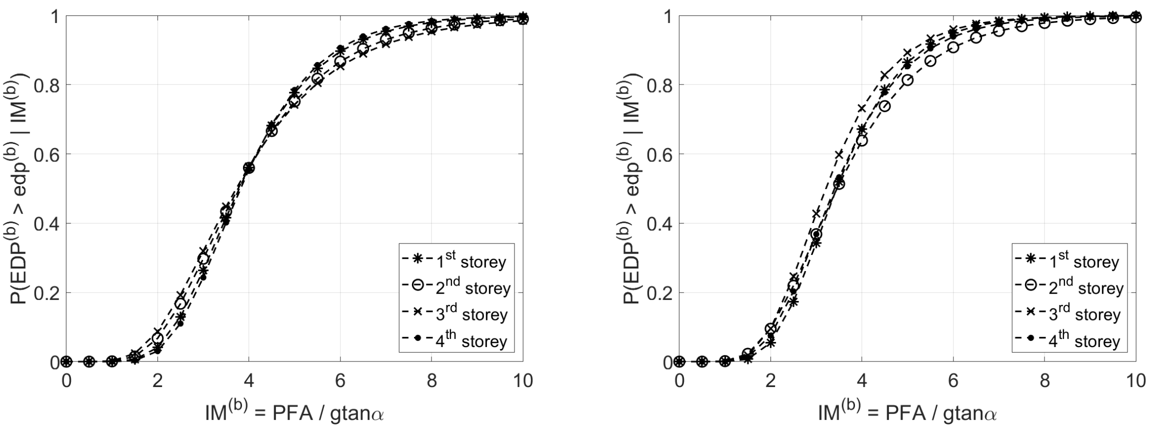

FIGURE 6.21: Storey overturning fragility curves: (a) slender symmetric block ($R = 1.0m, \alpha = 0.2$), (b) slender asymmetric block. The structure's collapse has been considered in both cases.

substantially different frequency content of the ground motions this in not always the rule. Of interest is also to show the fragilities obtained using as $IM^{(b)}$ the PFV instead of the PFA (Fig. 6.22). Adopting the PFV, the storey fragilities appear more dispersed compared to the $PFA/gtan\alpha$, which is more profound for the symmetric block. As a general conclusion, although qualitatively our conclusions are not affected by the $IM^{(b)}$, the fragility curves will differ and their interpretation requires attention.

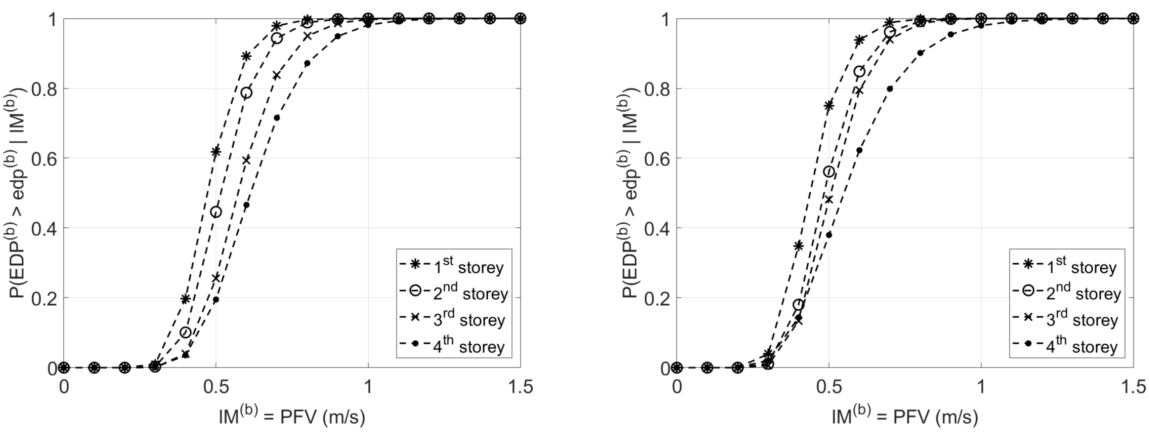

FIGURE 6.22: Storey overturning fragility curves using PFV as the IM of the block: (a) slender symmetric block ($R = 1.0m, \alpha = 0.2$), (b) slender asymmetric block. The structure's collapse has been adopted in both cases.

For the blocks considered, the MAFs of Eq. 6.8 are shown in Table 6.2 for the first and the fourth storey of the RC building considered. From the values of the MAFs it is obvious that a symmetric block is more stable than an asymmetric is all storeys of the structure. Especially, in the fourth storey the differences become important while

storey	$(\theta/\alpha \leq 0.3)$	$(\theta/\alpha \leq 0.5)$	$(\theta/\alpha \leq 1.0)$
$1^{st} symmetric$	1353 years	3427 years	5280 years
$1^{st} asymmetric$	1230 years	2838 years	4933 years
$4^{th} symmetric$	170 years	808 years	2478 years
$4^{th} asymmetric$	105 years	538 years	1226 years

TABLE 6.2: Limit-state MAFs obtained for a rocking block using the exact (Eq. 6.8) approach.

the values of the MAFs in the first storey are close for the symmetric and asymmetric case.

Chapter 7

Experimental testing of museum artefacts

In this chapter, the experimental seismic assessment and protection of museum artefacts, is presented. It has to be noted that, the notation was partially changed with respect to the original corresponding conference paper (Diamantopoulos and Fragiadakis, 2022) in order to be consistent with the notation used throughout the Thesis.

7.1 Introduction

Earthquake actions pose an immense threat to museums and their contents. For example, during the recent earthquakes on 21 July 2017 and 24 March 2020, in the island of Kos (Greece) and in Zagreb (Croatia), respectively, severe and widespread damage were reported in the archaeological museums of the cities. The earthquakes extensively damaged the sculpture exhibition, where many artefacts were dislocated, leaned against the walls, or over-turned. In the case of heavy and slender sculptures, the overturning mechanism, apart from damaging the sculptures themselves, poses a serious threat to other standing exhibits in the gallery and the visitors. It is, therefore, of paramount importance to develop methods and tools for characterizing the seismic risk of museum artefacts and, where necessary, propose cost-efficient protective measures.

The study of the seismic behaviour of museum assets and the investigation of novel and cost-effective risk mitigation schemes for improving the seismic resilience of European museums was the focus of the H2020-SERA project Seismic Resilience of Museum contEnts (SEREME). SEREME aims on filling this gap through extensive shake table tests on real-scale busts and statues. The aim of this large experimental campaign was to understand the seismic response of statues and busts and then develop novel and cost-effective risk mitigation schemes for improving the seismic resilience of museum valuable contents. The study focused on the investigation of the seismic response of two real-scale marble roman statues and three busts of roman emperors standing on pedestals of different types and size. Both isolated and non-isolated artefacts were considered, while two new and highly efficient base isolation systems, tailored to art objects, were tested. The tested isolators include a pendulum-based system and devices with Shape Memory Alloy (SMA) wires. Furthermore, the importance of the hosting building was examined. Specifically tailored, numerical models of varying complexity, for single and two-block rocking systems, were developed for the needs of this study and were assessed with the aid of the experimental results of the SEREME campaign.

The study of the seismic vulnerability of museum artefacts, especially of slender, human-formed statues, is related to the research on the dynamic response of rocking rigid blocks. The dynamic characteristics of the hosting structures are also important. This is evident from the fact that, on many occasions, damage to the structure was reported leaving the exhibits intact and vice-versa. Although the problem is coupled, it can be studied looking separately at the structure and its contents, provided that the contents are not attached to the building. The response of the artefacts is sensitive to acceleration and velocity-based quantities and also to their geometry. Today, there is lack of standards, while the existing approaches in the literature are general in concept and do not sufficiently address the mechanisms of the variety of rocking objects. The reliability of such analytical approaches has also been scarcely validated experimentally.

Museum exhibits can be seen as rocking freestanding objects, hence their response is sensitive to acceleration and velocity-based quantities. The geometrical properties of the artefacts also have significant effects on the dynamics and earthquake response of the components. Additionally, when freestanding components are placed on a pedestal, made either from marble or steel, their dynamic response is more difficult to be predicted with simple methods.

The seminal analytical work carried out on the seismic response of rocking objects in the 60's Housner, 1963 stimulated several quantitative studies that have focused primarily on numerical solutions Voyagaki et al., 2013; Zhang and Makris, 2001; Dimitrakopoulos and Fung, 2016; Diamantopoulos and Fragiadakis, 2019. Recently, however, Purvance et al., 2008 carried out extensive experimental and numerical studies in order to investigate the overturning response of symmetric and asymmetric blocks with both simple and complex basal contact conditions and also proposed block overturning fragilities. Similarly, ready-to-use fragility curves were proposed by Konstantinidis and Makris, 2009 through a comprehensive experimental program on full-scale freestanding laboratory equipment located on several floor levels. The latter studies, however, focused primarily on the behaviour of single blocks. Dual block systems were first studied numerically by Psycharis, 1990, while the recent experimental work of Wittich and Hutchinson, 2017 studied asymmetric free-standing component configurations. It is worth noting that, for rocking rigid objects, such as artefacts, the response, at least in terms of over-turning motion, is size-dependent, thus the scaling of the specimens is not possible and the experimental tests should be based on full-scale specimens.

Nowadays, considering the huge earthquake losses registered in recent earthquakes, especially in the Mediterranean region, it is also imperative to propose viable and cost-effective seismic protection measures for free-standing statues and busts. Podany, 2015 discussed a range of retrofitting measures based on the best practice followed by the J. Paul Getty Museum in Los Angeles, in California, where a newly developed base isolation device has been employed. Past research on the seismic protection of art objects using isolators, includes primarily several analytical and numerical investigations (e.g. Psycharis et al., 2013b; Calio and Marletta, 2003), while to our knowledge only few experimental studies can be found in literature. However, the effectiveness of the use of seismic isolators for light weight components should be further investigated to characterize thresholds for accelerations and horizontal displacements for an adequate seismic protection of the artefacts.

The H2020-SERA SEREME project aimed to fill the experimental gaps highlighted above and to include comprehensive shake-table tests of several configuration of free-standing and base isolated statues and busts. The freestanding artefacts were installed either directly on the marble floor, or on a pedestal. The objective of the campaign was to give insight on the seismic behaviour of statues and busts as well as to evaluate the effectiveness of two different seismic risk mitigation systems. A total of 5 pairs of real scale marble artefacts were tested, 3 busts installed on marble pedestals and 2 statues. Seven different testing arrangements (also termed "Configurations") were considered during this experimental campaign and more than 400 seismic tests were performed. Two innovative base isolation devices were utilized for seismic protection. The first system is a combination of friction pendulum isolators Contento and Di Egidio, 2014, a system designed for light components. The second system utilizes shape memory alloy wires in the horizontal plane. The isolation devices tested are patented systems, namely ISOLART® PENDULUM ISOLART® SMA, which are manufactured by the Italian company FIP Mec. In order to obtain a direct evaluation of the isolator effectiveness, for each test configuration, pairs of two similar artefacts were tested together in an isolated and a non-isolated arrangement. The shake-table tests were carried out considering uniaxial, biaxial and triaxial earthquake loadings at increasing amplitudes. In order to evaluate the influence of the frequency content and the directionality of the seismic excitation, 13 different waveforms were applied to the shake table (8 uni-directional motions, 3 bi-directional motions and 2 tri-directional motions). Regarding the instrumentation, the artefacts motions were recorded using accelerometers, gyroscopic velocity and displacement sensors.

7.2 Museum contents tested

The experimental campaign of SEREME project focused on the investigation of the seismic behaviour of real-scale marble statues and busts standing on pedestals. The case study statues and the busts were selected with different geometry and weights; they were replicas of ancient roman emperors. Five busts of roman emperors were tested: two of Emperor Traiano, two of Emperor Augusto and one of Emperor Tito. Furthermore, four statues were also purchased, two standing on a low height marble pedestal (quoted as "Figura Femminile") and two simple female form statues (quoted as "Fanciulla"). Since all specimens are made from solid marble, the average weight of the busts is 250-300kg, while that of the statues was 500-600kg. The replicas of the same statue/bust have approximately the same geometry, but they are not perfectly identical (Figure 7.1). The seismic response of a display case was also examined.

(a)

(b)

FIGURE 7.1: Components used for the shake table tests: (a) Busts and display case, (b) female statues.

The busts were placed on a pedestal which is used to bring the specimens to the eye-level of the visitor. Three different pedestal types were identified and then adopted for the experimental tests: *(i)* solid pedestal, with dimensions 45×45×100 cm, *(ii)* hollow pedestal, with dimensions 35×35×100 cm, and *(iii)* modern type metallic pedestals that were provided by the Italian manufacturer Fallani. The traditional, hollow and solid, pedestals were made of concrete which has a specific weight close to that of marble. To reproduce realistic conditions for in-situ friction, on the upper and the lower face of the pedestals, 3 cm thick marble plates were installed. Solid pedestals have large weights (nearly 500kg) and they also employ large bases, thus these pedestals are not prone to uplift. On the other hand, hollow pedestals are slender with weight 226kg and have a base with smaller width equal to 35c. Furthermore, its center of gravity is much higher compared to the solid case. The metallic pedestal has a large square base with side equal to 85 cm and it weighs only 85 kg. In order to simulate the floor of museums, where typically busts and statues are hosted, the non-isolated specimens were placed on a marble floor surface. The marble has thickness equal to 3 cm and it is positioned on stiff wood also 3 cm thick. Both marble and wood were directly bolted on the shake table. All specimens are placed on top of the marble floor and pedestal without any connection material. In the case of isolated specimens, the isolator was bolted on the table with the aid of specific holders that adjusts the holes of the table to the holes of the device. For the SMA isolators, marble plates were glued on the upper surface of the isolator, while the specimens are simply standing.

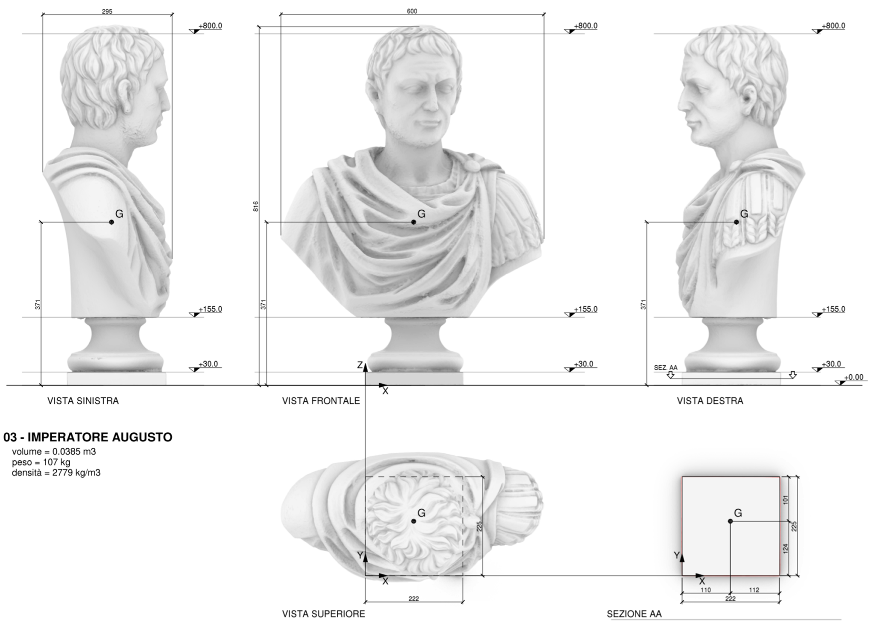

FIGURE 7.2: Geometric properties of the Emperor August bust.

The static friction coefficient was measured for the marble-marble interface with inclined tests. The inclined tests were repeated 10 times in order to determine the mean friction angle. For the plate-plate marble interface the mean friction coefficient μ was found equal to 0.79, while for the bust-plate interface it was found equal to 0.39. The values of the friction coefficient for plate-plate interface that were derived experimentally comply with those provided in the literature. Conversely, the friction marble-plate interface was found unexpectedly low. However, both mean values were also verified during the shake table tests where sliding was observed approximately at peak ground acceleration (PGA) values close to the ones measured (the condition to have friction is $PGA \geq \mu g$). To increase the friction coefficient, where necessary, a thin layer of a rubber material was glued at the bottom of the busts. The friction coefficient at the interface of the marble floor and the bottom of the statues was found sufficiently high and thus no measures were required.

Laser scanning was carried out by a joint research team before moving them the artefacts from the vendor to CEA. Digitalization with laser scanning provides the geometrical proper-ties of the specimens. The purpose of laser scanning is two-fold: *(i)* it provides a finite element (FE) mesh of the geometry of the artefacts that can be used to perform numerical simulations, and *(ii)* it allows the calculation of fundamental properties of the components, such as the center of mass (CM), the total mass, the rotational moments of inertia and the distance of the CM from the pivot points. Furthermore, the laser scanning verified that the specimens are made from solid marble through calculating the ratio of the scanned volume over the measured weight of each specimen. Example of laser scanning information obtained are shown in Figure 7.2 for the bust of Emperor August.

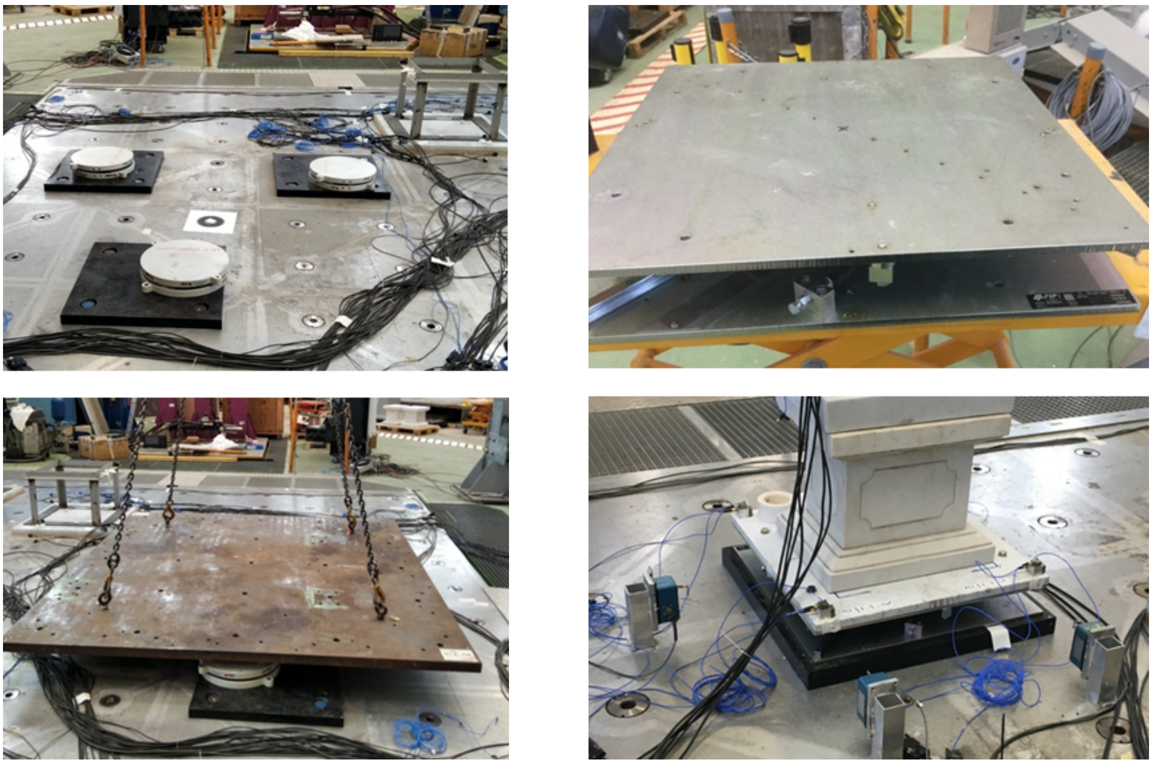

(a) (b)

FIGURE 7.3: Tested isolation systems: (a) friction pendulum isolator, (b) SMA isolator.

Two different base isolator technologies were adopted (Figure 7.3): a friction pendulum isolator and an innovative device with shape memory alloy (SMA) wires. The tested seismic isolator systems were manufactured by the Italian company FIP Mec srl: the selected isolators are marketed as ISOLART® SMA and ISOLART® PENDULUM, respectively. ISOLART® PENDULUM, is similar to common pendulum isolators used for structures, but it consists of different materials and it has been designed specifically for low-mass structures such as objects of art. The main difference between the two isolation devices is the range of mass of the objects to seismically isolate. For ordinary friction pendulum bearings, the friction can be large because of low vertical pressure. To overcome the problem, an increase of the vertical force, or a decrease of the friction coefficient is required. For this purpose, the friction pendulum was used to isolate several artefacts together which are standing on a heavy steel plate, thus increasing the vertical force (Figure 7.3a). Therefore, three pendulum isolators were employed to isolate a floor on which a group of artefacts (2 or 3 artefacts) was installed. The installation of the ISOLART® PENDULUM devices is shown in Figure 7.3a.

ISOLART® SMA, i.e. the SMA-based isolator, is a novel isolator based on SMA wires that are effective in limiting the horizontal displacements of the device. ISOLART® SMA is a patented isolation system which takes advantage of the super-elastic properties of SMA wires, i.e. their capacity to have a stress-induced non-linear behaviour similar to elastoplastic behaviour up to high deformations (about 7%) and unload to zero displacement. As shown in Figure 7.3b, the SMA isolator can be used to isolate a single specimen each time, which is a significant advantage. Although all SMA isolators adopted have the same dimensions, the properties of the SMA may differ. Three different types of SMA isolators were tested.

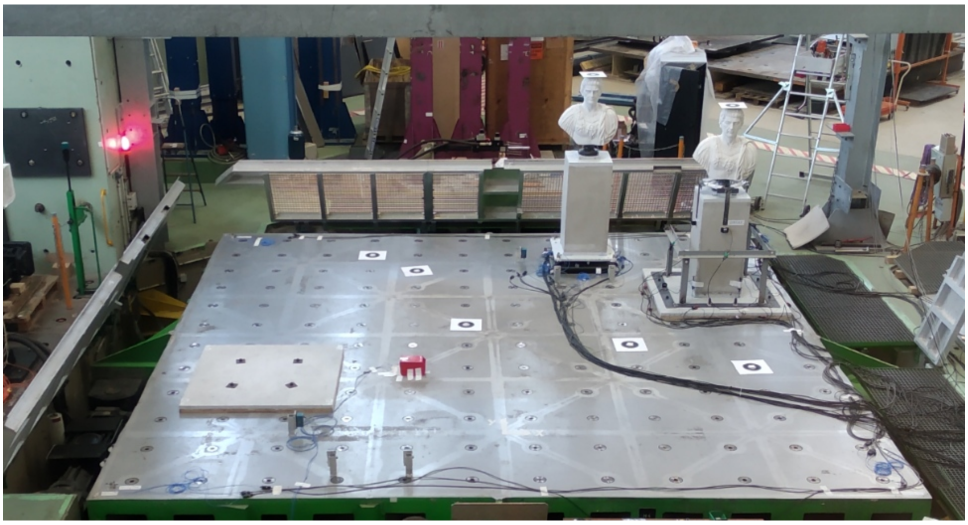

FIGURE 7.4: Configuration I-1: Traiano bust on solid pedestal; on marble and on SMA isolator

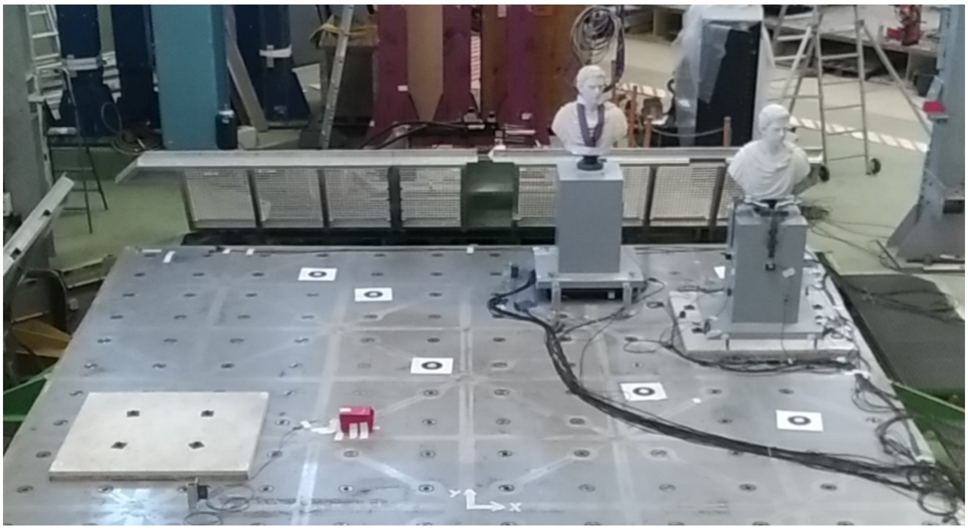

FIGURE 7.5: Traiano bust on steel metallic pedestal; on marble and on SMA isolator.

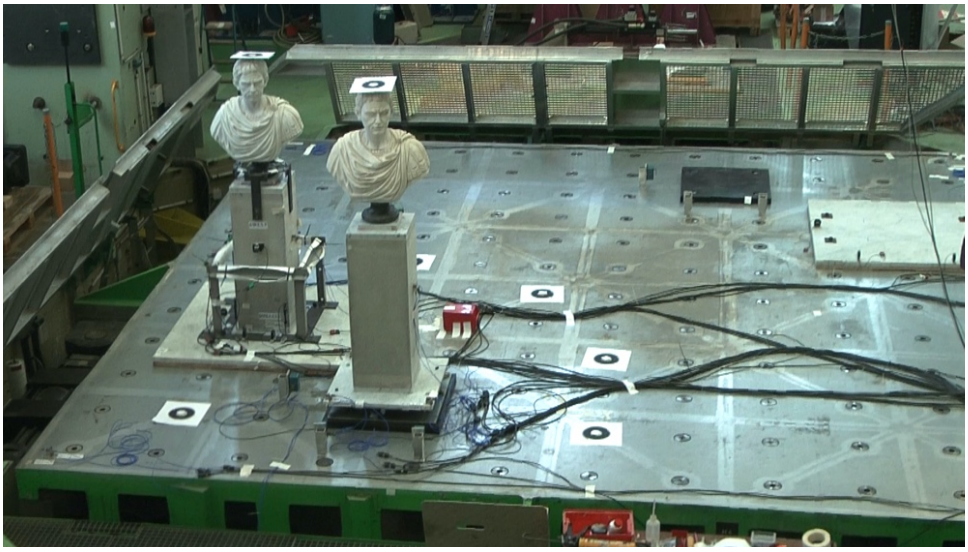

FIGURE 7.6: Configuration I-3: Augusto bust on hollow pedestal; on marble and on SMA isolator.

Due to the large variety of specimens, pedestals and isolators, seven different Configurations were analysed experimentally using the 6-DOFs shake table AZALEE. The seven testing configurations were designed taking into consideration the limited testing time available and also the needs of the project. The tests of each configuration lasted approximately 2, or 3 days. Configuration 1, was sub-divided into five sub-configurations, shown in Figure 7.4 up to Figure 7.8 and considers only the SMA isolators. The caption of each figure explains the properties of the tested configuration. In order obtain a direct comparison between the isolated and the non-isolated case,

FIGURE 7.7: Configuration I-4: Female statue (Figura femminile) standing on the ground pedestal and non-isolated display case and isolated display case (SMA isolator).

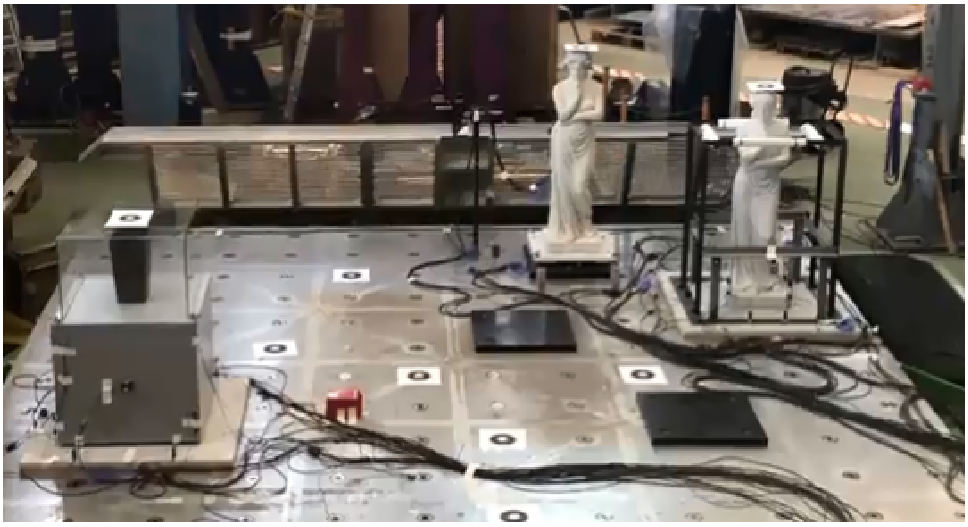

FIGURE 7.8: Configuration I-5: Female statue (Fanciulla) standing on the ground pedestal and non-isolated display case and non-isolated display case.

the sub-configurations compare pairs of two similar artefacts tested side-by-side in an isolated and a non-isolated arrangement. Instead of testing simultaneously more than a pair of specimens, single pairs were considered every time. This practice offered speed during the tests, while it also allowed to focus on one tested pair every time. In configurations I.4 and I.5 a display case was tested, first isolated and then non-isolated.

Configurations II and III are shown in Figure 7.9 and Figure 7.10, respectively. These two configurations test the friction pendulum as seismic isolator. In Figure 7.9,

FIGURE 7.9: Configuration II: Non-isolated vs isolated statues (friction pendulum system). The pairs of specimens com-pared are: (i) Traiano bust on solid pedestal, (ii) Fanciulla and (iii) Figura femminile.

FIGURE 7.10: Configuration III: Non-isolated vs isolated statues (friction pendulum system). The pairs of specimens com-pared are: (i) Tito bust on metallic pedestal, (ii) Augusto bust on solid pedestal, and (iii) Traiano bust on hol-low pedestal.

the two female statues and one bust were positioned on top of the friction pendulum isolators. The specimens were positioned on the steel plate in way that the center of mass of the specimens approximately coincides with the center of mass of the plate. Configuration III (Figure 7.10) compares simultaneously the three different types of pedestals. Since only five busts were available, for the metallic pedestals only the non-isolated case was considered. Furthermore, the upper face of the metallic pedestals was reinforced with an 8mm thick steel plate which considerable improved the performance of the system compared to Configuration I.2 (Figure 7.5).

7.3 Test setup

To evaluate the influence of frequency content of the excitation, as well as the directionality of the seismic input, five different earthquake ground motions were adopted in this experimental study. The ground motion records and their properties are shown in Table 7.1. The records were applied in different combinations every time, i.e. first the X-component was applied alone, the Y component afterwards and then the X and Y components were applied simultaneously.

TABLE 7.1: Ground motion records used for the testing campaign.

Earthquake	Date	M_w	Station	Dist.	Soil	PGA(g)
Emilia, Italy	29.05.2012	6.0	T0800	14.4	C(EC8)	L:0.33 T:0.25 V:0.33
Athens, Greece	07.09.1999	5.9	Syntagma Metro B	10.0	Stiff soil	L:0.109 T:0.086 V:0.087
L'Aquila, Italy	06.04.2009	6.3	Aterno river-AQA	≤ 2	Stiff soil	L:0.45 T:0.39 V:0.37
Kalamata, Greece	13.09.1986	6.2	Nomarchia	5.0	Stiff soil	L:0.22 T:0.29
Kobe, Japan	16.01.1995	6.9	Takatori, Japan	≤ 1.5	C(EC8)	L:0.068
Emilia – 1^{st} storey	29.05.2012	6.0	T0800	14.4	C(EC8)	L:0.37

The record combinations adopted are listed in Table 7.2. For each record combination, the ground motion amplitude was gradually scaled up. In general, the target intensity levels considered were: 0.15g, 0.20g, 0.25g, 0.35g, 0.40g and 0.50g. For simulations where simultaneously two, or three, components were considered, a uniform scaling factor was adopted for all record components considered, while the target acceleration refers either to the X-component or the Y-component. When both X and Y are present, it refers to the X-component. For the Takatori and the Kalamata records, the maximum permissible scaling factor is controlled by the maximum allowable displacement of the shake table that cannot exceed 10cm. As expected, differences between target PGA and the PGA measured as input to the shake table were observed. On average 25-40 shake table runs were performed for each of the seven tested configuration.

TABLE 7.2: Record combinations.

ID	Record	Components	Target PGA
1	Emilia	X	0.15, 0.25, 0.35, 0.40, 0.50
2	Emilia	Y	0.15, 0.25, 0.35, 0.40, 0.50
3	Emilia	XYZ	0.15, 0.25, 0.35, 0.40, 0.50
4	Emilia	XY	0.15, 0.25, 0.35, 0.40, 0.50
5	Emilia	Y(first floor)	0.15, 0.25, 0.35, 0.40, 0.50
6	Emilia	YZ(first floor)	0.15, 0.25, 0.35, 0.40, 0.50
7	Syntagma	X	0.15, 0.25, 0.35, 0.40, 0.50
8	Takatori	Y applied on X	0.10, 0.15
9	Takatori	YZ applied on X	0.10, 0.13, 0.20, 0.24
10	Takatori	Y	0.10, 0.18, 0.20, 0.24
11	L' Aquila	X	0.15, 0.25, 0.35, 0.40, 0.50
12	L' Aquila	XYZ	0.15, 0.25, 0.35, 0.40, 0.50
13	Kalamata	X	0.15, 0.20, 0.25, 0.30

Apart from five naturally recorded ground motions, the acceleration response history of the first floor of the museum was considered. The museum is the Archaeological museum of Pella in Greece. This is a new reinforced concrete building. The building was modelled with OpenSees software and it was subjected to the five ground motion records of Table 7.1. Since it is a two storey RC building with many shear walls, it is a quite stiff structure ($T_x = 0.17s$, $T_y = 0.14s$) and hence large amplifications were observed at the stories. Among the various floor acceleration histories, the first storey of the Emilia 2012 (Italy) response acceleration was adopted for the tests.

7.4 Simulations

Due to the complex geometry of museum exhibits and the uncertainties of the problem, the numerical simulation of artefacts and museum exhibit systems presents significant difficulties. Complex simulations should be repeated for each exhibit, or for groups of exhibits with similar geometrical characteristics. Moreover, despite the great value of museum exhibits, in practice all decisions about their safety are taken by museum curators, who have empirical knowledge, e.g. experience of past earthquakes, but no technical background to perform sophisticated computer simulations.

TABLE 7.3: Peak ground acceleration that initiate rocking and overturning velocity estimates.

Specimen	Standing conditions	Rocking (g) $a_{rock,B,x}/a_{rock,B,y}$	Overturning (mm/s) $v_{cr,x}/v_{cr,y}$
Figura Femminile with pedestal		0.244/ 0.207	0.446/0.344
Fanciulla		0.296/ 0.226	0.382/0.289
Emperor Traiano	Bust only	0.240/0.236	0.297/0.308
	Bust on solid pedestal	0.330/0.331	0.423/0.424
	Bust on hollow pedestal	0.207/0.208	0.280/0.281
	Bust on steel pedestal	0.293/0.292	
Emperor Tito	Bust only	0.283/ 0.254	0.262/0.309
Emperor Augusto	Bust on solid pedestal	0.283/0.253	0.257/0.304
	Bust on hollow pedestal	0.220/0.216	0.294/0.290
	Bust on steel pedestal	0.318/0.310	

The possible methods of analysis are either simplified calculations based on first principles, or advanced methods of analysis, e.g. analyses using FE modelling, or the discrete element method (DEM). Simplifications are based on simplifying the geometry to one or two rectangular, rigid bodies. These are basic geometric calculations that do not require engineering knowledge, but give useful information such as the maximum ground acceleration for which the system will slide or will engage into a rocking motion. When laser scanning information is available, these calculations are more accurate and, despite their simplicity, they are very important and helpful. Table 1 shows the peak ground acceleration values that initiate rocking for each of the specimen considered. In the case of busts standing on a pedestal, the two bodies are, crudely, assumed to behave as a single body. Table 7.3 also shows the velocity that triggers overturning motion according to the relationship proposed by Ishiyama, 1982a. This is a conservative lower bound estimation, as opposed to the rocking initiation acceleration which is exact.

Laser scanning was adopted for determining the geometric characteristics of the busts and of the statues that were tested. The scanning provides FE models that allow to perform simulations, but with increased CPU requirements. Furthermore, the accuracy of the scanning is very high and results to very fine and detailed finite element models which do not offer more accuracy but they require excessive memory and

CPU resources. It is, therefore, necessary to also have simple models for the seismic response prediction.

The FE method offers several advantages concerning the accuracy, but there are also difficulties in utilizing the analytical simulation approach. The surface-to-surface interaction between the upper surface of the pedestal and the lower surface of the bust requires knowledge of the friction coefficient and the damping ratio, while damping of the motion due to rocking impacts cannot be introduced in a straightforward manner. Also, the FE method is more realistic if the bodies have some flexibility. Introducing the flexibility and the real modulus of elasticity of the artefacts will increase the CPU time, thus making prohibitive a large number of simulations. On the other hand, the Discrete Element Method (DEM) assumes that the objects are rigid and consequently can be adopted with reduced computational costs. For the interaction between the surfaces, appropriately calibrated springs should be introduced in the model. Psycharis et al., 2013b have described the numerical model for the simulation of a multidrum ancient column which is subjected to natural ground motion records. The column consists of eight rigid bodies, the upper placed on the top of the lower. In this work the 3DEC software has been used for the simulation of a problem that has similarities to the problem at hand.

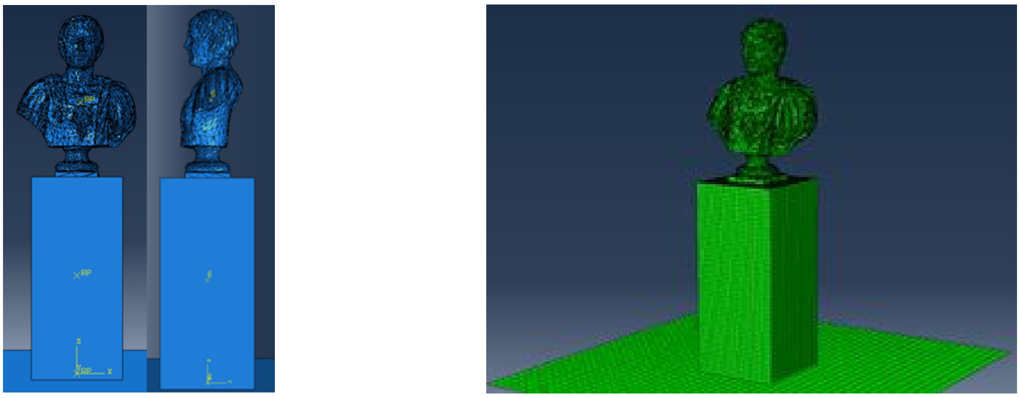

(a) (b)

FIGURE 7.11: (a) Finite Element model (pedestal-bust), (b) three-dimensional model.

Models that consider either two-block assemblies (pedestal-bust) or freestanding, symmetric or asymmetric, rocking blocks (a freestanding statue or a bust that rocks on a pedestal in rest) are a possible alternative to the costly FEM and DEM simulations. Such simple models are typically limited to one-direction simulations and hence the procedure should be repeated for both the longitudinal and the transverse direction due to the asymmetry of the specimens. A simplified approach is offered by using the equation of motion proposed by Housner, 1963. A possible way to handle the

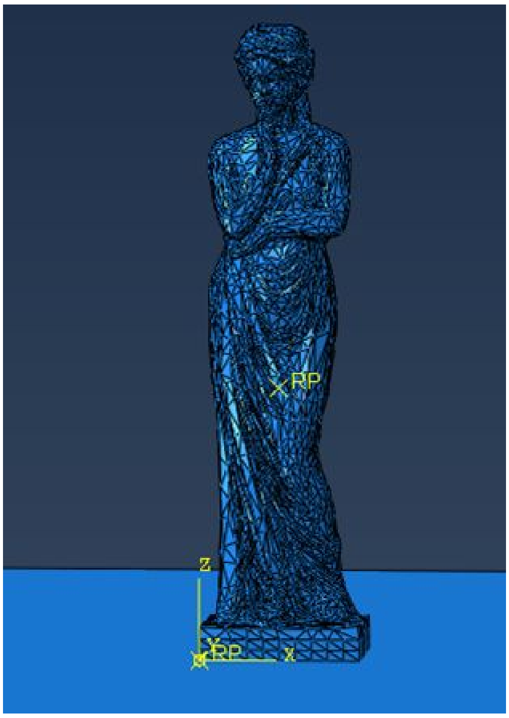

FIGURE 7.12: Finite Element Model used for the simulation of the Fanciulla statue.

equations of Housner, 1963 has been proposed by Diamantopoulos and Fragiadakis, 2019. For the two-block case and for simplicity reasons the work of Psycharis, 1990 can be adopted. Vlachos et al., 2019 presented a first attempt to extend the two-block problem in case of asymmetric upper block when the pedestal is symmetric.

Figure 7.11 presents the Finite Element Model adopted for the simulation of the Traiano bust when it is freestanding on the solid pedestal while Figure 7.12 presents the corresponding Finite Element Model for the simulation of the Fanciulla statue. The models have been introduced and analyzed as three-dimensional rigid bodies. The center of mass, the mass and inertia properties have been calculated using a CAD software and the exact dimensions came from the laser scanning. For the damping and sliding parameters, an appropriate calibration has been carried out.

7.5 Observations from the experimental campaign

A vast amount of data was obtained during the experimental campaign that lasted approximately two months. However, very interesting observations were made during the campaign. Due to the protection measures no major damage on the specimens occurred, while the most typical damage type observed is the failure at the corners of the specimens. This damage is shown in Figure 7.13 for both the bust and the statues.

This type of damage happened practically to all busts of Configuration I.1-I.5, while the damage of statue show in Figure 7.13b happened once. Since a large number of tests had to be repeated, the marble bases of the busts were replaced, while for the statue the failed wedge shown in Figure 12b was repaired by gluing it back and retesting the statue isolated. No damage occurred at the pedestals. The metallic modern pedestals when tested in Configuration I.2, exhibited some mild bending of their upper face, where the bust was standing. The lateral bending due to the self-weight of the bust affected the dynamic response. In order to mitigate this effect, in Configuration III, an 8mm thick plate was used to reinforce the pedestal.

(a)

(b)

FIGURE 7.13: Typical damage at the base of the specimens: (a) bust, (b) base of the statue.

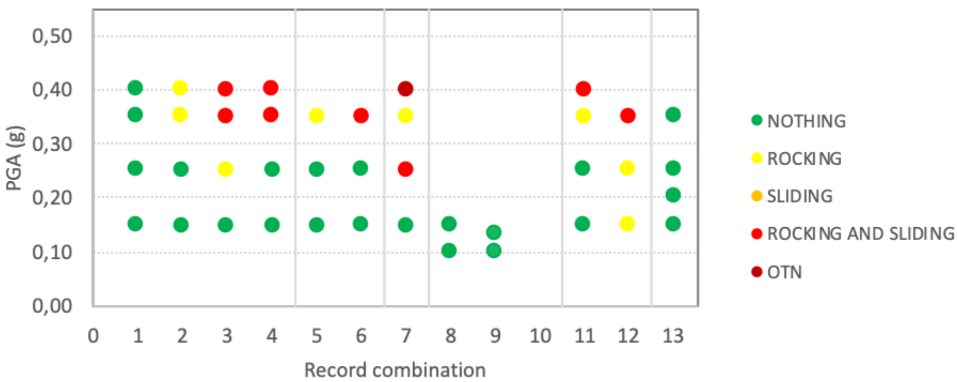

FIGURE 7.14: Response of the non-isolated bust of Configuration I.1.

Figure 7.14 summarizes the response of the non-isolated bust in Configuration I.1 where the bust of emperor Traiano was positioned on top of the solid pedestal. The solid pedestal, due to its massive geometry, never uplifted and hence only rocking of the bust was observed. As expected from the PGA values of Table 7.3, no uplift occurred for PGA values below 0.20g. Note that the accelerations of Figure 7.14 are the theoretical predictions; the latter differ, sometimes considerably, from the values recorded on the shake table. Comparing record combinations 1 and 2 to combinations 3 and 4, it is evident that the bidirectional ground shaking is more severe for the bust, since overturning was observed at much lower accelerations for the Emilia earthquake. This observation also holds for the L' Aquila record (combinations 11 and 12). The Takatori and Kalamata ground motions have a low recorded PGA and have a large frequency content. These records were scaled but they were not critical for the busts, as opposed to the Syntagma ground motion which was severe.

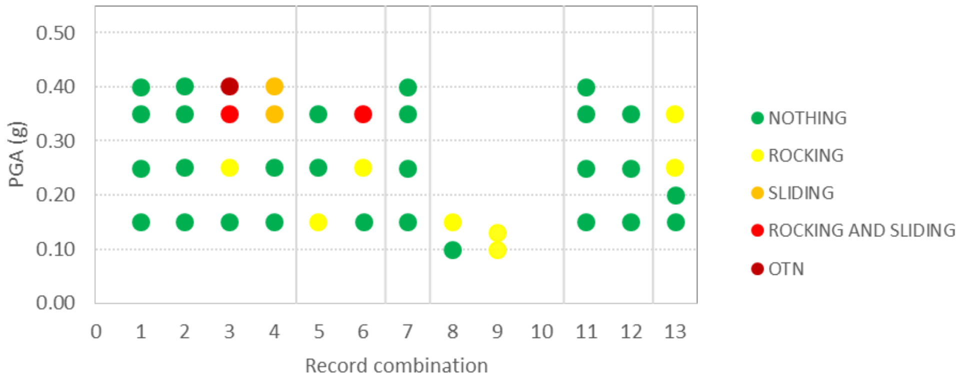

FIGURE 7.15: Response of the SMA-isolated bust of Configuration I.1.

Different observations hold also for the SMA isolated specimen. As show in Figure 7.15, the specimen was safe for most ground motion levels, practically for most ground motions. The Emilia XYZ ground motion produced sliding and rocking that threatened the bust for a PGA of 0.40g. This is attributed to the large vertical acceleration component. This was also seen for the first-floor response when a vertical component is present. Interestingly, rocking was observed also for the Takatori and the Kalamata ground motions. Important findings were obtained from the experimental campaign and are briefly summarized as follows:

- For high excitation intensity tests, the non-isolated artefacts are prone to show a complex rocking and sliding behaviour. The impact induced by the rocking motion can be a source of damage to the base of the busts, especially at the corner points of the base of the bust.

- The response of the busts on the solid and the on the hollow pedestal is substantially different. The uplift of the hollow pedestal was always small and difficult to identify visually. However, it is clear that it considerably affected the seismic response. Whether the bust is safer on the solid, or on the hollow pedestal is a topic that deserves further re-search; the tests have shown that the safety depends also on the ground motion frequency content.

- Tests where the friction coefficient between the bust and the pedestal was low, i.e. when friction coefficients vary between 0.20 and 0.30, revealed that sliding is a beneficial response mode for the bust. If the sliding motion of the rigid object is controlled, then some sliding is desirable.

- In most of the cases, the considered mitigation methods have been effective in the prevention of the rocking/sliding behaviour of the artefacts. As a result, these mitigation methods improved significantly the seismic behaviour of the artefacts. Especially the friction-pendulum system was very efficient in practically all tests. Some attention is required in the case of high vertical component. Although the vertical earthquakes considered were very strong, some attention is required in this respect.

- The metallic pedestals, due to their geometry, did not uplift and hence they were equally efficient as the solid ones, provided that they can fully support the weight of the artwork.

- The response of the statues was well predicted and with no surprises. When the input acceleration was below the rocking initiation threshold, the statues performed some high frequency oscillation.

- The base of some of the statues was not fully flat, due to structural imperfections. This lack of planarity affected the response and threatened the safety of the statues. This is-sue has been also reported in previous research in the literature.

- The simplified calculations, summarized in Table 7.1, are very important and useful. Such information should be always advised when taking seismic protection measures for artefacts.

7.6 Preliminary numerical results

Preliminary results that concern the investigation of the bust-pedestal system, modelled as a two-block problem are presented below. The busts considered are freestanding on a solid pedestal (Figure 7.11). The pedestal has dimensions $2b = 0.45m$ and $2h = 1.0m$, while the statue is made of marble and is symmetric with $2b = 0.22m$ and $h = 0.40m$, where h is the height of the center of mass, determined with the aid of laser scanning. The mass of the pedestal and of the statue are $511kg$ and $107kg$, respectively.

In the results shown in Figure 7.16 and 7.17 the distances of the center of mass from each pivot point of the upper block, have been assumed equal, i.e. symmetric two-block assemblies have been considered. The system is subjected to the Emilia,

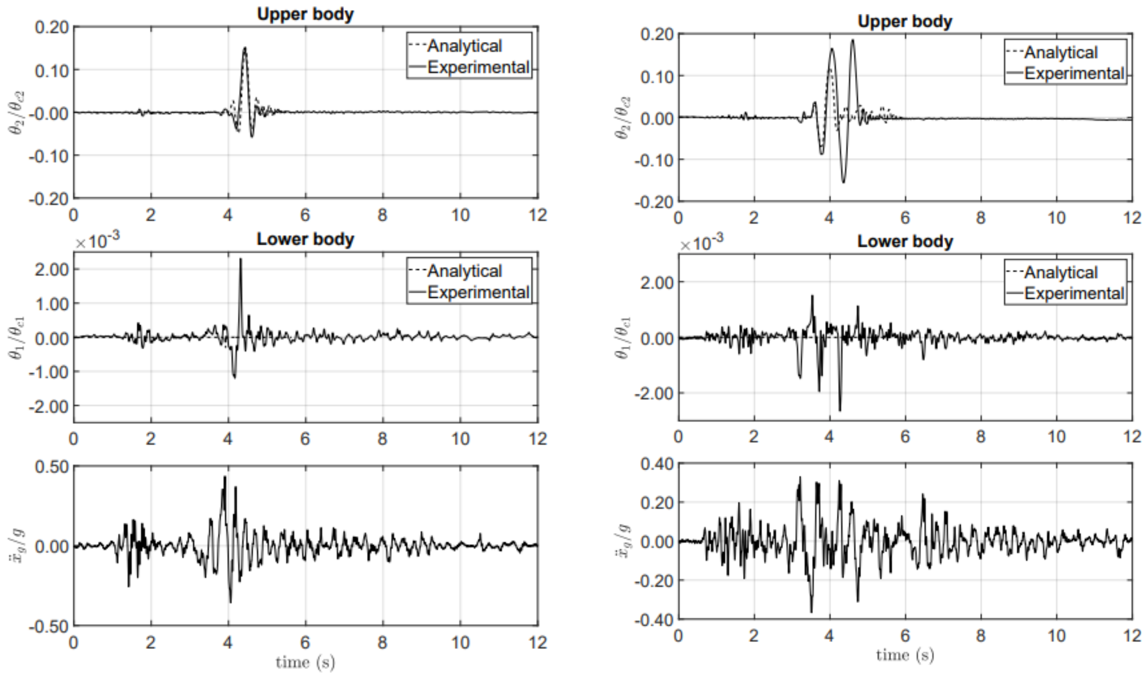

(a) (b)

FIGURE 7.16: Comparison of rocking rotation between experimental results: response history to record Emilia in direction (a) X (PGA=0.44g) and (b) Y (PGA=0.37g).

2012 record in X or Y direction and for different values of peak ground acceleration (*PGA*). The four records adopted have *PGA* in the range of $0.37 - 0.44g$. In both figures it is observed that the experimental results can not be assessed exactly but in the response of the "critical" upper block is adequately determined. This is because of the simplified equations adopted and due to the fact that the asymmetry of the upper block has not been considered in the simulations. Possible other sources of uncertainty are the damping of the system, the possible sliding and the three-dimensional motion that is not considered explicitly. In either case, the rotations of the pedestal are small compared to those of the statue since the pedestal requires large accelerations in order to be set in motion.

Representative results are presented also for the case of Fanciulla statue that is free-standing directly on the shake table. A fair agreement between the experimental behavior and the simulation output shown in Figures 7.18 and 7.19. Figure 7.18 presents the response time-histories of two representative runs (named here 312 and 313) of configuration I.5, while in Figure 7.19 runs 316 and 322 of configuration I.5 have been considered. In Figure 7.18a the record Emilia in X direction has been considered using a scaling value of 1.06 (i.e. the *PGA* is 6% larger than the *PGA* of the recorded signal)

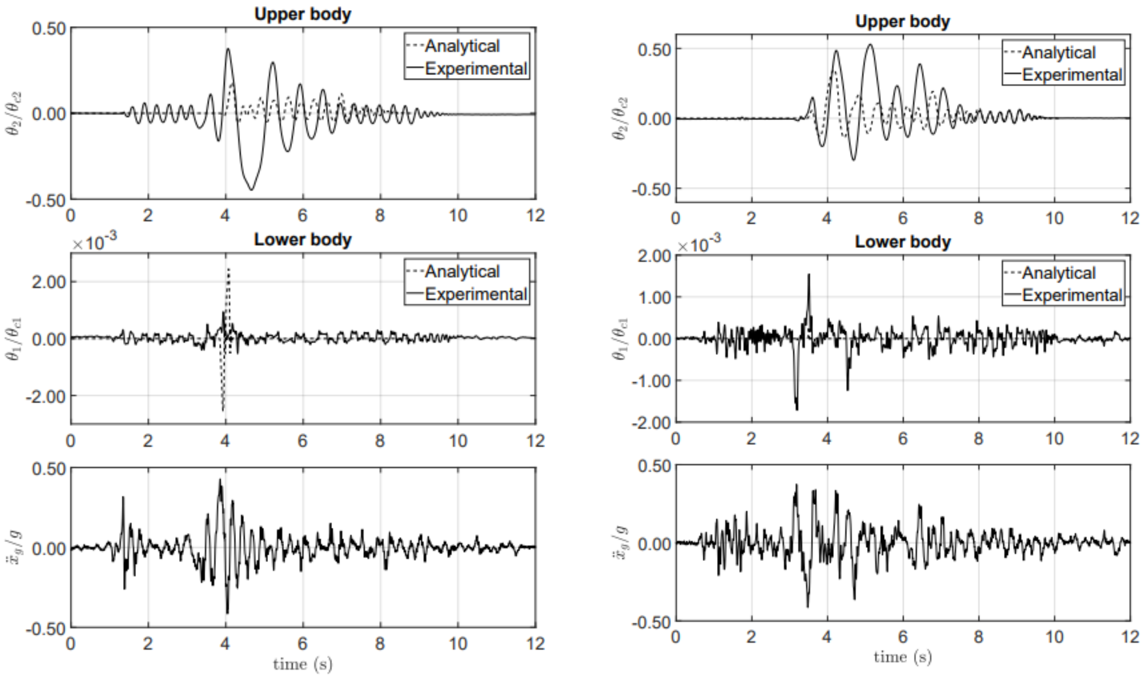

(a) (b)

FIGURE 7.17: Comparison of rocking rotation between experimental results: response history to record Emilia in direction (a) X (PGA=0.43g) and (b) Y (PGA=0.41g).

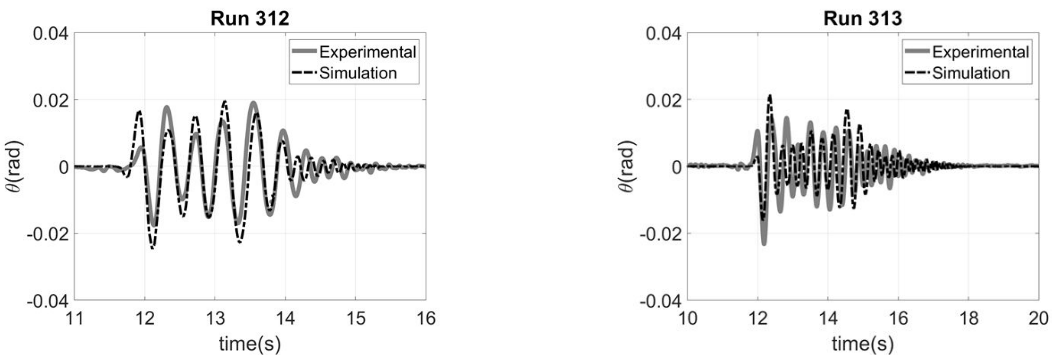

(a) (b)

FIGURE 7.18: Experimental vs numerical results: (a) run #312, (b) run #313.

while in Figure 7.18b the the same record scaled with 1.21. The above values correspond to target PGA 0.35g and 0.40g, respectively. In Figure 7.19a the record Emilia in Y direction has been considered using a scaling value of 1.40 (target $PGA = 0.35g$) while in Figure 7.19b the XYZ components of the same record scaled with 0.76 in order the target PGA in X direction to be equal to 0.25g. The comparison in the latter plot refers to the Y direction response. It can be shown that the simulation results are not

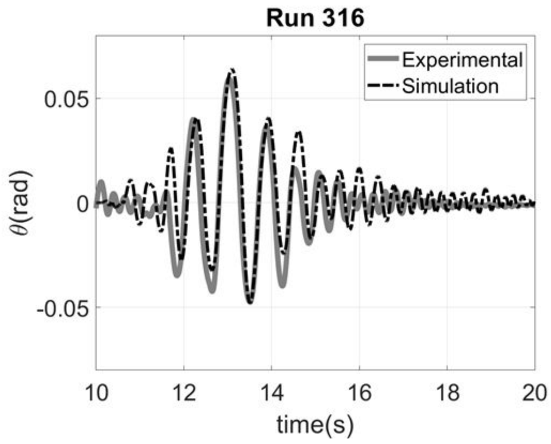

(a)

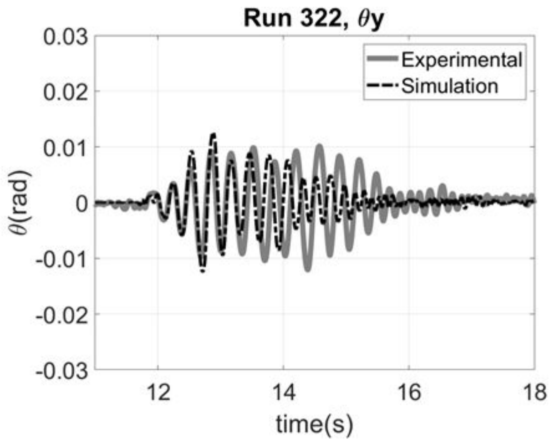

(b)

FIGURE 7.19: Experimental vs numerical results: (a) run #316, (b) run #322.

perfect but could be considered very close to the experimental ones, even if the number of uncertainties is large. Further investigations considering the input parameters of the Finite Element Model and parametric analyses are necessary.

Chapter 8

Conclusions and discussion

8.1 Summary

The seismic response assessment of different rocking structures using simplified models is presented. The modeling focuses on either rocking blocks or rocking frames which are rigid or flexible and freestanding or restrained. Furthermore, the fragility and risk assessment of rocking building contents that are assumed rigid is investigated and the structure's effect is introduced in the calculations. An experimental campaign on either statues or busts standing on a pedestal took place during the current Thesis and some preliminary results are presented. The conclusions are summarized below according to the previous chapters:

Initially, the use of simple single-degree-of-freedom oscillators for the seismic response assessment of rocking systems is discussed. The rocking block problem is solved using beam element models that are connected at their base with a nonlinear rotational spring. This modeling, although approximate in principle, it has been proven able to quickly and robustly solve the rocking problem for either solitary blocks, or other rocking systems. Despite the gap between the response of a real-world rocking structure and the theoretical solution, the proposed models can be seen as a step towards more accurate response estimates for rocking problems, since they permit various refinements thanks to the versatility of the FE method. In fact, four simple models have been proposed; the three models use a lumped mass approach and the fourth is a multimass model. All models are based on Housner's theory considering pure rocking motion of systems that are able to partially uplift and rock. The final choice among the proposed models, depends on the problem at hand, and on the features of the software code that will be adopted. More specifically, the choice between the Spring Models (SMs) and the multi-mass Spring Model (mmSM) case depends on the problem. If the mass can be considered as lumped (e.g. rigid block, restrained rigid blocks), the SM models are easier to implement and thus preferred over the mmSM option. The flexible block assumption depends purely on the properties of the structure. mmSM is preferred for modelling distributed mass deformable rocking bodies because higher mode effects can be better represented. The choice between the three single-mass (SM) models depends on the software adopted, since the SM1 and SM2 are practically identical, while the SM3 is suitable only for rigid blocks.

Moreover, we examined three moment-rotation $M - \theta$ relationships for the nonlinear springs which simulate the restoring moment of the rocking system. The performance of each $M - \theta$ relationship combined with each of the proposed models was assessed under both static and dynamic analysis. The coefficient of restitution, a critical parameter for rocking problems, has been directly considered implementing an "event-based" scheme pausing and resuming the analysis after every impact. The modeling proposed can be implemented in engineering software that follow the direct stiffness method and engineers are comfortable with. The implementation is possible either with an OpenSees script, or with home-made structural analysis software. Finally, two rocking systems were studied: a restrained rocking block and a coupled bending-rocking system where the block is either rigid or flexible. In all cases perfect agreement with results from the literature was achieved.

Extending the previous investigation, a novel modeling approach for the seismic response assessment of rocking frames is proposed. The presented methodology can be again implemented in a finite element framework and thus common civil engineering software can be adopted. The idea is based on the use of rotational springs with negative stiffness at the rocking interfaces, top and bottom of each column that consist a rocking frame. The efficiency of this approach was first shown by the authors for the solitary rocking block (Diamantopoulos and Fragiadakis, 2019) and is here extended to flexible rocking columns and then to rocking frames. The problem formulation is first discussed having as reference the freestanding rocking block which is revisited in order to obtain more accurate initial conditions. This is important for the seismic response assessment of flexible columns under large axial force, as is often the case of rocking bridge members. Furthermore, the modelling of rocking frames, first rigid and then flexible, using negative-stiffens rotational springs placed at the rocking interfaces is discussed in detail. The parameters of the springs are chosen depending on the analysis type, i.e. including or not the $P - \Delta$ effects, and the location of the spring. However, it is also critical to correctly chose the rotational moment inertia terms that enter into the mass matrix. A simplified alternative, suitable for the case of rigid frames can be obtained if the SDOF oscillator is adjusted to the generalized equation of the rocking problem. Restrained rocking systems are also addressed, since the use of restrainers is a commonly adopted for modern rocking bridges. The modelling presented can be extended to other rocking systems in a straightforward manner offering accurate solutions, reducing the computational cost and avoiding special treatment of the interaction among the structural members. All in all, the approach proposed is a useful and practical tool that can be extensively adopted for modeling any rocking system in engineering practice.

The thesis proposed also a Performance Based Earthquake Engineering (PBEE) risk and reliability assessment framework for freestanding monolithic ancient columns and colonnades. The efficient numerical modeling approach, previously discussed, is adopted. The numerical examples have shown the capacity of the proposed modeling to simulate a variety of problems and to provide accurate fragility assessment criteria within a fully performance-based framework. The findings of the work are summarized as follows: (*i*) A performance-based fragility and risk assessment framework has been proposed. The Engineering Demand Parameter (EDP) is always the normalized rotation θ/α, while there are various options for the Intensity Measure (IM). The average spectral acceleration S_a^{avg} is a useful and suitable IM which can be adopted for the fragility assessment of those systems. The fragility assessment can be performed with either a cloud or a multiple stripe analysis approach, but some caution is required for the simulations that produce overturning or do not uplift the structure. (*ii*) Fragility and risk assessment can be used in order to compare the capacity of different structural configuration and also to study the sensitivity of those ancient structures to different problem parameters.

On the other hand, the fragility assessment of freestanding building contents is discussed in the current work. The building contents were modelled as rigid blocks and it was assumed that they are hosted in a four-storey RC building. It has been shown that the problem addressed is complicated since the response of the structure and the contents are coupled. The findings of the study have been been obtained using a single two-dimensional, four-storey building and hence cannot be always generalized. For this reason, further research is required in order to fully understand the effect of the structure on the fragility of freestanding contents. Nevertheless, the work presented should be considered as an attempt to offer some first guidelines on how the rocking problem can be handled for freestanding objects that are hosted in a building. Some of the major conclusions of the current section are briefly summarized as follows: (*i*) An IDA-based (Incremental Dynamic Analysis) fragility-assessment methodology, tailored to freestanding building contents, is presented. It shown that freestanding building contents, when hosted in a structure, may be more or less vulnerable than they are in the ground. This depends on the geometry of the contents and the dynamic characteristics of the structure. Moreover, the fragility of the blocks should not be calculated independently of the collapse, or damage, of the building. (*ii*) A simplified approach that can be used for the fragility assessment of a block when both the fragilities of the structure and of the block are known is investigated. Furthermore, it is shown that it is important to use the IM of the structure for the risk assessment of the block since it ensures consistency between the block and the structure and it also allows to directly calculate the overturning MAF of the contents. Among the IMs examined, it has been found that the PFV, in general, is preferable. (*iii*) Depending on the post-processing of the results, cloud or multiple-stripe data are obtained. The proper post-processing in order to consistently handle rocking, non-rocking and overturned blocks should be considered; otherwise the fragilities will be underestimated. (*iv*) A stocky and a slender block have been considered, showing that the geometry of the block is critical. It is found that the more stocky blocks are more safe on the ground floor while the slender blocks are safer when hosted in the building. Of course this observations refers to the four-storey structure considered, but it clearly shows the importance of both building and block properties and also the fact that fragility of freestanding contents is very different from that anchored contents that are expected to behave as elastically deforming structures.

In a next step, an extensive experimental campaign on the seismic response of artefacts, is presented. The campaign is based on a work which emphasizes on statues and busts and has been addressed in collaboration with people that consist a team. The tests took place in the framework of SEREME project (Seismic Resilience of Museum Contents) at the AZALEE seismic simulator of CEA in Saclay, Paris under the auspices of the SERA project. The campaign aims to help us understand the seismic behaviour of the selected statues and busts and then to develop novel and cost-effective risk mitigation schemes for improving the seismic resilience of valuable objects hosted in European museums. Two real-scale marble (replicas are usually made from gypsum) roman statues and three busts of three roman emperors standing on three pedestals of different types and size are investigated concerning their response under seismic loading. The artefacts are considered either isolated or non-isolated. In the latter case, two new and highly efficient base isolation systems, tailored to art objects, are tested. The efficiency and the effectiveness of the isolators are of the main interest for the authors. The first isolator is a pendulum-based system, while the second utilizes Shape Memory Alloy wires. Different configurations were considered for examining all cases. The importance of the hosting building is also examined, i.e. building type, stiffness and story that hosts the artefacts. Specifically tailored, numerical models of varying complexity and Finite Element models for single and two-block rocking systems were developed for the needs of this study and are also assessed against the experimental results.

8.2 Future work

Some aspects that deserve further research are summarized below:

- Investigation of the interaction between sliding and rocking and how could it be modeled, thus extending the proposed approach. The extension can be based on simplified approaches and probably on an additional translational spring that considers sliding. According to the experimental investigation, the coupled rocking-sliding motion is common in museum artifacts or generally in building contents.

- More thorough investigation of the interaction between rocking and other non-linear phenomena, e.g. upthrow, deformability, inelasticity and damping following an impact. During a seismic excitation all the above should be considered although the rocking motion is predominant.

- Extension of the models to three-dimensional cases. Two-dimensional models are accurate and useful for the fragility assessment or approximate solutions of rigid or flexible structures. However, the tree-dimensional effects are neglected and thus an extension could be a useful tool in many applications.

- A more thorough investigation of the two-block problem using simplified approaches. Two-block assemblies are, also, common for museum artifacts and especially the case of asymmetric upper block. Therefore, simplified approaches either using Finite Element software or home-made codes is an important step for the risk mitigation of artefacts.

- Extension of the fragility and risk investigation using a three-dimensional building model to include the bidirectional effect of the earthquake, the torsional coupling and the direction of the earthquake. A more detailed building model and a detailed model for the contents is also of interest.

- Extension of the Finite Element models for modeling base-isolated statues and busts using the experimental data of SEREME project. The simulation of the isolation system is a challenging task. Furthermore, the seismic isolation of rocking systems is a topic that has not received the appropriate attention in the literature.

Bibliography

ABAQUS, Version 6.14-2 (2011). *SIMULIA (ABAQUS Inc., Providence, USA)*.

Acikgoz, S and M DeJong (2016). “Analytical modelling of multi-mass flexible rocking structures”. In: *Earthq Eng Struct Dyn* 45, pp. 2103–2122.

Acikgoz, S and MJ DeJong (2012). “The interaction of elasticity and rocking in flexible structures allowed to uplift”. In: *Earthq Eng Struct Dyn* 41.15, pp. 2177–2194.

Aghagholizadeh, M and N Makris (2018). “Seismic Response of a Yielding Structure Coupled with a Rocking Wall”. In: *Journal of Structural Engineering* 144.2, p. 4017196.

Ambraseys, N. and I. N. Psycharis (2012). “Assessment of the long-term seismicity of Athens from two classical columns”. In: *Bull Earthquake Eng* 10, pp. 1635–1666.

Anagnostopoulos, S et al. (2019). “Fractal-like overturning maps for stacked rocking blocks with numerical and experimental validation”. In: *Soil Dynamics and Earthquake Engineering* 125, p. 105659.

ASCE 43-05 (2005). *Seismic Design Criteria for Structures, Systems, and Components in Nuclear Facilities*. American Society of Civil Engineers (ASCE). Reston VA.

ASCE/SEI 41-06 (2007). *Seismic Rehabilitation of Existing Buildings*. American Society of Civil Engineers (ASCE). Reston VA.

Avgenakis, E and I Psycharis (2017). “Modeling of Rocking Elastic Flexible Bodies under Static Loading Considering the Nonlinear Stress Distribution at Their Base”. In: *Journal of Structural Engineering* 143.7, p. 04017051.

Baker, JW (2015). “Efficient Analytical Fragility Function Fitting Using Dynamic Structural Analysis”. In: *Earthquake Spectra* 31.1, pp. 579–599.

Bakhtiary, E and P Gardoni (2016). “Probabilistic seismic demand model and fragility estimates for rocking symmetric blocks”. In: *Engineering Structures* 114, pp. 25–34.

Caliò, I and A Greco (2016). “Large displacement behavior of a rocking flexible structure under harmonic excitation”. In: *Journal of Vibration and Control* 22.4, pp. 988–1002.

Calio, I and M Marletta (2003). “Passive control of the seismic rocking response of art objects”. In: *Engineering Structures* 25.8, pp. 1009–1018.

Chatzis, MN and AW Smyth (2012). “Robust modeling of the rocking problem”. In: *J. Eng. Mech.* 138.3, pp. 247–262.

Chatzis, MN et al. (2017). “Examining the Energy Loss in the Inverted Pendulum Model for Rocking Bodies”. In: *Journal of Engineering Mechanics* 143.5, p. 04017013.

Chen, Y et al. (2006). “Seismic isolation of viaduct piers by means of a rocking mechanism”. In: *Earthquake Engineering & Structural Dynamics* 35.6, pp. 713–736.

Cheng, CT (2008). “Shaking table tests of a self-centering designed bridge substructure”. In: *Eng Struct* 30.12, pp. 3426–3433.

Chopra, AK (1995). *Dynamics of Structures: Theory and Applications to Earthquake Engineering*. ISBN: 0-13-156174-X.

Chopra, AK and CS Yim (1985). “Simplified earthquake analysis of structures with foundation uplift”. In: *J. Struct. Eng.* 111, pp. 906–930.

Contento, A and A Di Egidio (2014). “On the use of base isolation for the protection of rigid bodies placed on a multi-storey frame under seismic excitation”. In: *Engineering Structures* 62-63, pp. 1–10.

Contento, A et al. (2019). “Probabilistic Models to Assess the Seismic Safety of Rigid Block-Like Elements and the Effectiveness of Two Safety Devices”. In: *Journal of Structural Engineering* 145.11, p. 04019133.

Cundall, P. A. and O. D. L. Strack (1979). “A discrete numerical model for granular assemblies”. In: *Géotechnique* 29.1, pp. 47–65.

Dar, A et al. (2016). “Evaluation of ASCE 43-05 Seismic Design Criteria for Rocking Objects in Nuclear Facilities”. In: *Journal of Structural Engineering* 142.11, p. 4016110.

Dar, A et al. (2018). “Seismic response of rocking frames with top support eccentricity”. In: *Earthquake Engineering & Structural Dynamics* 47.12, pp. 2496–2518.

Dar, A et al. (2019). “Seismic response of rocking frames with unsymmetrical piers”. In: 25th Conference on Structural Mechanics in Reactor Technology. Charlotte, NC, USA.

DeJong, MJ and EG Dimitrakopoulos (2014). “Dynamically equivalent rocking structures”. In: *Earthquake Engineering and Structural Dynamics* 43.10, pp. 1543–1563.

Di Egidio, A and A Contento (2009). “Base isolation of slide-rocking non-symmetric rigid blocks under impulsive and seismic excitations”. In: *Engineering Structures* 31.11, pp. 2723 –2734.

Diamantopoulos, S and M Fragiadakis (2019). “Seismic response assessment of rocking systems using single degree of freedom oscillators”. In: *Earthquake Engineering & Structural Dynamics* 48.7, pp. 689–708.

— (2022). “Modeling of rocking frames under seismic loading”. In: *Earthquake Engineering & Structural Dynamics* 51.1, pp. 108–128.

Dimitrakopoulos, E and M DeJong (2012a). “Revisiting the rocking block: closed-form solutions similarity laws”. In: *Proceedings of the Royal Society of London A: Mathematical, Physical and Engineering Sciences* 468, pp. 2294–2318.

Dimitrakopoulos, E and T Paraskeya (2015). "Dimensionless fragility curves for rocking response to near-fault excitations". In: *Earthq Eng Struct Dyn* 44.12, pp. 2015–2033.

Dimitrakopoulos, EG and MJ DeJong (2012b). "Revisting the rocking block: closed-form solutions and similarity laws". In: Proceedings of the Royal Society A. 468. London A: Mathematical, Physical and Engineering Sciences.

Dimitrakopoulos, E.G. and E.D.W. Fung (2016). "Closed-form rocking overturning conditions for a family of pulse ground motions". In: *Proceedings of the Royal Society of London A: Mathematical, Physical and Engineering Sciences* 472, p. 2016066220160662.

Dimitrakopoulos, EG and AI Giouvanidis (2015a). "Seismic response analysis of the planar rocking frame". In: *Journal of Engineering Mechanics* 141.7, p. 04015003.

— (2015b). "Seismic response analysis of the planar rocking frame". In: *Journal of Engineering Mechanics* 141.7, p. 04015003.

DiSarno, L et al. (2015). "Dynamic properties of typical consultation room medical components". In: *Engineering Structures* 100, pp. 442 –454.

Eads, Laura et al. (2015). "Average spectral acceleration as an intensity measure for collapse risk assessment". In: *Earthquake Engineering & Structural Dynamics* 44.12, pp. 2057–2073.

ElGawady, MA and A Sha'lan (2011). "Seismic Behavior of Self-Centering Precast Segmental Bridge Bents". In: *Journal of Bridge Engineering* 16.3, pp. 328–339.

FEMA (2012a). *FEMA E-74: Reducing the Risks of Nonstructural Earthquake Damage - A Practical Guide*.

— (2012b). *FEMA P-58-1: Seismic Performance Assessment of Buildings - Volume 1, Methodology*.

FEMA P-58-1 (2012). *Seismic Performance Assessment of Buildings*. Applied Technology Council.

FEMA P695 Federal Emergency Management Agency, (FEMA) (2009). *Quantification of Building Seismic Performance Factors*. Washington, D.C.

Fragiadakis, M and S Diamantopoulos (2020). "Fragility and risk assessment of freestanding building contents". In: *Earthquake Engineering & Structural Dynamics* 49.10, pp. 1028–1048.

Fragiadakis, M et al. (2015). "Seismic assessment of structures and lifelines". In: *Journal of Sound and Vibration* 334, pp. 29–56.

Fragiadakis, M et al. (2016). "Parametric Investigation of The Dynamic Response of Rigid Blocks Subjected to Synthetic Near-Source Ground Motion Records". In: ECCOMAS Congress 2016: VII European Congress on Computational Methods in Applied Sciences and Engineering. Crete Island, Greece.

Giouvanidis, A and E Dimitrakopoulos (2016a). “Nonsmooth dynamic analysis of sticking impacts in rocking structures”. In: *Bulletin of Earthquake Engineering* 15.5, pp. 2273–2304.

Giouvanidis, AI and EG Dimitrakopoulos (2016b). “The role of the prestressed tendons on the seismic performance of hybrid rocking bridge bents”. In: ECCOMAS Congress 2016 VII European Congress on Computational Methods in Applied Sciences and Engineering. Crete Island, Greece.

Giouvanidis, AI et al. (2015). “Seismic response of rocking bridge bents with parameterized flag-shaped hysteretic behavior”. In: Proceedings of the Tenth Pacific Conference on Earthquake Engineering Building an Earthquake-Resilient Pacific. Sydney, Australia.

Giouvanidis, AI et al. (2017). “Vulnerability assessment of flag-shaped hysteretic rocking bridge bentsS”. In: Rhodes, Greece: Proceedings of the 6th International Conference on Computational Methods in Structural Dynamics and Earthquake Engineering (COMPDYN 2017).

Group, Itasca Cosulting (1998). *Inc., 1998. 3-dimensional Distinct Element Code (3DEC), Theory and Background,* Minneapolis, Minnesota.

Housner, GW (1963). “The behavior of inverted pendulum structures during earthquakes”. In: *Bulletin of the Seismological Society of America* 53.2, pp. 404–417.

Ishiyama, Y (1982a). “Motions of rigid bodies and criteria for overturning by earthquake excitations”. In: *Earthq Eng Struct Dyn* 10.5, pp. 635–650.

— (1982b). “Motions of rigid bodies and criteria for overturning by earthquake excitations”. In: *Earthq Eng Struct Dyn* 10, pp. 635–650.

Jalayer, F (2003). “Direct probabilistic seismic analysis: Implementing non-linear dynamic assessments”. PhD thesis. Department of Civil and Environmental Engineering, Stanford University, CA.

Jalayer, F et al. (2017). “Analytical fragility assessment using unscaled ground motion records”. In: *Earthquake Engineering & Structural Dynamics* 46.15, pp. 2639–2663.

Kakouris, E et al. (2018). “A material point method for studying rocking systems”. In: 16ECEE, 16th European Conference on Earthquake Engineering. Thessaloniki, Greece.

Kalkan, E and V Graizer (2007). “Coupled Tilt and Translational Ground Motion Response Spectra”. In: *Journal of Structural Engineering* 133.5, pp. 609–619.

Kavvadias, I et al. (2017a). “Rocking spectrum intensity measures for seismic assessment of rocking rigid blocks”. In: *Soil Dynamics and Earthquake Engineering* 101, pp. 116–124.

Kavvadias, I et al. (2017b). “Seismic Response Parametric Study of Ancient Rocking Columns”. In: *International Journal of Architectural Heritage* 11.6, pp. 791–804.

Kohrangi, Mohsen et al. (2017). "Site dependence and record selection schemes for building fragility and regional loss assessment". In: *Earthquake Engineering & Structural Dynamics* 46.10, pp. 1625–1643.

Konstantinidis, D and N Makris (2009). "Experimental and analytical studies on the response of freestanding laboratory equipment to earthquake shaking". In: *Earthq Eng Struct Dyn* 38, pp. 827–848.

Konstantinidis, D and F Nikfar (2015). "Seismic response of sliding equipment and contents in base-isolated buildings subjected to broadband ground motions". In: *Earthq Eng Struct Dyn* 44, pp. 865–887.

Kounadis, A.N. et al. (2012). "Overturning instability of a two-rigid block system under ground excitation". In: *ZAMM - Journal of Applied Mathematics and Mechanics / Zeitschrift für Angewandte Mathematik und Mechanik* 92.7, pp. 536–557.

Lallemant, D et al. (2015). "Statistical procedures for developing earthquake damage fragility curves". In: *Earthq Eng Struct Dyn* 44, pp. 1373–1389.

Ma, QT and JW Butterworth (2012). "Simplified expressions for modelling rigid rocking structures on two-spring foundations". In: *Bulletin of the New Zealand Society for Earthquake Engineering* 45.1, 31–39.

Makris, N and M Aghagholizdeh (2017). "The dynamics of an elastic structure coupled with a rocking wall". In: *Earthq Eng Struct Dyn* 46.6, pp. 945–962.

Makris, N and D Konstantinidis (2003). "The rocking spectrum and the limitations of practical design methodologies". In: *Earthq Eng Struct Dyn* 32, pp. 265–289.

Makris, N and MF Vassiliou (2013). "Planar rocking response and stability analysis of an array of free-standing columns capped with a freely supported rigid beam". In: *Earthquake Engineering and Structural Dynamics* 42.3, pp. 431–449.

— (2015). "Dynamics of the Rocking Frame with Vertical Restrainers". In: *Journal of Structural Engineering* 141.10, p. 04014245.

Mander, JB and C-T Cheng (1997). *Seismic resistance of bridge piers based on damage avoidance design*. Tech. rep. Technical Report NCEER-97-0014. National Center for Earthquake Engineering Research, State Univ. of New York.

Mathey, C et al. (2016). "Behavior of rigid blocks with geometrical defects under seismic motion: an experimental and numerical study". In: *Earthq Eng Struct Dyn* 45.15, pp. 2455–2474.

Matlab (2016). *Matlab Version 2016a, The Language of Technical Computing*.

Mazzoni, S et al. (2006). *Opensees command language manual*. Pacific Earthquake Engineering Research (PEER) Centre, Berkeley, California, United States.

McKenna, F and GL Fenves (2001). *The OpenSees Command Language Manual*. Pacific Earthquake Engineering Research Centre, University of California, Berkeley.

Milne, J (1885). “Seismic Experiments”. In: *Transactions of the Seismological Society of Japan* 8, pp. 1–82.

NIST (2017). *ATC-120: Seismic Analysis, Design, and Installation of Nonstructural Components and Systems – Background and Recommendations for Future Work. GCR 17-917-44, prepared by the Applied Technology Council for the National Institute of Standards and Technology, Washington, D.C., USA.*

Palermo, A et al. (2007). “Design, modeling, and experimental response of seismic resistant bridge piers with posttensioned dissipating connections”. In: *J Struct Eng* 133.11, pp. 1648–1661.

Papantonopoulos, C. et al. (2002). “Numerical prediction of the earthquake response of classical columns using the distinct element method”. In: *Earthquake Engineering & Structural Dynamics* 31.9, pp. 1699–1717.

Pappas, A et al. (2017). “Efficiency of alternative intensity measures for the seismic assessment of monolithic free-standing columns”. In: *Bull Earthquake Eng* 15, pp. 1635–1659.

Petrone, C et al. (2017). “Numerical modelling and fragility assessment of typical free-standing building contents”. In: *Bulletin of Earthquake Engineering* 15.4, pp. 1609–1633.

Podany, J (2015). “An overview of Seismic Damage Mitigation for Museums”. In: International Symposium on Advances of Protection Devices for Museum Exhibits. Beijing & Shanghai, China.

Politopoulos, I (2010). “Response of seismically isolated structures to rocking-type excitations”. In: *Earthq Eng Struct Dyn* 39, pp. 325–342.

Priestley, MJN et al. (1978). “Seismic response of structures free to rock on their foundations”. In: *Bulletin of the New Zealand National Society for Earthquake Engineering* 11.3, pp. 141–150.

Priestley, MN et al. (1996). *Seismic design and retrofit of bridges*. ISBN 9780471579984. New York: Wiley.

Prieto, F et al. (2004). “Impulsive Dirac-delta forces in the rocking motion”. In: *Earthq Eng Struct Dyn* 33.7, pp. 839–857.

Przemieniecki, JS (1968). *Theory of matrix structural analysis*.

Psycharis, I and PC Jennings (1983). “Rocking of slender rigid bodies allowed to uplift”. In: *Earthq Eng Struct Dyn* 11.1, pp. 57–76.

Psycharis, I et al. (2013a). “Seismic reliability assessment of classical columns subjected to near-fault ground motions”. In: *Earthq Eng Struct Dyn* 42.14, pp. 2061–2079.

Psycharis, IN (1983). “Dynamics of flexible systems with partial lift-off”. In: *Earthq Eng Struct Dyn* 11.4, pp. 501–521.

Psycharis, I.N. (1990). “Dynamic behaviour of rocking two-block assemblies”. In: *Earthquake Engineering & Structural Dynamics* 19.4, pp. 555–575.

Psycharis, IN et al. (2013b). “Seismic reliability assessment of classical columns subjected to near-fault ground motions”. In: *Earthquake Engineering and Structural Dynamics* 42.14, pp. 2061–2079.

Purvance, M et al. (2008). “Freestanding block overturning fragilities: Numerical simulation and experimental validation”. In: *Earthq Eng Struct Dyn* 37, pp. 791–808.

Singhal, A and A Kiremidjian (1998). “Bayesian Updating of Fragilities with Application to RC Frames”. In: *Journal of Structural Engineering* 124.8, pp. 922–929.

Skinner, R et al. (1980). “Hysteretic dampers for the protection of structures from earthquakes”. In: *Bull. N. Z. Natl. Soc. Earthquake Eng.* 13.1, pp. 22–36.

Spanos, Pol D. et al. (2001). “Dynamic analysis of stacked rigid blocks”. In: *Soil Dynamics and Earthquake Engineering* 21.7, pp. 559–578.

Spyrakos, CC et al. (2016). “Application of predictive models to assess failure of museum artifacts under seismic loads”. In: *Journal of Cultural Heritage* 23.1, pp. 11–21.

Thomaidis, IM et al. (2020). “Dynamics and seismic performance of rocking bridges accounting for the abutment-backfill contribution”. In: *Earthquake Engineering & Structural Dynamics* 49.12, pp. 1161–1179.

Toumbakari, E and I.N. Psycharis (2010). “Parametric investigation of the seismic response of a column of the Aphrodite Temple in Amathus, Cyprus”. In: 14th European Conference on Earthquake Engineering (14 ECEE). Ohrid, FYROM.

Vamvatsikos, D and CA Cornell (2004). “Applied Incremental Dynamic Analysis”. In: *Earthquake Spectra* 20.2, pp. 523–553.

Vamvatsikos, D and M Fragiadakis (2010). “Incremental dynamic analysis for estimating seismic performance sensitivity and uncertainty”. In: *Earthq.Eng. Struct. Dyn* 39.2, pp. 141–163.

Vassiliou, MF and N Makris (2015). “Dynamics of the Vertically Restrained Rocking Column”. In: *J. Eng. Mech* 141.12, p. 04015049.

Vassiliou, MF et al. (2014). “A finite element model for seismic response analysis of deformable rocking frames”. In: *Earthq Eng Struct Dyn* 43.10, pp. 1463–1481.

Vassiliou, MF et al. (2015). “An analytical model of a deformable cantilever structure rocking on a rigid surface: development and verification”. In: *Earthq Eng Struct Dyn* 44.15, pp. 2775–2794.

Vassiliou, MF et al. (2016). “Dynamic response analysis of solitary flexible rocking bodies: modeling and behavior under pulse-like ground excitation”. In: *Earthq Eng Struct Dyn* 46.3, pp. 447–466.

Vlachos, N et al. (2019). "Seismic response assessment of artefacts freestanding on a solid pedestal". In: 4th Hellenic National Conference on Earthquake Engineering and Engineering Seismology. Athens, Greece.

Voyagaki, E et al. (2013). "Rocking response and overturning criteria for free standing rigid blocks to single—lobe pulses". In: *Soil Dynamics and Earthquake Engineering* 46, pp. 85 –95.

Wacker, JM et al. (2005). *Design of precast concrete piers for rapid bridge construction in seismic regions*. Tech. rep. Research Report. Washington State Transportation Center, Univ. of Washington, Seattle, Washington.

Wittich, C.E. and T.C. Hutchinson (2015). "Shake table tests of stiff, unattached, asymmetric structures". In: *Earthquake Engineering & Structural Dynamics* 44.14, 2425–2443.

— (2017). "Shake table tests of unattached, asymmetric, dual-body systems". In: *Earthquake Engineering & Structural Dynamics* 46.9, 1391–1410.

Yim, CS and AK Chopra (1985). "Simplified earthquake analysis of multistory structures with foundation uplift". In: *Earthq Eng Struct Dyn* 11.12, pp. 2708–2731.

Zentner, I et al. (2017). "Fragility analysis methods: Review of existing approaches and application". In: *Nuclear Engineering and Design* 323, pp. 245–258.

Zhang, J and N Makris (2001). "Rocking response of free-standing blocks under cycloidal pulses". In: *J. Eng. Mech, ASCE* 127.5, pp. 473–483.

Zhou, Y et al. (2019). "Shaking Table Tests of Post-Tensioned Rocking Bridge with Double-Column Bents". In: *Journal of Bridge Engineering* 24.8, p. 04019080.